AN INVESTIGATION OF THE MORPHOLOGY EVOLUTION IN EARLY-STAGE NUCLEATION AND GROWTH OF CARBOXYL AND THIOL CAPPED GOLD NANOPARTICLES

by

PAK LEUNG AIDAN YIU

A thesis submitted to the University of Birmingham for the degree of

DOCTOR OF PHILOSOPHY

School of Geography, Earth and Environmental Science

College of Lift and Environmental Sciences

University of Birmingham

January 2025

UNIVERSITY OF
BIRMINGHAM

University of Birmingham Research Archive

e-theses repository

This unpublished thesis/dissertation is copyright of the author and/or third parties. The intellectual property rights of the author or third parties in respect of this work are as defined by The Copyright Designs and Patents Act 1988 or as modified by any successor legislation.

Any use made of information contained in this thesis/dissertation must be in accordance with that legislation and must be properly acknowledged. Further distribution or reproduction in any format is prohibited without the permission of the copyright holder.

Abstract

This thesis explores the growth and stability of sub-10 nm gold nanoparticles (AuNPs) synthesized in aqueous media using various carboxyl and thiol based capping agents. An in-depth investigation into early nucleation stages and initial growth dynamics was conducted using high-angle annular dark-field scanning transmission electron microscopy (HAADF-STEM) and reactive molecular dynamics simulations (r-MD), with a focus on combining classical and non-classical nucleation pathways and the role of pre-nucleation clusters (PNCs).

The first research chapter examined the size and shape evolution of AuNPs synthesized with sodium borohydride as a reducing agent. Key factors such as pH, molar ratio of capping agents, and the chemical structure of carboxyl-based ligands were analysed. Findings revealed unexpected behaviours, such as the limited influence of higher molar ratios on particle size and the optimal stability at pH 6. Pre-nucleation clusters were identified as metastable intermediates across most conditions, indicating their potential role in influencing particle growth and morphology throughout the nucleation process.

The second research chapter compared the growth and morphology of AuNPs capped with L-cysteine and glutathione (both thiol group ligands) to those capped with carboxyl group ligands. Distinct ligand dependent behaviours were observed, with carboxyl group PNCs exhibiting tendency to aggregate, leading to structural transformations, while thiol-based PNCs displayed non aggregate behaviours,

promoting stable but distinct growth pathways. The persistence of PNCs in solution for up to 28 days, their size range, and their influence on aging processes, including the formation of non-spherical morphologies, were characterized, suggesting their influencing role in deviating from classical growth pathways.

The third research chapter applied reactive molecular dynamics simulations to provide atomistic insights into ligand mediated nucleation and growth mechanisms. Carboxyl groups were found to stabilize AuNPs through coordination interactions, while thiol groups formed robust covalent bonds that hindered growth but occasionally induced destabilization. Simulations highlighted the interplay between carboxyl and thiol ligands in guiding nanoparticle nucleation and growth, offering a detailed understanding of the structural evolution of AuNPs.

Overall, this thesis demonstrates the critical role of PNCs as intermediates in nanoparticle formation and growth, demonstrating their persistence, metastable nature, and ligand dependent behaviours. These findings bridge the classical and non-classical nucleation pathways, revealing how ligand chemistry governs PNC-mediated interactions, which in turn, influence the stability, morphology and unpredictable evolution of nanoparticles. This work provides new insights into the formation of PNCs and the interaction with crystallised NPs into irreversible changes of morphology.

Acknowledgements

First, I would like to express my deepest gratitude to my supervisor, Professor Eugenia Valsami-Jones. Her support and insightful guidance have been instrumental in bringing me to this point. Her direction in my research has been invaluable, and even when I decided to pursue a "wild goose chase," she continued to provide steadfast assistance over the past four years.

I am also sincerely grateful to my co-supervisor, Dr. Wolfgang Theis, from the Nanoscale Physics Research Laboratory at the University of Birmingham. He taught me how to use STEM and was always there when I needed technical assistance. His guidance not only strengthened my trust in my imaging skills but also laid a solid foundation for my thesis. He taught me how to extract critical information from STEM and EDS, offering invaluable insights into interpreting simulation results.

Next, I would like to thank all my colleagues in the Nano Group. The support and camaraderie we shared over these four years will remain unforgettable. From enduring broken instruments to hunting down missing chemicals and glassware, the struggles we faced together have left me with cherished memories. I will remember you all for the rest of my life.

Lastly, I would like to extend my heartfelt thanks to my family, especially my mother, for her financial support and unwavering belief in me, which allowed me to

focus on my studies without needing to work. I am also deeply grateful to my girlfriend, Michelle, for her love and patience over these four years overseas (and another four years during my master's degree). Words cannot adequately express the depth of my gratitude.

Table of Contents

ABSTRACT I

ACKNOWLEDGEMENTS III

TABLE OF CONTENTS V

LIST OF FIGURES XII

LIST OF TABLES XXXI

LIST OF ABBREVIATIONS XXXII

CHAPTER 1 : INTRODUCTION 1

1.1 Scientific rationale 1

1.2 Aims and objectives of research 2

1.3 Aim 1 3

1.4 Aim 2 3

1.5 Aim 3 4

1.6 Layout of thesis 4

CHAPTER 2: LITERATURE REVIEW 7

2.1 Introduction 7

2.2 Background of nanoscience 7

2.3 Methods of making nanoparticles 8

2.4 The science of nanomaterial synthesis 10

2.5 Growth and other related mechanisms 14

2.6 Colloidal stability 19

2.7 Importance of gold nanoparticles 22

2.8 Chemical synthesis of gold nanoparticles 24

2.9 Characterization techniques 27

2.10 Simulation 31
2.11 Recent advancements and future directions 35
3.12 Conclusion 36
CHAPTER 3: METHODOLOGY 38
3.1 Introduction 38
3.2.1 High-Angle Annular Dark Field Scanning Transmission Electron Microscopy (HAADF-STEM) 38
3.2.2 Mapping nanoparticles to the collector 40
3.2.3 Procedure of operating STEM 40
3.2.4 Beam shower 42
3.2.5 Procedure of extracting sample and imaging 42
3.3.1 Energy-Dispersive x-ray Spectroscopy (EDS) 43
3.3.2 Procedure of using EDS 44
3.4 Experimental approach 45
3.4.1 Acquisition of chemicals 45
3.4.2 Solution preparation 46
3.4.3 General synthesis of AuNPs 46
3.5 Image processing using Image J 47
3.5.1 FFT and intensity plot 47
3.5.2 Size distribution and circularity 48
3.6 Molecular Dynamics (MD) 48
3.6.1 Amsterdam Modelling Suite (AMS) 48
3.6.2 Trajectories of particles 49
3.6.3 Verlet method 50
3.6.4 Simulation box size 50

3.6.5 Periodic Boundary Conditions (PBC) 51
3.6.6 Temperature and pressure control 52
3.6.6.1 Berendsen thermostat 53
3.6.6.2 Nose-Hoover thermostat 53
3.7 Reactive Force-Field (ReaxFF) 54
3.7.1 Principles of ReaxFF 54
3.7.2 Components of ReaxFF 55
3.7.3 Calculating ReaxFF parameters 55
3.8 Radial distribution function (RDF) g(r) 56
3.8.1 Calculating RDF 56
3.8.2 Interpreting RDF results 57
3.9 Simulation detail 58
3.9.1 Generating 100Au cluster, relaxing to 300 K 58
3.9.2 Generating molecule for capping agents, relaxing to 300 K 59
3.9.3 Making the simulation mixture 60
3.9.4 Running the MD to equilibrium 300 K 60
3.9.5 Running the simulation to 3.8M steps, 950 ps 61
CHAPTER 4: AGING EFFECT OF CARBOXYL GROUP CAPPING AGENT ON SUB-10 NM AUNPS 62
4.1 Introduction 62
4.2 Experiment 65
4.3 Layout of the result section (4.4 – 4.8) 69
4.4 Aging of different carboxyl molecule capped AuNPs (acetic acid) 71
4.4.1 Aging of acetate capped AuNPs in different pH at molar ratio of 1:3.5 71
4.4.2 Aging of acetate capped AuNPs in different molar ratio 77

4.5 Aging of different carboxyl molecule capped AuNPs (oxalic acid) 83
4.5.1 Aging of oxalate capped AuNPs in different pH at molar ratio of 1:3.5 83
4.5.2 Aging of oxalate capped AuNPs in different molar ratio 89
4.6 Aging of different carboxyl molecule capped AuNPs (citric acid) 95
4.6.1 Aging of citrate capped AuNPs in pH 6.7 at molar ratio of 1:3.5 95
4.6.2 Aging of citrate capped AuNPs in different molar ratio 96
4.7 Aging of different carboxyl molecule capped AuNPs (propionic acid) 102
4.7.1 Aging of propionic acid capped AuNPs in pH 9.3 at molar ratio of 1:3.5 102
4.7.2 Aging of propionic acid capped AuNPs in different molar ratio 104
4.8 No capping agent 107
4.9 Discussion 108
4.9.1 Comparing acetate pH difference 109
4.9.2 Comparing acetate molar difference 110
4.9.3 Comparing pH 6 acetate molar ratio difference 112
4.10.1 Comparing oxalate pH difference 114
4.10.2 Comparing oxalate molar difference 115
4.10.3 Comparing pH 6 oxalate molar ratio difference 116
4.11 Comparing pH 6 citrate molar ratio difference 118
4.12.1 Comparing 1:1 molar ratio at low pH carboxyl capping agent 119
4.12.2 Comparing 1:1.5 molar ratio at low pH carboxyl capping agent 122
4.12.3 Comparing 1:3.5 molar ratio at pH 6 carboxyl capping agent 123
4.12.4 Comparing 1:7 molar ratio at pH 6 carboxyl capping agent 125
4.13.1 Comparing acetate and propionic acid 1:7 and 1:10.6 at pH 6 126
4.14 Contamination 128
4.15 Effect of pH 129

4.16 Relationship between PNCs and growth kinetics (aging) 129
4.17 Role of capping agent, reduction mechanics and growth prediction 131
4.18 Surface coverage 132
4.19 Circularity discussion for carboxyl group 133
4.20 Conclusion 135
4.21 Future work 136
CHAPTER 5: THE PROPERTIES OF PRENUCLEATION CLUSTERS (PNCS) AND THE INTERACTION WITH THIOL AND CARBOXYL GROUP CAPPED GOLD NANOPARTICLES 137
5.1 Introduction 137
5.2 Experiment 137
5.3 Aging of different thiol molecule capped AuNPs 139
5.3.1 Aging of L-cysteine capped AuNPs in pH 7.5 at molar ratio of 1:3.5 139
5.3.2 Aging of L-cysteine capped AuNPs in pH 8.4 at molar ratio of 1:3.5 141
5.3.3 Aging of glutathione capped AuNPs in pH 8.0 at molar ratio of 1:3.5 142
5.4 Aging of uncapped and citrate capped AgNPs 144
5.4.1 Aging of no capped AgNPs in pH 6.3 144
5.4.2 Aging of citric acid capped AgNPs in pH 6.9 at molar ratio of 1:3.5 145
5.5 Result summary 146
5.6 Properties of PNCs under STEM imaging 147
5.7 Formation and structural dynamics of PNCs in liquid media 150
5.8 Origins of PNCs around AuNPs and AgNPs 152
5.9 Core crystalline AuNPs and shell PNCs 159
5.10 Bridging of PNCs between AuNPs and AgNPs 162
5.11 Crystallization of amorphous PNCs into solid NPs 164
5.12 Adhesion of PNCs on solid AuNPs 166

5.13 PNCs-induced aging vs classical growth mechanisms 168
5.14 PNC-induced nano-string formation 172
5.15 Impact of functional groups on PNCs behaviour 177
5.16 Beam induced growth with PNC to core NPs 179
5.17 Conclusion 181
5.19 Future work 182
CHAPTER 6: MOLECULAR DYNAMICS OF GOLD NANOPARTICLE NUCLEATION AND GROWTH WITH LIGANDS IN AQUEOUS MEDIA 184
6.1 Introduction 184
6.1.1 Advancing nucleation studies through MD simulations 185
6.1.2 Breakthrough in modelling chemical reactions via ReaxFF 186
6.1.3 Objectives of this chapter 186
6.2.1 Role of ligands in nucleation: carboxyl and thiol functional groups 187
6.2.2 Crystallographic considerations for Au 191
6.2.3 Radial distribution function (RDF) analysis 192
6.3 Nucleation with free gold atoms in water without ligands 192
6.4.1 Nucleation with carboxyl group ligand in water (acetic acid) 194
6.4.2 Nucleation with carboxyl group ligand in water (oxalic acid) 196
6.4.3 Nucleation with carboxyl group ligand in water (citric acid) 197
6.4.4 Nucleation with carboxyl group ligand in water (propionic acid) 198
6.5 Nucleation with citric acid pre-bound to 3 Au atoms 199
6.6.1 Nucleation with thiol group ligands (L-Cysteine) 203
6.6.2 Nucleation with thiol group ligands (glutathione) 204
6.7 Comparison of nucleation rates 205
6.8 Citric acid with 100Au NPs 207

6.9 Growth of citrate-capped AuNPs with free gold atoms 210
6.10.1 Growth with carboxyl group ligands (acetic acid) 212
6.10.2 Growth with carboxyl group ligands (oxalic acid) 214
6.11 Comparison of growth rate of carboxyl ligand capped AuNPs 215
6.12 Correlation between growth rates and carboxyl group numbers 217
6.13 Comparison of single carboxyl group ligands (acetic acid vs propionic acid) 219
6.14 Comparison of thiol ligands (L-cys, GSH) with citric acid 220
6.15 Conclusion 221
6.16 Future work 224
CHAPTER 7: CONCLUSIONS AND FUTURE WORK 225
CHAPTER 8: FUTURE DIRECTIONS 234
REFERENCES 237
APPENDIX I 272
APPENDIX II 279
APPENDIX III 282

List of Figures

FIGURE 2. 1 ILLUSTRATION OF TOP-DOWN AND BOTTOM-UP APPROACH (HABIBA ET AL., 2014)..... 9

FIGURE 2. 2 ILLUSTRATION OF THE CHANGE OF GIBBS FREE ENERGY CURVE TO THE CRITICAL SIZE NUCLEUS OF NUCLEATION WITH DIFFERENT NUCLEATION PATHWAY (OU ET AL., 2022)..... 11

FIGURE 2. 3 ILLUSTRATION OF CLASSICAL NUCLEATION AND NON-CLASSICAL NUCLEATION PATHWAY (GEBAUER ET AL., 2014). 13

FIGURE 2. 4 ILLUSTRATION OF GROWTH MECHANISMS, A) AGGLOMERATION, B) AGGREGATION, C) COALESCENCE, D) OSTWALD RIPENING ON TOP AND DIGESTIVE RIPENING ON BOTTOM. 16

FIGURE 2. 5 ILLUSTRATION OF ORIENTED ATTACHMENT MECHANISM (LIU ET AL., 2019B). . 17

FIGURE 2. 6 SCHEMATICS OF DIFFERENT MODELLING AND THEIR STRENGTH (LIN AND WANG, 2023)..... 33

FIGURE 3. 1 ILLUSTRATION OF HAADF-STEM INSTRUMENT (ZHANG ET AL., 2022). 39

FIGURE 3. 2 ILLUSTRATION OF RONCHIGRAM WHEN CALIBRATING THE STEM (PONCE ET AL., 2012)..... 41

FIGURE 3. 3 ILLUSTRATION OF EDS INTERACTION WITH THE SAMPLE (LONG ET AL., 2021). 45

FIGURE 3. 4 ILLUSTRATION OF PBC IN MD (KATIYAR AND JHA, 2018)..... 52

FIGURE 3. 6 FORMULA FOR CALCULATING RDF (RAPAPORT, 2004). 57

FIGURE 4. 1 ILLUSTRATION OF CARBOXYL GROUP CAPPING AGENT AGENTS USED IN THIS STUDY AND THEIR RELATIVE NUMBER OF CARBOXYL GROUPS AND CARBON CHAIN LENGTH. 65

FIGURE 4. 2 A), TOP LEFT PLOT SHOWS THE SIZE DISTRIBUTION OF 1:3.5 ACETATE CAPPED AUNPS IN PH 4.3. B) TOP RIGHT PLOT SHOWS THE CIRCULARITY. C) BOTTOM STEM IMAGES OF SAMPLES COLLECTED AT DIFFERENT TIME POINTS, AFTER THE START OF THE EXPERIMENT: 5 MINUTES, 60 MINUTES, 1 DAY AND 7 DAYS. WHITE ARROWS INDICATE BRIDGING OR STICKING BETWEEN PARTICLES. GREEN ARROWS INDICATE A SHELL FORMATION OR SOFT STRUCTURE AROUND A CRYSTALLINE AUNP. ORANGE ARROWS INDICATE PRESUMED PRE-NUCLEATION CLUSTERS. 72

FIGURE 4. 3. A) TOP LEFT PLOT SHOWS THE SIZE DISTRIBUTION OF 1:3.5 ACETATE CAPPED AUNPS IN PH 5.3. B) TOP RIGHT PLOT SHOWS THE CIRCULARITY C) BOTTOM STEM IMAGES OF SAMPLES COLLECTED AT DIFFERENT TIME POINTS, AFTER THE START OF THE EXPERIMENT: 5 MINUTES, 60 MINUTES, 1 DAY AND 7 DAYS. WHITE ARROWS INDICATE BRIDGING OR STICKING BETWEEN PARTICLES. GREEN ARROWS INDICATE A SHELL FORMATION OR SOFT STRUCTURE AROUND A CRYSTALLINE AUNP. ORANGE ARROWS INDICATE PRESUMED PRE-NUCLEATION CLUSTERS. 74

FIGURE 4. 4 A) TOP LEFT PLOT SHOWS THE SIZE DISTRIBUTION OF 1:3.5 ACETATE CAPPED AUNPS IN PH 6.1. B) TOP RIGHT PLOT SHOWS THE CIRCULARITY. C) BOTTOM STEM IMAGES OF SAMPLES COLLECTED AT DIFFERENT TIME POINTS, AFTER THE START OF THE EXPERIMENT: 5 MINUTES, 60 MINUTES, 1 DAY AND 7 DAYS. GREEN ARROWS INDICATE A SHELL FORMATION OR SOFT STRUCTURE AROUND A CRYSTALLINE AUNP. ORANGE ARROWS INDICATE PRESUMED PRE-NUCLEATION CLUSTERS. THE SAMPLE AT 1 DAY FAILED TO OBSERVE ANY AUNPS. 75

FIGURE 4. 5. A) TOP LEFT PLOT SHOWS THE SIZE DISTRIBUTION OF 1:3.5 ACETATE CAPPED AUNPS IN PH 10.3. B) TOP RIGHT PLOT SHOWS THE CIRCULARITY. C) BOTTOM STEM IMAGES OF SAMPLES COLLECTED AT DIFFERENT TIME POINTS, AFTER THE START OF THE EXPERIMENT: 5 MINUTES, 60 MINUTES, 1 DAY AND 7 DAYS. WHITE ARROWS INDICATE

BRIDGING OR STICKING BETWEEN PARTICLES. GREEN ARROWS INDICATE A SHELL FORMATION OR SOFT STRUCTURE AROUND A CRYSTALLINE AUNP. ORANGE ARROWS INDICATE PRESUMED PRE-NUCLEATION CLUSTERS. 76

FIGURE 4. 6. A) TOP LEFT PLOT SHOWS THE SIZE DISTRIBUTION OF 1:1 ACETATE CAPPED AUNPS IN PH 3.6. B) TOP RIGHT PLOT SHOWS THE CIRCULARITY. C) BOTTOM STEM IMAGES OF SAMPLES COLLECTED AT DIFFERENT TIME POINTS, AFTER THE START OF THE EXPERIMENT: 5 MINUTES, 60 MINUTES, 1 DAY AND 7 DAYS. GREEN ARROWS INDICATE A SHELL FORMATION OR SOFT STRUCTURE AROUND A CRYSTALLINE AUNP. ORANGE ARROWS INDICATE PRESUMED PRE-NUCLEATION CLUSTERS..... 78

FIGURE 4. 7. A) TOP LEFT PLOT SHOWS THE SIZE DISTRIBUTION OF 1:1.5 ACETATE CAPPED AUNPS IN PH 3.7. B) TOP RIGHT PLOT SHOWS THE CIRCULARITY. C) BOTTOM STEM IMAGES OF SAMPLES COLLECTED AT DIFFERENT TIME POINTS, AFTER THE START OF THE EXPERIMENT: 5 MINUTES, 60 MINUTES, 1 DAY AND 7 DAYS. WHITE ARROWS INDICATE BRIDGING OR STICKING BETWEEN PARTICLES. GREEN ARROWS INDICATE A SHELL FORMATION OR SOFT STRUCTURE AROUND A CRYSTALLINE AUNP. ORANGE ARROWS INDICATE PRESUMED PRE-NUCLEATION CLUSTERS. 80

FIGURE 4. 8. A) TOP LEFT PLOT SHOWS THE SIZE DISTRIBUTION OF 1:7 ACETATE CAPPED AUNPS IN PH 6.6. B) TOP RIGHT PLOT SHOWS THE CIRCULARITY. C) BOTTOM STEM IMAGES OF SAMPLES COLLECTED AT DIFFERENT TIME POINTS, AFTER THE START OF THE EXPERIMENT: 5 MINUTES, 60 MINUTES, 1 DAY AND 7 DAYS. WHITE ARROWS INDICATE BRIDGING OR STICKING BETWEEN PARTICLES. GREEN ARROWS INDICATE A SHELL FORMATION OR SOFT STRUCTURE AROUND A CRYSTALLINE AUNP. ORANGE ARROWS INDICATE PRESUMED PRE-NUCLEATION CLUSTERS. 81

FIGURE 4. 9. A) TOP LEFT PLOT SHOWS THE SIZE DISTRIBUTION OF 1:10.6 ACETATE CAPPED AUNPS IN PH 6.1. B) TOP RIGHT PLOT SHOWS THE CIRCULARITY. C) BOTTOM STEM

IMAGES OF SAMPLES COLLECTED AT DIFFERENT TIME POINTS, AFTER THE START OF THE EXPERIMENT: 5 MINUTES, 60 MINUTES, 1 DAY AND 7 DAYS. GREEN ARROWS INDICATE A SHELL FORMATION OR SOFT STRUCTURE AROUND A CRYSTALLINE AUNP. ORANGE ARROWS INDICATE PRESUMED PRE-NUCLEATION CLUSTERS. 82

FIGURE 4. 10. A) TOP LEFT PLOT SHOWS THE SIZE DISTRIBUTION OF 1:3.5 OXALATE CAPPED AUNPS IN PH 2.8. B) TOP RIGHT PLOT SHOWS THE CIRCULARITY. C) BOTTOM STEM IMAGES OF SAMPLES COLLECTED AT DIFFERENT TIME POINTS, AFTER THE START OF THE EXPERIMENT: 5 MINUTES, 60 MINUTES, 1 DAY AND 7 DAYS. ORANGE ARROWS INDICATE PRESUMED PRE-NUCLEATION CLUSTERS. 84

FIGURE 4. 11. A) TOP LEFT PLOT SHOWS THE SIZE DISTRIBUTION OF 1:3.5 OXALATE CAPPED AUNPS IN PH 3.9. B) TOP RIGHT PLOT SHOWS THE CIRCULARITY. C) BOTTOM STEM IMAGES OF SAMPLES COLLECTED AT DIFFERENT TIME POINTS, AFTER THE START OF THE EXPERIMENT: 5 MINUTES, 60 MINUTES, 1 DAY AND 7 DAYS. WHITE ARROWS INDICATE BRIDGING OR STICKING BETWEEN PARTICLES. 86

FIGURE 4. 12. A) TOP LEFT PLOT SHOWS THE SIZE DISTRIBUTION OF 1:3.5 OXALATE CAPPED AUNPS IN PH 6.6. B) TOP RIGHT PLOT SHOWS THE CIRCULARITY. C) BOTTOM STEM IMAGES OF SAMPLES COLLECTED AT DIFFERENT TIME POINTS, AFTER THE START OF THE EXPERIMENT: 5 MINUTES, 60 MINUTES, 1 DAY AND 7 DAYS. WHITE ARROWS INDICATE BRIDGING OR STICKING BETWEEN PARTICLES. GREEN ARROWS INDICATE A SHELL FORMATION OR SOFT STRUCTURE AROUND A CRYSTALLINE AUNP. ORANGE ARROWS INDICATE PRESUMED PRE-NUCLEATION CLUSTERS. 87

FIGURE 4. 13. A) TOP LEFT PLOT SHOWS THE SIZE DISTRIBUTION OF 1:3.5 OXALATE CAPPED AUNPS IN PH 10.7. B) TOP RIGHT PLOT SHOWS THE CIRCULARITY. C) BOTTOM STEM IMAGES OF SAMPLES COLLECTED AT DIFFERENT TIME POINTS, AFTER THE START OF THE EXPERIMENT: 5 MINUTES, 60 MINUTES, 1 DAY AND 7 DAYS. WHITE ARROWS INDICATE

BRIDGING OR STICKING BETWEEN PARTICLES. GREEN ARROWS INDICATE A SHELL FORMATION OR SOFT STRUCTURE AROUND A CRYSTALLINE AUNP. ORANGE ARROWS INDICATE PRESUMED PRE-NUCLEATION CLUSTERS. 89

FIGURE 4. 14. A) TOP LEFT PLOT SHOWS THE SIZE DISTRIBUTION OF 1:1 OXALATE CAPPED AUNPS IN PH 3.2. B) TOP RIGHT PLOT SHOWS THE CIRCULARITY. C) BOTTOM STEM IMAGES OF SAMPLES COLLECTED AT DIFFERENT TIME POINTS, AFTER THE START OF THE EXPERIMENT: 5 MINUTES, 60 MINUTES, 1 DAY AND 7 DAYS. WHITE ARROWS INDICATE BRIDGING OR STICKING BETWEEN PARTICLES. GREEN ARROWS INDICATE A SHELL FORMATION OR SOFT STRUCTURE AROUND A CRYSTALLINE AUNP. ORANGE ARROWS INDICATE PRESUMED PRE-NUCLEATION CLUSTERS. 90

FIGURE 4. 15. A) TOP LEFT PLOT SHOWS THE SIZE DISTRIBUTION OF 1:1.5 OXALATE CAPPED AUNPS IN PH 3.0. B) TOP RIGHT PLOT SHOWS THE CIRCULARITY. C) BOTTOM STEM IMAGES OF SAMPLES COLLECTED AT DIFFERENT TIME POINTS, AFTER THE START OF THE EXPERIMENT: 5 MINUTES, 60 MINUTES, 1 DAY AND 7 DAYS. WHITE ARROWS INDICATE BRIDGING OR STICKING BETWEEN PARTICLES. ORANGE ARROWS INDICATE PRESUMED PRE-NUCLEATION CLUSTERS. 92

FIGURE 4. 16. A) TOP LEFT PLOT SHOWS THE SIZE DISTRIBUTION OF 1:7 OXALATE CAPPED AUNPS IN PH 6.2. B) TOP RIGHT PLOT SHOWS THE CIRCULARITY. C) BOTTOM STEM IMAGES OF SAMPLES COLLECTED AT DIFFERENT TIME POINTS, AFTER THE START OF THE EXPERIMENT: 5 MINUTES, 60 MINUTES, 1 DAY AND 7 DAYS. WHITE ARROWS INDICATE BRIDGING OR STICKING BETWEEN PARTICLES. GREEN ARROWS INDICATE A SHELL FORMATION OR SOFT STRUCTURE AROUND A CRYSTALLINE AUNP. ORANGE ARROWS INDICATE PRESUMED PRE-NUCLEATION CLUSTERS. 93

FIGURE 4. 17. A) TOP LEFT PLOT SHOWS THE SIZE DISTRIBUTION OF 1:10.6 OXALATE CAPPED AUNPS IN PH 6.4. B) TOP RIGHT PLOT SHOWS THE CIRCULARITY. C) BOTTOM

STEM IMAGES OF SAMPLES COLLECTED AT DIFFERENT TIME POINTS, AFTER THE START OF THE EXPERIMENT: 5 MINUTES, 60 MINUTES, 1 DAY AND 7 DAYS. WHITE ARROWS INDICATE BRIDGING OR STICKING BETWEEN PARTICLES. ORANGE ARROWS INDICATE PRESUMED PRE-NUCLEATION CLUSTERS. 94

FIGURE 4. 18. A) TOP LEFT PLOT SHOWS THE SIZE DISTRIBUTION OF 1:3.5 CITRATE CAPPED AUNPS IN PH 6.7. B) TOP RIGHT PLOT SHOWS THE CIRCULARITY. C) BOTTOM STEM IMAGES OF SAMPLES COLLECTED AT DIFFERENT TIME POINTS, AFTER THE START OF THE EXPERIMENT: 5 MINUTES, 60 MINUTES, 1 DAY AND 7 DAYS 96

FIGURE 4. 19. A) TOP LEFT PLOT SHOWS THE SIZE DISTRIBUTION OF 1:1 CITRATE CAPPED AUNPS IN PH 4.4. B) TOP RIGHT PLOT SHOWS THE CIRCULARITY. C) BOTTOM STEM IMAGES OF SAMPLES COLLECTED AT DIFFERENT TIME POINTS, AFTER THE START OF THE EXPERIMENT: 5 MINUTES, 60 MINUTES, 1 DAY AND 7 DAYS. WHITE ARROWS INDICATE BRIDGING OR STICKING BETWEEN PARTICLES. GREEN ARROWS INDICATE A SHELL FORMATION OR SOFT STRUCTURE AROUND A CRYSTALLINE AUNP. ORANGE ARROWS INDICATE PRESUMED PRE-NUCLEATION CLUSTERS. 97

FIGURE 4. 20. A) TOP LEFT PLOT SHOWS THE SIZE DISTRIBUTION OF 1:1.5 CITRATE CAPPED AUNPS IN PH 4.5. B) TOP RIGHT PLOT SHOWS THE CIRCULARITY. C) BOTTOM STEM IMAGES OF SAMPLES COLLECTED AT DIFFERENT TIME POINTS, AFTER THE START OF THE EXPERIMENT: 5 MINUTES, 60 MINUTES, 1 DAY AND 7 DAYS. WHITE ARROWS INDICATE BRIDGING OR STICKING BETWEEN PARTICLES. PURPLE ARROWS INDICATE A SHELL FORMATION OR SOFT STRUCTURE AROUND A CRYSTALLINE AUNP. ORANGE ARROWS INDICATE PRESUMED PRE-NUCLEATION CLUSTERS. 99

FIGURE 4. 21. A) TOP LEFT PLOT SHOWS THE SIZE DISTRIBUTION OF 1:7 CITRATE CAPPED AUNPS IN PH 6.3. B) TOP RIGHT PLOT SHOWS THE CIRCULARITY. C) BOTTOM STEM IMAGES OF SAMPLES COLLECTED AT DIFFERENT TIME POINTS, AFTER THE START OF THE

EXPERIMENT: 5 MINUTES, 60 MINUTES, 1 DAY AND 7 DAYS. WHITE ARROWS INDICATE BRIDGING OR STICKING BETWEEN PARTICLES. GREEN ARROWS INDICATE A SHELL FORMATION OR SOFT STRUCTURE AROUND A CRYSTALLINE AUNP. ORANGE ARROWS INDICATE PRESUMED PRE-NUCLEATION CLUSTERS. 100

FIGURE 4. 22. A) TOP LEFT PLOT SHOWS THE SIZE DISTRIBUTION OF 1:10.6 CITRATE CAPPED AUNPS IN PH 6.3. B) TOP RIGHT PLOT SHOWS THE CIRCULARITY. C) BOTTOM STEM IMAGES OF SAMPLES COLLECTED AT DIFFERENT TIME POINTS, AFTER THE START OF THE EXPERIMENT: 5 MINUTES, 60 MINUTES, 1 DAY AND 7 DAYS. WHITE ARROWS INDICATE BRIDGING OR STICKING BETWEEN PARTICLES. GREEN ARROWS INDICATE A SHELL FORMATION OR SOFT STRUCTURE AROUND A CRYSTALLINE AUNP. ORANGE ARROWS INDICATE PRESUMED PRE-NUCLEATION CLUSTERS. 101

FIGURE 4. 23. A) TOP LEFT PLOT SHOWS THE SIZE DISTRIBUTION OF 1:3.5 PROPIONIC ACID CAPPED AUNPS IN PH 9.3. B) TOP RIGHT PLOT SHOWS THE CIRCULARITY. C) BOTTOM STEM IMAGES OF SAMPLES COLLECTED AT DIFFERENT TIME POINTS, AFTER THE START OF THE EXPERIMENT: 5 MINUTES, 60 MINUTES, 1 DAY AND 7 DAYS. ORANGE ARROWS INDICATE PRESUMED PRE-NUCLEATION CLUSTERS. 103

FIGURE 4. 24. A) TOP LEFT PLOT SHOWS THE SIZE DISTRIBUTION OF 1:7 PROPIONIC ACID CAPPED AUNPS IN PH 6.4. B) TOP RIGHT PLOT SHOWS THE CIRCULARITY. C) BOTTOM STEM IMAGES OF SAMPLES COLLECTED AT DIFFERENT TIME POINTS, AFTER THE START OF THE EXPERIMENT: 5 MINUTES, 60 MINUTES, 1 DAY AND 7 DAYS. WHITE ARROWS INDICATE BRIDGING OR STICKING BETWEEN PARTICLES. ORANGE ARROWS INDICATE PRESUMED PRE-NUCLEATION CLUSTERS. 105

FIGURE 4. 25. A) TOP LEFT PLOT SHOWS THE SIZE DISTRIBUTION OF 1:10.6 PROPIONIC ACID CAPPED AUNPS IN PH 6.4. B) TOP RIGHT PLOT SHOWS THE CIRCULARITY. C) BOTTOM STEM IMAGES OF SAMPLES COLLECTED AT DIFFERENT TIME POINTS, AFTER THE START

of the experiment: 5 minutes, 60 minutes, 1 day and 7 days. White arrows indicate bridging or sticking between particles. Green arrows indicate a shell formation or soft structure around a crystalline AuNP. Orange arrows indicate presumed pre-nucleation clusters..... 106
Figure 4. 26. a) top left plot shows the size distribution of no capping agent AuNPs in pH 9.0. b) top right plot shows the circularity. c) bottom STEM images of samples collected at different time points, after the start of the experiment: 5 minutes, 60 minutes, 1 day and 7 days. White arrows indicate bridging or sticking between particles. Green arrows indicate a shell formation or soft structure around a crystalline AuNP. Orange arrows indicate presumed pre-nucleation clusters. 108
Figure 4. 27 Size distribution of acetate-capped AuNPs with 1:3.5 molar ratio in different pH environments during a 7 day period. The size distribution is represented using a box-and-whisker plot. The box in the plot represents the interquartile range, indicating the spread of the dataset. The whiskers extend from the box to show the rest of the distribution, excluding outliers. The sample at 1 day failed to observe any AuNPs. 110
Figure 4. 28. Top figure showing the different molar ratio and pH of acetate capped AuNPs with different pH and aging time. Bottom figure showing the same horizontal axis range but zooming in a smaller size range 0-20 nm of the vertical axis, to provide a more detailed view of the size range in each experiment. The size distribution is represented using a box-and-whisker plot. The box in the plot represents the interquartile range, indicating the spread of the dataset. The whiskers extend from the box to show the rest

OF THE DISTRIBUTION, EXCLUDING OUTLIERS. THE SAMPLE AT 1 DAY FAILED TO OBSERVE ANY AUNPS. 112
FIGURE 4. 29 DIFFERENT MOLAR RATIO OF PH 6 ACETATE CAPPED AUNPS SIZE CHANGES WITH RESPECT TO THEIR AGING TIME. THE SIZE DISTRIBUTION IS REPRESENTED USING A BOX-AND-WHISKER PLOT. THE BOX IN THE PLOT REPRESENTS THE INTERQUARTILE RANGE, INDICATING THE SPREAD OF THE DATASET. THE WHISKERS EXTEND FROM THE BOX TO SHOW THE REST OF THE DISTRIBUTION, EXCLUDING OUTLIERS. 113
FIGURE 4. 30. SIZE DISTRIBUTION OF 1:3.5 MOLAR RATIO OF OXALATE CAPPED AUNPS WITH DIFFERENT PH AND AGING TIME. THE SIZE DISTRIBUTION IS REPRESENTED USING A BOX-AND-WHISKER PLOT. THE BOX IN THE PLOT REPRESENTS THE INTERQUARTILE RANGE, INDICATING THE SPREAD OF THE DATASET. THE WHISKERS EXTEND FROM THE BOX TO SHOW THE REST OF THE DISTRIBUTION, EXCLUDING OUTLIERS. 115
FIGURE 4. 31. DIFFERENT MOLAR RATIO OF OXALATE CAPPED AUNPS WITH DIFFERENT PH AND AGING TIME. THE SIZE DISTRIBUTION IS REPRESENTED USING A BOX-AND-WHISKER PLOT. THE BOX IN THE PLOT REPRESENTS THE INTERQUARTILE RANGE, INDICATING THE SPREAD OF THE DATASET. THE WHISKERS EXTEND FROM THE BOX TO SHOW THE REST OF THE DISTRIBUTION, EXCLUDING OUTLIERS. 116
FIGURE 4. 32. DIFFERENT MOLAR RATIO OF OXALATE CAPPED AUNPS WITH PH 6 AND AGING TIME. THE SIZE DISTRIBUTION IS REPRESENTED USING A BOX-AND-WHISKER PLOT. THE BOX IN THE PLOT REPRESENTS THE INTERQUARTILE RANGE, INDICATING THE SPREAD OF THE DATASET. THE WHISKERS EXTEND FROM THE BOX TO SHOW THE REST OF THE DISTRIBUTION, EXCLUDING OUTLIERS. 117
FIGURE 4. 33. DIFFERENT MOLAR RATIO OF CITRATE CAPPED AUNPS WITH PH 6 AND AGING TIME. THE SIZE DISTRIBUTION IS REPRESENTED USING A BOX-AND-WHISKER PLOT. THE BOX IN THE PLOT REPRESENTS THE INTERQUARTILE RANGE, INDICATING THE SPREAD OF

THE DATASET. THE WHISKERS EXTEND FROM THE BOX TO SHOW THE REST OF THE DISTRIBUTION, EXCLUDING OUTLIERS. 119
FIGURE 4. 34. SIZE DISTRIBUTION OF 1:1 MOLAR RATIO OF CARBOXYL GROUP CAPPED AUNPS WITH LOW PH AND AGING TIME. THE SIZE DISTRIBUTION IS REPRESENTED USING A BOX-AND-WHISKER PLOT. THE BOX IN THE PLOT REPRESENTS THE INTERQUARTILE RANGE, INDICATING THE SPREAD OF THE DATASET. THE WHISKERS EXTEND FROM THE BOX TO SHOW THE REST OF THE DISTRIBUTION, EXCLUDING OUTLIERS. 120
FIGURE 4. 35. SIZE DISTRIBUTION OF 1:1.5 MOLAR RATIO OF CARBOXYL GROUP CAPPED AUNPS WITH LOW PH AND AGING TIME. THE SIZE DISTRIBUTION IS REPRESENTED USING A BOX-AND-WHISKER PLOT. THE BOX IN THE PLOT REPRESENTS THE INTERQUARTILE RANGE, INDICATING THE SPREAD OF THE DATASET. THE WHISKERS EXTEND FROM THE BOX TO SHOW THE REST OF THE DISTRIBUTION, EXCLUDING OUTLIERS. 122
FIGURE 4. 36. SIZE DISTRIBUTION OF 1:3.5 MOLAR RATIO OF CARBOXYL GROUP CAPPED AUNPS WITH PH 6 AND AGING TIME. THE SIZE DISTRIBUTION IS REPRESENTED USING A BOX-AND-WHISKER PLOT. THE BOX IN THE PLOT REPRESENTS THE INTERQUARTILE RANGE, INDICATING THE SPREAD OF THE DATASET. THE WHISKERS EXTEND FROM THE BOX TO SHOW THE REST OF THE DISTRIBUTION, EXCLUDING OUTLIERS. 124
FIGURE 4. 37 1:7 MOLAR RATIO OF CARBOXYL GROUP CAPPED AUNPS WITH PH 6 AND AGING TIME. 1THE SIZE DISTRIBUTION IS REPRESENTED USING A BOX-AND-WHISKER PLOT. THE BOX IN THE PLOT REPRESENTS THE INTERQUARTILE RANGE, INDICATING THE SPREAD OF THE DATASET. THE WHISKERS EXTEND FROM THE BOX TO SHOW THE REST OF THE DISTRIBUTION, EXCLUDING OUTLIERS. 125
FIGURE 4. 38 1:10.6 MOLAR RATIO OF CARBOXYL GROUP CAPPED AUNPS WITH PH 6 AND AGING TIME. THE SIZE DISTRIBUTION IS REPRESENTED USING A BOX-AND-WHISKER PLOT. THE BOX IN THE PLOT REPRESENTS THE INTERQUARTILE RANGE, INDICATING THE

spread of the dataset. The whiskers extend from the box to show the rest of the distribution, excluding outliers. 126
Figure 4. 39. 1:7 and 1:10.6 molar ratio of acetate and propionic acid capped AuNPs with pH 6 and aging time. The size distribution is represented using a box-and-whisker plot. The box in the plot represents the interquartile range, indicating the spread of the dataset. The whiskers extend from the box to show the rest of the distribution, excluding outliers. 127
Figure 4. 40 EDS of Core-shell motif. From left to right, Core, and shell EDS from Figure 4. 13 respectively. 128
Figure 4. 41. Citrate crown formation on AuNPs of size A) 14nm and B) 6nm (Perfilieva et al., 2019). 133
Figure 5. 1. a) top left plot shows the size distribution of L-cysteine capped AuNPs at pH 7.5 with molar ratio 1:3.5. b) top right plot shows the circularity. c) bottom STEM images of samples collected at different time points, after the start of the experiment: 5 minutes, 60 minutes, 1 day and 7 days. 140
Figure 5. 2. a) top left plot shows the size distribution of L-cysteine capped AuNPs at pH 8.4 with molar ratio 1:3.5. b) top right plot shows the circularity. c) bottom STEM images of samples collected at different time points, after the start of the experiment: 5 minutes, 60 minutes, 1 day and 7 days. 142
Figure 5. 3 Glutathione capped AuNPs at pH 8 with molar ratio 1:3.5. STEM images of samples collected at different time points, after the start of the experiment: 5 minutes, 60 minutes, 1 day and 7 days. 143

FIGURE 5. 4 AGNPS WITH NO CAPPING AGENT ADDED AT PH 6.3. STEM IMAGES OF SAMPLES COLLECTED AT DIFFERENT TIME POINTS, AFTER THE START OF THE EXPERIMENT: 5 MINUTES, 60 MINUTES, 1 DAY AND 7 DAYS. 145
FIGURE 5. 5 CITRIC ACID CAPPED AGNPS AT PH 6.9 WITH MOLAR RATIO OF 1:3.5. STEM IMAGES OF SAMPLES COLLECTED AT DIFFERENT TIME POINTS, AFTER THE START OF THE EXPERIMENT: 5 MINUTES, 60 MINUTES, 1 DAY AND 7 DAYS. 146
FIGURE 5. 6. A) PNCS WITH ACETATE CAPPED AUNPS ON PH 6.1 AT 5 MINUTES WITH MOLAR RATIO 1:3.5. B) PNCS FOUND INSIDE CITRATE CAPPED AUNPS ON PH 6.7 28 DAYS WITH MOLAR RATIO 1:3.5. ORANGE ARROWS INDICATE PRESUMED PRE-NUCLEATION CLUSTERS. 148
FIGURE 5. 7. A) STEM IMAGE OF PNC WITH ACETATE CAPPED AUNPS ON PH 5.3 60 MINUTES. B) INTENSITY VS DISTANCE ALONG THE YELLOW LINE INDICATOR ON THE STEM IMAGE. 149
FIGURE 5. 8. STEM IMAGES OF A) PNCS GROUP AND A CRYSTALLINE AUNPS FROM ACETATE CAPPED AUNPS ON PH 6.1 WITH 1:10.6 MOLAR RATIO AT 60 MINUTES. B) MAGNIFIED IMAGE OF THE CORE-SHELL AUNPS PNCS OF 5.8A. C) LINE PATTERN OF PNCS WITH CRYSTALLINE AUNPS FROM ACETIC CAPPED AUNPS ON PH 6.1 WITH MOLAR RATIO 1:10.6 AT 1 DAY. D) MAGNIFIED IMAGE OF THE LINE PATTERN ON 5.8C. ORANGE ARROWS INDICATE PRESUMED PRE-NUCLEATION CLUSTERS. GREEN ARROWS INDICATE PNCS IN A LINE FORMATION. 151
FIGURE 5. 9. STEM IMAGES OF A) ACETIC CAPPED AUNPS ON PH 6.1 AT 1 DAY WITH MOLAR RATIO 1:10.6. B) OXALIC CAPPED AUNPS WITH 1:1.5 ON PH 3 AT 7 DAYS. C) CITRIC CAPPED AUNPS ON PH 6.2 AT 5 MINUTES. D) L-CYSTEINE CAPPED AUNPS ON PH 8.4 AT 60 MINUTES. 152

FIGURE 5. 10. STEM IMAGES OF A) OXALIC CAPPED AUNPS WITH 1:1.5 PH 3 7 DAYS. B) BF IMAGE OF 5.10A WITH A YELLOW ARROW INDICATES THE CLOUD STRUCTURE PNC. C) FFT OF 5.10B CLOUD STRUCTURE INDICATED BY YELLOW SQUARE. 153

FIGURE 5. 11. STEM IMAGES OF A) OXALIC CAPPED AUNPS WITH 1:1.5 AT 7 DAYS. B) BF IMAGE OF 5.11A. C) FFT OF 5.11B CLOUD STRUCTURE INDICATED BY YELLOW SQUARE. 154

FIGURE 5. 12. MAGNIFICATION OF FIGURE 5.9D, L-CYSTEINE CAPPED AUNPS ON PH 8.4 AT 60 MINUTES, WITH PNCS CLOUD AROUND THE AUNPS CORE AT MAGNIFICATION OF A) X300K, B) X600K, C) X1M, D) X2M. ORANGE ARROWS INDICATE PRESUMED PRE-NUCLEATION CLUSTERS. 155

FIGURE 5. 13. STEM IMAGES OF A) CYSTEINE CAPPED AUNPS WITH PH 8 AT 1 DAY. B,C) ARE THE MAGNIFIED IMAGES OF THE YELLOW SQUARE SECTION IN 5.13A. 157

FIGURE 5. 14. STEM IMAGES OF A) GSH CAPPED AUNPS ON PH 8 AT 5 MINUTES. 5.14B, BF IMAGE OF 5.14A. 5.14C, FFT OF THE YELLOW SQUARE SECTION INDICATED IN 5.14B. 157

FIGURE 5. 15. CITRIC CAPPED AGNPS ON PH 6.9 AT 60 MINUTES. A) DF IMAGES SHOWING CRYSTALLIZED AGNPS INDICATED BY NUMBER 1, AMORPHOUS AGPNCS INDICATED BY BLUE NUMBER 2 AND 3, PNCS SHOWING LATTICE STRUCTURE INDICATED BY BLUE NUMBER 4. B) BF IMAGES OF A. C) INTENSITY PLOT OF THE LATTICE STRUCTURE INDICATED BY THE BLUE LINE IN 5.15B. D) FFT OF THE YELLOW SQUARE INDICATED IN 5.15B. 158

FIGURE 5. 16. A) CITRATE CAPPED AGNPS ON PH 6.9 AT 1 DAY. CRYSTALLIZED AGNPS WERE INDICATED BY BLACK NUMBER 1, AGPNCS WERE INDICATED BY BLUE NUMBER 2. B) BF OF IMAGE 5.16A. 159

FIGURE 5. 17 SCHEMATIC OF NUCLEATION OF CLASSICAL PATH AND NON-CLASSICAL NUCLEATION PATH WITH PNCS AND THE FORMATION OF CORE SHELL AUNPS..... 160

FIGURE 5. 18. STEM IMAGES OF A,B) CITRATE CAPPED AUNPS AT PH 6.3 WITH 1:7 MOLAR RATIO AT 5 MINUTES. WHITE ARROW INDICATES THE BRIDGES FORMATION. GREEN ARROW INDICATES SHELL MOTIF. ORANGE ARROW INDICATES PNCS..... 162

FIGURE 5. 19 STEM IMAGES OF A) NO CAPPING AGENT OF AGNPS WITH PH 6.3 AT 5 MINUTES. B) MAGNIFIED IMAGE OF 5.19A YELLOW SQUARE SECTION. C) BF IMAGE OF 5.19B. D) IS THE INTENSITY PLOT OF THE BLUE ARROW INDICATED IN 5.19C FOR CALCULATING THE LATTICE DISTANCE OF THE SUBSTANCE BETWEEN AGNPS 1, 2, 3. E) FFT OF THE AREA INDICATED BY BLUE ARROW AND SQUARE IN 5.19C. 5.19F, THE SURFACE PLOT OF THE REGION INDICATED BY YELLOW SQUARE IN 5.19A. 164

FIGURE 5. 20. STEM IMAGES OF A) CITRATE CAPPED AUNPS WITH PH 6 AT 5 MINUTES, SOFT SHELL INDICATED BY WHITE ARROW ON THE LEFT IMAGE. B) CITRATE CAPPED AUNPS WITH PH 4.8 AT 60 MINUTES, HARD SHELL INDICATED BY BLUE ARROW ON THE RIGHT IMAGE. 165

FIGURE 5. 21. STEM IMAGE OF A) ACETIC CAPPED AUNPS WITH 1:7 AT PH 6.6 5 MINUTES. B) INTENSITY PLOT ALONG THE YELLOW INDICATOR ON FIGURE 5.21A..... 167

FIGURE 5. 22 STEM IMAGE OF ACETIC CAPPED AUNPS AT PH 5.3 AT 60 MINUTES. 168

FIGURE 5. 23. A) AGNPS WITH NO CAPPING AGENT AT 60 MINUTES. B) INTENSITY PLOT ALONG THE YELLOW INDICATOR IN FIGURE 5.23A. 169

FIGURE 5. 24 STEM IMAGE OF AUNPS CAPPED WITH L-CYSTEINE AT PH 7.5 AT MOLAR RATIO 1:3.5 AT 1 DAY. 171

FIGURE 5. 25 STEM IMAGE OF CITRIC CAPPED AUNPS WITH 1:3.5 AT PH 6.3 AT 5 MINUTES. 173

FIGURE 5. 26. STEM IMAGE OF C) CITRIC CAPPED AUNPS WITH 1:3.5 ON PH 6.3 AT 5 MINUTES, SHELL STRUCTURE INDICATED BY GREEN ARROW, BRIDGE STRUCTURE INDICATED BY WHITE ARROW, PNCS INDICATED BY ORANGE ARROW. B) INTENSITY PLOT ALONE THE YELLOW INDICATOR IN 5.26A. 175
FIGURE 5. 27. STEM IMAGES OF A) CITRIC CAPPED AUNPS WITH 1:1 AT PH 4.4 AT 60 MINUTES. B) MAGNIFIED IMAGE ON THE TOP RIGHT CORNER OF 5.27A. 176
FIGURE 5. 28. STEM IMAGES OF A) CITRIC CAPPED AUNPS WITH MOLAR RATIO 1:1 ON PH 4.4 AT 60 MINUTES AS AN UNPREDICTABLE MORPHOLOGY OF NANO-STRING. B) NPS WITH CIRCLE FORMATION THAT POTENTIALLY WILL EVOLVE INTO A NANO-STRING. 177
FIGURE 5. 29. A) SIZE DISTRIBUTION AFTER 7 DAYS OF THE SYNTHESIS. ACETATE CAPPED AUNPS INDICATED BY BLUE COLOUR, OXALATE CAPPED AUNPS INDICATED BY YELLOW COLOUR, CITRATE CAPPED AUNPS INDICATED BY GREEN COLOUR, AND CYSTEINE CAPPED AUNPS INDICATED BY RED COLOUR. C) THE CIRCULARITY OF THE AUNPS WITH DIFFERENT CAPPING AGENTS IN 5.29A. 178
FIGURE 5. 31 STEM ELECTRONS BEAM INDUCED GROWTH ON AUNPS ON TIMESTAMP OF A) T = 0 S, B) T = 20 S, C) T = 40 S, D) T = 60 S. BLUE ARROW INDICATE SINGLE GOLD ATOM. GREEN ARROWS INDICATE THE SHELL FORMATION. WHITE ARROWS INDICATE THE NECK FORMATION BETWEEN TWO AUNPS. ORANGE ARROWS INDICATE PNCS. 180
FIGURE 5. 32 STEM ELECTRONS BEAM INDUCED NUCLEATION AND GROWTH ON AUNPS ON TIMESTAMP OF A) T = 0 S, B) T = 20 S, C) T = 40 S, D) T = 60 S. PURPLE ARROW INDICATES THE NUCLEATION OF AUNPS. 180
FIGURE 6. 1 BALL AND STICK STYLE ILLUSTRATION OF THE ATOMIC ARRANGEMENT OF THREE CARBOXYL GROUP LIGANDS, ACETATE, OXALATE, CITRATE, USED IN THE SIMULATIONS. DARK GREY: CARBON ATOMS, RED: OXYGEN ATOMS, LIGHT GRAY: HYDROGEN ATOMS. 188

FIGURE 6. 2 BALL AND STICK STYLE ILLUSTRATION OF THE ATOMIC ARRANGEMENT OF TWO CARBOXYL GROUP LIGANDS, ACETATE AND PROPIONATE, USED IN THE SIMULATIONS. DARK GREY: CARBON ATOMS, RED: OXYGEN ATOMS, LIGHT GRAY: HYDROGEN ATOMS. 189

FIGURE 6. 3 BALL AND STICK STYLE ILLUSTRATION OF THE ATOMIC ARRANGEMENT OF TWO THIOL GROUP LIGANDS, L-CYSTEINE (CYS) AND GLUTATHIONE (GSH), USED IN THE SIMULATIONS. DARK GREY: CARBON ATOMS, RED: OXYGEN ATOMS, LIGHT GRAY: HYDROGEN ATOMS, BLUE: NITROGEN, YELLOW: SULPHUR. 190

FIGURE 6. 4 SNAPSHOT OF 100 FREE GOLD ATOMS WITH 1000 WATER MOLECULES AT: A) 200K STEP, 50 PS. B) 3.8M STEP, 950 PS. C) RDF OF ALL THE CALCULATED SNAPSHOTS COMBINED. 194

FIGURE 6. 5 SNAPSHOT OF 10 ACETIC ACID AND 100 FREE GOLD ATOMS WITH 1000 WATER MOLECULES AT A) 200K STEP, 50 PS. B) 3.8M STEP, 950 PS. C) RDF OF ALL THE CALCULATED SNAPSHOTS COMBINED. 195

FIGURE 6. 6 SNAPSHOT OF 10 OXALIC ACID AND 100 FREE GOLD ATOMS WITH 1000 WATER MOLECULES AT A) 200K STEP, 50 PS. B) 3.8M STEP, 950 PS. C) RDF OF ALL THE CALCULATED SNAPSHOTS COMBINED. 196

FIGURE 6. 7 SNAPSHOT OF 10 CITRIC ACID AND 100 FREE GOLD ATOMS WITH 1000 WATER MOLECULES AT A) 200K STEP, 50 PS. B) 3.8M STEP, 950 PS. C) RDF OF ALL THE CALCULATED SNAPSHOTS COMBINED. 198

FIGURE 6. 8 SNAPSHOT OF 10 PROPIONIC ACID AND 100 FREE GOLD ATOMS WITH 1000 WATER MOLECULES AT A) 200K STEP, 50 PS. B) 3.8M STEP, 950 PS. C) RDF OF ALL THE CALCULATED SNAPSHOTS COMBINED. 199

FIGURE 6. 9 MOLECULES CONSISTS OF 1 CITRIC ACID WITH 3 GOLD ATOMS ATTACHED. THIS HYBRID MOLECULES WERE SIMULATED AS MENTIONED IN CHAPTER 3 SECTION 3.9.2. 200

FIGURE 6. 10 SNAPSHOT OF 33 CITRIC ACID ALREADY BONDED WITH 3 AU ATOMS WITH 1000 WATER MOLECULES AT A) 200K STEP, 50 PS. B) 3.8M STEP, 950 PS. C) RDF OF ALL THE CALCULATED SNAPSHOTS COMBINED. 201

FIGURE 6. 11 SNAPSHOT OF A) 33 CITRIC ACIDS ALREADY BONDED WITH 3 AU ATOMS WITH 1000 WATER MOLECULES AT 3.8M STEP, 950 PS. B) 100 AU ATOMS WITH 1000 WATER MOLECULES AT 3.8M STEP, 950 PS. C) RDF OF 6.11A AND 6.11B AT 3.8M STEP, 950 PS. 202

FIGURE 6. 12 SNAPSHOT OF 10 L-CYSTEINE WITH 100 AU ATOMS WITH 1000 WATER MOLECULES AT A) 200K STEP, 50 PS. B) 3.8M STEP, 950 PS. C) RDF OF ALL THE CALCULATED SNAPSHOTS COMBINED. 204

FIGURE 6. 13 SNAPSHOT OF 10 GSH WITH 100 AU ATOMS WITH 1000 WATER MOLECULES AT A) 200K STEP, 50 PS. B) 3.8M STEP, 950 PS. C) RDF OF ALL THE CALCULATED SNAPSHOTS COMBINED. 205

FIGURE 6. 14 SNAPSHOT OF THE NUCLEATION WITH DIFFERENT LIGANDS AT 3.8M STEP, 950 PS. A) 100-AU CLUSTER IN VACUUM (ALSO SHOWN ON APPENDIX 3 FIGURE A.3.1). B) ACETIC ACID. C) OXALIC ACID. D) CITRIC ACID. E) PROPIONIC ACID. F) L-CYS. G) GSH. H) 100 FREE GOLD ATOMS IN WATER. I) RDF OF ALL THE DIFFERENT LIGANDS AT 3.8M STEP, 950 PS. 207

FIGURE 6. 15 SNAPSHOT OF 30 CITRIC ACID WITH 100-AU CLUSTER WITH 1000 WATER MOLECULES. ARROW INDICATES AN ETCHED AU ATOM. A) 200K STEP, 50 PS. B) 600K STEP, 150 PS. C) 1M STEP, 250 PS. D) 1.4M STEP, 350 PS. E) 2.2M STEP, 550 PS. F)

3M STEP, 750 PS. G) 3.8M STEP, 950 PS. H) 6.14G WITH WATER MOLECULES. I) RDF OF ALL THE SNAPSHOT COMBINED. 210
FIGURE 6. 16 SNAPSHOT OF 30 CITRIC ACID WITH 90 FREE AU ATOMS AND 100 AU CLUSTER WITH 1000 WATER MOLECULES AT A) 200K STEP, 50 PS. B) 3.8M STEP, 950 PS. C) RDF OF ALL THE SNAPSHOTS COMBINED. 212
FIGURE 6. 17 SNAPSHOT OF 30 CITRIC ACID ALREADY BONDED WITH 3 AU ATOMS AND 100 AU CLUSTER WITH 1000 WATER MOLECULES AT A) 200K STEP, 50 PS. B) 3.8M STEP, 950 PS. C) RDF OF ALL THE SNAPSHOTS COMBINED. 212
FIGURE 6. 18 SNAPSHOT OF A) 30 ACETIC ACIDS WITH 30 AU ATOMS AND 100-AU CLUSTER WITH 1000 WATER MOLECULES AT 3.8M STEP, 950 PS. B) 30 ACETIC ACIDS WITH 90 AU ATOMS AND 100-AU CLUSTER WITH 1000 WATER MOLECULES AT 3.8M STEP, 950 PS. C) RDF OF 6.18A AND 6.18B AT 3.8M STEP, 950 PS. 213
FIGURE 6. 19 SNAPSHOT OF A) 30 OXALIC ACIDS WITH 60 AU ATOMS AND 100-AU CLUSTER WITH 1000 WATER MOLECULES AT 3.8M STEP, 950 PS. B) 30 OXALIC ACIDS WITH 90 AU ATOMS AND 100-AU CLUSTER WITH 1000 WATER MOLECULES AT 3.8M STEP, 950 PS. C) RDF OF 6.19A AND 6.19B AT 3.8M STEP, 950 PS. 215
FIGURE 6. 20 SNAPSHOT OF A) 30 ACETIC ACIDS WITH 90 FREE GOLD ATOMS AND 100-AU CLUSTER WITH 1000 WATER MOLECULES AT 3.8M STEP, 950 PS. B) 30 OXALIC ACIDS WITH 90 FREE GOLD ATOMS AND 100-AU CLUSTER WITH 1000 WATER MOLECULES AT 3.8M STEP, 950 PS. C) 30 CITRIC ACIDS WITH 90 AU ATOMS AND 100-AU CLUSTER WITH 1000 WATER MOLECULES AT 3.8M STEP, 950 PS. D) 30 PROPIONIC ACIDS WITH 90 AU ATOMS AND 100-AU CLUSTER WITH 1000 WATER MOLECULES AT 3.8M STEP, 950 PS. E) RDF OF 6.20A, 6.20B, 6.20C AND 6.20D AT 3.8M STEP, 950 PS..... 217
FIGURE 6. 21 SNAPSHOT OF A) 30 ACETIC ACIDS WITH 30 FREE GOLD ATOMS AND 100-AU CLUSTER WITH 1000 WATER MOLECULES AT 3.8M STEP, 950 PS. B) 30 OXALIC ACIDS

WITH 60 FREE GOLD ATOMS AND 100-AU CLUSTER WITH 1000 WATER MOLECULES AT 3.8M STEP, 950 PS. C) 30 CITRIC ACIDS WITH 90 AU ATOMS AND 100-AU CLUSTER WITH 1000 WATER MOLECULES AT 3.8M STEP, 950 PS. D) RDF OF 6.21A, 6.21B AND 6.21C AT 3.8M STEP, 950 PS. 218

FIGURE 6. 22 SNAPSHOT OF A) 30 ACETIC ACIDS WITH 90 FREE GOLD ATOMS AND 100-AU CLUSTER WITH 1000 WATER MOLECULES AT 3.8M STEP, 950 PS. B) 30 PROPIONIC ACIDS WITH 90 FREE GOLD ATOMS AND 100-AU CLUSTER WITH 1000 WATER MOLECULES AT 3.8M STEP, 950 PS. C) RDF OF 6.22A AND 6.22B AT 3.8M STEP, 950 PS. 220

FIGURE 6. 23 SNAPSHOT OF A) 30 CYS WITH 90 FREE GOLD ATOMS AND 100-AU CLUSTER WITH 1000 WATER MOLECULES AT 3.8M STEP, 950 PS. B) 30 GSH WITH 90 FREE GOLD ATOMS AND 100-AU CLUSTER WITH 1000 WATER MOLECULES AT 3.8M STEP, 950 PS. C) 30 CITRIC ACIDS WITH 90 AU ATOMS AND 100-AU CLUSTER WITH 1000 WATER MOLECULES AT 3.8M STEP, 950 PS. D) RDF OF 6.23A, 6.23 AND 6.23C AT 3.8M STEP, 950 PS. 221

FIGURE 7. 1. SUPER-LATTICE STRUCTURE OBSERVED IN STEM IMAGES OF A) ACETATE CAPPED AUNPS ON PH 6.1 AT 1 DAY WITH MOLAR RATIO 1:10.6. B) OXALATE CAPPED AUNPS WITH 1:1.5 ON PH 3 AT 7 DAYS. C) SIMULATION OF COSMIC WEB WITH DARK MATTER (SOUSBIE ET AL., 2011). D) SIMULATION OF SELF-ASSEMBLY METAL-ORGANIC FRAMEWORK (YONEYA ET AL., 2015). 231

List of tables

TABLE 2. 1 SUMMARIZED THE SIZE RANGE, RESOLUTION AND LIMITATION OF TECHNIQUES (MOURDIKOUDIS ET AL., 2018) THAT ARE USED FOR STUDYING THE MORPHOLOGY OF NMS. 31

TABLE 4. 1 LIST OF CAPPING AGENTS USED WITH NUMBER OF CARBOXYL GROUP..... 66

TABLE 4. 2 LIST OF EXPERIMENTS USING ACETIC ACID AS CAPPING AGENT. 67

TABLE 4. 3 LIST OF EXPERIMENTS USING OXALIC ACID AS CAPPING AGENT. 67

TABLE 4. 4 LIST OF EXPERIMENTS USING CITRIC ACID AS CAPPING AGENT. 68

TABLE 4. 5 LIST OF EXPERIMENTS USING PROPIONATE ACID AS CAPPING AGENT. 68

TABLE 5. 1 LIST OF EXPERIMENTS USING THIOL AS CAPPING AGENT. 138

TABLE 5. 2 LIST OF EXPERIMENTS OF AGNPS..... 138

TABLE 6. 1 INFLUENCE ON NUCLEATION AND GROWTH RATE WITH RESPECT TO LIGAND TYPE. 222

List of Abbreviations

-COOH	Carboxylic acid group
AA	Acetic acid
ADF	Annular Dark Field
AgNPs	Silver nanoparticles
AgPNCs	Silver Pre-nucleation clusters
AMBER	Assisted Model Building with Energy Refinement
AMS	Amsterdam modelling suite
AuNMs	Gold nanomaterials
AuNPs	Gold nanoparticles
AuPNCs	Gold Pre-nucleation clusters
BF	Bright Field
CA	Citric acid
CHARMM	Chemistry at Harvard Macromolecular Mechanics
CNT	Classical nucleation theory
CYS	L-Cysteine
DFT	Density Functional Theory
DIW	Deionized Water
DLS	Dynamic Light Scattering

DLVO	Derjaguin–Landau–Verwey–Overbeek
DR	Digestive Ripening
EAM	Embedded Atom Method
EDS/X	Energy-Dispersive X-ray Spectroscopy
FCC	Face-Centered Cubic
FFT	Fast Fourier Transform
GSH	Glutathione
HAADF	High-Angle Annular Dark Field
HAuCl4	Chloroauric acid
HR-TEM	High-Resolution Transmission Electron Microscopy
LJ	Lennard-Jones
LSPR	Localized Surface Plasmon Resonance
MD	Molecular dynamics
mM	Millimolar
NaBH4	Sodium borohydride
NMs	Nanomaterials
NPs	Nanoparticles
NRs	Nanorods
OA	Oriented attachment
OA	Oxalic acid

OR	Ostwald ripening
PA	Propionic acid
PBC	Periodic Boundary Condition
PDI	Polydispersity Index
pH	Measure of acidity or basicity in an aqueous solution
PNCs	Pre-nucleation clusters
r-MD	Reactive Molecular dynamics
RDF	Radial Distribution Function
ReaxFF	Reactive Force Field
SAXS	Small-Angle X-ray Scattering
SEM	Scanning Electron Microscopy
STEM	Scanning Transmission Electron Microscopy
STM	Scanning Tunnelling Microscopy
UV-Vis	Ultra-Violet visible spectroscopy
VDW	Van Der Waals
WAXS	Wide-Angle X-ray Scattering
XRD	X-ray Diffraction

Chapter 1 : Introduction

1.1 Scientific rationale

Nanoparticles (NPs) are advanced materials with sizes typically in the range of 1 to 100 nm. They show unique physical and chemical properties due to their small size and high surface area to volume ratio (Haiss et al., 2007) compared to their bulk counterparts, introducing property modification that lead to a variety of novel applications (Agrawal et al., 2021, Li et al., 2018, Khan et al., 2019).

Among all nanomaterials, gold nanoparticles (AuNPs) are a class of transition metals that have attracted considerable attention due to their tuneable properties (Ji et al., 2007). AuNPs can be synthesized through various methods (Oliveira et al., 2023), especially chemical reduction, and they can be functionalized with different ligands (Thai et al., 2022), such as carboxyl and thiol groups, to modify their surface properties (Romain et al., 2023).

The ability to control the synthesis processes is crucial for producing nanoparticles with desirable characteristics, such as uniform size and shape (Pattadar and Zamborini, 2019). Furthermore, the ability to understand the stability with ligand (Zhang et al., 2021) can manipulate the surface properties of AuNPs, which are also key to their reactivity

and function (Le Goas et al., 2022). Understanding how different ligands affect AuNPs is important to develop a safe by design nanomaterials (Kus-Liskiewicz et al., 2021).

With recent advancement of molecular dynamics simulations, this approach can provide a deeper understanding of how these ligands affect the nucleation and growth mechanisms by modelling the interactions between the gold atoms and the ligands (Suarez-Lopez et al., 2022).

By combining the principles of nanoparticle synthesis, gold nanoparticle chemistry, and molecular dynamics simulations, these methods offer a comprehensive approach to studying the growth and stability of AuNPs. Understanding these mechanisms is crucial for designing nanoparticles with desired properties for various applications.

1.2 Aims and objectives of research

The main aim of this research was to investigate the synthesis, growth, and structural evolution of transition metal nanoparticles, with a particular interest on AuNPs capped with different ligands, with a focus on understanding the effects of capping agents on nanoparticle behaviour during nucleation and growth.

To study the change in size and morphology with respect to time (aging) of sub-10 nm AuNPs capped with carboxyl group ligands in aqueous media, this project will be focusing on the impact of factors such as pH, molar ratio of the capping agent to gold,

the number of carboxyl groups, and the size of the capping agent, and characterize using HAADF-STEM. To further investigate the effect of ligand on aging with sub-10 nm AuNPs, the study expands to thiol group capping agent namely L-cysteine (Cys) and glutathione (GSH).

Eventually, the study utilized the advance of reactive molecular dynamics to bridge all findings, providing an atomistic view of the early nucleation stages and initial growth of AuNPs in the presence of carboxyl and thiol capping agents.

1.3 Aim 1

The objective of the first research chapter was to study the temporal size and shape evolution of sub-10 nm AuNPs in aqueous media. These nanoparticles were synthesized using sodium borohydride as the reducing agent. This chapter emphasizes the influence of key parameters, including pH, the molar ratio of the capping agent to gold, the number of carboxyl groups in the capping agent, and the capping agent's molecular size, on the growth behaviour of AuNPs, analysed through HAADF-STEM.

1.4 Aim 2

The objective of the second research chapter was to examine the temporal changes in size and morphology of AuNPs capped with L-cysteine and glutathione, as well as other transitional metal nanoparticles like silver nanoparticles (AgNPs) capped with citric acid and L-cysteine. This chapter focuses on comparing the nucleation and growth behaviours of AuNPs capped with carboxyl groups versus thiol groups and gaining insights into the nature of PNCs.

1.5 Aim 3

The objective of the third chapter was to use reactive molecular dynamics simulations to connect the findings from the first two chapters by providing an atomistic view of the early nucleation stages and initial growth of AuNPs in the presence of carboxyl and thiol capping agents.

1.6 Layout of thesis

This thesis contains eight chapters: (1) Introduction, (2) Literature Review, (3) Methodology, three experimental chapter that talk about, (4) the aging effect of carboxyl group capping agent on sub-10 nm AuNPs, (5) the properties of pre-nucleation cluster and the interaction with nanoparticles, and (6) a simulations chapter that models the

nucleation and growth with ligands of AuNPs in aqueous media, finishing with (7) conclusion and (8) future work.

The introduction will cover the general areas of the research topics and a brief introduction of the objectives of the thesis.

The Literature Review Chapter will cover the background of nanoscience, method of making nanoparticles, nucleation and growth mechanisms, colloidal stability, importance of gold nanoparticles, wet chemistry synthesis and characterizing techniques, molecular dynamics and recent advancement with future direction.

The methodology chapter will discuss the operation of STEM as a characterization technique used in this thesis and discuss the simulation protocol with reactive molecular dynamics.

Chapter 4 will examine the growth of AuNPs capped by different carboxyl group ligands, namely acetic acid, oxalic acid, citric acid, and propionic acid, with varying molar ratios and pH. The goal is to study the correlation between the number of carboxyl groups and other experimental conditions (pH, ligand/Au ratios) on the stability of AuNPs.

Chapter 5 will focus on the result of thiol group capped AuNPs, and the details of PNCs formation and how AuNPs age differently when thiol group ligands, namely L-cysteine and glutathione (GSH), are used compared to carboxyl group-capped AuNPs.

Chapter 6 will study the nucleation with ligands of AuNPs and the effect of ligand shell morphology in terms of growth rate of AuNPs using molecular dynamics (MD) simulations, aiming to integrate and complete the research across all chapters.

The conclusion chapter will summarize all the findings of the thesis, highlight the agreements and disagreements in the results and comparing findings with existing literature, and offer insights into future directions for addressing the remaining unanswered questions.

Chapter 2: Literature Review

2.1 Introduction

This chapter discusses topics related to this thesis, beginning with the background of nanoscience and progressing to the general methods of synthesizing nanoparticles, as well as the science behind their nucleation and growth mechanisms. It then addresses stability-related topics, such as colloidal stability and its relationship with ligands. The chapter also highlights the significance of gold nanoparticles, methods for their synthesis, advancements in molecular dynamics, and recent discoveries in the field.

2.2 Background of nanoscience

Nanoscience is the field that studies materials and their behaviour on the 1–100 nm scale. At this nanoscale, materials exhibit different physicochemical properties compared to their bulk counterparts due to their increased surface area-to-volume ratios (Haiss et al., 2007, Sonnichsen et al., 2002) and quantum effects (Zeng et al., 2016, Negishi et al., 2015). These pronounced effects allow nanomaterials (NMs) to interact with their surroundings and behave in novel ways, opening up new possibilities across various fields such as catalysis (Agrawal et al., 2021) drug

delivery (Li et al., 2018), imaging (Peng et al., 2020) and medicine (Zhang et al., 2021).

The ability to manufacture and engineer NMs (Patil et al., 2022) thus provides an important steppingstone to transform different industries (Kapil et al., 2021), improve performance, efficiency (Chen et al., 2017) and eventually sustainability. Nanoscience represents a pivotal field when it comes to innovation, especially as new methods and technique will enable a more precise control and understanding of NMs' physicochemical properties, subsequently expanding the scope of their applications and bringing society impact (Zhang et al., 2020) underscoring the need for a thorough understanding of NM science.

2.3 Methods of making nanoparticles

Top-down and bottom-up approaches (Biswas et al., 2012, Abid et al., 2022) are the two primary pathways for NP synthesis (Figure 2.1). While both can ultimately produce NMs, the products differ significantly in terms of their properties and applications.

The top-down approach involves breaking down bulk material into nanoscale entities. This method is typically used for fabricating patterned materials, such as semiconductors. However, NMs produced via the top-down method often suffer from surface defects, and the size of the resulting particles is limited. Techniques

like ball milling (Xing et al., 2013), which grinds bulk materials into nanometer-sized particles, and lithography (Pan et al., 2021) are commonly used in this approach.

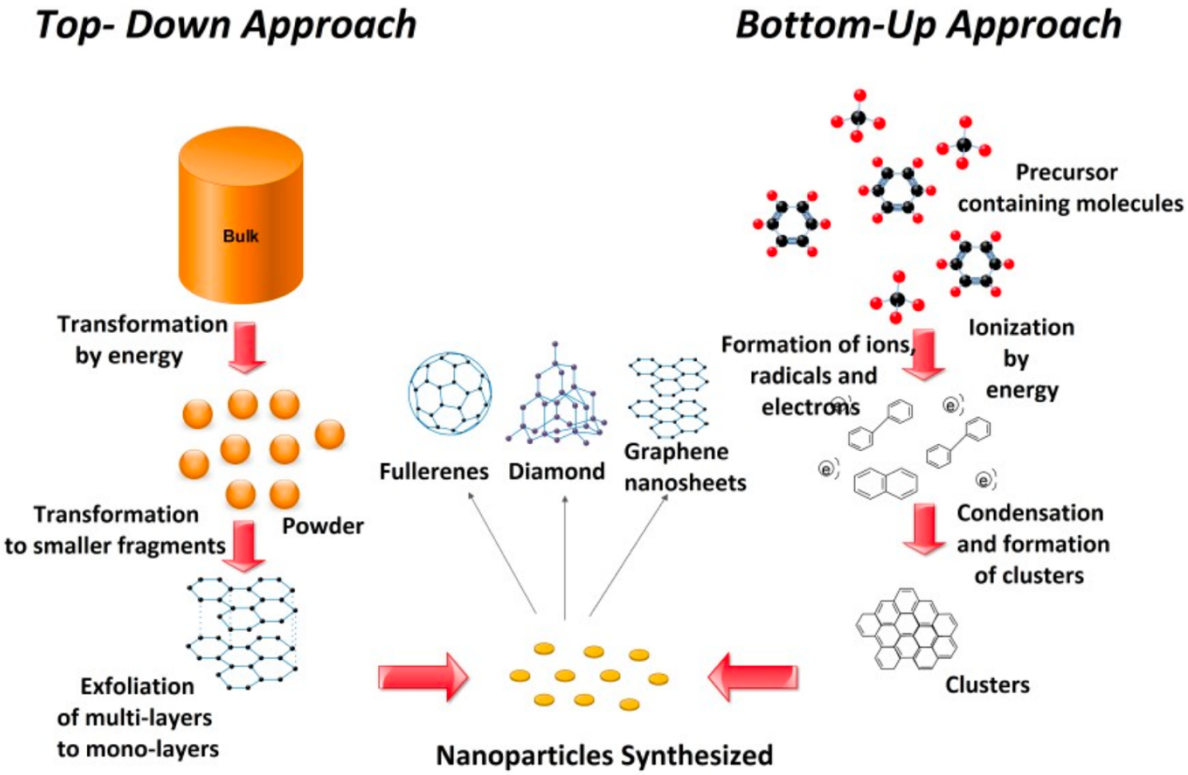


Figure 2. 1 Illustration of top-down and bottom-up approach (Habiba et al., 2014).

In contrast, the bottom-up approach constructs NMs from basic building blocks, such as atoms or molecules, starting from molecular precursors. This method is commonly employed in wet chemistry synthesis, offering precise control over the properties and morphology of the resulting nanoparticles (Daruich De Souza et al., 2019). However, it requires careful consideration of various reaction conditions, including temperature, pH, concentration, and the choice of ligands (Dong et al., 2020). For example, the Turkevich method (Turkevich et al., 1951) and the two-step Brust method (Brust et al., 1994) are widely used for synthesizing AuNPs,

utilizing citrate and sodium borohydride as reducing agents, respectively. These methods are popular because they are scalable, versatile, and allow control over key parameters, as well as ligand exchange for various applications.

2.4 The science of nanomaterial synthesis

Understanding the formation of nanomaterials requires a solid grasp of the fundamental principles that govern their synthesis. This process includes a trigger mechanism (eg reduction), nucleation, and subsequent growth. Several theories explain these phenomena, including classical nucleation theory (CNT) (Karthika et al., 2016), which describes how atoms coalesce to form stable nuclei, Gibbs free energy principles that govern the energies of the process, and newer insights into non-classical nucleation and formation of pre-nucleation clusters (PNCs) (Ramamoorthy et al., 2020).

Reduction mechanisms are a critical step in the synthesis of many NPs. This chemical process reduces metal ions to their zero-valent form. For example, in the synthesis of AuNPs, the Turkevich method (Turkevich et al., 1951) employs citrate as a reducing agent, while stronger reducing agents like sodium borohydride ($NaBH_4$) are used in certain protocols (Brust et al., 1994) to create a more vigorous nucleation, yielding smaller and more monodisperse NPs.

Once the precursor is reduced, fundamental principles explain the nucleation and growth processes. CNT, coupled with Gibbs free energy considerations, provides a foundational understanding of nucleation in terms of surface and volume energy. According to CNT, a critical Gibbs free energy is required for a stable nucleus to form (Figure 2.2). Particles smaller than the critical size dissolve, while those larger are thermodynamically stable.

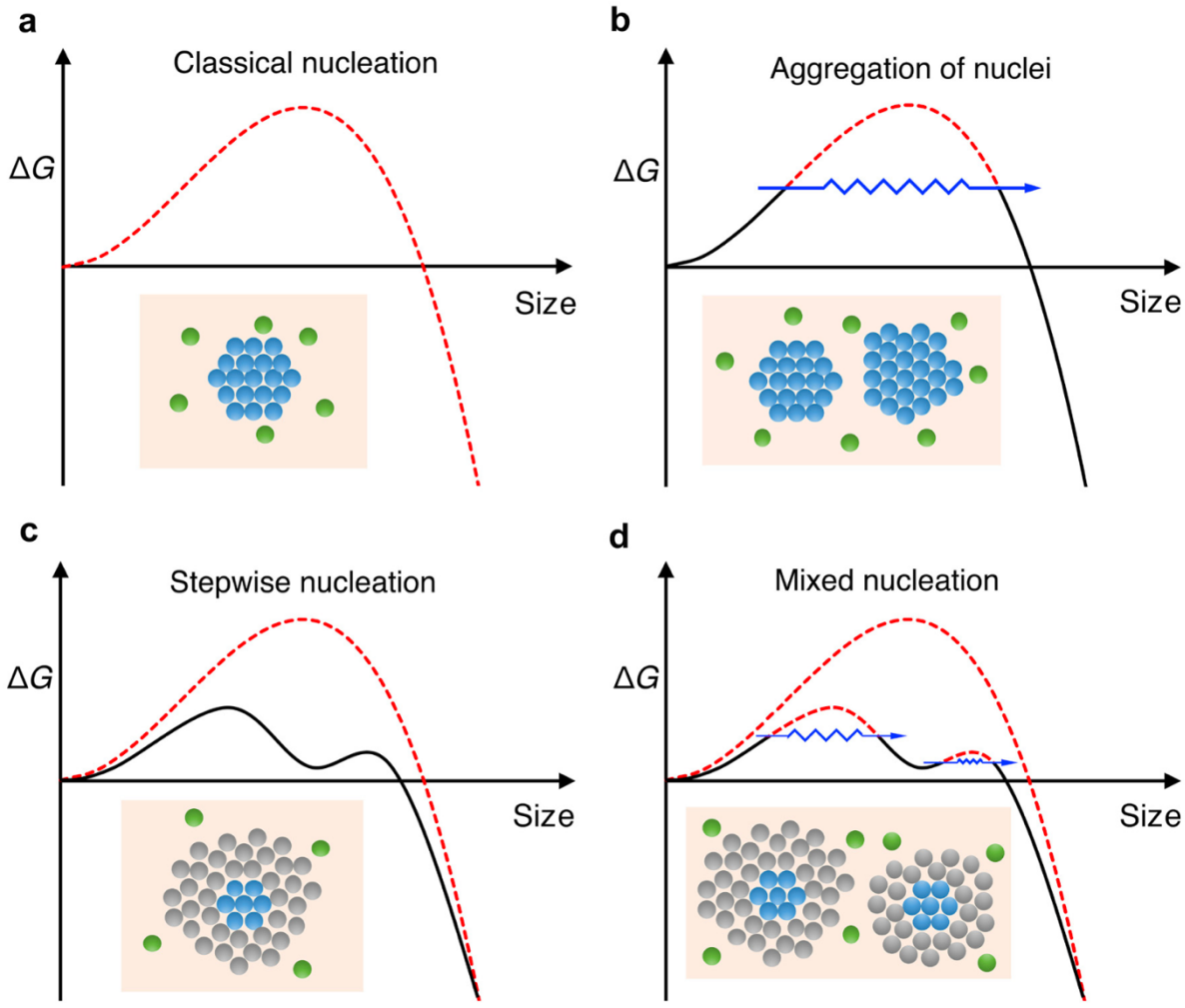


Figure 2. 2 Illustration of the change of Gibbs free energy curve to the critical size nucleus of nucleation with different nucleation pathway (Ou et al., 2022)

The LaMer model (LaMer and Dinegar, 1950) further describes nucleation and growth in terms of supersaturation, emphasizing the need for a burst of nucleation followed by controlled growth to produce monodisperse particles.

Additionally, Fick's law (Wen et al., 2014) describes material flow within a solution, influenced by concentration gradients. These principal sheds light on particle growth rates and the limitations imposed after nucleation.

Following nucleation, colloidal stability is crucial for determining nanoparticle behaviour. The Derjaguin–Landau–Verwey–Overbeek (DLVO) theory (Agmo Hernández, 2023) explains stability as a balance between electrostatic repulsion and van der Waals (VDW) attraction forces. Stable colloids prevent agglomeration, maintaining monodispersity. Conversely, instability arises from an imbalance between these forces, leading to aggregation, sintering, and uncontrolled particle growth.

While classical theories provide a strong foundation, they do not fully address aspects such as non-classical nucleation, pre-nucleation clusters (PNCs), or amorphous intermediates (Habraken et al., 2013, Gebauer et al., 2014). The effect of ligand on the nucleation and growth of NMs will change the morphology of the NPs via the mechanism of selective binding (Meena and Sulpizi, 2016). This will allow the possibility of anisotropic growth, leading to special structure such as nanorods (NRs), high-index morphology (Zhang et al., 2015, Zhang and Wang, 2014, Hong et al., 2012, Lee et al., 2018). However, CNT does not include the

reaction kinetics involving ligands which are one of the driving factors that cause the morphology changes in NPs.

To address these challenges, non-classical nucleation theory is in development. Non-classical nucleation considers metastable intermediates and suggests nucleation as a continuous process (Lee et al., 2016). For example, this theory allows small assemblies of atoms or ions such as PNCs to exists (Figure 2.3), and particles can form as amorphous clusters before crystallizing into NPs (Gebauer et al., 2014). These factors are critical because they suggest the nucleation is not simply an aggregation of monomers but can involve complex interaction, such as solvent effects and dynamic ligand exchanges.

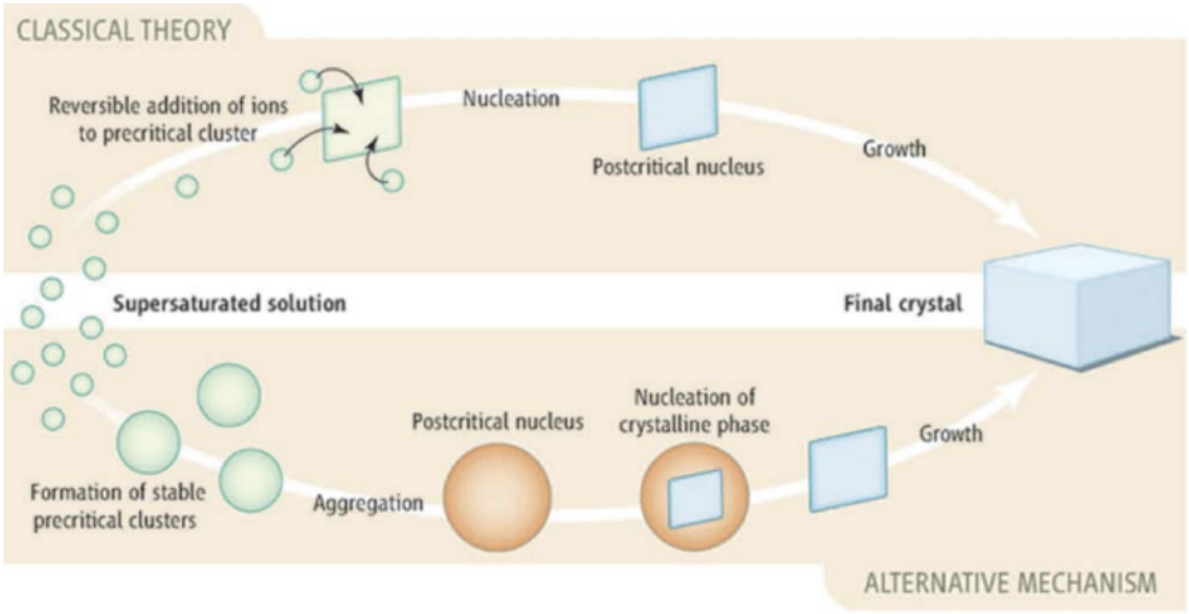


Figure 2. 3 Illustration of classical nucleation and non-classical nucleation pathway (Gebauer et al., 2014).

In non-classical nucleation, PNCs (Dachraoui et al., 2021b) are one key factor to study to fully understand the nucleation mechanics. PNCs are metastable structures that exist in a local equilibrium with the surrounding solution. These PNCs can act as precursors to nucleation unlike the classical nuclei suggested by CNT. These clusters can provide a seed for further growth by reducing the energy barrier for nucleation. PNCs can also affect the size distribution of the NPs as the morphology of PNCs can change and react to solution conditions.

This perspective highlights the complexity of nucleation as more than a simple aggregation of monomers, involving solvent effects and dynamic ligand exchanges. Non-classical nucleation theory, therefore, expands the understanding of nanoparticle synthesis.

The formation of nanoparticles is governed by reduction kinetics, energetics, and dynamic interactions in solution. While CNT offers a foundational framework, non-classical nucleation theory reveals the intricacies of synthesis. Understanding these principles is essential for optimizing methods to achieve precise control over nanoparticle properties. This foundational knowledge underpins advancements in growth, stabilization, and the broader applications of nanoscience.

2.5 Growth and other related mechanisms

Nanoparticle growth involves several complex processes that dictate the size, shape, and overall stability of the particles (Thanh et al., 2014). Understanding these mechanisms is crucial for tailoring nanoparticles for specific applications.

Other related mechanisms include (Figure 2.4):

Agglomeration, which refers to the physical clustering of NPs without chemical bonding or fusion between them. This phenomenon primarily occurs when attractive forces, such as VDW forces, overpower repulsive forces such as electrostatic or steric stabilization. Agglomeration can be mitigated by employing capping agents or surfactants to reduce the attraction between NPs, thus enhancing colloidal stability.

Aggregation, which, in contrast, involves the irreversible bonding or fusing of nanoparticles, leads to the formation of larger, often less desirable, structures. Aggregation is typically driven by prolonged contact between NPs, resulting in a fused morphology. To prevent aggregation, effective capping ligands can be employed alongside careful control of synthesis parameters such as temperature and pH (Yazdani et al., 2021).

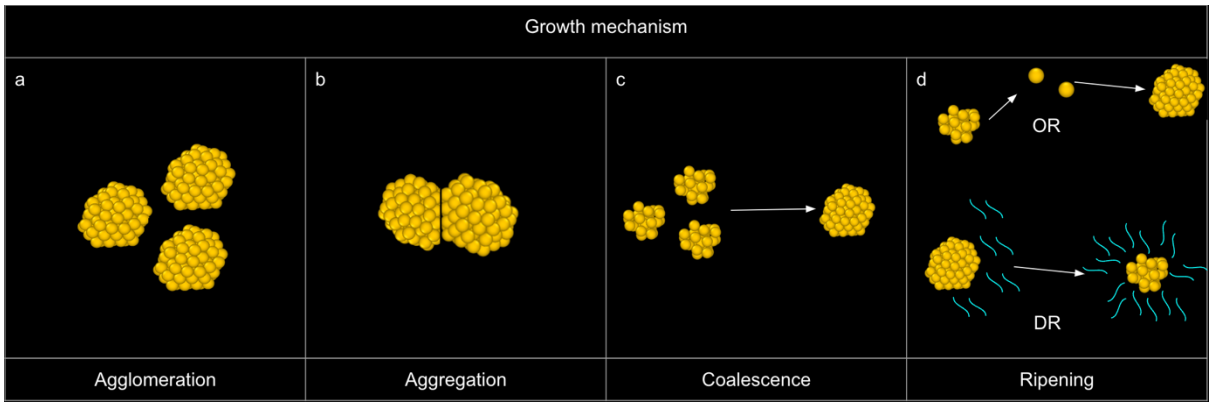


Figure 2. 4 Illustration of growth mechanisms, a) agglomeration, b) aggregation, c) coalescence, d) Ostwald ripening on top and digestive ripening on bottom.

Coalescence, also known as sintering, which is the merging of two or more NPs into a single, larger NP. This process is driven by the minimization of surface energy. When two NPs come into close contact, their surfaces dissolve and reorganize, resulting in a single, more stable structure (Wang et al., 2016). Coalescence leads to a decrease in the total Gibbs free energy, making the process thermodynamically favourable as the particles reach a lower energy state.

Oriented attachment (OA) (Figure 2.5), which is a unique growth mechanism in which NPs align and merge along specific crystal planes (Li et al., 2023). This process is often observed in the synthesis of anisotropic NMs, such as nanorods (NRs) or nanowires (NWs). During OA, the merging NPs align their crystal lattices in a specific orientation before fusion. The resulting crystal structure of the fused particle is based on the lattice of one of the original NPs. This eliminates the need for individual atoms to realign and overcome the faulting energy barrier required

for recrystallization into a unified structure (Ingham et al., 2011). Instead, OA enables NPs to "click" together seamlessly along a favourable crystal plane, leading to a stable, low-energy state (Li et al., 2012).

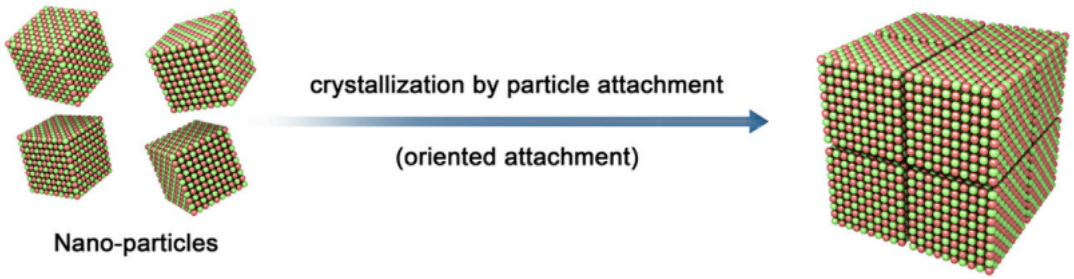


Figure 2. 5 Illustration of Oriented attachment mechanism (Liu et al., 2019b).

Ripening, which refers to the redistribution of material among NPs, leading to their size evolution over time. Two primary ripening mechanisms, Ostwald Ripening (OR) and Digestive Ripening (DR), govern this process, each with distinct characteristics and applications.

Ostwald ripening (OR), first described by Ostwald in 1897 (Ostwald, 1897) occurs when smaller NPs dissolve, and their material is redistributed onto larger NPs. This phenomenon arises because smaller NPs possess higher surface energy and are thus more soluble. Over time, colloidal systems undergoing OR evolve toward a thermodynamically stable state characterized by fewer, larger NPs with lower overall Gibbs free energy (Lifshitz and Slyozov, 1961, Wagner, 1961). This process is particularly relevant in NP synthesis, as it provides a means of controlling particle size distribution. Additionally, electrochemical OR leverages this mechanism to synthesize NPs with desired properties (Jang et al., 2011),

suggesting that growth mechanisms should be utilized as a tool to direct a NPs growth to a favourable morphology (Ustarroz et al., 2013).

Digestive ripening (DR), in contrast to OR, works in an inverse manner (Lee et al., 2007, Shimpi et al., 2017). DR involves heating a dispersion of NPs in the presence of stabilizing agents (ligands) to promote the dissolution of larger particles and the growth of smaller ones. Ligands preferentially bind to specific facets of the NPs, driving this redistribution of material. DR is particularly effective for fine-tuning NP size and dispersity, making it a valuable tool in synthesizing monodisperse NPs. Moreover, it provides a sustainable approach for reprocessing NPs that have grown to undesired sizes, ensuring efficient reuse of materials (Stoeva et al., 2005).

In fact, the growth of NPs may be governed by a combination of the above mechanisms, including agglomeration, aggregation, coalescence, OA, OR, and DR. These mechanisms often occur simultaneously, collectively influencing the final size distribution, morphology, and stability of the synthesized NPs.

To achieve NPs with specific characteristics, it is crucial to tailor and precisely control the synthesis conditions. Factors such as the choice of ligands, stabilizing agents, and environmental conditions (e.g., temperature, pH, and reaction time) play a pivotal role in determining the outcome. By optimizing these parameters, researchers can produce NPs with the desired properties, enabling their application across various fields.

2.6 Colloidal stability

Understanding the behaviour of NPs, including their stability and the ability to predict the morphology and physicochemical properties shift with respect to time are essential. These factors are largely influenced by the ligands present in the synthesis medium. Ligands bind to the surface of NPs, impacting not only surface chemistry and interactions but also the long-term properties of the colloidal system (Nam et al., 2023), ultimately determining the stability and predictability of the NPs.

A thorough understanding of the physical and chemical interactions between ligands and NP surfaces is crucial. Ligand binding can influence surface passivation, effectively preventing agglomeration or aggregation, as discussed earlier. Moreover, appropriate ligand selection can induce electrostatic repulsion between NPs, such as through zeta potential, enhancing stability (Beurton et al., 2020). Additionally, the size and structure of the ligand can provide steric hindrance (Choi et al., 2023), physically preventing NPs from coming into close contact and thereby reducing the likelihood of aggregation.

Building upon this foundation, ligand coverage plays a crucial role in determining the evolution of NPs (Heuer-Jungemann et al., 2019). Ligand coverage refers to the distribution of organic or inorganic ligands on the surface of NPs (Wang et al., 2011). Typically, a uniform layer of ligands on the NP surface provides high stability (Schulz et al., 2016), forming an electric double layer (Park and

Shumaker-Parry, 2014) that “shields” the particles, restricting or ending any further reactions and stabilising their behaviour. The ligands passivate the NP surface, controlling their solubility and enhancing colloidal stability (Nishigaki et al., 2012, Krommenhoek et al., 2012). Furthermore, optimal ligand coverage creates a full steric hindrance around the NP surface, preventing undesirable particle-to-particle interactions.

Conversely, insufficient ligand coverage on the NP surface leads to exposed "landing spots," where free atoms can adhere to the NPs. This can result in inhomogeneous growth, or even aggregation or sintering, ultimately undermining the desired stability and uniformity of the nanoparticles.

To tailor NPs for specific applications, ligand exchange is often employed. This process involves replacing the initial ligands on the NP surface with new types of ligands. When ligand exchange is successfully carried out, it often enhances the stability of the NPs (Jin et al., 2016). However, incomplete ligand exchange can destabilize the NPs, leading to undesirable changes in size or physicochemical properties.

Ligands are critical in determining the stability and behaviour of NPs. The stability of NPs refers to their ability to maintain consistent morphology and dispersity over time, while their behaviour relates to the predictability of this stability, which directly impacts their performance in applications. Several factors contribute to the stability of NPs. For instance, the use of strongly binding ligands, such as thiol versus carboxyl groups on AuNPs, ensures better surface passivation (Le Goas et

al., 2022). Full coverage of the NP surface with ligands provides both physical (steric hindrance) and chemical (surface passivation) protection. Additionally, the possibility of ligand desorption when NPs are transferred from one medium to another can also influence their stability. NPs with enhanced stability naturally exhibit more predictable behaviour, making them more reliable for various applications.

However, the absence of ligands on the surface of NPs can lead to aggregation or coalescence, as free atoms may adhere to the surface, promoting processes such as OR. Additionally, an inhomogeneous distribution of ligands across the NP surface may cause only certain particles to dissolve during OR, resulting in a more polydisperse nanoparticle population. Inadequate ligand coverage can also weaken the bond between the ligand and the NP surface, allowing for atomic rearrangement on the NP surface. These factors can influence the time-dependent evolution of the NP's physicochemical properties and morphology, ultimately leading to undesirable growth or aging.

Ligands are essential for maintaining the functionality and stability of NPs. By selecting the appropriate ligands with optimal binding to the NP surface and ensuring uniform coverage, as well as successful ligand exchange, the NPs' physicochemical properties and morphology can be made predictable and stable in solution (Thai et al., 2022). Conversely, failure to control these factors may result in unwanted growth and aging, making the NP's properties less predictable. By thoughtfully designing the synthesis and stabilization strategies, it is possible to create stable and predictable NPs with tailored properties.

2.7 Importance of gold nanoparticles

AuNPs are known for their exceptional properties, which have positioned them at the spotlight of nanotechnology research and applications. Their unique combination of optical (Hong et al., 2012), chemical, and biological properties (Khan et al., 2019) makes them invaluable across diverse disciplines, including medicine (Dreaden et al., 2012), catalysis (Haruta et al., 1987, HARUTA et al., 1989, Haruta, 2004, Pal and Pal, 2015), electronics (Ghobashy et al., 2024), and environmental science (Liu et al., 2019a).

One of the significant attributes of AuNPs is their localized surface plasmon resonance (LSPR) (Haiss et al., 2007). This phenomenon occurs when conduction electrons on the nanoparticle surface oscillate in resonance with incident light. The result is a striking ability to absorb and scatter light intensely (Li et al., 2009). Unlike many other materials, the optical properties of gold nanoparticles are highly tuneable by adjusting their size, shape, and aggregation state (Ji et al., 2007). This tunability is leveraged in applications such as biosensing (Chen et al., 2017), photothermal cancer therapy (Gharatape et al., 2016), and advanced imaging techniques (Eyvazzadeh et al., 2017).

Another characteristic of AuNPs is their chemical stability. Gold's natural resistance to oxidation and corrosion ensures that these nanoparticles are more

likely to remain stable over time. Furthermore, some sizes of AuNPs are inherently biocompatible, meaning they are believed to post the least toxicity risks at appropriate concentrations (Kus-Liskiewicz et al., 2021). This, combined with their ability to be functionalized with biological molecules like DNA (Huang et al., 2022), proteins (An et al., 2015), or antibodies (Pissuwan et al., 2007), has unlocked a range of applications in drug delivery (Zhang et al., 2021) and targeted therapeutic interventions (Kesharwani et al., 2023).

Gold nanoparticles also exhibit remarkable catalytic activity, particularly for chemical reactions involving oxidation (del Río et al., 2016) and reduction (Higuchi et al., 2015) due to the high surface area to volume ratio and unique electronic structure allow them to act as efficient catalysts under different conditions (Ishida et al., 2020). This catalytic efficiency is widely applied in industrial processes (Xia et al., 2024) and environmental remediation (Turan et al., 2019).

The versatility of gold nanoparticles is further enhanced by the ease of their synthesis and functionalization. Researchers can precisely control the size and shape of AuNPs (Patil et al., 2022) whether spheres, rods, or stars (Lee et al., 2018) during their synthesis. Moreover, their surfaces can be modified with various ligands (Heuer-Jungemann et al., 2019), enabling customization for specific purposes such as targeted drug delivery (Amina and Guo, 2020) or biosensing (Zhou et al., 2020).

Gold nanoparticles represent a remarkable platform for applying advanced materials science for practical application. Their unmatched combination of

tuneable optical properties, chemical stability, biocompatibility, and catalytic efficiency has made them an indispensable tool in modern research and technology. While other nanoparticles have their own specialized uses, AuNPs' versatility and reliability ensure their continued prominence in the nanotechnology landscape.

2.8 Chemical synthesis of gold nanoparticles

Building on this foundation, the synthesis of AuNPs has been optimized and refined over the years. Various techniques and modifications have been developed to precisely control the morphology, stability, and time-dependent behaviour of AuNPs.

The Turkevich method (Turkevich et al., 1951, Frens, 1972) is the most used chemical synthesis protocol for producing monodisperse, spherical AuNPs, typically in the size range of 10-50 nm (Wuithschick et al., 2015). In this method, chloroauric acid is dissolved in water, and the solution is boiled. Citrate is then added as both a reducing agent and a capping agent for the AuNPs. Nucleation and growth occur simultaneously during the boiling process.

This method is widely adopted due to its reproducibility and the ability to control the size of the nanoparticles by adjusting the citrate-to-gold molar ratio (Tran et al., 2016, Karimi et al., 2019, Ji et al., 2007), temperature (Mendez et al., 2021), pH

(Kettemann et al., 2016) and reaction time of the synthesis (Yazdani et al., 2021). However, one limitation of the Turkevich method is that it is challenging to synthesize AuNPs smaller than 10 nm or larger than 50 nm. Additionally, it is primarily limited to producing spherical AuNPs.

The inverse Turkevich method (Ojea-Jiménez et al., 2011, Schulz et al., 2014) is a variation of the Turkevich method designed to improve control over the morphology and dispersity of AuNPs. Unlike the traditional Turkevich method, where citrate is added to the boiling gold precursor, the inverse Turkevich method involves adding the gold precursor to the boiling citrate solution. This modification leads to a small burst of nucleation, resulting in the formation of smaller AuNPs.

Several other methods, which are variations of the original Turkevich protocol with slight modifications have also been developed. For example, the addition of an impurity like $AgNO_3$ to the mixture can reduce the particle size to around 6 nm, and further reduction to 2 nm can be achieved by using glutathione (GSH) in the process (Xia et al., 2016). Another variation involves changing the reducing agent to tannic acid (Piella et al., 2016) or ascorbic acid (Guo et al., 2012), each of which tailors the resulting AuNP morphology. These modifications demonstrate the versatility of the Turkevich method, where careful adjustments to the chemicals used or the sequence of their addition can significantly influence the size and shape of the synthesized AuNPs.

To synthesize smaller AuNPs, the two-step Brust nucleation method (Brust et al., 1994, Perala and Kumar, 2013)can be employed. This method separates the

nucleation and growth phases, allowing for more precise control over particle size and dispersity (Hosseini et al., 2018). In this process, the gold precursor is first transferred from an aqueous phase to an organic phase, such as toluene. Thiol is then added to the organic phase to partially reduce the gold precursor without reaching the zero-valent state. Afterward, a strong reducing agent, borohydride, is introduced into the organic phase, quickly reducing the gold ions and initiating a burst of nucleation, which produces seed AuNPs for further growth.

The growth phase typically involves modifying reaction conditions, such as introducing a new ligand with different binding affinities or adjusting the temperature, depending on the desired type of gold nanomaterials (AuNMs). This two-step method is particularly advantageous for controlling shape and size, and it can produce smaller AuNPs, even at the atomic scale (Krommenhoek et al., 2012, Nishigaki et al., 2012, Qian et al., 2012), exhibiting “magic number” quantum confinement effects (Zeng et al., 2016, Negishi et al., 2015).

Like the Turkevich method, various modifications of the two-step Brust method have been developed. For example, adjusting the molar ratio of thiol (Sardar and Shumaker-Parry, 2011) can influence the size of the AuNPs. A combined method using both the strong reducing power of borohydride and the absence of citrate under ice-cold temperatures has been proposed to create a one-pot synthesis method (Karimi et al., 2019, Al-Johani et al., 2017) further demonstrating that understanding the growth mechanism is key to optimizing synthesis protocols. Studies on the choice of ligands for synthesis (Prasad et al., 2002, Bhaskar et al.,

2014) have led to the development of AuNPs synthesis methods based on DR mechanisms (Sahu and Prasad, 2012, Sahu and Prasad, 2014, Sahu et al., 2017).

Each method has its own advantages and limitations. The Turkevich method is widely adopted for its simplicity and scalability, while the two-step Brust method offers superior control over size and shape by separating the nucleation and growth phases. By studying the growth mechanisms of NPs, new techniques can be developed, and the appropriate synthesis method can be selected to meet the specific requirements of an application.

2.9 Characterization techniques

With the variety of synthesis methods available, it is crucial to ensure that the NMs produced are well-characterized. This requires a solid understanding of characterization techniques. Various methods can be used to determine the morphology, surface properties, crystal structure, and optical behaviour of AuNPs (Mourdikoudis et al., 2018). This section provides an overview of key techniques that can be used to study the size and shape, along with their strengths and limitations for characterizing AuNPs.

One of the most used techniques for characterization is Transmission Electron Microscopy (TEM) due to its ability to provide precise information on NPs size, shape, and dispersity. TEM works by transmitting a high-energy electron beam

through a thin sample, generating images with resolution as low as sub-nanometer scale. When high-resolution TEM (HRTEM) is used, it can even reveal atomic lattices, which enables the study of the crystal structure of the material (Jin et al., 2018). However, TEM requires careful sample preparation and is time-intensive, which can be a limitation for rapid characterization. It is also an ex-situ method, meaning that particle properties may change after being extracted from the medium where they formed.

Scanning Electron Microscopy (SEM) also utilizes an electron beam, but it generates signals based on surface interactions (Kuo et al., 2011). This technique is effective for revealing detailed surface features of NMs, and it typically requires simpler sample preparation compared to TEM. However, SEM has lower resolution than TEM, making it less suitable for atomic-scale imaging and cannot provide structural information.

Scanning Transmission Electron Microscopy (STEM), or High-Angle Annular Dark Field (HAADF) STEM, is a hybrid technique combining elements of both TEM and SEM. In STEM, an electron beam scans across the sample grid, with a detector capturing both scattered and transmitted electrons. STEM can achieve atomic-level spatial resolution, making it ideal for studying small features (Dachraoui et al., 2021b). This technique is often paired with Energy-Dispersive X-ray Spectroscopy (EDS), which maps the distribution of elements across the sample. Additionally, Liquid-cell STEM allows for the study of samples in suspension, enabling real-time observation of processes in liquids, but not always available because of the complexity of setting up liquid-cell. Like TEM, STEM also requires

sample preparation prior to imaging, presenting a challenge in terms of time and resources and it is also an ex-situ technique.

Scanning Tunnelling Microscopy (STM) offers atomistic resolution by using the tunnelling current between the sample surface and the conductive probe. This technique is sensitive to the electron density states, allowing the study for atomic arrangement and electronic properties of NMs (Hakkinen, 2012). However, it requires the sample to be put on a conductive substrate and under controlled environment conditions.

Dynamic Light Scattering (DLS) measures the scattering of light by particles in a liquid medium. This technique is commonly used to assess the hydrodynamic size and dispersity of NMs, as well as to measure the zeta potential of the suspension, which helps estimate the stability of the nanoparticles (Hussain et al., 2020). DLS is quick, non-destructive, and provides a general overview of the sample. However, since DLS only measures the hydrodynamic size and is not suitable for very small particles, additional techniques, such as TEM or STEM, are required to determine the actual size of the NMs.

UV-Vis Spectroscopy (UV-Vis) measures the absorbance of light in the ultraviolet and visible ranges, providing information about the localized surface plasmon resonance (LSPR) of the NMs (Zhang et al., 2014). The LSPR data can be used to infer the morphology of the nanoparticles based on the characteristics of the LSPR curve. Like DLS, UV-Vis is a fast and simple technique that can be applied while

the nanoparticles are in suspension. However, it only provides insights into the surface optical properties of the NMs.

X-ray Diffraction (XRD) is used to analyse the diffraction pattern of NMs when they interact with an X-ray beam. This technique is particularly useful for studying lattice parameters or crystal structures (Fleury et al., 2015). However, XRD requires the sample to be in a crystalline form, making it unsuitable for amorphous materials.

Small-Angle X-ray Scattering (SAXS) measures X-rays scattered at small angles to determine the size, shape, and internal structure of NMs in liquid media (Pauw et al., 2017). SAXS provides in situ information about the size and dispersion of nanoparticles in a colloidal system (Polte et al., 2010). While SAXS can reveal details of small NMs in suspension, it requires a synchrotron X-ray source for high resolution (Pauw et al., 2017, Pauw et al., 2021, Mourdikoudis et al., 2018). In contrast, wide-angle x-ray scattering (WAXS) extends the range of scattering to a larger angle, providing atomistic resolution to examine crystal structure and interplanar distances (Chen et al., 2015).

Each of these techniques, summarised in Table 2.1, provides unique insights into the physicochemical properties of NMs. Depending on the specific goals of the study, a combination of techniques can be employed for comprehensive characterization. However, there is still a need for need for even higher resolution and imaging technique that are viable in suspensions to study the nucleation state of NMs and to better understand the behaviour of PNCs.

Table 2. 1 Summarized the size range, resolution and limitation of techniques (Mourdikoudis et al., 2018) that are used for studying the morphology of NMs.

Technique	Size Range	Resolution	Conditions
(HR)TEM	1 - 1000 nm	0.1 – 0.2 nm	High vacuum
SEM	5 nm – 1 mm	1nm	Conductive samples
HAADF-STEM	0.1 – 1000 nm	0.1 – 0.2 nm	High vacuum
STM	0.1 – 100 nm	0.1 nm	Conductive sample
DLS	1 nm – 10000 nm	1 nm	Suspension
UV-Vis	2 – 100 nm	LSPR	Suspension
XRD	>2 nm	2 nm	Powdered
SAXS	1 – 100 nm	1 nm	Solution
WAXS	0.1 – 100 nm	0.1 – 0.2 nm	Solution

2.10 Simulation

To address these challenges, simulation techniques can serve as a valuable modelling tool to gain insights into atomistic and molecular phenomena, which are currently difficult to study experimentally. By utilizing these modelling techniques (Figure 2.6), processes such as classical or non-classical nucleation, reduction,

the formation of intermediate species between precursor and pre-nucleation clusters, the growth of NMs, and their stability can be investigated.

Molecular Dynamics (MD) model the motion of atoms and molecules by solving their equations of motion. Each entity, whether an atom or molecule, is treated as a particle within the simulation box, and their interactions are defined by a potential energy function or force field.

The Lennard-Jones (LJ) potential describes weak interactions, such as VDW forces, between two atoms or molecules. While the LJ potential is easy to implement and parameterize, it oversimplifies real-world interactions by assuming isotropic interaction and neglecting covalent or hydrogen bonding, which limits its applicability in more complex systems.

For metal-metal interactions, the Embedded Atom Method (EAM), a semi-empirical potential based on the local environment of the system, is commonly used. It provides a good approximation of interactions within large systems of metals or alloys where metallic bonds dominate (Essajai and Hassanain, 2018, Essajai et al., 2018). MD simulations using EAM are efficient for large atomic systems but are not suitable for systems involving ionic or covalent bonds.

To model complex systems involving chemical reactions and various types of bonds, reactive MD (r-MD) can be employed. This approach is essentially MD with the use of the Reactive Force Field (ReaxFF) (Duin et al., 2001, Liang et al., 2013) potential integrated into the simulation. ReaxFF (Senftle et al., 2016, Chenoweth

et al., 2008) is an advanced class of force fields specifically designed to handle the formation and breaking of bonds between atoms and molecules. This allows the modelling of chemical reactions and structural changes. By using ReaxFF, complex systems, such as the reduction mechanism of AuNPs, can be studied with the appropriate potential, enabling the exploration of interactions between ligands, metal ions and other processes that govern NM synthesis.

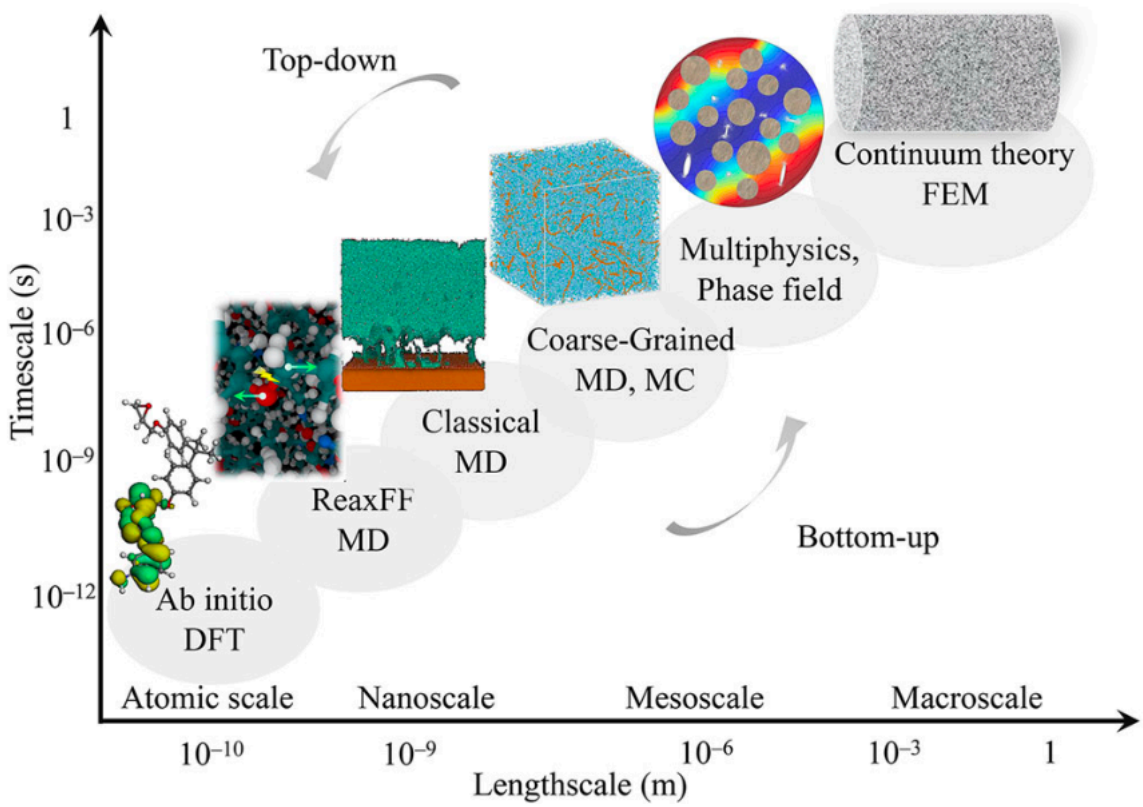


Figure 2. 6 Schematics of different modelling and their strength (Lin and Wang, 2023).

However, compared to classical MD, r-MD is computationally intensive due to the dynamic calculations of bond orders and chemical reactions. As a result, r-MD is typically used for simulating smaller systems. To develop a ReaxFF potential,

Density Functional Theory (DFT) is required to calculate the quantum mechanical equations for electronic structure and atomic-level interactions (Monti et al., 2016b). After performing DFT calculations, various parameters can be fitted into the ReaxFF model and optimized for use in r-MD simulations.

In a simulation, a thermostat can be chosen to control the system's temperature, ensuring that the environment remains thermally realistic and suitable for studying temperature-dependent phenomena such as annealing or relaxation. For instance, the Berendsen thermostat (Berendsen et al., 1984, Lemak and Balabaev, 1994) places the system in a heat bath at a fixed temperature, adjusting the particle velocities to regulate the temperature. This thermostat is commonly used during the equilibration phase of MD simulations due to its ability to quickly and stably control temperature. However, it can artificially distort energy fluctuations between particles, deviating from a true canonical ensemble. In contrast, the Nose-Hoover thermostat allows for natural temperature fluctuations while maintaining an average temperature, creating a true canonical ensemble. This makes it more suitable for studying realistic thermal behaviour, but at a higher computational cost.

Simulation and modelling offer atomistic-level insights that are difficult to achieve experimentally. By controlling macroscopic variables such as temperature, pressure, and concentration, MD simulations can focus on specific phenomena without interference from other factors. The flexibility of simulations also allows for the study of individual NPs with ligand modifications and environmental variables, providing a robust method for investigating the stability of NMs, something that

would be challenging to measure experimentally. For example, simulations have enabled studies on NPs size as a function of ligand shell structure (Kister et al., 2018) ligand length (Monego et al., 2018), and the effect of solvent (Monego et al., 2020) were made possible with simulation and modelling which are impossible to measure in real life experiment. Critical information such as citrate bridging with gold adatoms (Grys et al., 2020), ligand adsorption (Wright et al., 2014) the nature of ligand shell morphology (Perfilieva et al., 2019) as well as nucleation and growth mechanism (Meena and Sulpizi, 2016, Yu et al., 2010) has also been gained through simulations.

While simulations and modelling cannot fully replace experiments due to their inherent limitations, they are powerful tools for complementing experimental methods and addressing uncertainties or gaps in characterization. By combining experimental measurements with modelling, the reduction mechanisms and non-classical nucleation processes can be studied in greater detail.

2.11 Recent advancements and future directions

Nanoparticles, particularly AuNPs, have been at the forefront of nanotechnology research due to their unique physicochemical properties and diverse applications. Recent breakthroughs in synthesis techniques, such as green synthesis (Santhosh et al., 2022), electrochemical methods (Pattadar et al., 2019, Haro-González et al., 2019), microwave-assisted synthesis (Huang et al., 2022), alongside

advancements in characterization methods such as liquid-cell STEM (Dachraoui et al., 2021b), and synchrotron X-ray imaging, have illuminated new ways to study NMs. Additionally, the application of modelling techniques such as r-MD (Suarez-Lopez et al., 2022) has expanded our ability to simulate and predict the behaviour of NMs. Despite these advances, challenges such as nanotoxicity (Khan et al., 2019), the predictability of the NMs behaviours (Balfourier et al., 2020) the stability of ligand structure (Kang et al., 2019, Pfeiffer et al., 2014, Le Goas et al., 2022) and the aging of AuNP (Gubicza et al., 2013, Lacava et al., 2015), remain significant. Moreover, the development of new materials, such as “goldene” (Kashiwaya et al., 2024), and advances in technology like robotics and artificial intelligence optimized synthesis methods (Jiang et al., 2022) present exciting new opportunities for future research.

3.12 Conclusion

In conclusion, this literature review chapter provides an overview of the relevant topics underlying the main objectives of this thesis. A general introduction to nanoscience and nanomaterials is presented, followed by methods for synthesizing nanomaterials and the science behind nucleation and growth mechanisms. Using this knowledge, an optimized synthesis protocol can be developed with a deeper understanding of ligand interactions and colloidal stability. Although the process of making nanoparticles appears straightforward, the ability to predict changes in size and morphology is still lacking.

Therefore, the experimental chapters aim to understand the factors that govern the evolution of size and morphology of AuNPs by studying macro factors such as pH, molar ratio, and capping agents, which are closely related to nanoparticle stability. The goal is to find correlations between these macro factors and the micro phenomena that govern the size and shape changes (aging) of nanoparticles.

Chapter 3: Methodology

3.1 Introduction

This chapter provides detailed information on the synthesis procedure, the characterization techniques used in this project, and the simulation methods. It begins by introducing HAADF-STEM and EDS as the main characterization techniques, along with the procedure for using them. Next, the synthesis protocol is presented, followed by a detailed explanation of the procedure for extracting useful information.

The second part of this chapter focuses on the simulations. It details the parameters used in the simulation work and the procedure for creating the model.

3.2.1 High-Angle Annular Dark Field Scanning Transmission Electron Microscopy (HAADF-STEM)

HAADF-STEM provides an atomistic image that depends on the atomic number of the sampled elements. HAADF-STEM is a special mode of STEM that uses a highly focused electron beam to scan the sample in a similar manner to SEM. The accelerated electron will first pass through the condenser lenses, aperture,

objective lenses, reaching the sample holder that is holding the grid with samples. There, it interacts with the sampled NMs electrostatic forces from the nuclei and electron clouds. The affected electrons are subsequently scattered at different angles because of the elastic Rutherford scattering (Mourdikoudis et al., 2018) and are eventually captured by the bright field and the annular dark field (ADF) detectors on the bottom of the STEM instrument (Figure 3.1).

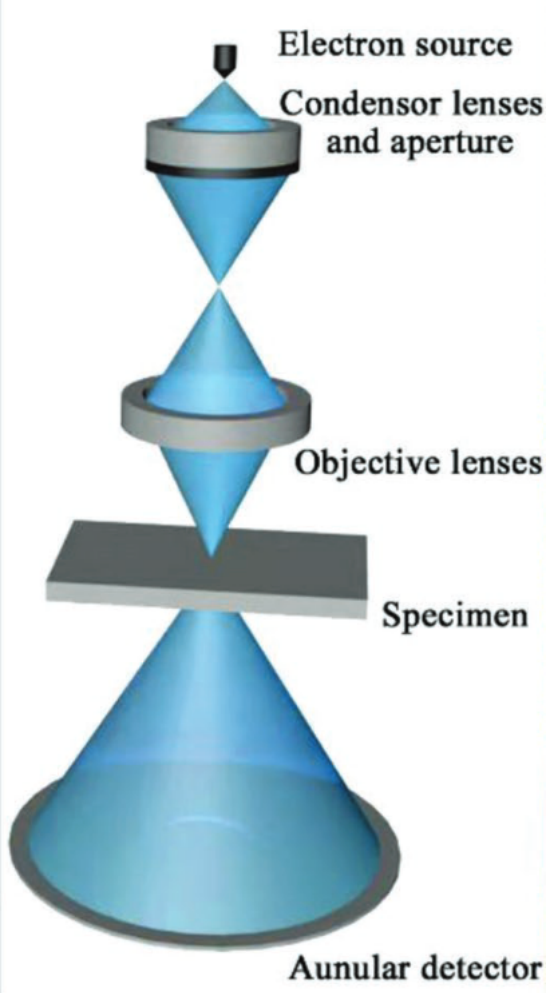


Figure 3. 1 Illustration of HAADF-STEM instrument (Zhang et al., 2022).

3.2.2 Mapping nanoparticles to the collector

The ADF detector is placed at a relatively high angle position in relation to the transmitted beam. If a denser element were sampled, more electrons will be deflected resulting in a higher electron count on the ADF detectors. As a result, NM samples with heavier atoms will appear brighter in the image, providing Z-contrast.

3.2.3 Procedure of operating STEM

Before operating the STEM, a few general checks are needed. First, the pressure of the valve of the microscope vacuum system is checked to be at the operating value. Secondly, the location of the sample holder will need to be at the neutral position for sample transmitting, else it may damage the microscope. Next, the cooling water and the CS corrector water flow will need to be checked. After that, the column vacuum should be kept at 10-5 PA range with the current value should be reading less than 4. Eventually, the temperature of the room and the water cooler is also checked before the start of the operation.

After everything is normal, liquid nitrogen is poured into the ACD reservoir and should be filled every 8 hours when operating STEM for a long duration. To insert the sample, the beam valve should be closed, apertures are in the original position, EDS detector should be at the location more than 10 cm indicating the

detector is fully out, stage is neutralized as mentioned before, and the vacuum values are normal.

After inserting the sample, a few minutes waiting time is required for the main column pressure to reach the allowed vacuum values again (< 2x10-5 P). If the gauge reading of the column vacuum reaches below 2, the electron beam is allowed to be used.

To reach an atomistic resolution image, the focus of the electron beam is needed. First the z-height of the sample grid will be adjusted to be very close to the surface of the grid. Next, the adjustment of the Ronchigram is required. A good Ronchigram can be achieved if there is no axial coma which is caused by the bright tilt and the astigmatism which is corrected using the Cs corrector (Figure 3.2). The values of the Cs corrector are usually already calibrated thanks to the helpful college in the Physics department.

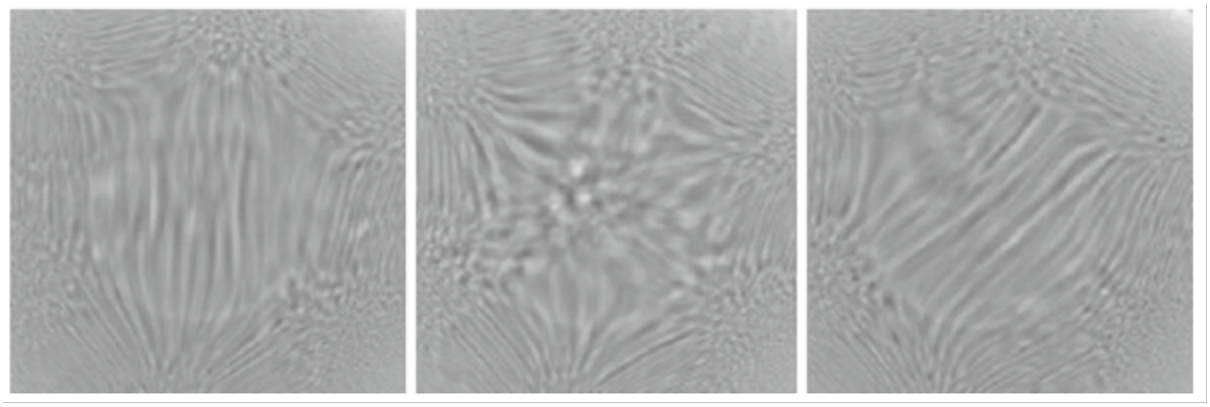


Figure 3. 2 Illustration of Ronchigram when calibrating the STEM (Ponce et al., 2012).

3.2.4 Beam shower

Occasionally, a beam shower is performed to ensure a clear image when atomic resolution is desired. This is done by defocusing the sample to 30,000 nm and moving the sample holder as far from the electron beam's focal point as possible for 3–5 minutes. This process should reduce visible contamination temporarily. However, as this technique can also damage the sample, it should be used with caution.

3.2.5 Procedure of extracting sample and imaging

To prepare for characterization, 0.2 mL of the gold colloid sample from the synthesis was taken from the main solution at 5 minutes, 60 minutes, 1 day, and 7 days after the addition of $NaBH_4$. Each sample was then mixed with 1 mL of deionized water and prepared for centrifugation and sonication.

The diluted gold nanoparticle mixture was subjected to centrifugation for 30 minutes at 7500 rpm. However, no visible pellet formed after centrifugation. Therefore, 100 µL of the suspension was collected with a pipette from the bottom of the centrifugation tube and added to 0.5 mL of deionized water. The resulting mixture was sonicated for 20 seconds at room temperature to disperse the nanoparticles for easier imaging.

The samples were then drop-casted onto a copper-carbon TEM grid from Agar Scientific for HAADF-STEM characterisation, using a 200 kV JEOL 2100F STEM with spherical aberration corrector and an emission current and beam current around 106 μA and 10 pA respectively. The probe convergence semi-angle was 19 mrad and the collection angle range of the annular dark field (ADF) detector was 36 to 82 mrad. Images were taken with contrast and brightness settings of 2750 and captured with an electron probe current of 10 pA and a pixel dwell time of 10 μs with a 1024 × 1024 pixel scanning area (69.3 electron per area angstrom). Also, since the samples usually accumulate organic ligands from the solutions, images were taken quickly to avoid contamination showing up in the microscope and minimized the effect of electron beam induced in the sample. The resulting images were analysed using ImageJ (Schneider et al., 2012).

3.3.1 Energy-Dispersive x-ray Spectroscopy (EDS)

EDS is an analytical technique that usually works in combination with high-energy electron beam instruments like HAADF-STEM. EDS provides valuable information of the elemental composition of the sample (Mourdikoudis et al., 2018). When an electron with high enough energy is shot to the sample, the energy of the electron can be transferred to the sample atoms and excite the inner electron shell to a higher energy state or even completely eject the original electrons.

After an electron from the atom is excited, the atom can be stabilized by emitting x-rays, resulting from electrons moving from a higher energy shell to a lower-energy shell (Figure 3.3). The emitted x-rays are different from element to element because they correspond to the difference between the energy levels of the two electron shells. These characteristic x-rays are then received by the detector and by measuring this signal, the respective element that emits the x-rays can be calculated, and the count of the signal can be used to determine the concentration of the corresponding element in the sample.

3.3.2 Procedure of using EDS

EDS are used when a clear image is achieved already in HAADF-STEM. The operation of EDS is simple, and involves simply inserting the EDS detector, selecting a point or multipoint line, or mapping of an area in the selected position. The measuring time of the EDS was usually set to 120 s, whereas a normal EDS measuring time can take up to 600s, a shorter measuring time is chosen to avoid contamination showing up in the image because the nature of the samples might contain organic molecules.

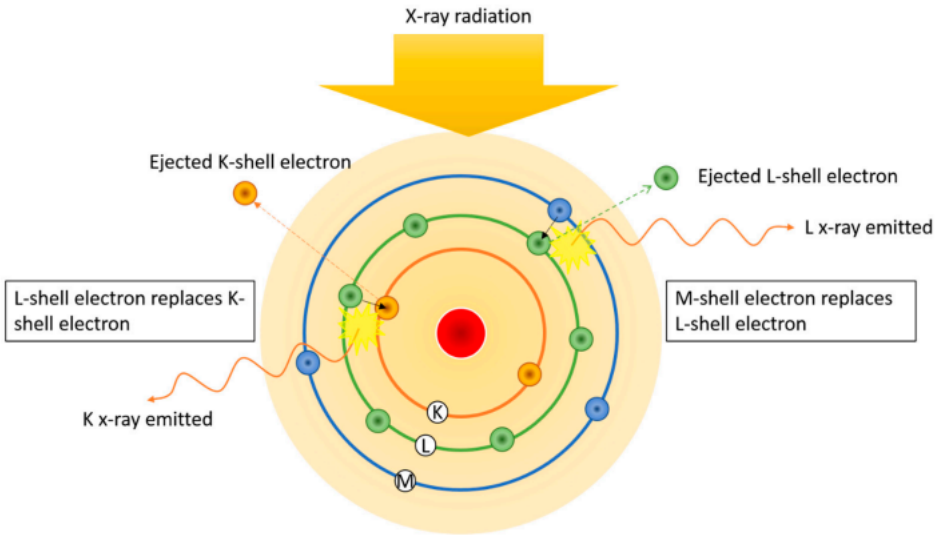


Figure 3. 3 Illustration of EDS interaction with the sample (Long et al., 2021).

Initially, an attempt to use EDS to map the element location (Cha et al., 2022) of the PNCs around the AuNPs was planned. However, because the sample contains a noticeable number of organic molecules, it is not possible as it will cause the EDS mapping to be inaccurate. Hence, a short duration of EDS measuring time was chosen to balance the probability of contamination that required a beam shower, and the information received.

3.4 Experimental approach

3.4.1 Acquisition of chemicals

Chemicals used in the following experiments, including sodium acetate (≥99.0%), oxalic acid (98%), trisodium citrate (98%), propionic acid (99.5%), L-cystine (98%), glutathione (GSH, 98%), sodium hydroxide (97%), sodium borohydride (98%), gold(III) chloride hydrate (99.995%, trace metals basis), and silver nitrate (99%), were purchased from Sigma-Aldrich or Fisher. TEM grids (AGS160 Carbon Film 200 Mesh Cu) for drop-casting were purchased from Agar Scientific.

3.4.2 Solution preparation

Stock solutions of all reagents, including capping agents like sodium acetate, oxalic acid, and trisodium citrate, were prepared in advance. Chloroauric acid solutions were also prepared in advance. Before each synthesis, all equipment was cleaned with aqua regia and rinsed with Milli-Q water to minimize contamination.

3.4.3 General synthesis of AuNPs

A commonly used synthesis method for citrate-capped AuNPs using sodium borohydride was adopted (Al-Johani et al., 2017, Karimi et al., 2019). In this procedure, 0.45 mL of 25 mM (0.011 mmol) chloroauric acid ($HAuCl_4$) was added to 45 mL of deionized water (DIW) under vigorous stirring at room temperature. After 1 minute, the capping agent was added to the mixture, which continued

stirring for another minute. If needed, a specific volume of 1 M sodium hydroxide (NaOH) was added to the solution to adjust the pH to the desired value.

After adjusting the pH to the desired value, 1 mL of freshly prepared sodium borohydride ($NaBH_4$) solution (0.7 mg/mL in ice-cold DIW) was added to the mixture under vigorous stirring. The solution colour instantly changed from clear to ruby red, indicating the formation of AuNPs. After 60 minutes, the gold colloid was stored in a refrigerator for further aging studies at 1 day and 7 days.

3.5 Image processing using Image J

ImageJ (Schneider et al., 2012) was used for all image processing in this study. Typically, a dark-field raw image with 1M/2M magnification from STEM is taken and used for size distribution calculations. The scale of the image is first set accordingly, and thresholding is applied to each image to ensure that the characterization of NPs and PNCs is preserved with minimal changes compared to the raw image.

3.5.1 FFT and intensity plot

Fast Fourier Transform (FFT) (REEVES, 2008) was used in ImageJ to calculate the distance between intensity fringes. Additionally, an intensity plot was

generated to compare the intensity of crystallized NPs and PNCs. The same intensity plot was also used to calculate the distance between intensity fringes.

3.5.2 Size distribution and circularity

Size distribution and circularity calculations were then performed using ImageJ. The lower threshold for each entity was set to 4-pixel units to minimize noise and avoid counting individual atoms around the NPs as separate entities. Regarding the size characterisation method, PNCs and AuNPs are both treated the same. Thresholding is adjusted individually for each raw image to balance the intensity as to minimized data loss for both PNCs and AuNPs. Because the intensity of PNCs is much lower than AuNPs. The resulting size distribution and circularity data from ImageJ were then processed using Python. To calculate the distribution and circularity data of the AuNPs, generally a sample of 100 particles were analysed. However, some samples failed to observe NPs, or the number of particles imaged were insufficient, therefore the size distribution and circularity curve are normalized to provide a better readability.

3.6 Molecular Dynamics (MD)

3.6.1 Amsterdam Modelling Suite (AMS)

AMS is a simulation package recently developed by van Duin and colleagues (van Duin et al., 2024). Unlike older packages such as ABINIT and GAMESS, AMS features a graphical user interface, offering a straightforward solution for users who are not familiar with coding and scripting. This makes it an accessible alternative for performing simulations without requiring an in-depth understanding of complex coding.

AMS includes various modules for different modelling purposes. The DFTB and ParAMS packages can be used to optimize parameters in ReaxFF potential files, while the ReaxFF package serves as a molecular dynamics (MD) simulation platform, capable of handling up to 30,000 particles.

Initially, simulations were planned to be conducted on the BlueBear supercomputer at the University of Birmingham using LAMMPS. However, after considering the challenges associated with using BlueBear and the user-friendly experience provided by AMS, the latter was selected as the simulation package for this study.

3.6.2 Trajectories of particles

MD treats individual atoms or molecules as particles. In such, it is required to calculate the trajectories of atoms and molecules to simulate a model under different circumstances (Sharma et al., 2019). Newtonian mechanics form the

basis of the particle's trajectory. MD calculations are based on Newton's second law of motion, which states the force acting on a particle is equal to the product of the acceleration on the mass of the object. In the simulation, the location and velocity of the particles can be found by integrating the equation of motion over time (Sharma et al., 2019). To calculate the distance the particles moved, we also need to know the intensity of the forces acting on the system. Forces in the simulation are predefined as a potential profile. This profile can be a simple potential energy function like L-J potential (Wang et al., 2020), or as complex as a ReaxFF force field (Duin et al., 2001), which will be mentioned later. To manage the number of tasks and input required to run a simulation, a numerical method is needed.

3.6.3 Verlet method

The Verlet method (Sharma et al., 2019) in MD is a technique that calculates the trajectories of particles. It is a simple numerical integration method that is stable for a system involving many particles. Because of its simplicity, the Verlet method is generally adopted in a lot of simulation packages such as LAMMPS (Thompson et al., 2022) and Amsterdam modelling suite (van Duin et al., 2024).

3.6.4 Simulation box size

To perform any simulation, it is necessary to initially define the dimensions of a simulation box. The size of the simulation box is an important parameter in MD simulations. This box must be chosen carefully to incorporate all particles into the system, but not too small to disturb or to influence the simulation (Sharma et al., 2019). For example, if the simulation box is too small, the system will be too dense, and energy might not be correctly approximated. On the other hand, if the simulation box is too big the particles might not even interact. A well-chosen simulation box size can balance computational cost and the accuracy of the model by ensuring sufficient space for the particles to interact and accurately calculate the position of the particles.

3.6.5 Periodic Boundary Conditions (PBC)

After a simulation box size is chosen, it is important to determine the boundary conditions of the box. Usually, periodic boundary conditions (PBC) are favourable. PBC allows the simulation box to replicate itself in all x, y, z directions (Sharma et al., 2019). Thus, if the particles leave the simulation box on one side, it will re-enter the simulation box on the opposite side, approximating a real-world situation (Figure 3.4). This parameter eliminates effects such as particles bombarding an invisible wall in fixed boundary conditions and is generally adopted in large scale simulation.

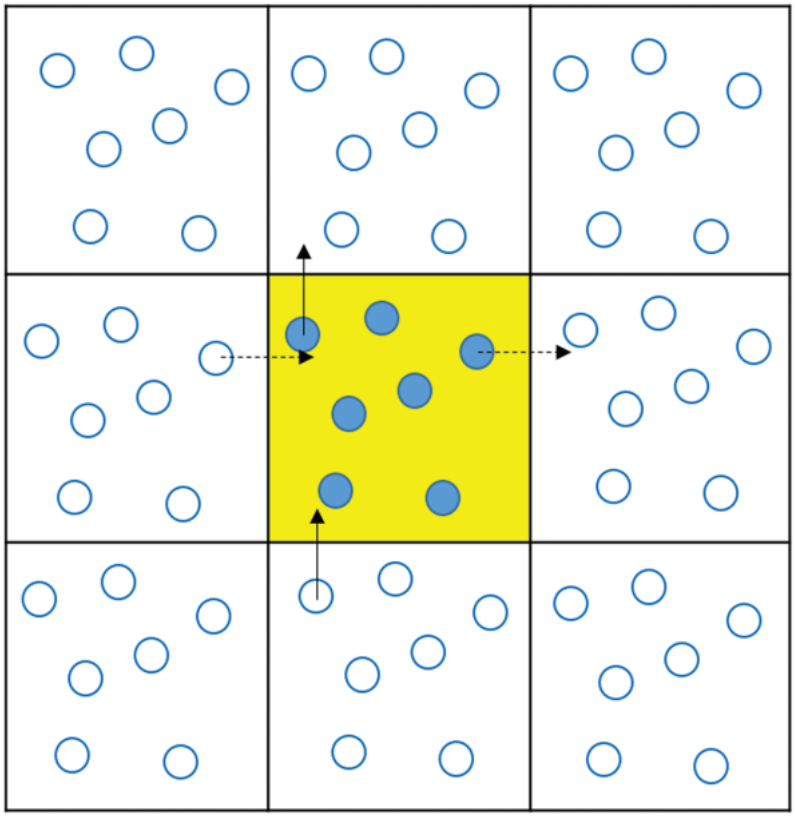


Figure 3. 4 Illustration of PBC in MD (Katiyar and Jha, 2018).

3.6.6 Temperature and pressure control

To start a simulation, parameters that describe how the system is going to evolve are needed. The temperature of the system can be controlled by various methods. For example, a fixed temperature across all particles can be adopted, or an algorithm can be applied to the system with a specific way to influence the system without harshly impacting the system with fixed temperature, making it unrealistic. Nose-Hoover (Nosé, 1984) and Berendsen (Berendsen et al., 1984, Lemak and

Balabaev, 1994) thermostats are the two thermostats that were adopted in this thesis.

3.6.6.1 Berendsen thermostat

The Berendsen thermostat (Berendsen et al., 1984) in MD simulation is used to control the temperature of the simulated system by putting the system in an external heat bath. To adjust the temperature, this thermostat adjusts the velocities of the system's particles to adjust the kinetic energy to influence temperature eventually. It does not force the temperature of the system to a target value but allows a steady adjustment, avoiding a sudden change in the system's dynamics (Lemak and Balabaev, 1994). However, Berendsen thermostats do not mimic the natural fluctuation of temperature among the system's particles, so it is usually used during the equilibration phase to quickly and gradually achieve the targeted temperature (Sharma et al., 2019).

3.6.6.2 Nose-Hoover thermostat

On the other hand, the Nose-Hoover thermostat (Nosé, 1984) influences the temperature of the model by creating a heat bath that interacts with the kinetic energy of the system. This allows the system to remain a canonical ensemble (NVT) by adding a degree of freedom that scales the velocities of the particles

(Sidler and Riniker, 2019). Thus, the Nose-Hoover thermostat also does not create a sudden change in temperature forcing a jump in the system's dynamics, so it is generally used to study the structural stability of materials (Sharma et al., 2019).

3.7 Reactive Force-Field (ReaxFF)

3.7.1 Principles of ReaxFF

After all the basic parameters are settled, a potential for the system is needed to accurately approximate the behaviour of the atoms and molecules interaction. ReaxFF (Duin et al., 2001, Chenoweth et al., 2008), as the middle ground of classical MD and quantum MD, provides a solid foundation for simulating chemical reactions in MD. This force field, unlike other force fields such as Chemistry at Harvard Macromolecular Mechanics (CHARMM) (Turpin et al., 2014) and Assisted Model Building with Energy Refinement (AMBER) (Love et al., 2023), ReaxFF is designed to mimic chemical reaction including the dynamics of forming and breaking of bond between molecules (Senftle et al., 2016). Although ReaxFF MD is a lot more computation heavy, the capability of simulating chemical reaction allows the modelling of combustion or catalysis, which is a reactive system in nature.

3.7.2 Components of ReaxFF

To describe the system correctly in a potential, a different component is needed in the calculation of the ReaxFF parameters. The ReaxFF potential can be summarised by the equation below (Senftle et al., 2016, Duin et al., 2001).

$$E_{\text{system}} = E_{\text{bond}} + E_{\text{over}} + E_{\text{under}} + E_{\text{val}} + E_{\text{pen}} + E_{\text{tors}} + E_{\text{conj}} + E_{\text{vdWaals}} + E_{\text{Coulomb}}$$

Eq 3.1 energy calculation for ReaxFF potential.

Here, the equation includes the calculation of individual items namely (Duin et al., 2001), the bond order and bond energy terms that describe the energy related to bonds forming between atoms with respect to their distance. The atom over coordination and under coordination terms govern the coordination of atoms based on atomic valence rules (Senftle et al., 2016). The valence and torsional angle energy terms that describe the energies with the strain of the angles in molecules. The conjugated system terms that describe any special energy in the system. And the non-bonded VDW interaction terms and the coulomb terms describing the electrostatic forces between atoms.

3.7.3 Calculating ReaxFF parameters

To generate the ReaxFF potential needed to describe a system correctly, an optimisation process is needed. This can be done using the ReaxFF, DFTB and ParAMS package inside the AMS simulation package (van Duin et al., 2024). The creation of new ReaxFF potentials and the optimisation process are not needed because these already created by Monti et al (Monti et al., 2016b). Nonetheless, the development of AMS with ParAMS provides a very easy entry to the creation of ReaxFF and optimisation process.

3.8 Radial distribution function (RDF) g(r)

3.8.1 Calculating RDF

To extract useful information after the simulation is completed, the calculation of RDF is needed. RDF is the fundamental quantitative calculation in MD that describes the particle's density with respect to distance from a reference particle (Monti et al., 2016a). This shows the fundamental properties of the system, such as crystal structure. RDF is defined as the average number of atoms at a distance from a reference atom (Thompson et al., 2022) can be calculated with the following equation:

$$g(\boldsymbol{r}_1, \boldsymbol{r}_2) = \frac{N_m(N_m - 1) \int e^{-U(\boldsymbol{r}_1, \ldots \boldsymbol{r}_{N_m})/T} \, d\boldsymbol{r}_3 \cdots \boldsymbol{r}_{N_m}}{\rho^2 \int e^{-U(\boldsymbol{r}_1, \ldots \boldsymbol{r}_{N_m})/T} \, d\boldsymbol{r}_1 \cdots \boldsymbol{r}_{N_m}}$$

Figure 3. 5 Formula for calculating RDF (Rapaport, 2004).

The above equation is used to calculate the number density of particles at distance r to the average number density of the system. Calculating the RDF of the system with pairwise element can generate the structure of the system by understanding the coordination number and bond lengths, allowing the study of the crystal structure of the NPs.

3.8.2 Interpreting RDF results

RDF generated from the simulation usually have different meanings. For example, a higher count in RDF means particles are more likely to be found at this distance, showing a high possibility of crystal structured, and periodic arranged particles located at this distance. On the other hand, a lower count will suggest a weaker correlation to crystal lattice structure and the system will show a more amorphous arrangement. By comparing the RDF of different simulations, it is possible to study the structure stability of AuNPs influenced by different ligands.

3.9 Simulation detail

In the simulation section, all molecular dynamics simulation were performed using the AMS package (van Duin et al., 2024) . The parameters selected aimed to balance the realism of the modelling with the constraints of computational resources. Since the AMS package requires a licensed CPU/GPU to operate, it cannot be run on supercomputer nodes. As a result, all simulations were conducted on my personal laptop, which limited the ability to simulate larger systems.

To achieve a balance between realistic modelling and computational resources, preliminary MD simulations were conducted to refine the parameters. A total of 1,000 water molecules were selected to accelerate the nucleation rate of gold atoms by increasing the likelihood of interactions between gold atoms, thereby facilitating the establishment of nucleation sites. The ratio of capping ligands to gold atoms was determined based on experimental results and initial test simulations, which revealed discrepancies that will be discussed in detail in Chapter 6.

3.9.1 Generating 100Au cluster, relaxing to 300 K

The base model of 100 gold atom cluster in vacuum were made by importing 100 free gold atoms into AMS with a Reactive force field potential file C/H/O/N/S/Mg/P/Na/Ti/Cl/F/Au (Monti et al., 2016a). The free gold atoms were

generated with initial velocities set to zero, and the temperature was slowly increased to room temperature (300 K) under the Berendsen thermostat (Berendsen et al., 1984) with a time damping factor (τ) of 100 fs over 100,000 steps, each with a 0.25 fs timestep. After the 100-gold atom cluster reached equilibrium at 300 K, it was used as the foundation for AuNPs in subsequent molecular dynamics simulations.

3.9.2 Generating molecule for capping agents, relaxing to 300 K

In this group of MD simulations, acetic acid, oxalic acid, citric acid, propionic acid, cysteine, and glutathione (GSH) were created inside the simulation box using the AMS package (van Duin et al., 2024). Each molecule was initially created at 300 K and relaxed under the Nose-Hoover thermostat (Nosé, 1984) with a 300 K thermal bath, using a time damping factor of 2 ps over 100,000 steps, each with a 0.25 fs timestep. After relaxation at 300 K, the molecules reached equilibrium and were used to create a mixture for further simulations.

Additionally, special hybrid molecules were synthesized, with each molecule consisting of one citric acid and three gold atoms. These molecules were created using the same method described above.

3.9.3 Making the simulation mixture

To create the simulation mixture, Packmol (Martinez et al., 2009,´NEZ and´NEZ, 2003) was used for convenience and ease. This package is used to create the initial configuration of the mixture of the simulation by packing different molecules in the simulation box at the desired location or region.

The simulation mixture was divided into two sections: nucleation and further growth. Generally, the mixture consisted of three types of molecules: solvent (H_2O), capping agents, and free gold atoms in the nucleation MD. Each nucleation mixture started with 1000 H_2O molecules, 30 corresponding capping agents (acetic acid, oxalic acid, citric acid, propionic acid, cysteine, and GSH), and 100 free gold atoms in a simulation box with a size of 70 Å. Each individual molecule was given a tolerance of 5 Å, meaning the molecules were separated by at least 5 Å to avoid overlapping. For the further growth MD, an additional 100-gold atom cluster (created above) was placed at the centre, along with the other molecules. The mixture was then generated and imported into AMS for relaxation and simulation.

3.9.4 Running the MD to equilibrium 300 K

To initialize the MD, the mixture coordinates were imported into the AMS package (van Duin et al., 2024) once again. Since the mixture was created with a box size

of 70 Å, it was placed inside a simulation box with a side length of 80 Å to avoid overlapping under periodic boundary conditions. The periodic boundary condition was applied in all directions. The same ReaxFF potential file C/H/O/N/S/Mg/P/Na/Ti/Cl/F/Au (Monti et al., 2016b, Monti et al., 2016a, Monti et al., 2017) was used for the remainder of the simulation. The MD started with an initial velocity of zero and used the Berendsen thermostat to increase the temperature to 300 K over 20,000 steps, each with a timestep of 0.25 fs. The Berendsen thermostat was set with a damping factor of 100 fs. During this equilibrium and relaxation phase, the total momentum and angular momentum were not preserved.

3.9.5 Running the simulation to 3.8M steps, 950 ps

After the equilibrium and relaxation phase, the MD will run for an additional 3.8 million steps (950 ps). The Nose-Hoover thermostat (Nosé, 1984) will be used during this phase, maintaining a constant temperature of 300 K with a damping time factor of 2 ps. In this phase, both total momentum and angular momentum are preserved. Snapshots of the simulation box will be taken at 200,000 steps, 600,000 steps, 1 million steps, 1.4 million steps, 2.2 million steps, 3 million steps, and 3.8 million steps, corresponding to 50 ps, 150 ps, 250 ps, 350 ps, 550 ps, 750 ps, and 950 ps, respectively. The radial distribution function (RDF) will be generated with a step size of 1,000 and pairwise per element to study the nucleation process and growth of the NPs.

Chapter 4: Aging effect of carboxyl group capping agent on sub-10 nm AuNPs

4.1 Introduction

Citrate is a well-recognized capping agent for AuNPs due to its ability to control colloidal gold size by adjusting the citrate-to-gold molar ratio. Additionally, citrate provides a stable surface for larger AuNPs (approximately 20 nm) and its non-toxic nature and surface functionality make it suitable for various biomedical applications.

The Turkevich method utilizes trisodium citrate as both a reducing and capping agent. By varying the molar ratio of gold to citrate, the size of AuNPs can be effectively controlled (Tran et al., 2016). However, using a single reagent with multiple functions in a synthesis can limit the ability to precisely control both the growth and reduction mechanisms. As a result, the Turkevich method cannot produce ultrasmall AuNPs. Instead, the synthesis of sub-10 nm AuNPs has been achieved by employing sodium borohydride as a more stronger reducing agent (Karimi et al., 2019, Al-Johani et al., 2017, Daruich De Souza et al., 2019).

While the study of growth mechanisms is crucial for achieving precise synthesis methods, it is equally important not to overlook the understanding of any processes continuing after synthesis stops (described as aging) (Le Goas et al.,

2022). Aging refers to any changes to the properties or features of the NPs including size, morphology, crystallinity and any other particle characteristics that may be affected by time.

To comprehend the aging of NPs, concepts of stability must be considered alongside growth. Investigating how nanoparticles evolve over time is essential to ensure their stability and predict their behaviour in various applications.

This chapter will focus on growth as a term encompassing factors that are relatively controllable in the synthesis process. For instance, the size distribution of NPs can be controlled by adjusting the ligand-to-gold molar ratio (Yazdani et al., 2021), pH value (Kettemann et al., 2016), reaction temperature (Mendez et al., 2021, Tran et al., 2016), and the concentration of reducing agent (Karimi et al., 2019). These factors can be manipulated during synthesis to achieve desired outcomes.

Once the synthesis process is stopped, any changes to the particles are described as aging. Aging of nanoparticles should be considered as a phenomenon that is not easily predicted and subsequently controlled. Processes such as aggregation, agglomeration, and OR can lead to changes in the morphology of NPs, but as they occur after the synthesis process is terminated, they alter the properties of the primary particles. Any post-synthesis changes in the size and shape of NPs should be classified as aging rather than growth. Aging factors often involve complex interactions between the NPs and the surrounding environment, and their effects are challenging to predict and control in the same way as growth. Failure to

understand the evolution of colloidal AuNPs may result in undesirable particle sizes and shapes that cannot be functionalized and may even exhibit unpredictable toxicity.

In this chapter, sodium borohydride was used as a rapid reduction agent to synthesize sub-10 nm AuNPs. The objective of the study was to investigate the nucleation, growth and subsequent aging effects on the very small AuNPs synthesis resulting from the use of different carboxylic capping agents.

Since carboxyl groups are used to capture gold atoms, either from the surface of AuNPs to form a capping layer or from free gold atoms in the solution, an increase in the number of carboxyl groups in the solution should result in smaller AuNPs. Regarding the aging duration of particles in the solution, the longer the particles remain in the presence of an excess of carboxyl groups ligands, the higher the colloidal stability of the AuNPs should be, with their size remaining unchanged over time.

This chapter will be specifically focusing on the influence of various factors such as pH, molar ratio of capping agent on AuNPs, and relationship of number of carboxyl groups on capping agent on the aging process. The aim was to gain a deeper understanding of the aging factors and their impact on the synthesized small AuNPs within different environmental conditions.

4.2 Experiment

In this chapter, carboxyl containing ligands, specifically acetic acid, oxalic acid, citric acid, and propionic acid are chosen to be the capping agent for the AuNPs (Figure 4.1). These molecules primarily interact with the surface of AuNPs through their carboxylic acid (-COOH) groups, which play a crucial role in binding and stabilization. While their specific binding behaviour varies based on molecular structure, the general mechanism involves the deprotonation of the carboxyl group and interaction with the gold surface.

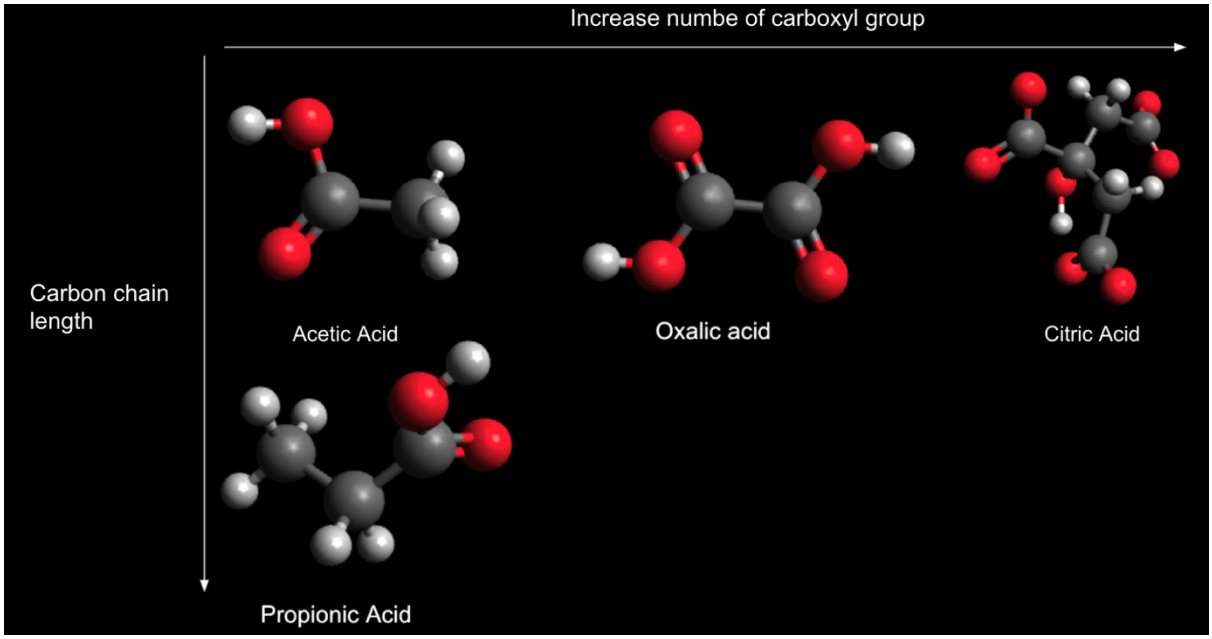


Figure 4. 1 Illustration of carboxyl group capping agent agents used in this study and their relative number of carboxyl groups and carbon chain length.

During AuNPs synthesis, the deprotonation of -COOH groups becomes $-COO^-$. The negatively charged carboxylate group is driven to the gold atoms because of the electrostatic attractive interaction. Thus, the number of bonds formed by the

capping agent should depend on the number of carboxyl groups, provided they are deprotonated, a process which depends on the media pH. The capping agents used here possess either one carboxyl group (acetic acid and propionic acid) or two (oxalic acid) or three (citric acid). The binding strength of the capping agent should highly be correlated to the number of carboxyl groups during synthesis and hence determine the capping power and stabilization process (Table 4.1).

Table 4. 1 List of capping agents used with number of carboxyl group.

Capping agent	Number of carboxyl group	Number of possible bonds to Au
Acetic Acid	1	1
Propionic Acid	1	1
Oxalic Acid	2	2
Citric Acid	3	3

In the following syntheses, acetate, oxalate, citrate, and propionic acid should only act as a capping agent because the strong reduction power of sodium borohydride should reduce all Au(III) to Au(0) immediately.

A commonly used synthesis of citrate-capped AuNPs using sodium borohydride is adopted (Karimi et al., 2019, Al-Johani et al., 2017). Here, 0.45mL of 25mM (0.011 mmol) chloroauric acid (HAuCl4) was added to 45mL of deionized water (DIW), under vigorous stirring at room temperature as mentioned in chapter 3 section 3.4.3. After 1-minute, a capping agent was added to the mixture and the media continue to be stirred for another minute. If required, a certain volume of 1M

sodium hydroxide (NaOH) was added to the solution for adjusting pH to the desired value. Detailed configuration of each experiment is shown in Tables 4.2 to 4.5.

Table 4. 2 List of experiments using acetic acid as capping agent.

pH	Capping agent to gold molar ratio	38.8mM capping agent [mL]	1M NaOH [mL]
4.3	3.5	1	0
5.3	3.5	1	0.02
6.1	3.5	1	0.03
10.3	3.5	1	0.05
3.6	1	0.28	0
3.7	1.5	0.43	0
6.6	7.1	2	0.03
6.1	10.6	3	0.03

Table 4. 3 List of experiments using oxalic acid as capping agent.

pH	Capping agent to gold molar ratio	38.8mM capping agent [mL]	1M NaOH [mL]
2.8	3.5	1	0
3.9	3.5	1	0.08
6.6	3.5	1	0.1

10.7	3.5	1	0.13
3.2	1	0.28	0
3.0	1.5	0.43	0
6.2	7.1	2	0.19
6.4	10.6	3	0.27

Table 4. 4 List of experiments using citric acid as capping agent.

pH	Capping agent to gold molar ratio	38.8mM capping agent [mL]	1M NaOH [mL]
3.6	11.7	1	0
4.8	5.3	1	0
6.0	3.6	1	0
7.1	3.5	1	0.03
8.6	3.5	1	0
10.6	3.5	1	0.05
6.2	3.5	1	0.13
6.7	3.5	1	0.025
4.4	1	0.28	0
4.5	1.5	0.43	0
6.3	7.1	2	0
6.3	10.7	3	0

Table 4. 5 List of experiments using propionate acid as capping agent.

pH	Capping agent to gold molar ratio	38.8mM capping agent [mL]	1M NaOH [mL]
9.3	3.5	0.003 99.5%	0.06
6.4	7.1	0.006 99.5%	0.14
6.4	10.6	0.009 99.5%	0.18

After adjusting pH to the desired value, a freshly prepared sodium borohydride (NaBH4) of 1mL 0.7mg in ice cold DIW is added to the mixture while maintaining vigorous stirring. The colour of the solution instantly turns from clear to ruby red indicating the formation of AuNPs. After 60 minutes, the gold colloid is stored in a refrigerator for further aging studies. General sample extraction and characterization procedure is mentioned in Methodology Chapter 3.2.5 and 3.4.

4.3 Layout of the result section (4.4 – 4.8)

As the results collected from all synthesis procedures are extensive and quantitative, this chapter will categorize the results into two groups. First, I will discuss aging in terms of both the size and circularity of AuNPs with respect to each individual environmental factor, such as pH, molar ratio, and the number of carboxyl groups on the capping agent.

The results of the first part of this study, concerning the changes in size and circularity of AuNPs over time (aging), are as follows:

1- Acetic acid with a molar ratio of 1:3.5 at different pH levels
2- Acetic acid with varying molar ratios at low and neutral pH levels
3- Oxalic acid with a molar ratio of 1:3.5 at different pH levels
4- Oxalic acid with varying molar ratios at low and neutral pH levels
5- Citric acid with a molar ratio of 1:3.5 at pH 6
6- Citric acid with varying molar ratios at low and neutral pH levels
7- Propionic acid with varying molar ratios at low and neutral pH levels
8- No capping agent

All the plots display the size distribution and circularity of the particles. In the size distribution plot, the x-axis represents the size, and the y-axis shows the probability of finding the respective size, normalized to account for the total number of particles counted. The duration of aging is represented by colour.

The second part of this study will compare the aging effects across different environments, with a specific focus on the number of carboxyl groups on the capping agents. The size distribution will be presented as quantile plots, rather than solely using mean values, to account for the polydispersity of the synthesized particles, which is also considered an aging effect.

As stated, this chapter defines growth as a controllable process, while any other unwanted changes in morphology are considered aging.

4.4 Aging of different carboxyl molecule capped AuNPs (acetic acid)

4.4.1 Aging of acetate capped AuNPs in different pH at molar ratio of 1:3.5

Aging of acetate capped AuNPs in pH 4.3

In the pH 4.3 synthesis environment, bridging between NPs and PNCs was observed, indicated by white and orange arrows, respectively, at the 5-minute time point. This suggests that an aging process may have already started due to the formation of bridges between the NPs.

Bridging formation and PNCs were also observed at the 60-minute and 1-day time points. Additionally, a core-shell structure was observed at these time points, indicated by green arrows, this structure will be discussed in the next Chapter. The shell formation possibly results from PNCs covering the crystallized NPs, causing the NPs to adhere to more molecules, including both acetate and acetate-containing gold. On the other hand, a growing layer should show as a clear crystal layer structure with a narrower gap between the layer and the original NPs. Hence, this is not the case of a not fully crystallised growth layer.

At the 7-day mark, no PNCs were observed, and the NPs appeared to have completely crystallised, as evidenced by the absence of bridges and core-shell structures. It is also notable that many particles have fused together, suggesting inefficient capping.

However, due to the lack of a clear trend in both the changes of size and circularity, as shown in (Figures 4.2a and 4.2b), it is possible that the NPs had already crystallised before the 5-minute mark, or, in other words, they had become stable even in the initial solution.

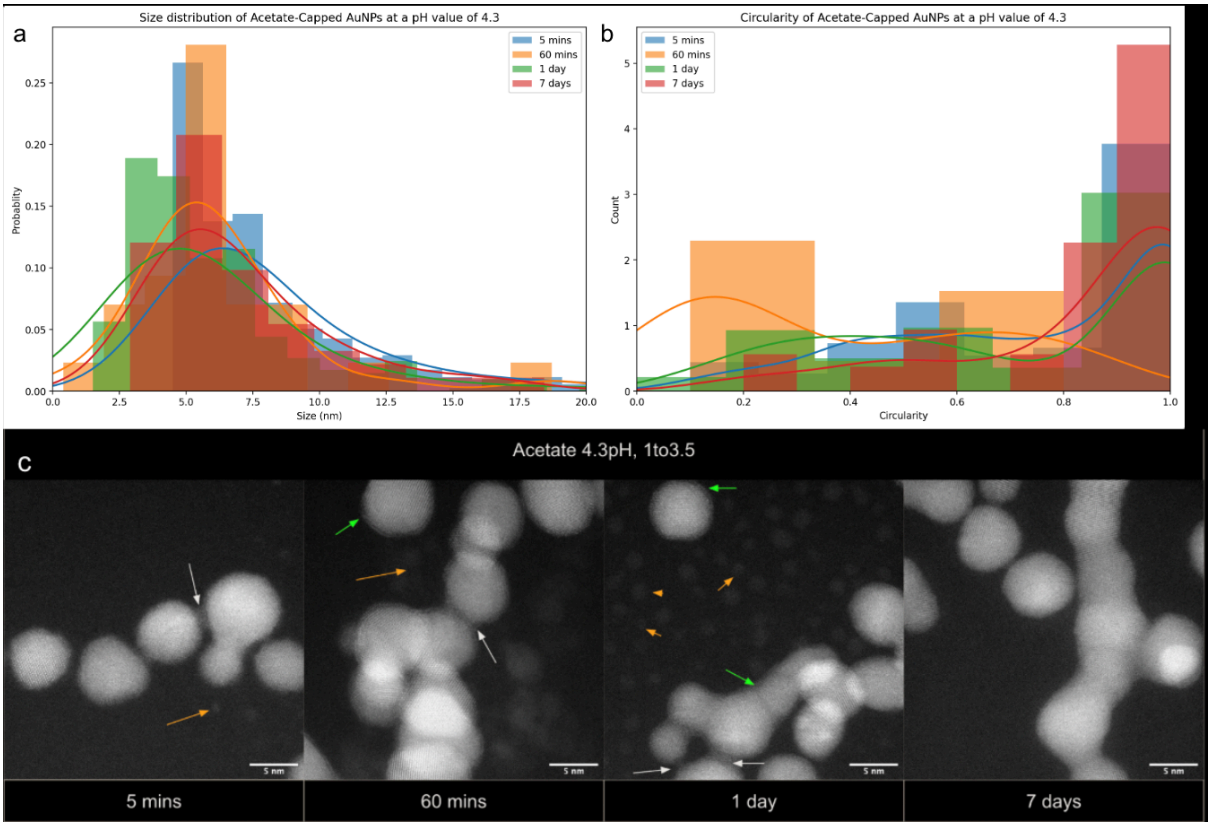


Figure 4. 2 a), top left plot shows the size distribution of 1:3.5 acetate capped AuNPs in pH 4.3. b) top right plot shows the circularity. c) bottom STEM images of samples collected at different time points, after the start of the experiment: 5

minutes, 60 minutes, 1 day and 7 days. White arrows indicate bridging or sticking between particles. Green arrows indicate a shell formation or soft structure around a crystalline AuNP. Orange arrows indicate presumed pre-nucleation clusters.

Aging of acetate capped AuNPs in pH 5.3

In the pH 5.3 environment, extensive bridging between particles, resulting in long chains of fused particles was observed at the 5-minute mark, indicating poorly controlled nucleation and growth very early in the process.

At the 60-minute mark, a core-shell motif and PNCs were observed, indicated by green and orange arrows, respectively. This suggests an ongoing aging process due to the presence of PNCs; this will be discussed in more detail in the next chapter. At the 1-day mark, bridging formation was observed, indicated by a white arrow. A completely aged sample was observed at the 7-day mark.

From Figures 4.3a and 4.3b, the spike at the 60-minute mark indicates the formation of many PNCs. However, PNCs have a lower density than crystallized NPs due to their looser structure, and therefore the intensity of PNCs is lower compared to crystallized NPs. Overall, the size remains relatively constant in the 7 days period of observation.

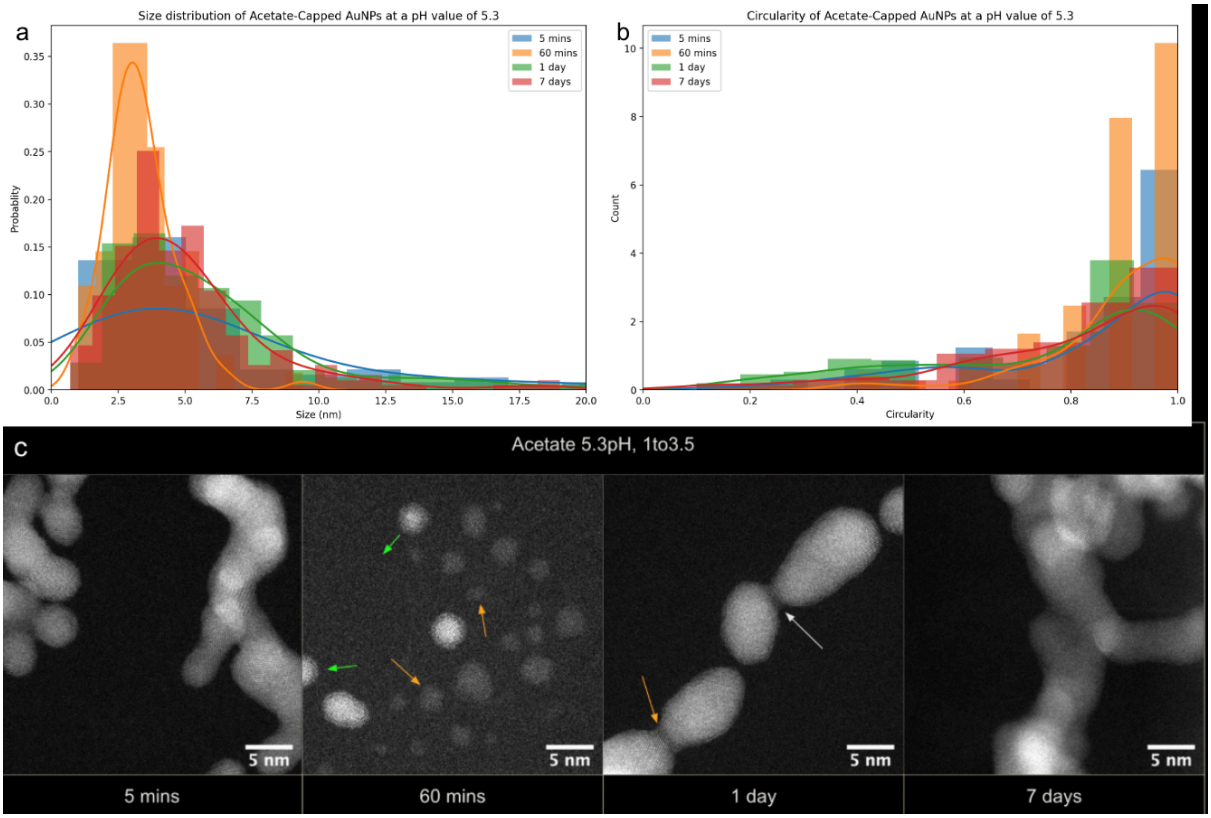


Figure 4. 3. a) top left plot shows the size distribution of 1:3.5 acetate capped AuNPs in pH 5.3. b) top right plot shows the circularity c) bottom STEM images of samples collected at different time points, after the start of the experiment: 5 minutes, 60 minutes, 1 day and 7 days. White arrows indicate bridging or sticking between particles. Green arrows indicate a shell formation or soft structure around a crystalline AuNP. Orange arrows indicate presumed pre-nucleation clusters.

Aging of acetate capped AuNPs in pH 6.1

In the pH 6.1 environment, PNCs and a core-shell motif were observed at the 5-minute mark. Subsequently, a consolidated crystallized string of fused particle's structure was observed at the 60-minute and 7-day marks.

From Figure 4.4a, the size of the NPs in this environment changes gradually, transitioning from a monodisperse state, including the presence of PNCs, to a polydisperse state after 7 days. The mean size of the NPs increases from 3 nm to 5 nm over this period. From Figure 4.4b, the circularity decreases, reflecting the fusing of particles.

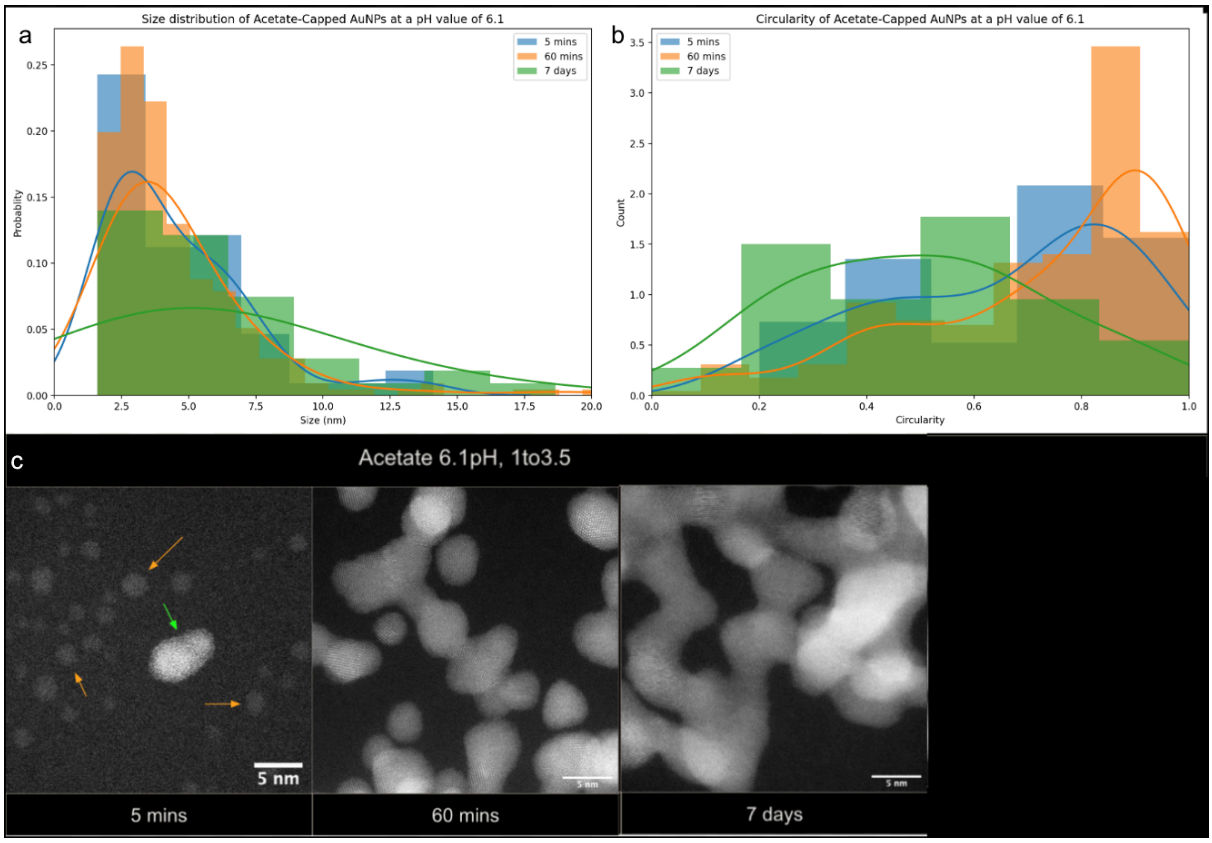


Figure 4. 4 a) top left plot shows the size distribution of 1:3.5 acetate capped AuNPs in pH 6.1. b) top right plot shows the circularity. c) bottom STEM images of samples collected at different time points, after the start of the experiment: 5 minutes, 60 minutes, 1 day and 7 days. Green arrows indicate a shell formation or soft structure around a crystalline AuNP. Orange arrows indicate presumed pre-nucleation clusters. The sample at 1 day failed to observe any AuNPs.

Aging of acetate capped AuNPs in pH 10.3

In the pH 10.3 environment, a core-shell motif and bridging were observed at the 5-minute mark, indicated by green and white arrows, respectively in Figure 4.5. Both PNCs and bridge motifs were found at the 1-day and 7-day marks. This indicates that the mother solution is already in a stable state. So, the PNCs should be stable and exist in the solution, which are also mentioned in other study (Ramamoorthy et al., 2020). There were also very slow changes in size, as shown in Figure 4.5a, and a similar circularity trend in Figure 4.5b.

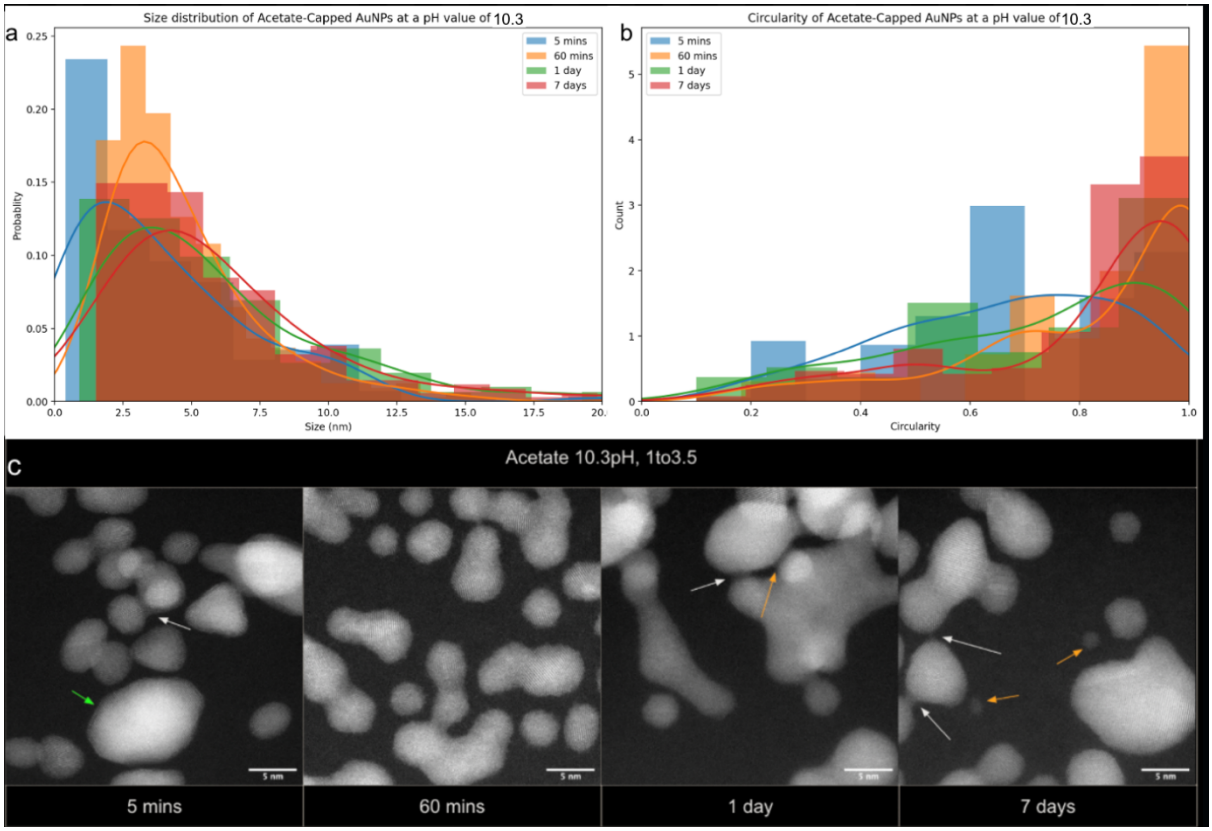


Figure 4. 5. a) top left plot shows the size distribution of 1:3.5 acetate capped AuNPs in pH 10.3. b) top right plot shows the circularity. c) bottom STEM images

of samples collected at different time points, after the start of the experiment: 5 minutes, 60 minutes, 1 day and 7 days. White arrows indicate bridging or sticking between particles. Green arrows indicate a shell formation or soft structure around a crystalline AuNP. Orange arrows indicate presumed pre-nucleation clusters.

4.4.2 Aging of acetate capped AuNPs in different molar ratio

Aging of acetate capped AuNPs in pH 3.6 at molar ratio 1:1

The decrease in number of the molar ratio of acetic to gold is expected to result in increased nanoparticle size due to inadequate surface coverage by single bonds from the carboxyl group of acetic acid, as this capping agent can only occupy a single gold atom, which may not sufficiently stabilize the nanoparticle surface.

In an environment with pH 3.6, a 1:1 molar ratio of acetate was employed. Poorly structured particles were observed within 5 minutes. By 60 minutes, a cloud of presumably PNCs, indicated by an orange arrow, alongside a core-shell motif indicated by a green arrow, was observed (Figure 4.6). The NPs exhibited significant growth at 1 day and much more so after 7 days.

The size indicated from Figure 4.6a shows the NPs slowly aged after synthesis and eventually reached up to 50nm. All structures indicating the existence of PNCs did not exist at 1 days and 7 days marks.

The circularity indicated from Figure 4.6b shows the NPs become more spherical over time, attributed to surface energy favouring spherical structures over strings of fused particles. In the absence of PNCs, neither sticky bridges nor the core-shell motif was observed. This phenomenon could be attributed to either surface diffusion or Ostwald ripening. Nevertheless, the insufficient presence of acetate as a capping agent facilitated the gradual growth of the NPs, to an average size of 50 nm after 7 days.

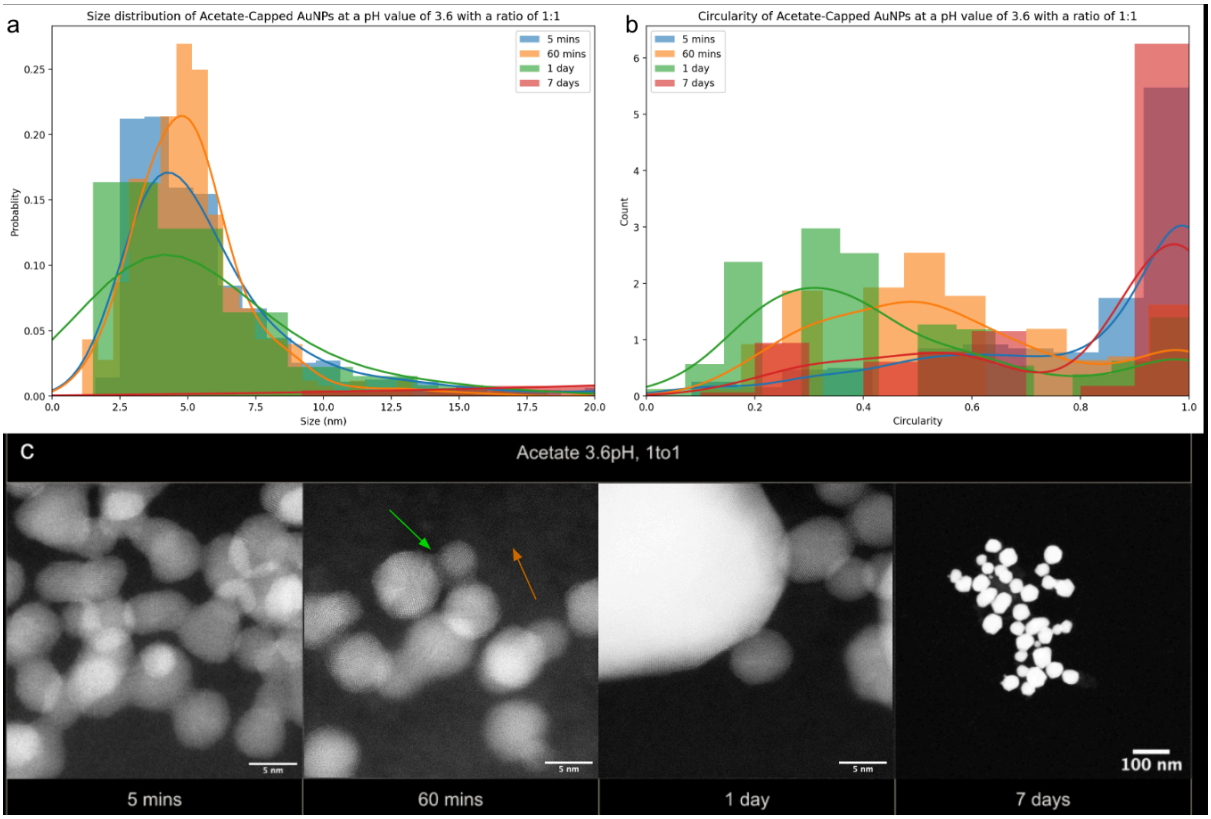


Figure 4. 6. a) top left plot shows the size distribution of 1:1 acetate capped AuNPs in pH 3.6. b) top right plot shows the circularity. c) bottom STEM images of samples collected at different time points, after the start of the experiment: 5 minutes, 60 minutes, 1 day and 7 days. Green arrows indicate a shell formation or

soft structure around a crystalline AuNP. Orange arrows indicate presumed pre-nucleation clusters.

Aging of acetate capped AuNPs in pH 3.7 at molar ratio 1:1.5

Similarly, in a pH 3.7 environment with a molar ratio of 1:1.5, NP growth proceeded at a lower rate. Within 5 minutes, clear evidence of PNCs was observed. A PNC cloud was evident at the top left corner of Figure 4.7c at 5 minutes, indicated by an orange arrow, along with bridging between crystallized NPs (white arrow) and a core-shell motif (green arrow). These phenomena persisted at the 60-minute mark but diminished by 1 day and 7 days.

A significant increase in NP size from 5 nm to 50 nm was observed after 1 day. Interestingly, PNCs were still observed at the 7-day mark, indicated by an orange arrow. The presence of PNCs in the solution after 7 days, despite NP growth, raises questions about why PNCs still form or exist after such a long time.

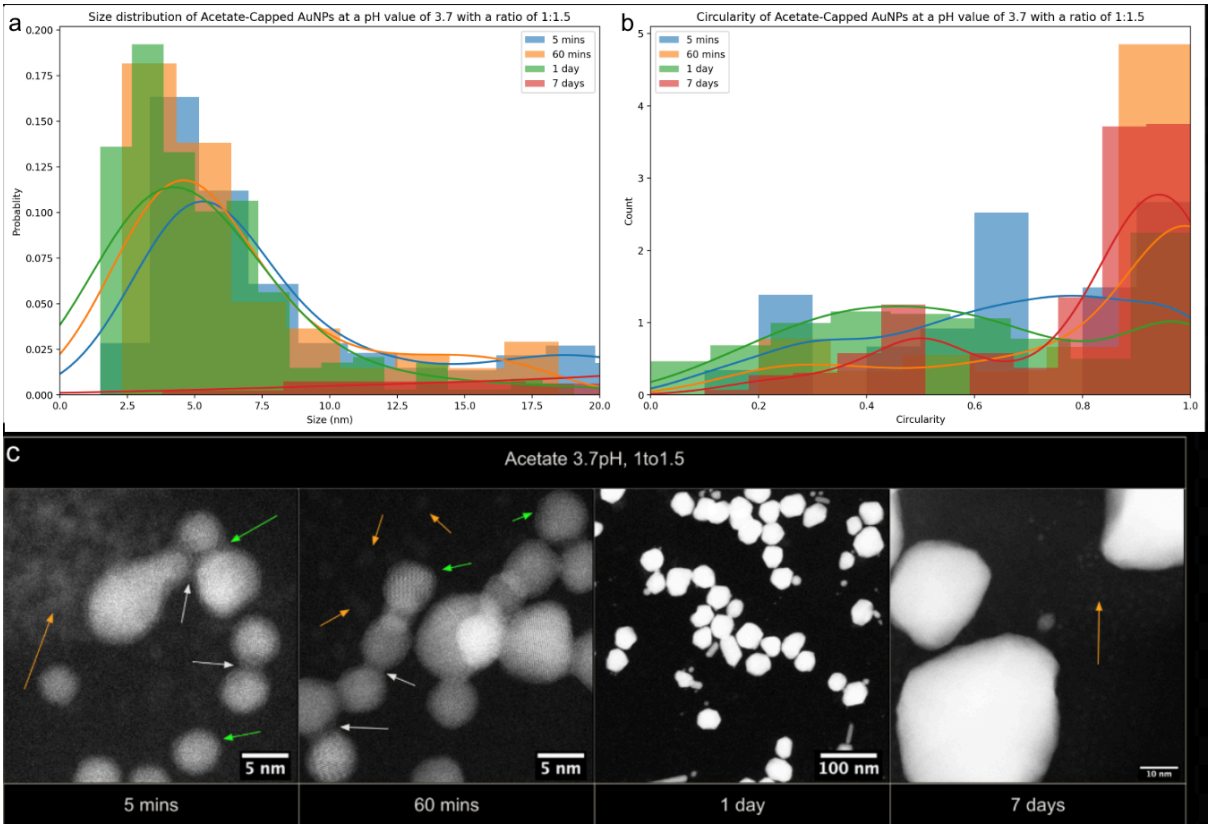


Figure 4. 7. a) top left plot shows the size distribution of 1:1.5 acetate capped AuNPs in pH 3.7. b) top right plot shows the circularity. c) bottom STEM images of samples collected at different time points, after the start of the experiment: 5 minutes, 60 minutes, 1 day and 7 days. White arrows indicate bridging or sticking between particles. Green arrows indicate a shell formation or soft structure around a crystalline AuNP. Orange arrows indicate presumed pre-nucleation clusters.

Aging of acetate capped AuNPs in pH 6.6 at molar ratio 1:7

At pH 6.6 with a molar ratio of 1:7, the presence of PNCs, bridging between particles and core-shell motifs was observed consistently at 5 minutes, 60

minutes, and 1-day intervals. The NPs exhibited gradual aging and polydispersity in size after 1 day, as indicated in Figure 4.8a.

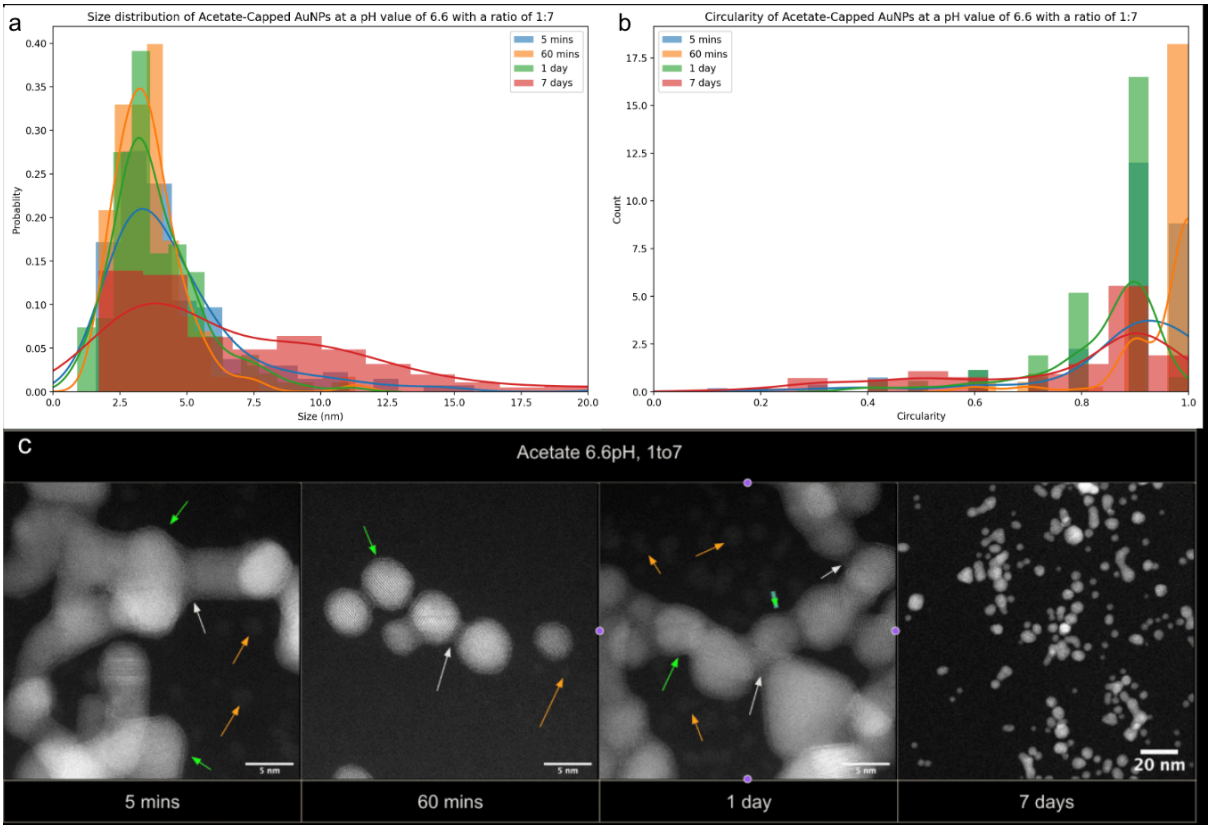


Figure 4. 8. a) top left plot shows the size distribution of 1:7 acetate capped AuNPs in pH 6.6. b) top right plot shows the circularity. c) bottom STEM images of samples collected at different time points, after the start of the experiment: 5 minutes, 60 minutes, 1 day and 7 days. White arrows indicate bridging or sticking between particles. Green arrows indicate a shell formation or soft structure around a crystalline AuNP. Orange arrows indicate presumed pre-nucleation clusters.

Aging of acetate capped AuNPs in pH 6.6 at molar ratio 1:10.6

At pH 6.1 with a molar ratio of 1:10.6, the presence of PNCs and a core-shell motif were observed, indicated by an orange arrow and green arrow, respectively.

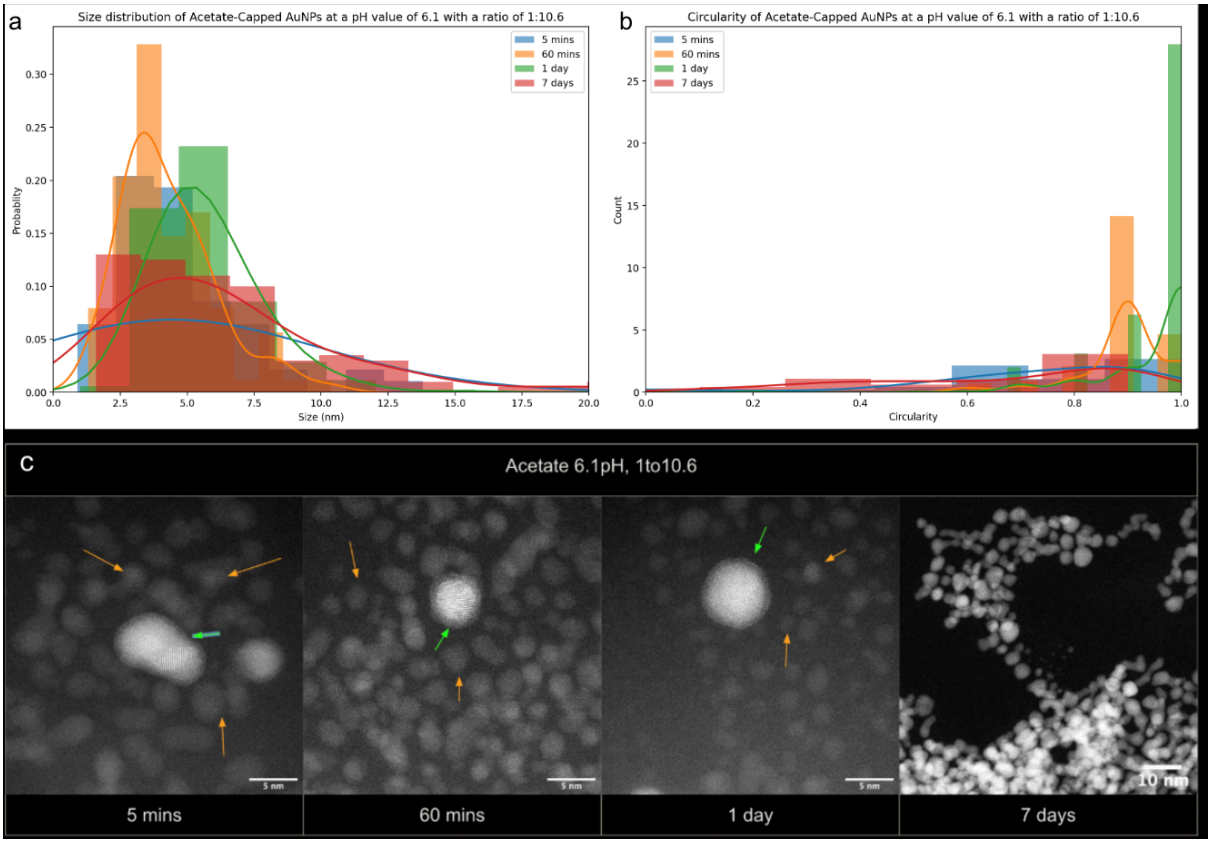


Figure 4. 9. a) top left plot shows the size distribution of 1:10.6 acetate capped AuNPs in pH 6.1. b) top right plot shows the circularity. c) bottom STEM images of samples collected at different time points, after the start of the experiment: 5 minutes, 60 minutes, 1 day and 7 days. Green arrows indicate a shell formation or soft structure around a crystalline AuNP. Orange arrows indicate presumed pre-nucleation clusters.

4.5 Aging of different carboxyl molecule capped AuNPs (oxalic acid)

The next capping agent containing two carboxyl groups in its molecule is oxalic acid. The additional carboxyl group in the capping agent enables binding with more than one gold atom, leading to the synthesis of NPs that are expected to exhibit increased particle to particle adhesiveness ("stickiness").

4.5.1 Aging of oxalate capped AuNPs in different pH at molar ratio of 1:3.5

Aging of oxalate capped AuNPs in pH 2.8

At pH 2.8 with a molar ratio of 1:3.5, particle to particle sticking was observed early on at 5 minutes, 60 minutes, and 1-day time points (Figure 4.10). They exhibited extensive signs of interparticle bridging, with neighbouring NPs forming a string of particles structure with solid necks and crystalline structures. This phenomenon is hypothesized to result from PNCs enveloping solid crystallized NPs.

Interestingly, at the 7-day mark, colloidal gold exhibited signs of PNCs, indicated by an orange arrow and reduced bridging (Figure 4.10c). The reappearance of PNCs raises questions regarding whether their formation represents an intermediate stage in the reduction mechanism or nucleation process.

Given the use of sodium borohydride as a potent reducing agent in these experiments, complete reduction of chloroauric acid and nucleation were expected to occur and conclude before the 5-minute mark. The appearance of PNCs at 7 days, along with a size trend that peaks back towards smaller sizes, raises uncertainty about whether these PNCs formed later in the mother solution or existed from the beginning of synthesis but failed to stabilize into crystallized NPs. Although the use of sodium borohydride is excessive, PNCs still exists in the solutions suggests that the nucleation is inhomogeneous, allowing multiple state of nucleation to be seen in the sample.

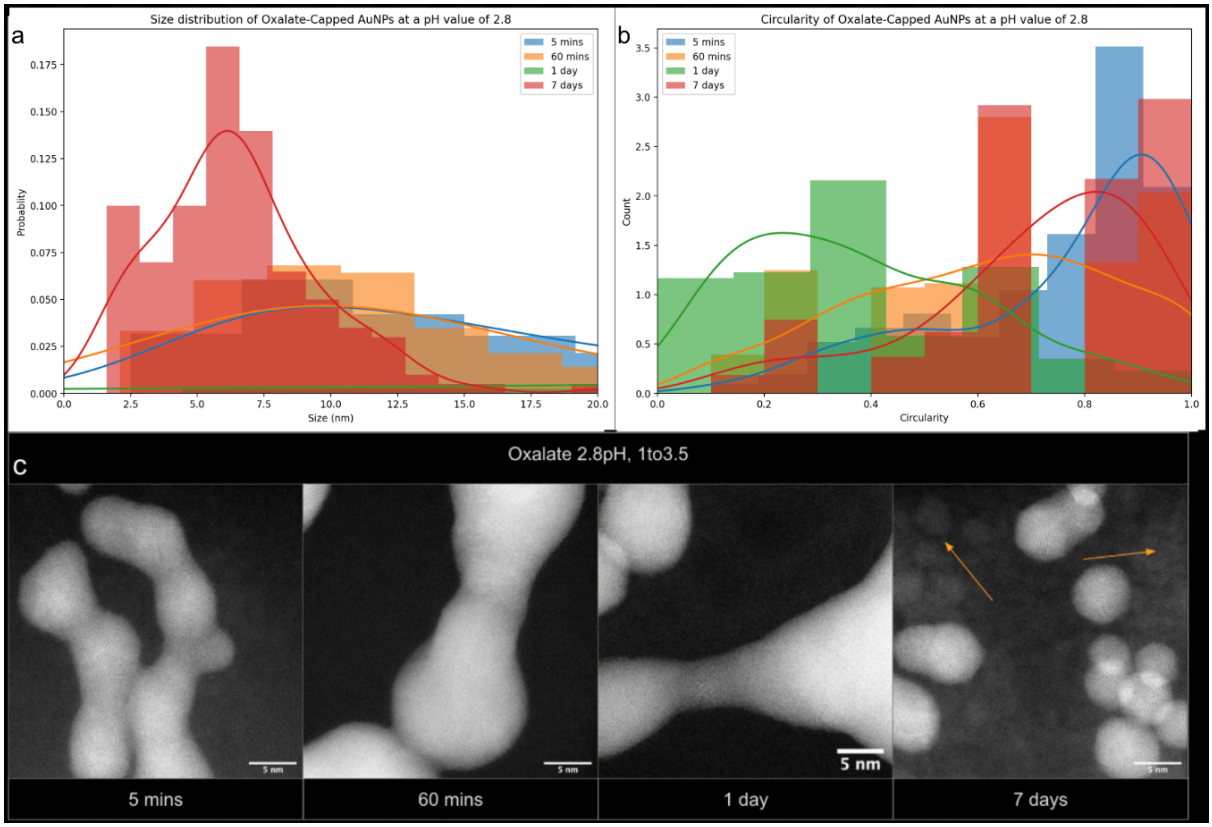


Figure 4. 10. a) top left plot shows the size distribution of 1:3.5 oxalate capped AuNPs in pH 2.8. b) top right plot shows the circularity. c) bottom STEM images of samples collected at different time points, after the start of the experiment: 5

minutes, 60 minutes, 1 day and 7 days. Orange arrows indicate presumed pre-nucleation clusters.

Aging of oxalate capped AuNPs in pH 3.9

At pH 3.9, only bridge formations were observed at the 60-minute and 1-day marks. However, these bridges, as depicted in Figure 4.11c, were already crystallized. This crystallization resulted from PNCs, which act as soft structures carrying gold atoms, adhering between crystallized NPs or enveloping groups of crystallized NPs and subsequently crystallizing into a rigid nanowire structure.

Figure 4.11a illustrates that under these conditions, NPs exhibited gradual growth in size and became polydisperse. Additionally, circularity data in Figure 4.11b indicates a transition from a predominantly spherical structure to a nano-string motif.

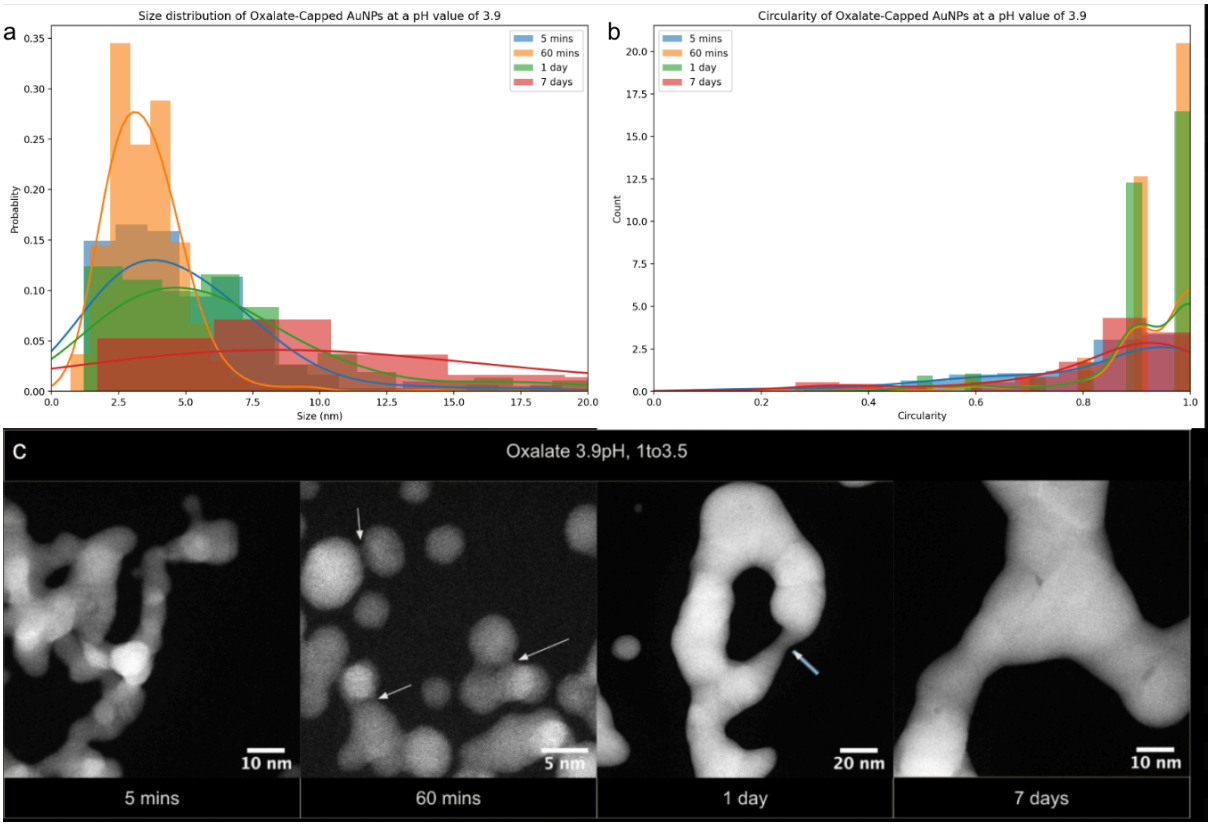


Figure 4. 11. a) top left plot shows the size distribution of 1:3.5 oxalate capped AuNPs in pH 3.9. b) top right plot shows the circularity. c) bottom STEM images of samples collected at different time points, after the start of the experiment: 5 minutes, 60 minutes, 1 day and 7 days. White arrows indicate bridging or sticking between particles.

Aging of oxalate capped AuNPs in pH 6.6

In a pH 6.6 environment, although PNCs were not initially observed at the 5-minute mark, evidence of PNCs became apparent at the 60-minute, 1-day, and 7-day intervals. The persistence of PNCs in the solution even after 7 days was unexpected

Figures 4.12a and 4.12b indicate that the size and polydispersity of the AuNPs remained relatively stable over time, suggesting the solution is in a stable state. Because the size and polydispersity data collected also includes PNCs, this raises questions about whether PNCs represent a stable structure in this solution or if their formation and disappearance should be considered stable on a macroscopic scale, thereby not significantly affecting measurements like size variation over time.

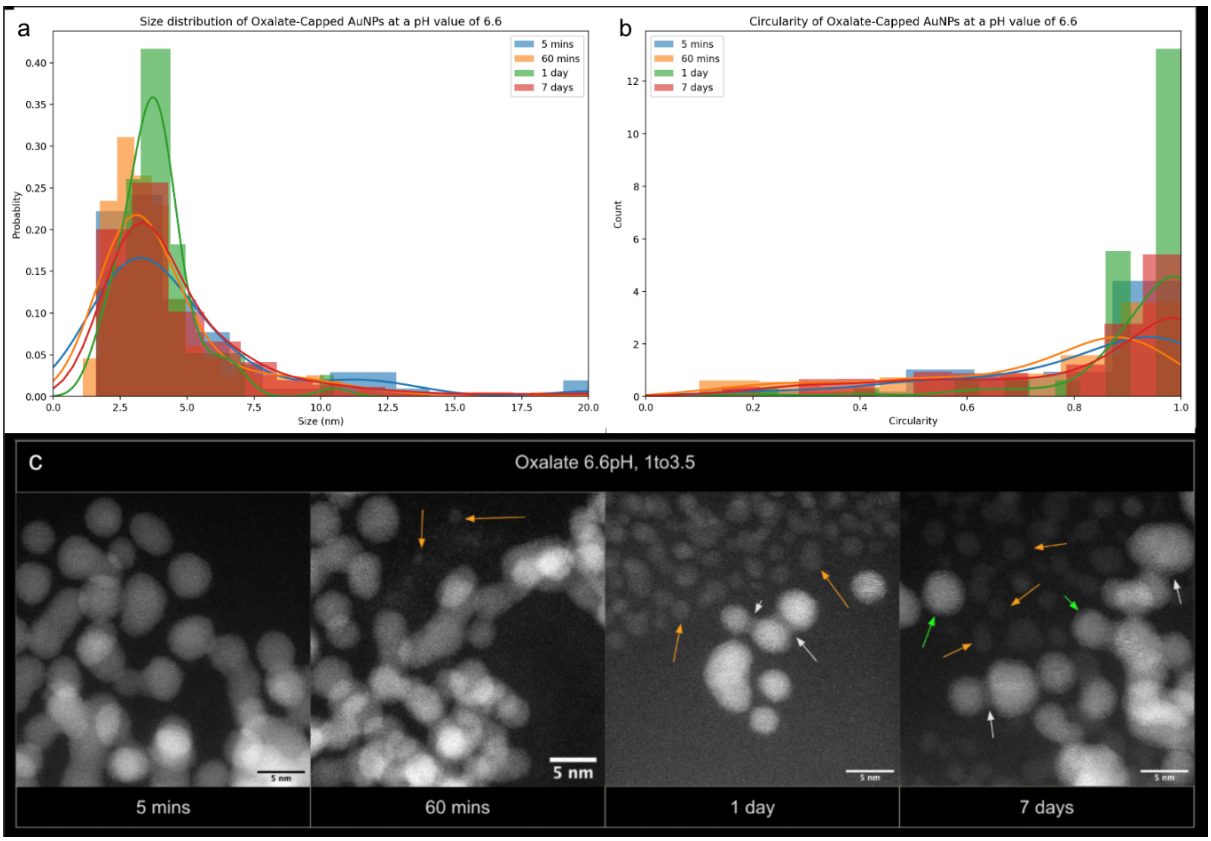


Figure 4. 12. a) top left plot shows the size distribution of 1:3.5 oxalate capped AuNPs in pH 6.6. b) top right plot shows the circularity. c) bottom STEM images of samples collected at different time points, after the start of the experiment: 5 minutes, 60 minutes, 1 day and 7 days. White arrows indicate bridging or sticking

between particles. Green arrows indicate a shell formation or soft structure around a crystalline AuNP. Orange arrows indicate presumed pre-nucleation clusters.

Aging of oxalate capped AuNPs in pH 10.7

At pH 10.7, both PNCs and a core-shell motif were observed within 5 minutes. This suggests that the PNCs adhere to the surfaces of already crystallized NPs, forming core-shell structures indicated by green arrows. This adhesive behaviour caused the NPs to bridge with neighbouring crystallized NPs, resulting in the formation of a fused structure observed later in the solution.

The mean size of the NPs did not exhibit significant change over the 7-day period. However, they gradually became polydisperse, and Figure 4.13b indicated a decrease in circularity, indicating increased irregular morphologies that may be linked to aging.

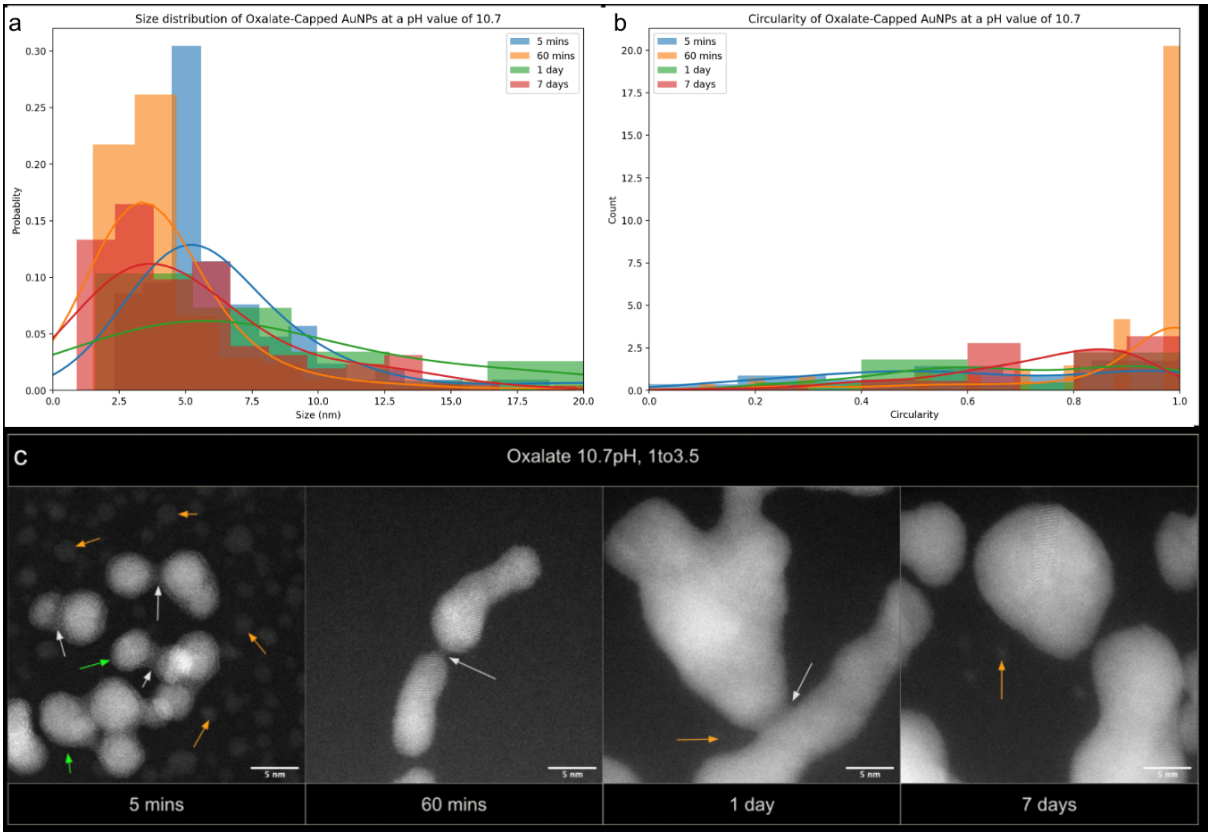


Figure 4. 13. a) top left plot shows the size distribution of 1:3.5 oxalate capped AuNPs in pH 10.7. b) top right plot shows the circularity. c) bottom STEM images of samples collected at different time points, after the start of the experiment: 5 minutes, 60 minutes, 1 day and 7 days. White arrows indicate bridging or sticking between particles. Green arrows indicate a shell formation or soft structure around a crystalline AuNP. Orange arrows indicate presumed pre-nucleation clusters.

4.5.2 Aging of oxalate capped AuNPs in different molar ratio

Aging of oxalate capped AuNPs in pH 3.2 at molar ratio 1:1

At pH 3.2 with a molar ratio of 1:1, poorly growth of NPs was observed. Signs of PNCs and PNC clouds were seen at the 5-minute, 60-minute, and 7-day marks. Additionally, bridge formations and a core-shell motif were observed throughout the 7-day period.

Figure 4.14a illustrates that the size of the NPs transitioned from monodisperse and smaller sizes to polydisperse and larger sizes. The extension of the red curve suggests the presence of small NPs or PNCs still in the solution, with some crystallized AuNPs growing uncontrollably. Furthermore, Figure 4.14b indicates a decrease in circularity, suggesting that the NPs aged into non-spherical shapes.

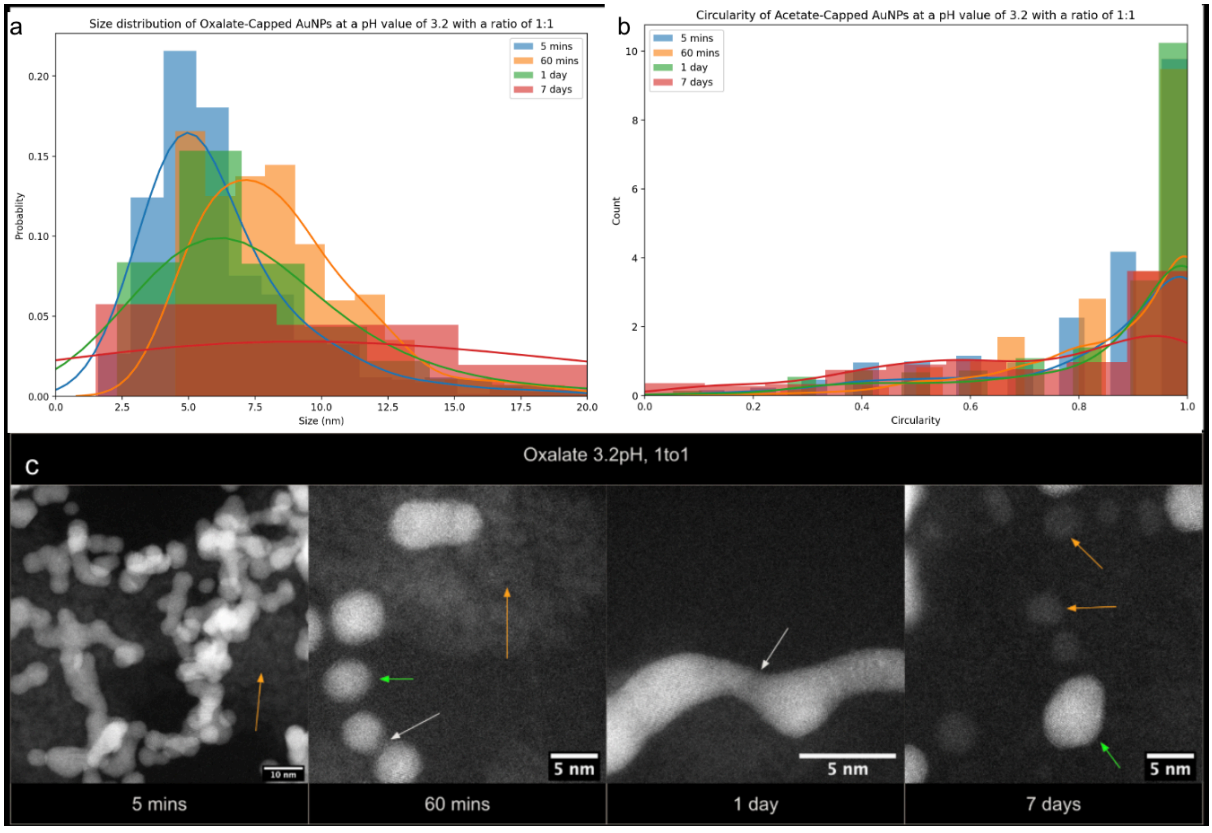


Figure 4. 14. a) top left plot shows the size distribution of 1:1 oxalate capped AuNPs in pH 3.2. b) top right plot shows the circularity. c) bottom STEM images of samples collected at different time points, after the start of the experiment: 5

minutes, 60 minutes, 1 day and 7 days. White arrows indicate bridging or sticking between particles. Green arrows indicate a shell formation or soft structure around a crystalline AuNP. Orange arrows indicate presumed pre-nucleation clusters.

Aging of oxalate capped AuNPs in pH 3.0 at molar ratio 1:1.5

At pH 3.0 with a molar ratio of 1:1.5, bridge formations were observed at the 5-minute, 60-minute, and 1-day marks. The bridging effects observed at 60 minutes and the donut shape observed at the 1-day mark suggest that the NPs were influenced by poorly controlled growth and subsequent consolidation into these unexpected structures.

At the 7-day time point, an extensive low density structure is observed, hereby descried as a PNCs cloud, indicated by an orange arrow in Figure 4.15c. Such feature has not been observed in any previous experiment and may be indicative of coalescence of multiple PNCs.

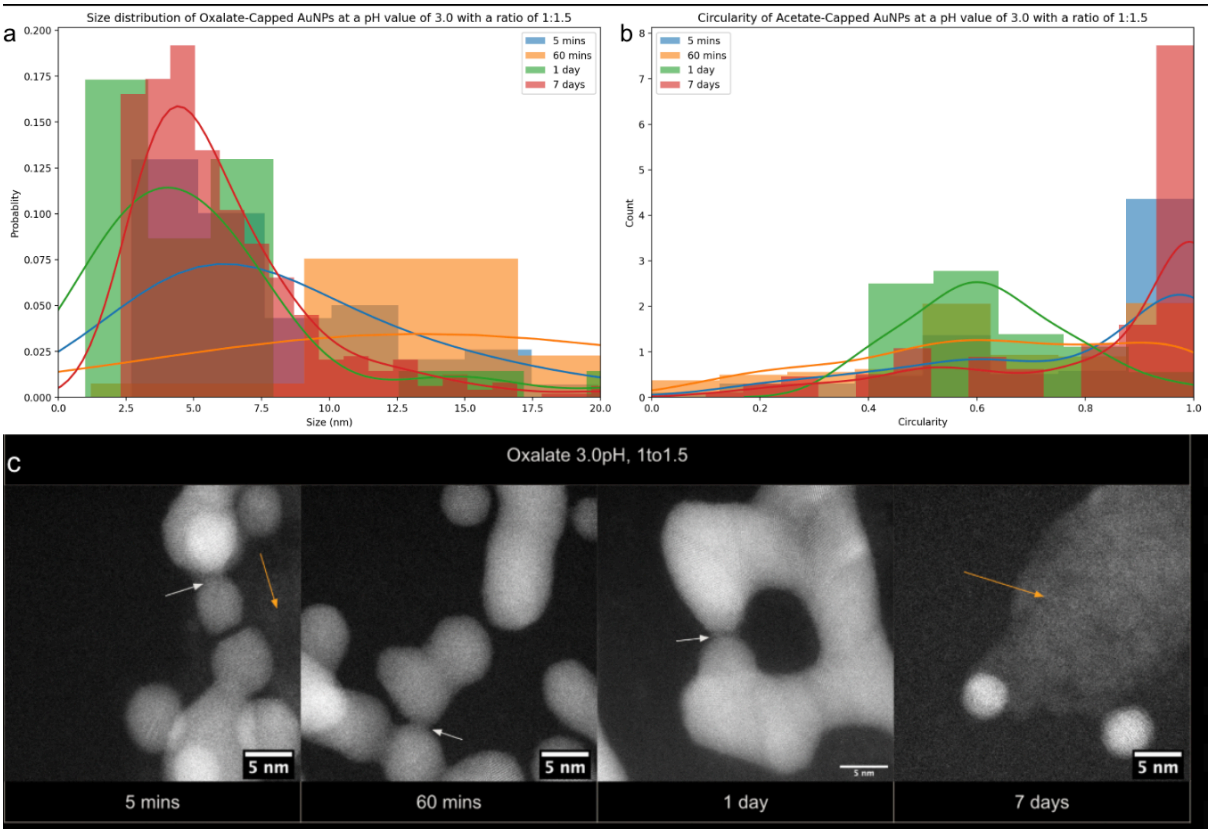


Figure 4. 15. a) top left plot shows the size distribution of 1:1.5 oxalate capped AuNPs in pH 3.0. b) top right plot shows the circularity. c) bottom STEM images of samples collected at different time points, after the start of the experiment: 5 minutes, 60 minutes, 1 day and 7 days. White arrows indicate bridging or sticking between particles. Orange arrows indicate presumed pre-nucleation clusters.

Aging of oxalate capped AuNPs in pH 6.2 at molar ratio 1:7

At pH 6.2 with a molar ratio of 1:7, some bridging was observed at the 5-minute and 60-minute marks in Figure 4.16c. Additionally, core-shell motifs, bridges between nanoparticles NPs, and PNCs were observed after 1 day and 7 days.

Despite the presumed presence of PNCs in the solution, the size and dispersity of the particles remained relatively stable compared to other synthesis conditions.

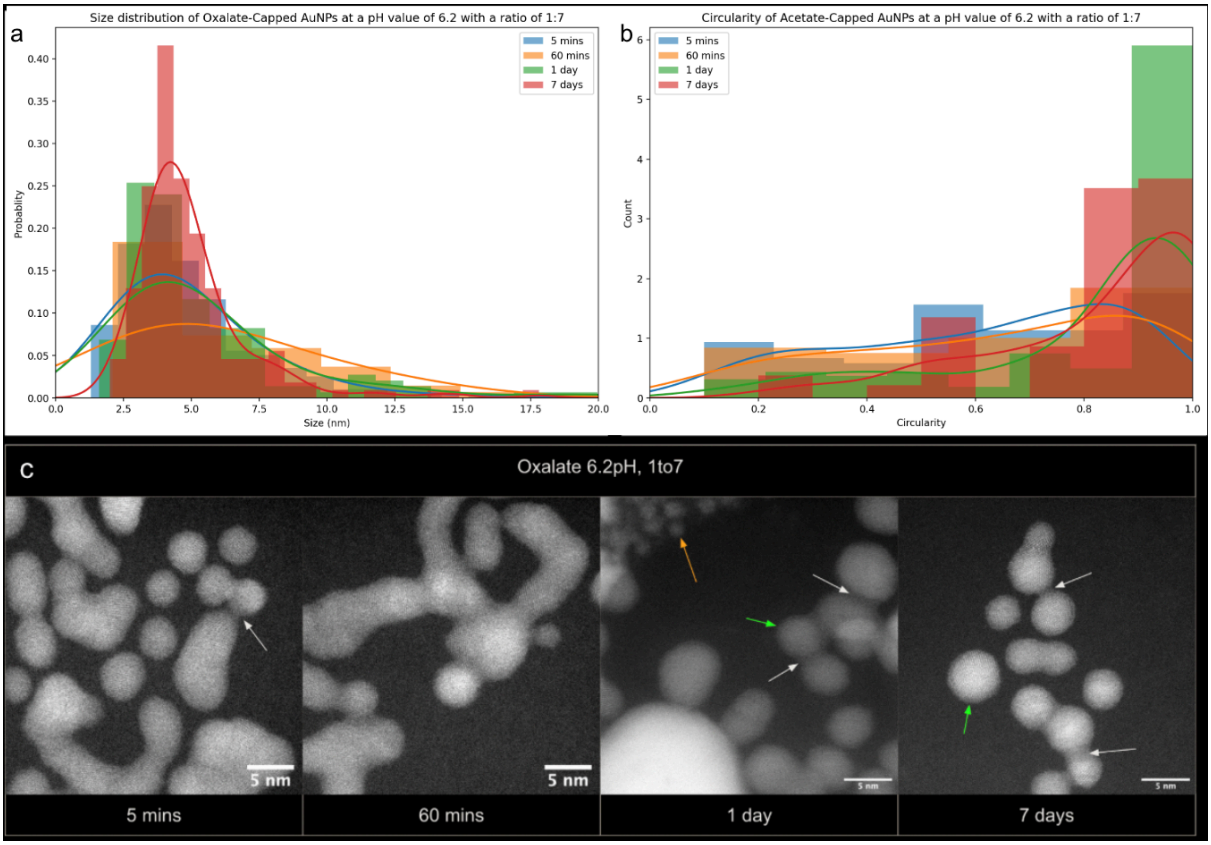


Figure 4. 16. a) top left plot shows the size distribution of 1:7 oxalate capped AuNPs in pH 6.2. b) top right plot shows the circularity. c) bottom STEM images of samples collected at different time points, after the start of the experiment: 5 minutes, 60 minutes, 1 day and 7 days. White arrows indicate bridging or sticking between particles. Green arrows indicate a shell formation or soft structure around a crystalline AuNP. Orange arrows indicate presumed pre-nucleation clusters.

Aging of oxalate capped AuNPs in pH 6.4 at molar ratio 1:10.6

At pH 6.4 (Figure 4.17), despite using a higher molar ratio of 1:10.6, which would be expected to optimise well defined structures, PNCs and bridges were observed throughout the 7-day period, as indicated by orange and white arrows. The size and distribution of nanoparticles remained relatively unchanged during the period of observation.

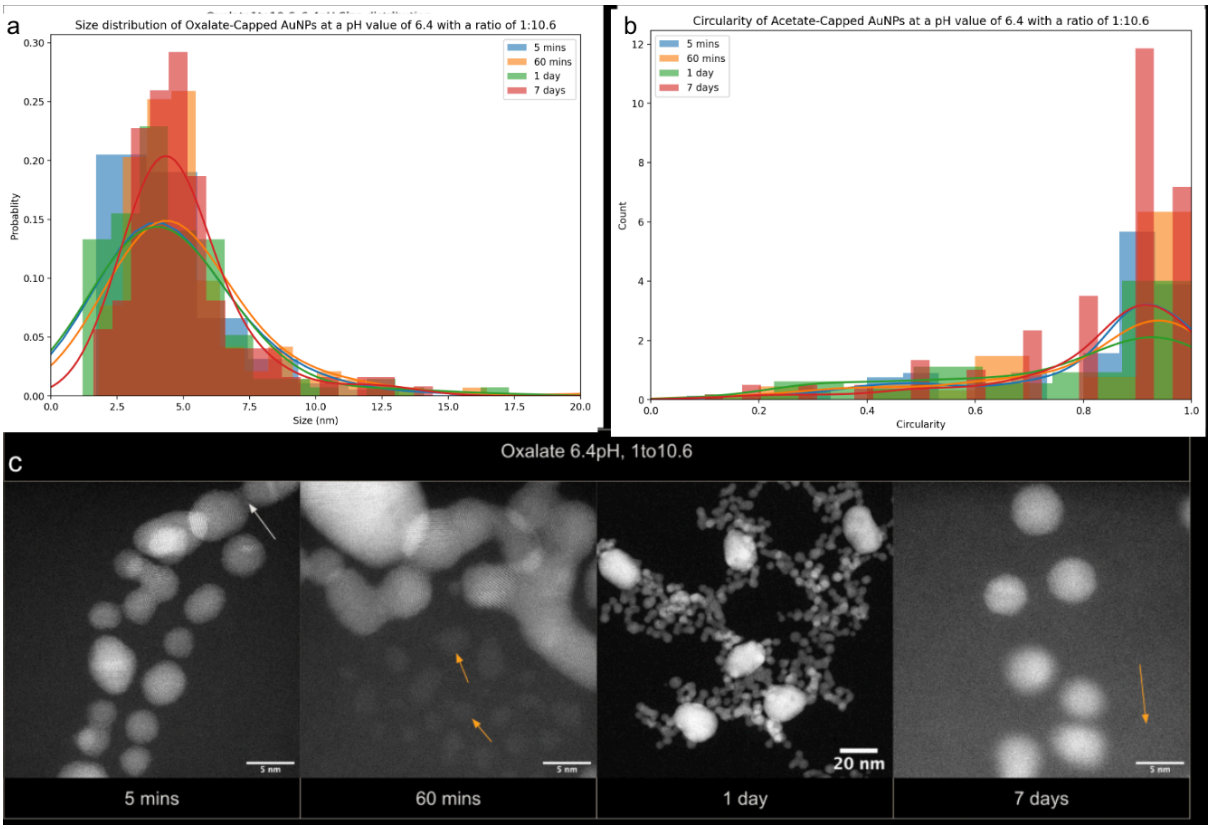


Figure 4. 17. A) top left plot shows the size distribution of 1:10.6 oxalate capped AuNPs in pH 6.4. b) top right plot shows the circularity. c) bottom STEM images of samples collected at different time points, after the start of the experiment: 5 minutes, 60 minutes, 1 day and 7 days. White arrows indicate bridging or sticking between particles. Orange arrows indicate presumed pre-nucleation clusters.

4.6 Aging of different carboxyl molecule capped AuNPs (citric acid)

Citric acid, a commonly used capping agent, contains three carboxyl groups. The presence of multiple carboxyl groups in the capping agent facilitates binding with more than one gold atom. Consequently, it may be expected that core-shell motifs, bridge formations, and PNCs will occur more frequently.

4.6.1 Aging of citrate capped AuNPs in pH 6.7 at molar ratio of 1:3.5

Using citrate at neutral pH with a molar ratio of 1:3.5 is a typical setup in the Turkevich method. When sodium borohydride is employed under these conditions, NPs synthesized exhibit improved size stability and polydispersity. As shown in Figure 4.18a, the width of the size distribution curve remains nearly unchanged over the 7-day observation period. Figure 4.18b also indicates signs of Ostwald ripening, as evidenced by the NPs tending towards a more spherical shape. Interestingly, no signs of PNCs were observed in this synthesis.

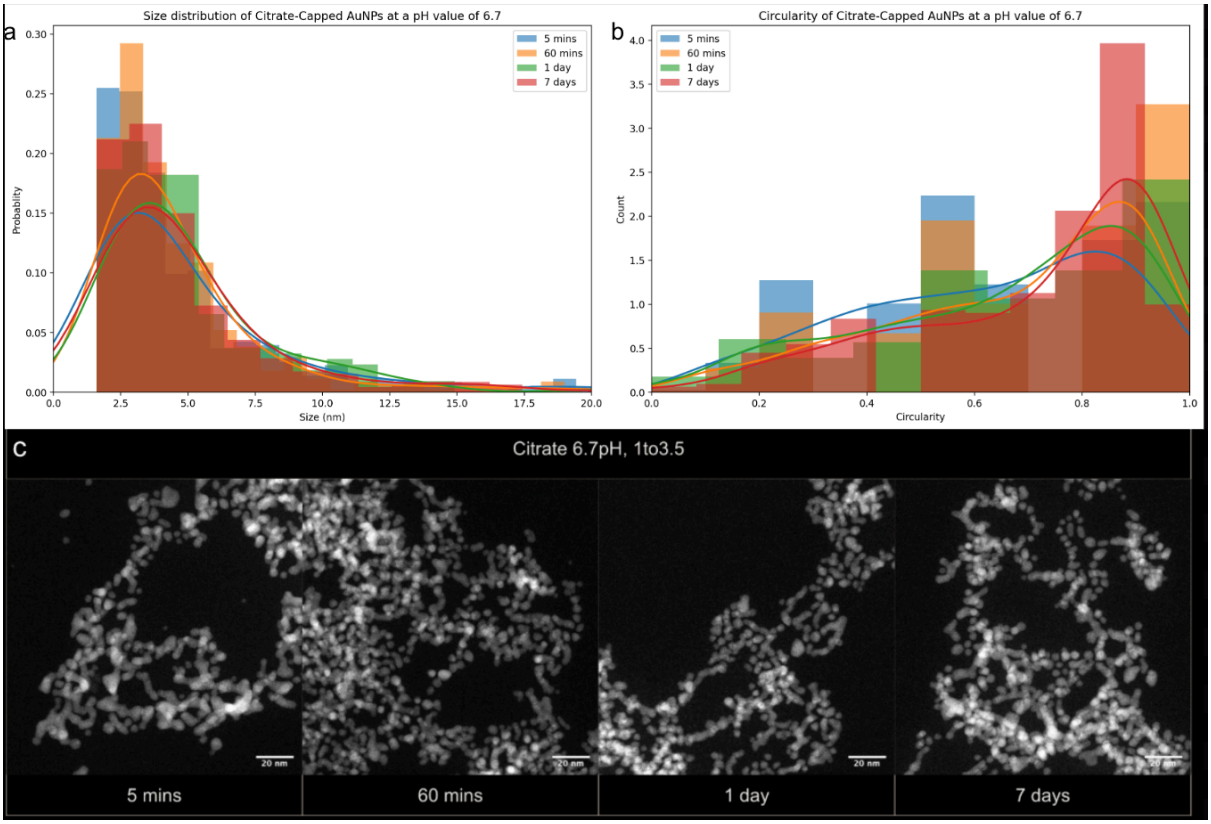


Figure 4. 18. a) top left plot shows the size distribution of 1:3.5 citrate capped AuNPs in pH 6.7. b) top right plot shows the circularity. c) bottom STEM images of samples collected at different time points, after the start of the experiment: 5 minutes, 60 minutes, 1 day and 7 days

4.6.2 Aging of citrate capped AuNPs in different molar ratio

Aging of citrate capped AuNPs in pH 4.4 at molar ratio 1:1

Using citrate as a capping agent in a suboptimal setup such as this typically results in unpredictable NPs size and morphology changes. Here, employing citrate at pH 4.4 with a molar ratio of 1:1 yielded NPs that exhibited signs of poorly

controlled growth as early as 5 minutes. By the 60-minute mark, a crystallized soft-shell structure was evident, indicated by a blue arrow. This structure formation resulted from the recrystallization of a core-shell structure observed in previous images, this formation will be discussed in chapter 5. The aging process of the original NPs was facilitated by the recrystallization of surface PNCs, as indicated by green and white arrows, eventually leading to the formation of a fused particle structure with broad bridging (blue arrow) showing high crystallinity. With insufficient capping agent in this synthesis, Figure 4.19a shows a gradual increase in NP size.

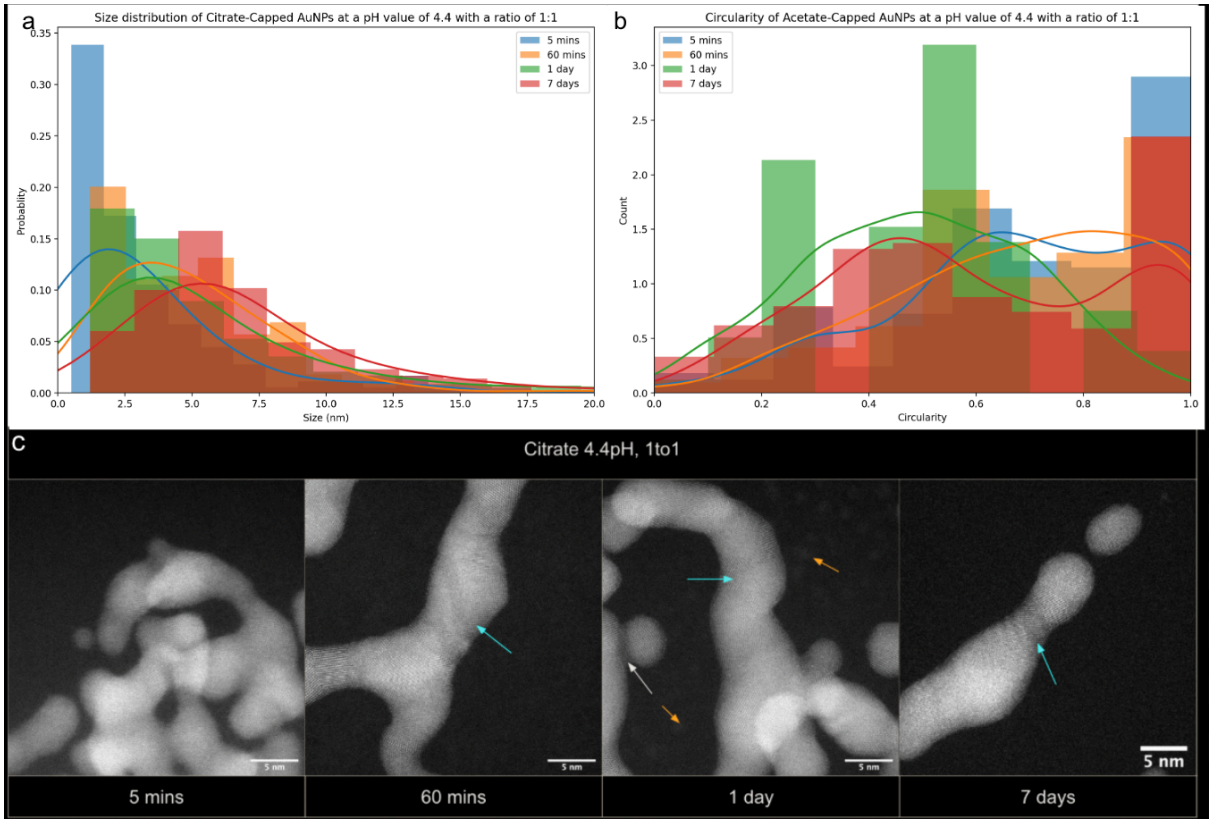


Figure 4. 19. a) top left plot shows the size distribution of 1:1 citrate capped AuNPs in pH 4.4. b) top right plot shows the circularity. c) bottom STEM images of samples collected at different time points, after the start of the experiment: 5 minutes, 60 minutes, 1 day and 7 days. White arrows indicate bridging or sticking

between particles. Green arrows indicate a shell formation or soft structure around a crystalline AuNP. Orange arrows indicate presumed pre-nucleation clusters.

Aging of citrate capped AuNPs in pH 4.5 at molar ratio 1:1.5

Increasing the molar ratio to 1:1.5 compared to the last set of conditions, slows the growth of NPs in this synthesis over the 7-day period of observation. This effect can be attributed to the formation of a poorly crystallised shell covering the core, creating a core-shell motif or broad bridge formations, which eventually age into a poorly defined structure. In Figure 4.20a, the size of the NPs increases only marginally from 2.5 nm to 3.75 nm. However, the NPs become highly polydisperse, as indicated by the increase in dispersity. Furthermore, Figure 4.20b shows a decrease in circularity, suggesting that the aging NPs are influenced by the presence of PNCs.

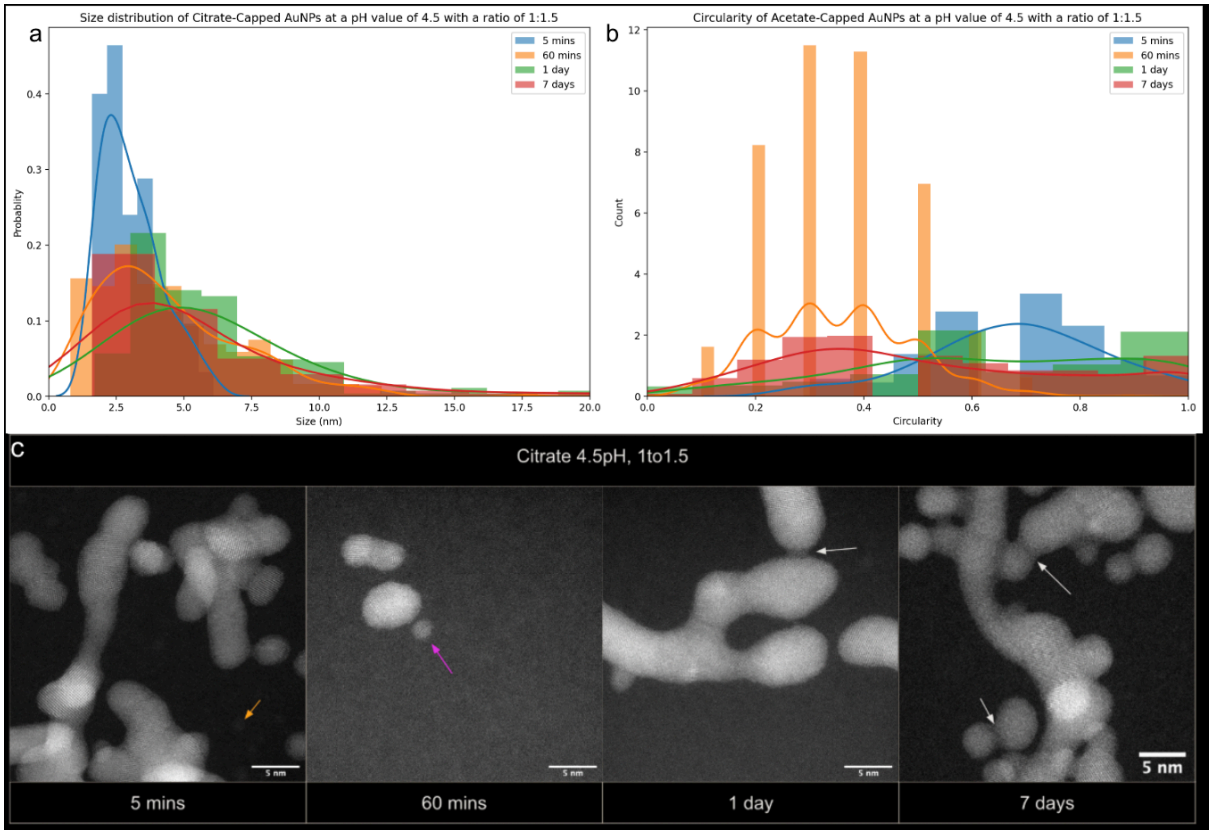


Figure 4. 20. a) top left plot shows the size distribution of 1:1.5 citrate capped AuNPs in pH 4.5. b) top right plot shows the circularity. c) bottom STEM images of samples collected at different time points, after the start of the experiment: 5 minutes, 60 minutes, 1 day and 7 days. White arrows indicate bridging or sticking between particles. Purple arrows indicate a shell formation or soft structure around a crystalline AuNP. Orange arrows indicate presumed pre-nucleation clusters.

Aging of citrate capped AuNPs in pH 6.3 at molar ratio 1:7

When AuNPs was synthesised under pH 6.3 environment, it is typically considered optimal for NP stability. Thus, using a higher amount of capping agent with a molar ratio of 1:7, a smaller average size of NPs was expected.

Figure 4.21c illustrates the presence of PNCs throughout the entire 7-day observation period. At the 5-minute mark, a core-shell motif and soft bridges were observed. Figures 4.21a and 4.21b indicate the unstable and non-spherical nature of the NP size over these 7 days. Interestingly, the increased use of capping agents did not lead to smaller NP sizes or mono-dispersity. Instead, the NPs exhibited signs of lesser well controlled growth.

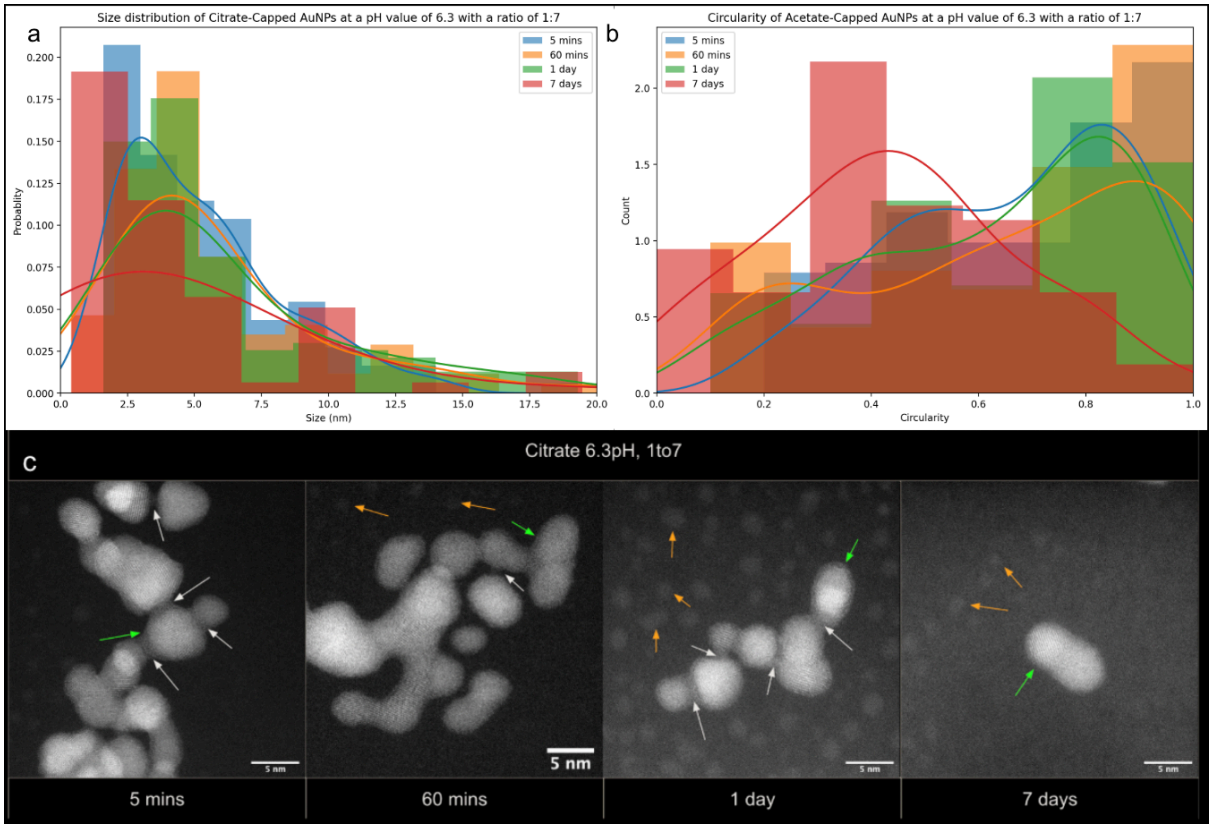


Figure 4. 21. a) top left plot shows the size distribution of 1:7 citrate capped AuNPs in pH 6.3. b) top right plot shows the circularity. c) bottom STEM images of samples collected at different time points, after the start of the experiment: 5 minutes, 60 minutes, 1 day and 7 days. White arrows indicate bridging or sticking between particles. Green arrows indicate a shell formation or soft structure around a crystalline AuNP. Orange arrows indicate presumed pre-nucleation clusters.

Aging of citrate capped AuNPs in pH 6.3 at molar ratio 1:10.6

A similar scenario occurred when increasing the molar ratio to 1:10.6. Despite using more capping agent in a neutral pH environment, these conditions did not result in the production of smaller and monodisperse AuNPs (Figure 4.22), even though neutral pH is considered optimal for AuNP synthesis. Conversely, PNCs were observed throughout the 7-day observation period, as indicated by the orange arrow.

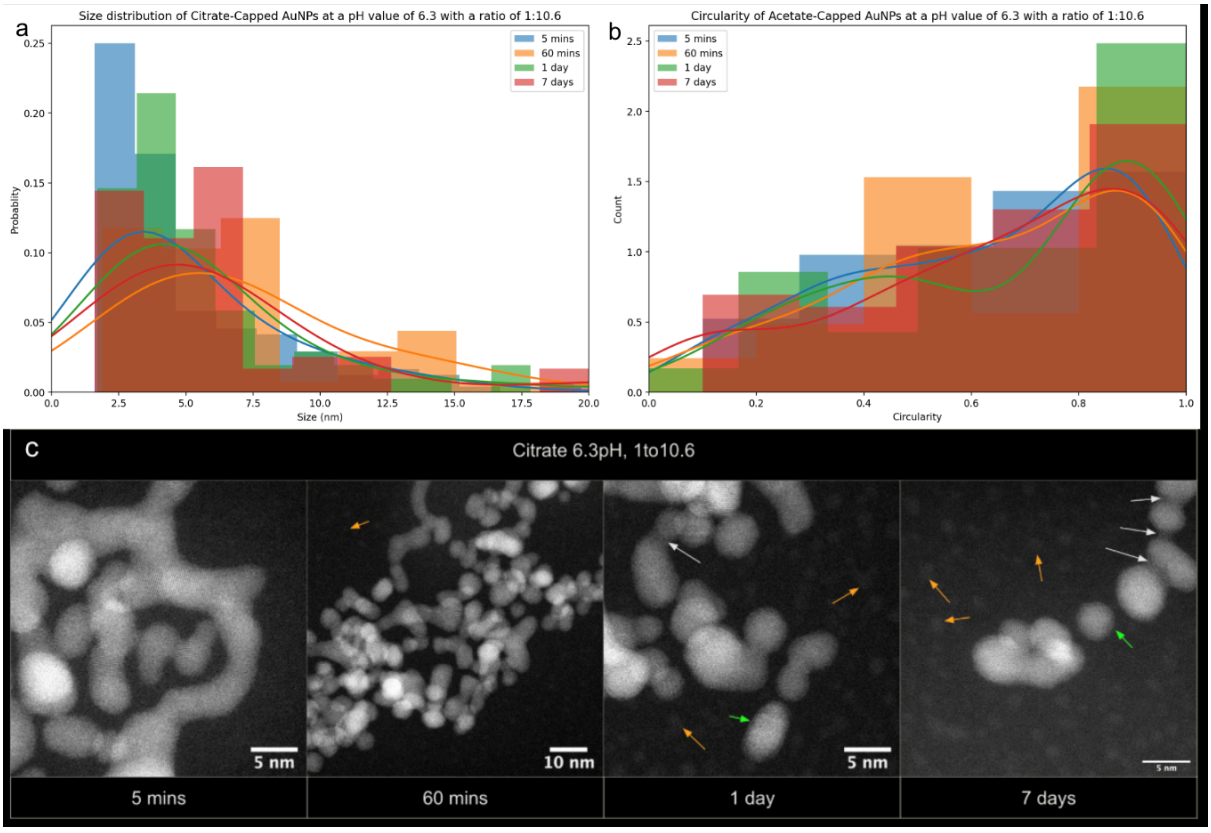


Figure 4. 22. a) top left plot shows the size distribution of 1:10.6 citrate capped AuNPs in pH 6.3. b) top right plot shows the circularity. c) bottom STEM images of samples collected at different time points, after the start of the experiment: 5

minutes, 60 minutes, 1 day and 7 days. White arrows indicate bridging or sticking between particles. Green arrows indicate a shell formation or soft structure around a crystalline AuNP. Orange arrows indicate presumed pre-nucleation clusters.

4.7 Aging of different carboxyl molecule capped AuNPs (propionic acid)

Propionic acid, despite containing only a single carboxyl group, occupies a larger volume compared to acetate. This size disparity in the capping agent is expected to influence the size of the synthesized NPs.

4.7.1 Aging of propionic acid capped AuNPs in pH 9.3 at molar ratio of 1:3.5

At pH 9.3 with a molar ratio of 1:3.5, the NPs nucleated to a size like those synthesized in previous experiments with alternative capping agents. In Figure 4.23c, no core-shell motifs or bridge formations were observed at the 5-minute, 60-minute, and 1-day marks, but PNCs were visible by the 7-day mark.

Figure 4.23a and 4.23b show a decrease in mean size and improved dispersity, indicating the potential reformation of PNCs in the solution after the initial NP

nucleation. Over the 7-day period, the shape of the NPs shifted towards spherical, a distinctive characteristic compared to other syntheses.

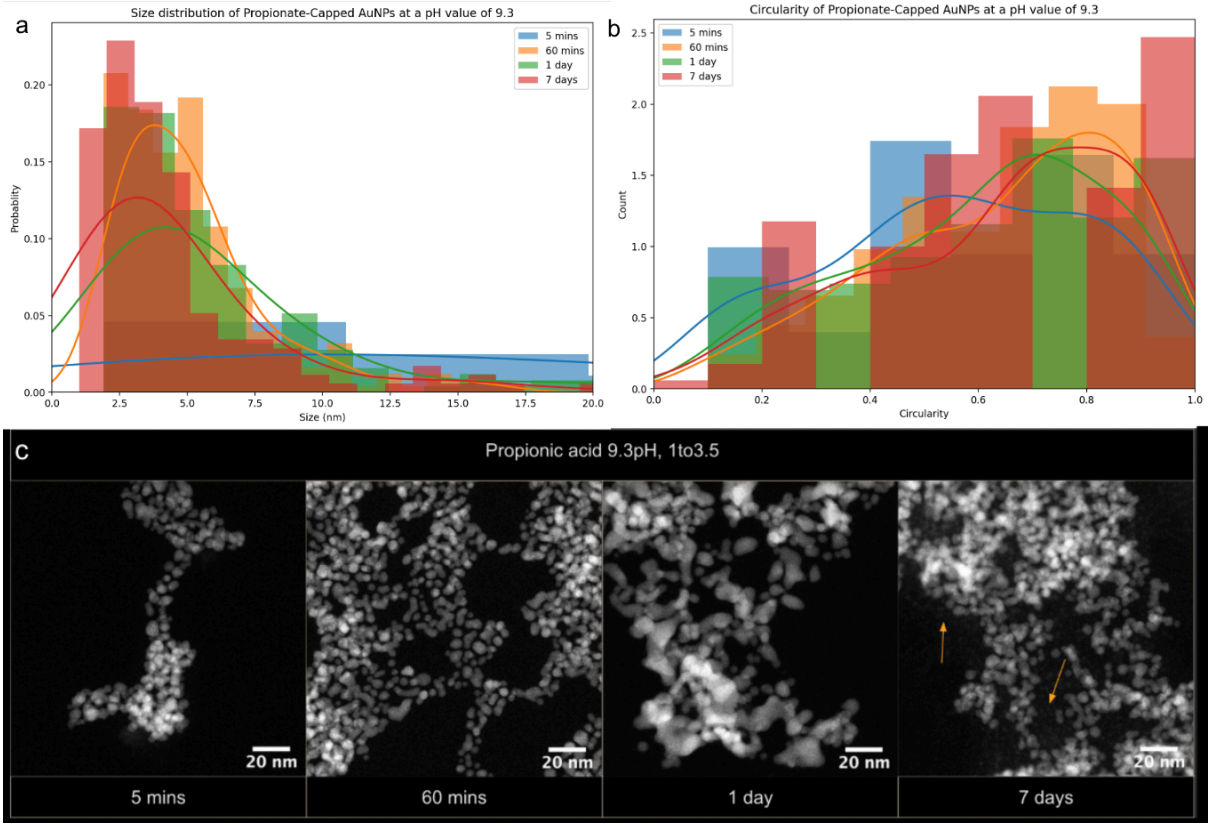


Figure 4. 23. a) top left plot shows the size distribution of 1:3.5 propionic acid capped AuNPs in pH 9.3. b) top right plot shows the circularity. c) bottom STEM images of samples collected at different time points, after the start of the experiment: 5 minutes, 60 minutes, 1 day and 7 days. Orange arrows indicate presumed pre-nucleation clusters.

4.7.2 Aging of propionic acid capped AuNPs in different molar ratio

Aging of propionic acid capped AuNPs in pH 6.4 at molar ratio 1:7

At pH 6.4 with a molar ratio of 1:7, PNCs were observed at the 5-minute, 60-minute, and 1-day marks, as indicated by the orange arrow in Figure 4.24c. Bridge formations were also observed after 7 days, likely resulting from core-shell and soft bridge formations.

Despite the more neutral pH, the NPs tended towards a stable aging pathway. However, as shown in Figure 4.24a, the size of the NPs still increased from 3 nm to 5 nm. Additionally, after 7 days, the NPs became more polydisperse as the curve widen in Figure 4.24a.

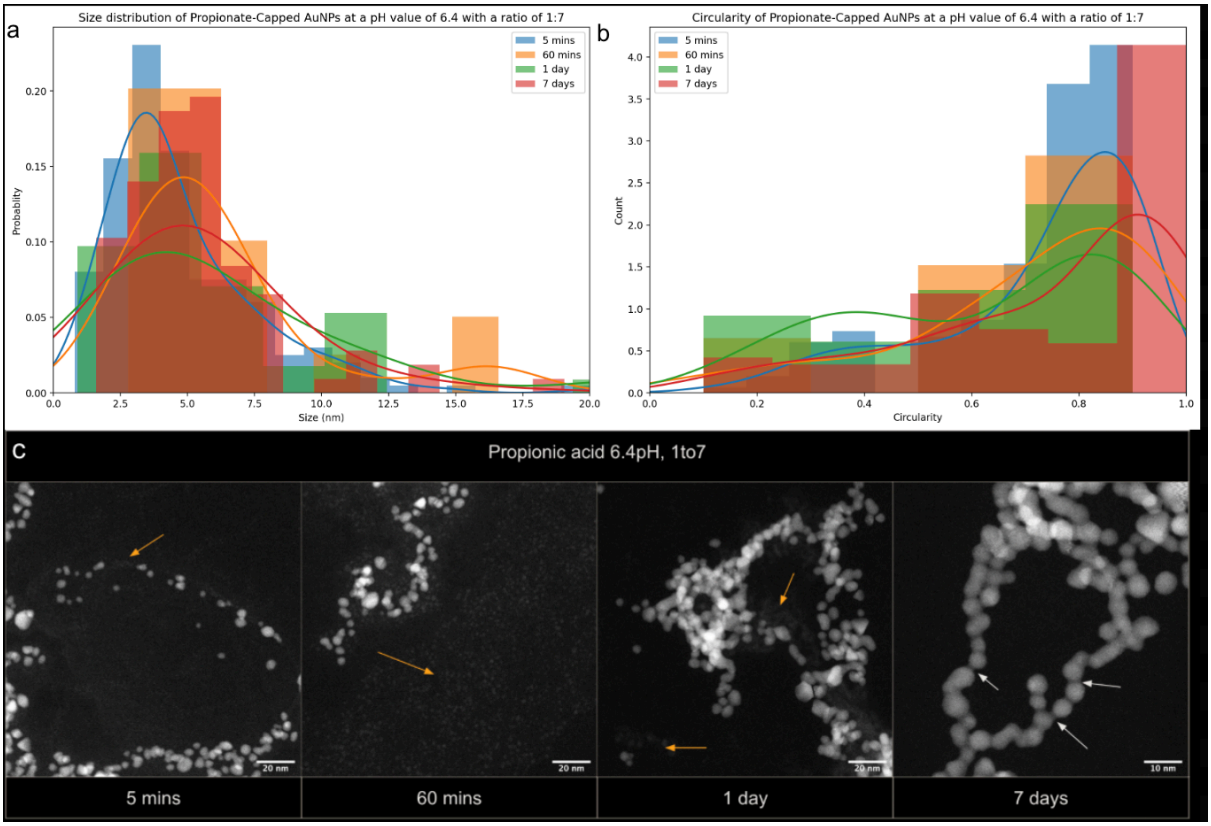


Figure 4. 24. a) top left plot shows the size distribution of 1:7 propionic acid capped AuNPs in pH 6.4. b) top right plot shows the circularity. c) bottom STEM images of samples collected at different time points, after the start of the experiment: 5 minutes, 60 minutes, 1 day and 7 days. White arrows indicate bridging or sticking between particles. Orange arrows indicate presumed pre-nucleation clusters.

Aging of propionic acid capped AuNPs in pH 6.4 at molar ratio 1:10.6

At pH 6.4, increasing the amount of propionic acid as a capping agent did not result in the production of smaller NPs. In Figure 4.25c, a cloud of PNCs was observed at the 5-minute mark, along with a core-shell motif and bridge

formations. Signs of PNCs were also visible at the 60-minute mark but were absent at the 1-day and 7-day marks. The NPs exhibited signs of aging when PNCs were not present.

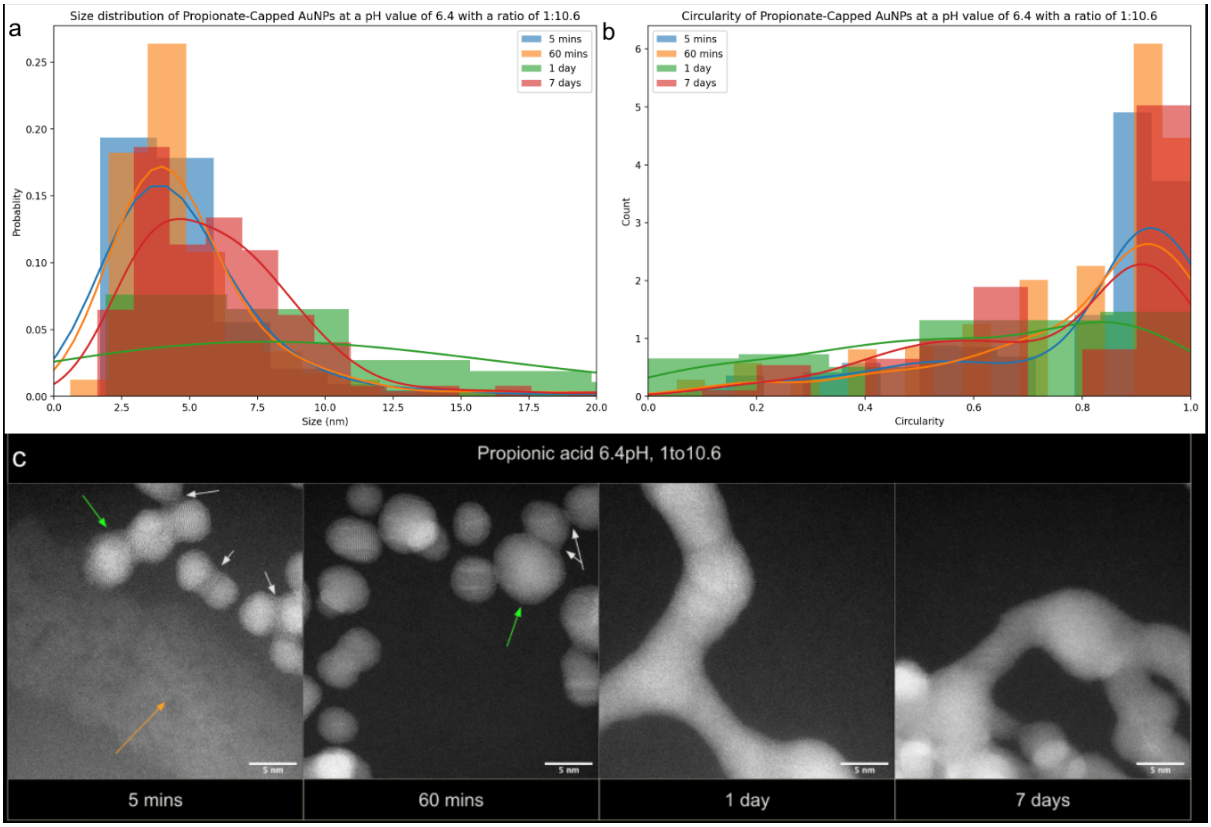


Figure 4. 25. a) Top left plot shows the size distribution of 1:10.6 propionic acid capped AuNPs in pH 6.4. b) top right plot shows the circularity. c) bottom STEM images of samples collected at different time points, after the start of the experiment: 5 minutes, 60 minutes, 1 day and 7 days. White arrows indicate bridging or sticking between particles. Green arrows indicate a shell formation or soft structure around a crystalline AuNP. Orange arrows indicate presumed pre-nucleation clusters.

4.8 No capping agent

Up to this point, one might question why adding more capping agents does not prevent the growth of small NPs. To explore this, we synthesized AuNPs without any capping agent. In theory, without a capping agent to inhibit adatom growth, NPs would nucleate freely, resulting in larger sizes. However, the pH adjustment of this synthesis is tricky, because by only adding the reducing agent sodium borohydride, the pH already reaches 9. To avoid adding more reagent in the solution, I decided not to add any other solution to balance the pH value.

Aging with no capping agent AuNPs at pH 9

Surprisingly in Figure 4.26, the synthesized AuNPs remained small (<5nm) even without any capping agent. PNCs were observed on the 1-day mark, suggesting that PNC formation can occur without the presence of added capping agents. Bridging also occurred at 1 day. However, the size of the NPs increased over the 7-day period, indicating ongoing growth, although the growth rate was similar to that observed in syntheses with capping agents.

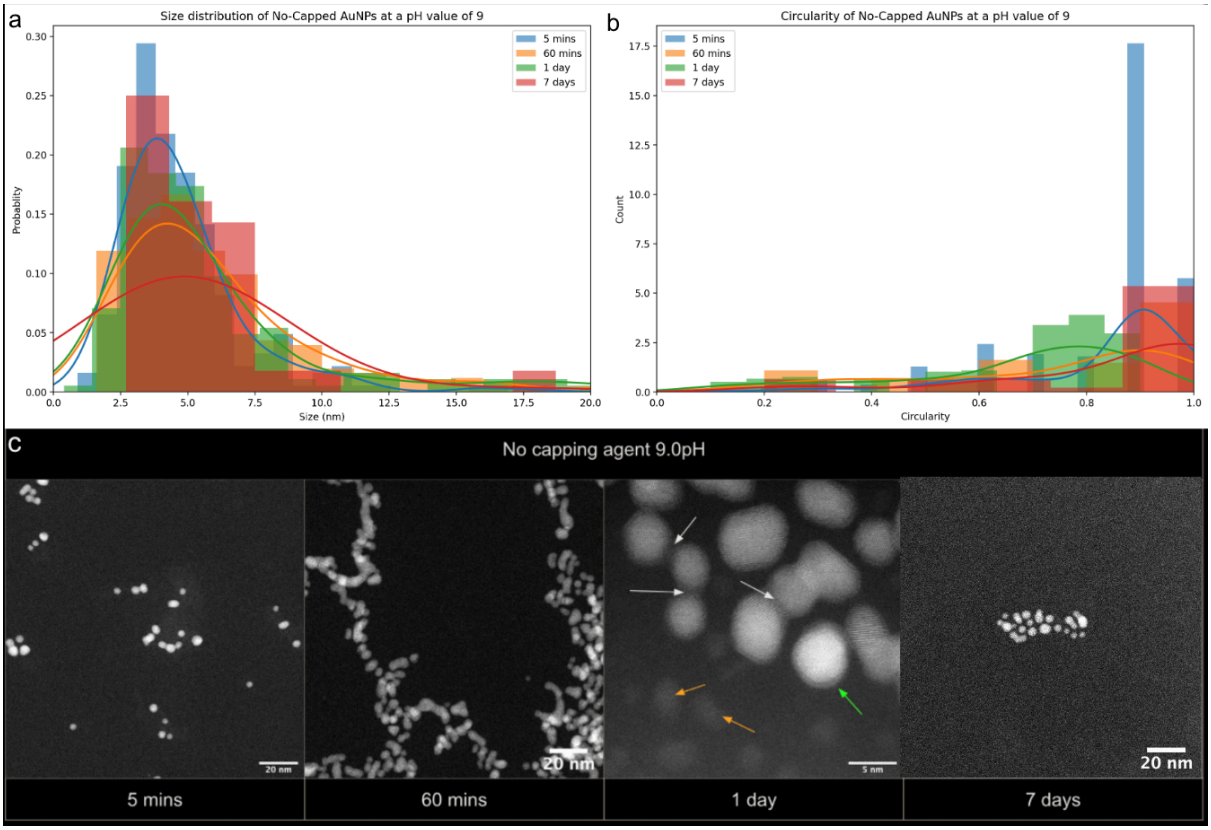


Figure 4. 26. a) top left plot shows the size distribution of no capping agent AuNPs in pH 9.0. b) top right plot shows the circularity. c) bottom STEM images of samples collected at different time points, after the start of the experiment: 5 minutes, 60 minutes, 1 day and 7 days. White arrows indicate bridging or sticking between particles. Green arrows indicate a shell formation or soft structure around a crystalline AuNP. Orange arrows indicate presumed pre-nucleation clusters.

4.9 Discussion

In this section, we will discuss the differences between each synthesis based on variations in the number of carboxyl groups in the capping agent, pH conditions, and molar ratios.

First, we will discuss the findings of acetate-capped AuNPs, which contain a single carboxyl group in the molecule. We will compare the effects on NP size under different pH conditions and molar ratios.

4.9.1 Comparing acetate pH difference

By maintaining a fixed gold to acetate molar ratio of 1:3.5, varying the pH of the synthesis setup did not significantly affect the size of the NPs. Figure 4.27 illustrates the growth of synthesized NPs over time following the addition of sodium borohydride. While smaller NPs were initially observed at higher pH values within the first 5 minutes, any correlation between pH and NP size disappeared after 60 minutes.

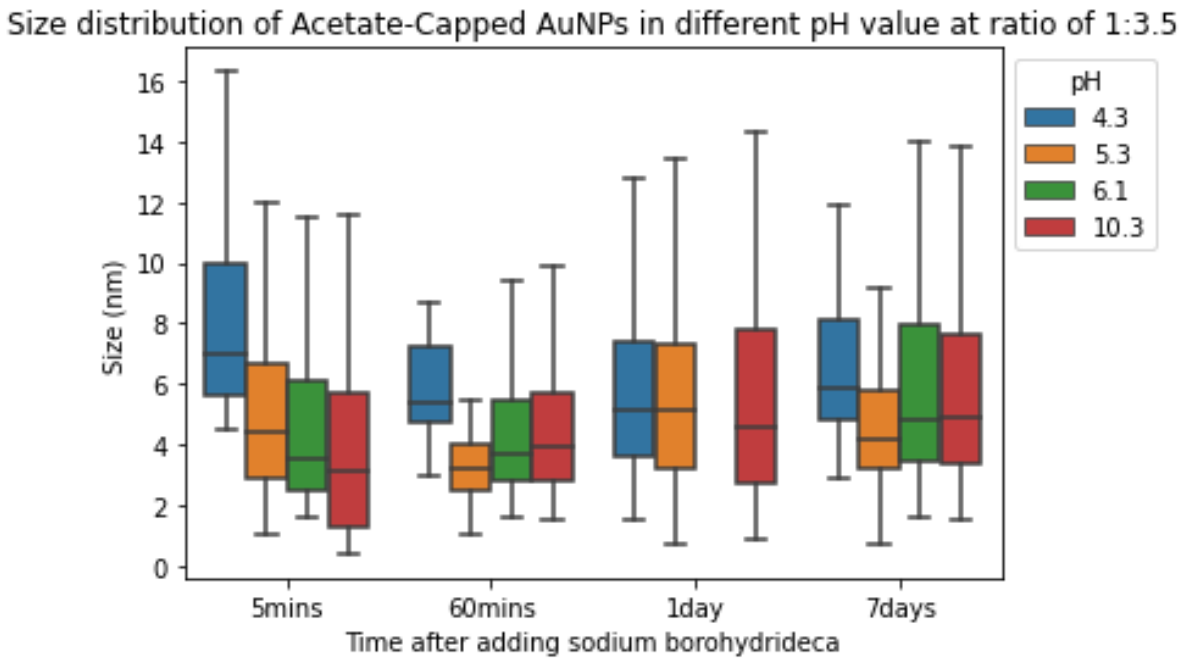
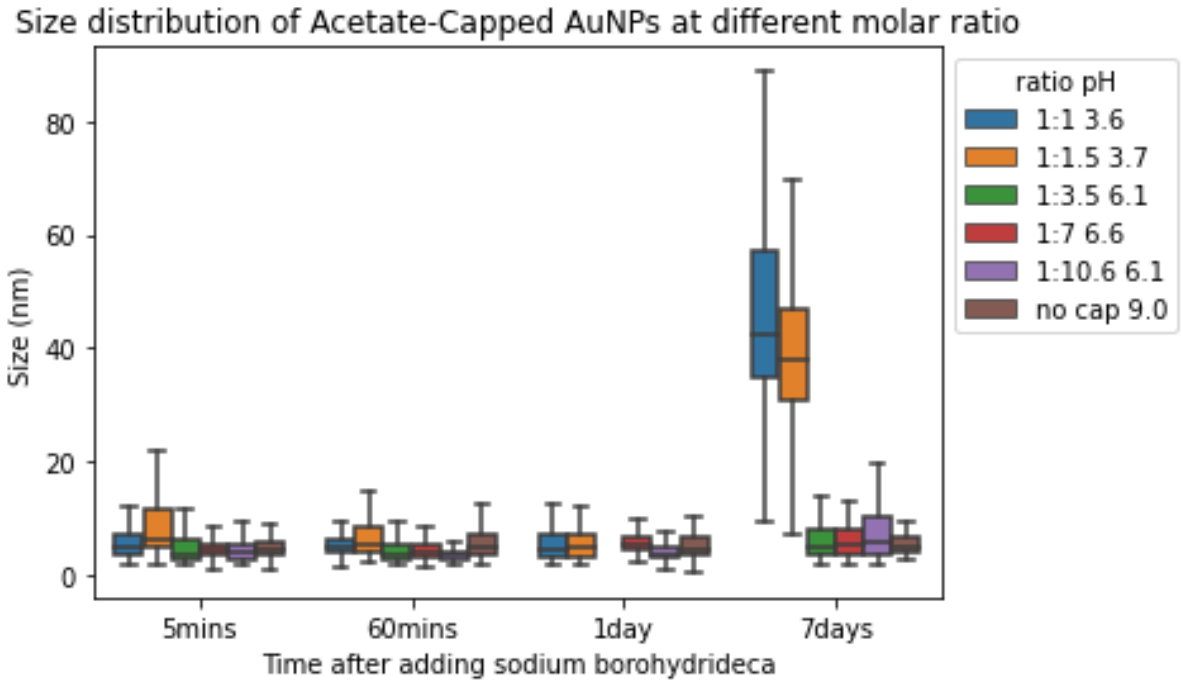


Figure 4. 27 Size distribution of acetate-capped AuNPs with 1:3.5 molar ratio in different pH environments during a 7 day period. The size distribution is represented using a box-and-whisker plot. The box in the plot represents the interquartile range, indicating the spread of the dataset. The whiskers extend from the box to show the rest of the distribution, excluding outliers. The sample at 1 day failed to observe any AuNPs.

4.9.2 Comparing acetate molar difference

Maintaining a fixed pH, on the other hand, proved challenging. The use of sodium acetate, with its low molar ratio as a capping agent, naturally led to lower pH values. In Figure 4.28, both the 1:1 and 1:1.5 molar ratios of gold to acetate exhibited a significant increase in size after 7 days. In contrast, other syntheses

with more neutral pH conditions (higher sodium concentration) and higher molar ratios (1:3, 1:7, and 1:10.6) showed relatively stable sizes. Interestingly, the synthesis of AuNPs without any capping agent also resulted in similar sizes to those where acetate was present.



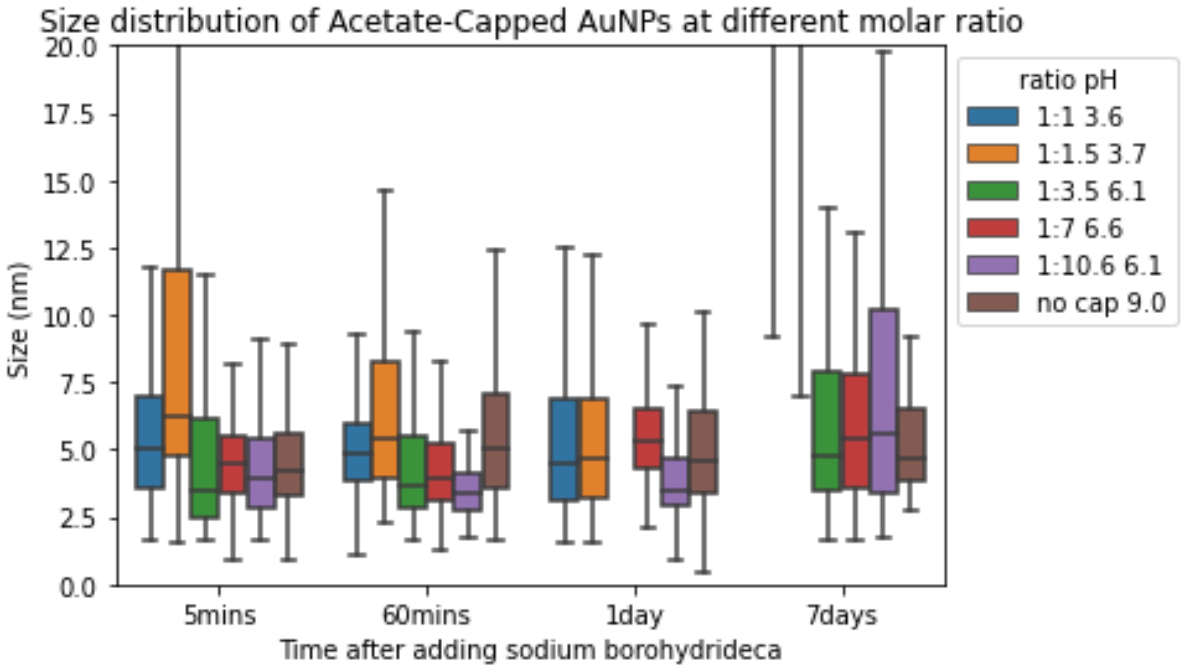


Figure 4. 28. Top figure showing the different molar ratio and pH of acetate capped AuNPs with different pH and aging time. Bottom figure showing the same horizontal axis range but zooming in a smaller size range 0-20 nm of the vertical axis, to provide a more detailed view of the size range in each experiment. The size distribution is represented using a box-and-whisker plot. The box in the plot represents the interquartile range, indicating the spread of the dataset. The whiskers extend from the box to show the rest of the distribution, excluding outliers. The sample at 1 day failed to observe any AuNPs.

4.9.3 Comparing pH 6 acetate molar ratio difference

Maintaining the pH value at 6 and varying the molar ratio, the size of the NPs generally follows a similar aging trend. Figure 4.29 illustrates that the synthesized NPs remain stable for the first few days but noticeably increase in size and polydispersity by day 7 judging from the box plot (Figure 4.29). Increasing the amount of acetate does not prevent the NPs from growing after synthesis, nor does it lead to the synthesis of smaller NPs despite the presence of more capping agents.

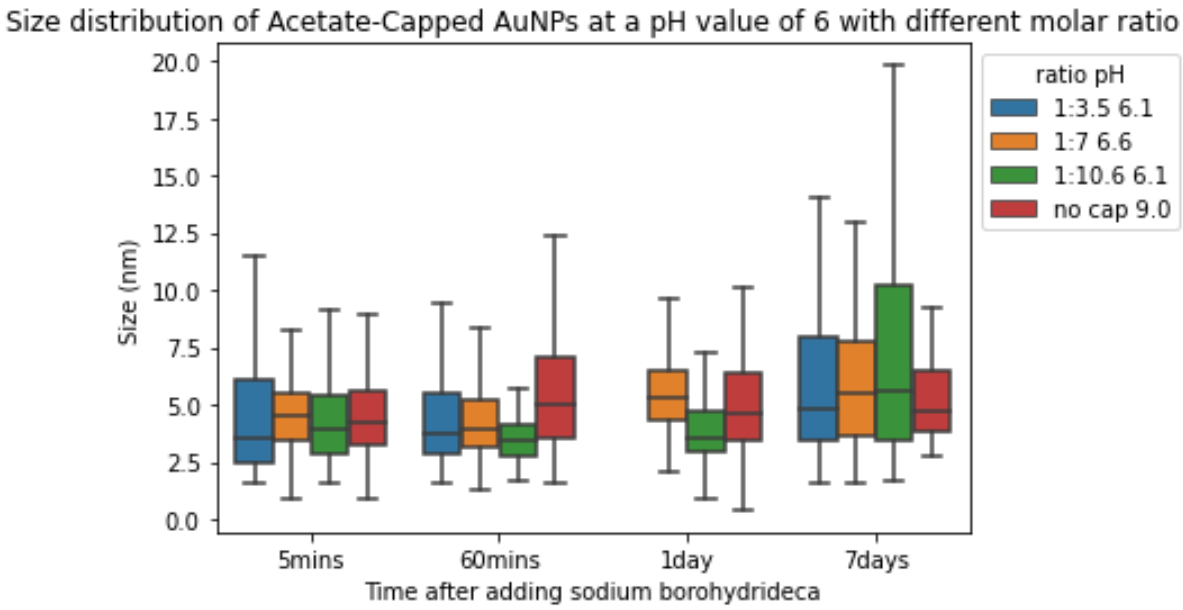


Figure 4. 29 Different molar ratio of pH 6 acetate capped AuNPs size changes with respect to their aging time. The size distribution is represented using a box-and-whisker plot. The box in the plot represents the interquartile range, indicating the spread of the dataset. The whiskers extend from the box to show the rest of the distribution, excluding outliers.

Acetate as a capping agent did produce a small size of AuNPs. However, the size of the AuNPs continues to grow over the 7-day period. This suggests that the capping ability of acetate is insufficient to halt the growth of AuNPs, even with an excess of acetate present in the solution and regardless of pH.

Next, I will investigate the use of oxalate as a capping agent, focusing on its interaction with varying pH and molar ratios.

4.10.1 Comparing oxalate pH difference

Using oxalate as a capping agent, is expected to have a more pronounced control on nucleation and growth due to its twin carboxyl groups, which can efficiently bind free gold atoms and promote bridging motifs as illustrated in Figure 4.10. In Figure 4.30, at a 1:3.5 molar ratio, low pH values did not result in smaller NPs compared to other synthesis conditions in this experiment. NPs synthesized at pH 2.8 exhibited signs of aging during the initial 3 sample points up to 1 day. However, PNCs were observed at the 7-day mark, which correlates with the drastic decrease in size observed between the 1-day and 7-day measurements. Other synthesis followed a general trend of slow size increase, particularly noticeable at pH 3.9.

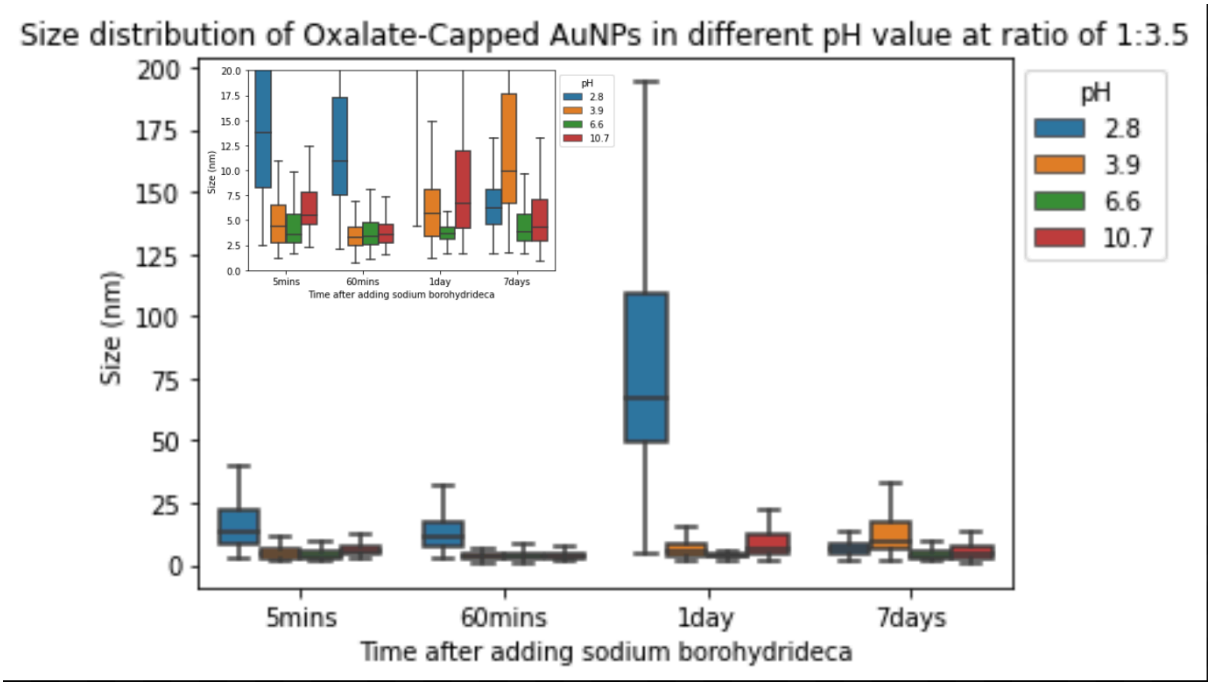


Figure 4. 30. Size distribution of 1:3.5 molar ratio of oxalate capped AuNPs with different pH and aging time. The size distribution is represented using a box-and-whisker plot. The box in the plot represents the interquartile range, indicating the spread of the dataset. The whiskers extend from the box to show the rest of the distribution, excluding outliers.

4.10.2 Comparing oxalate molar difference

Comparing different oxalate molar ratios, NPs synthesized at low molar ratios and pH values (e.g., 1:1 and 1:1.5, pH 3 and 3.2) showed an increase in size, as shown in Figure 4.31. In contrast, NPs synthesized at pH 6 and higher molar ratios (greater than 1:3.5) behaved as expected, as they maintained a size around 5 nm. Interestingly, the growth in size of NPs synthesized without any capping agent fell within the range observed for NPs synthesized with oxalate.

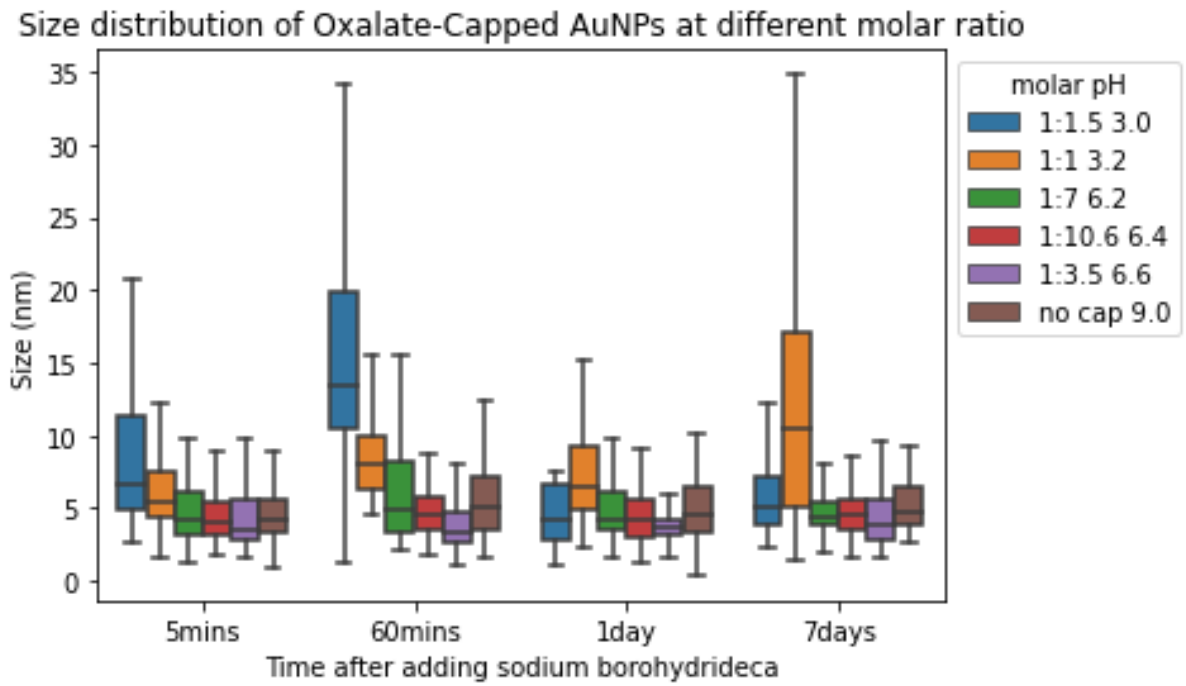


Figure 4. 31. Different molar ratio of oxalate capped AuNPs with different pH and aging time. The size distribution is represented using a box-and-whisker plot. The box in the plot represents the interquartile range, indicating the spread of the dataset. The whiskers extend from the box to show the rest of the distribution, excluding outliers.

4.10.3 Comparing pH 6 oxalate molar ratio difference

Oxalate-capped AuNPs generally maintain consistent sizes in neutral pH environments. Despite varying the molar ratio of oxalate capping agent added during synthesis, excess capping did not result in smaller NPs, even though more gold atoms should theoretically be bound by the carboxyl groups of oxalic acid and rendered unavailable for nucleation and growth. Nevertheless, all syntheses using

oxalate with excess molar ratios still yielded NPs of similar sizes compared to syntheses conducted without any capping agent.

Oxalate capped AuNPs generally remains the same in the 7 days period in Figure 4.32. However, compared to acetate capped AuNPs at pH 6 (Figure 4.29), there are no sign of growth by day 7 indicating the AuNPs are much more stable capped with oxalic acid. Similarly, with acetate-capped AuNPs, the size of the NPs cannot be controlled by increasing the molar ratio of the capping agent.

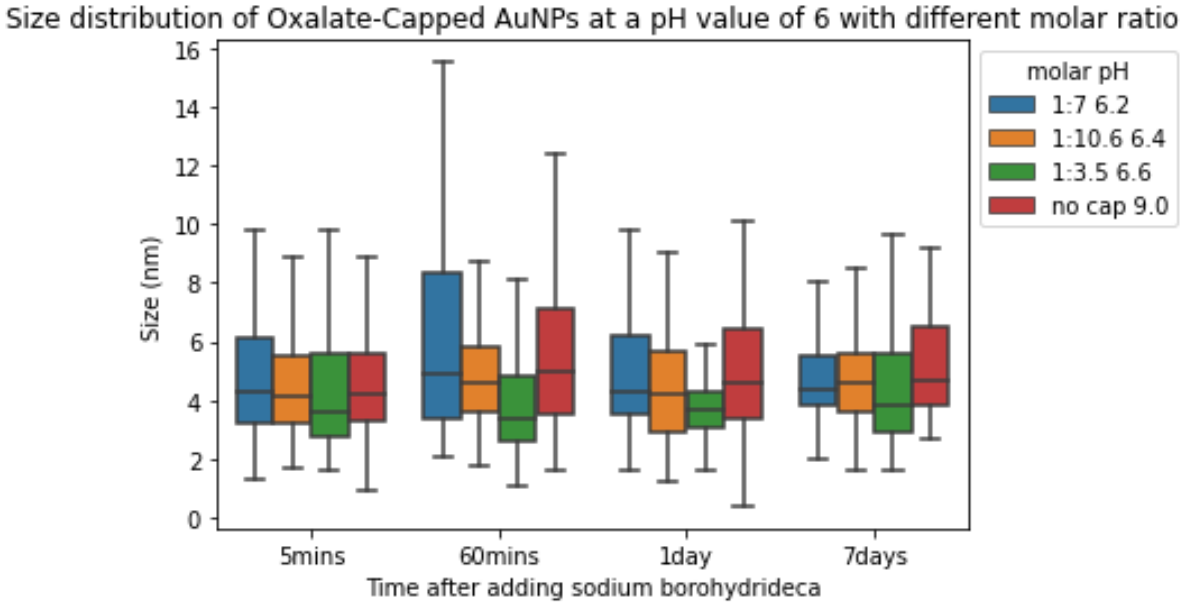


Figure 4. 32. Different molar ratio of oxalate capped AuNPs with pH 6 and aging time. The size distribution is represented using a box-and-whisker plot. The box in the plot represents the interquartile range, indicating the spread of the dataset. The whiskers extend from the box to show the rest of the distribution, excluding outliers.

Next, we will be investigating the effect of pH and molar ratio of the typically used citrate as a capping agent when synthesizing AuNPs.

4.11 Comparing pH 6 citrate molar ratio difference

The size of AuNPs synthesized using citrate as a capping agent, under more neutral pH conditions, falls within the same range as oxalate-capped AuNPs. NPs synthesized under these parameters generally maintain their size over a 7-day period.

The growth of AuNPs using citrate as a capping agent exhibits a stable trend during the 7-day period in Figure 4.33. However, the polydispersity of the NPs appears to be influenced by the molar ratio of citrate. Lower molar ratio (1 to 3.5) shows a better AuNPs polydispersity, while a higher molar ratio (1 to 7, 1 to 10.5) displays a wider size range.

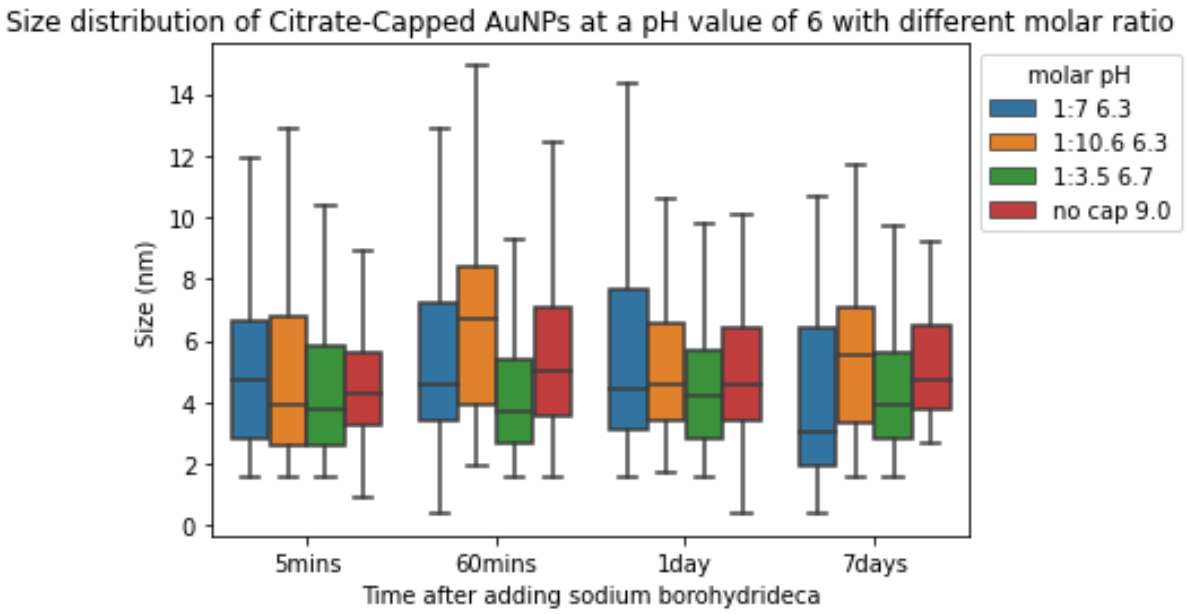


Figure 4. 33. Different molar ratio of citrate capped AuNPs with pH 6 and aging time. The size distribution is represented using a box-and-whisker plot. The box in the plot represents the interquartile range, indicating the spread of the dataset. The whiskers extend from the box to show the rest of the distribution, excluding outliers.

Having demonstrated the effects of molar ratio and pH on NP growth with different capping agents, the next section will explore the impact of the number of carboxyl groups in the capping agent under various molar ratios and pH conditions.

4.12.1 Comparing 1:1 molar ratio at low pH carboxyl capping agent

Here in Figure 4.34, we compared the effect of the number of carboxyl groups in the capping agent on the size of AuNPs in a low pH and low molar ratio environment. At pH 3 and a 1:1 molar ratio, all capping agents includes acetate(5 nm to 40 nm), oxalate (5 nm to 10 nm), and citrate (2.5 nm to 5 nm) showed an increase in size over the 7-day period.

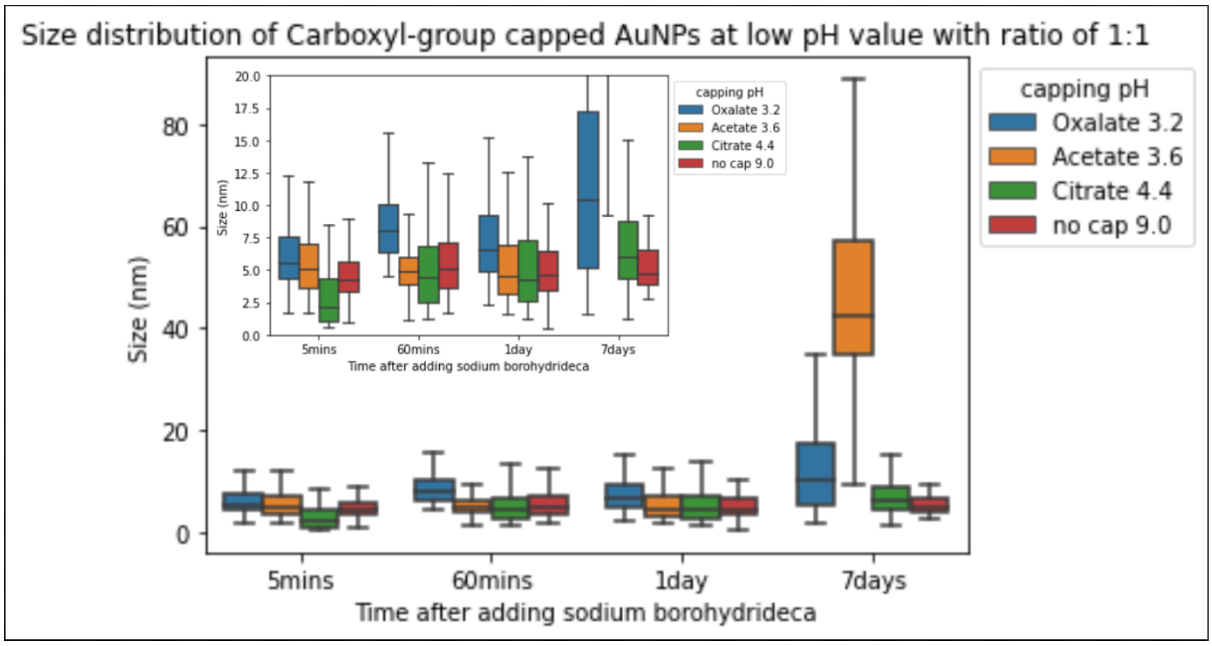


Figure 4. 34. Size distribution of 1:1 molar ratio of carboxyl group capped AuNPs with low pH and aging time. The size distribution is represented using a box-and-whisker plot. The box in the plot represents the interquartile range, indicating the spread of the dataset. The whiskers extend from the box to show the rest of the distribution, excluding outliers.

Acetate, with a single carboxyl group, proved ineffective in stopping NP growth during this period. Its limited capability to capture only one free gold atom per

molecule results in insufficient surface coverage, allowing growth to proceed and leading to larger NPs after 7 days.

Oxalate, with two carboxyl groups, also exhibited AuNPs growth but at a slower rate (5 nm to 10 nm) compared to acetate-capped AuNPs (5 nm to 40nm) under similar conditions. The additional carboxyl group allows oxalate to capture two free gold atoms, providing better surface coverage and reducing the probability of growth.

Citrate, with three carboxyl groups, showed the slowest growth rate among the capping agents tested. Its ability to bind three free gold atoms per molecule and occupy more surface area on the AuNPs results in a stable surface configuration that inhibits further growth. However, due to the lower molar ratio of citrate to gold, AuNPs still grew at a slower pace compared to acetate and oxalate under similar pH conditions.

Surprisingly, AuNPs synthesized without any capping agent did not exhibit uncontrolled growth as expected at this smaller size range. Figure 4.34 shows that the size of uncapped AuNPs remained like that of carboxyl-capped AuNPs. This raises questions about the role of capping agents and the mechanisms governing NP growth, which we will discuss in the next chapter.

4.12.2 Comparing 1:1.5 molar ratio at low pH carboxyl capping agent

In Figure 4.35, we investigated the growth rate of AuNPs using different carboxyl group capping agents in a low pH environment at a 1 to 1.5 molar ratio. AuNPs synthesized with higher concentrations of capping agent exhibited greater stability and mono-dispersity.

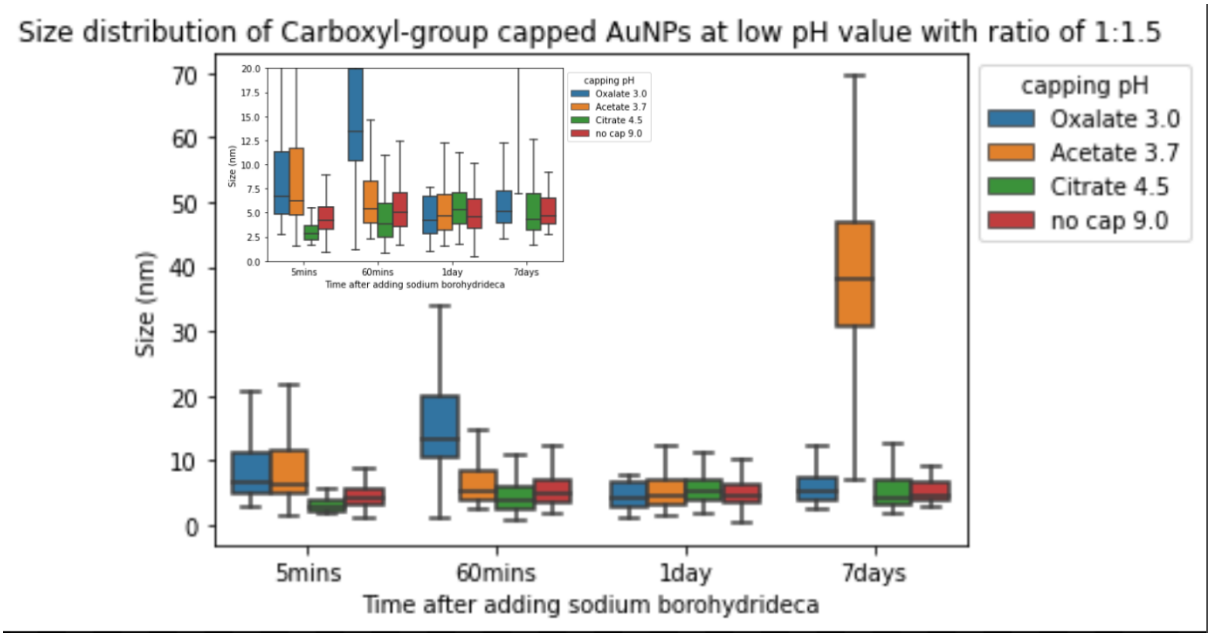


Figure 4. 35. Size distribution of 1:1.5 molar ratio of carboxyl group capped AuNPs with low pH and aging time. The size distribution is represented using a box-and-whisker plot. The box in the plot represents the interquartile range, indicating the spread of the dataset. The whiskers extend from the box to show the rest of the distribution, excluding outliers.

Both acetate and oxalate capped AuNPs at low pH and a 1:1.5 molar ratio showed growth over the 7-day period because neither acetate nor oxalate at low molar ratio provided sufficient surface coverage to fully prevent further NP growth.

In contrast, citrate also demonstrated growth under these conditions but at a slower rate compared to acetate and oxalate. It is likely that this is due to citrate's larger size, which allows for more effective surface coverage, reducing the availability of free gold atoms for particle growth. Citrate's ability to bind not only one but potentially two or three gold atoms per molecule contributes to a more monodisperse and stable NP size.

4.12.3 Comparing 1:3.5 molar ratio at pH 6 carboxyl capping agent

Here in Figure 4.36, we compared the size and dispersity of AuNPs synthesized using different carboxyl group capping agents at pH 6 and a 1:3.5 molar ratio.

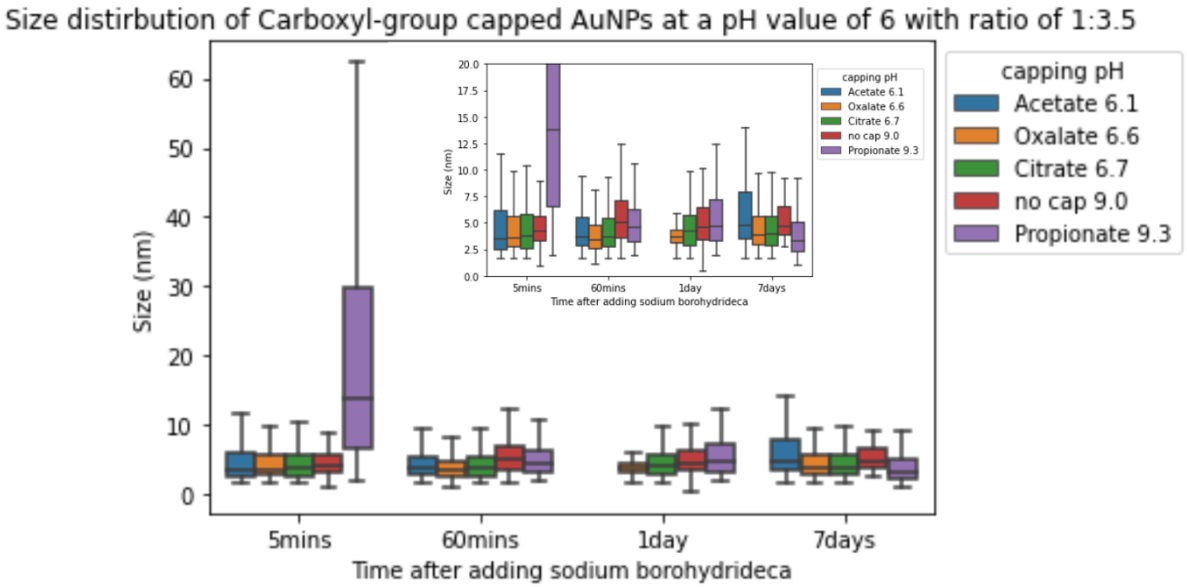


Figure 4. 36. Size distribution of 1:3.5 molar ratio of carboxyl group capped AuNPs with pH 6 and aging time. The size distribution is represented using a box-and-whisker plot. The box in the plot represents the interquartile range, indicating the spread of the dataset. The whiskers extend from the box to show the rest of the distribution, excluding outliers.

At higher molar ratios and a more neutral pH, acetate-capped AuNPs initially exhibit similar size and polydispersity to those capped with other carboxyl group agents on the first day. However, acetate-capped AuNPs show increased polydispersity by the 7-day mark compared to the others.

Oxalate, citrate, and propionic acid-capped AuNPs all exhibit similar polydispersity and size profiles, except for propionic acid-capped AuNPs at the 5-minute mark, which initially showed agglomeration. However, they stabilized after 1 day and maintained consistent size and dispersity throughout the observation period.

4.12.4 Comparing 1:7 molar ratio at pH 6 carboxyl capping agent

At neutral pH and higher molar ratios, the size of AuNPs capped with various carboxyl group capping agents becomes very similar. The influence of the number of carboxyl groups in the capping agent starts to diminish. For instance, as seen in Figures 4.34-4.38, the growth of acetate-capped AuNPs and oxalate-capped AuNPs is significantly faster than that of citrate-capped AuNPs at lower molar ratios. However, this difference diminishes as the molar ratio of the capping agent exceeds 1:3.5.

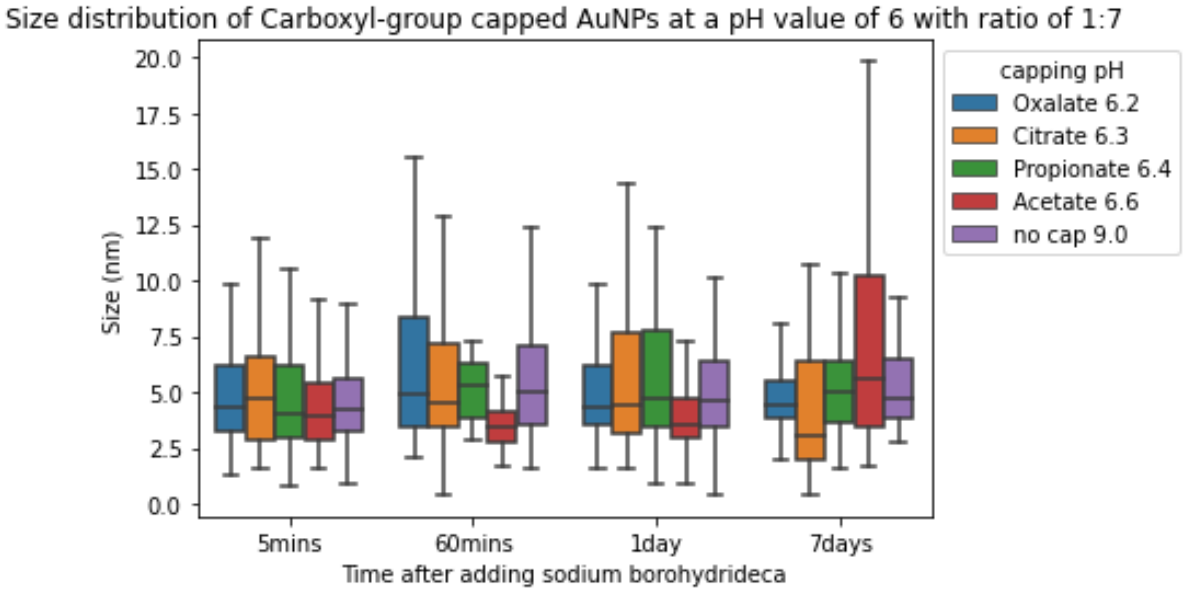


Figure 4. 37 1:7 molar ratio of carboxyl group capped AuNPs with pH 6 and aging time. 1The size distribution is represented using a box-and-whisker plot. The box in the plot represents the interquartile range, indicating the spread of the dataset. The whiskers extend from the box to show the rest of the distribution, excluding outliers.

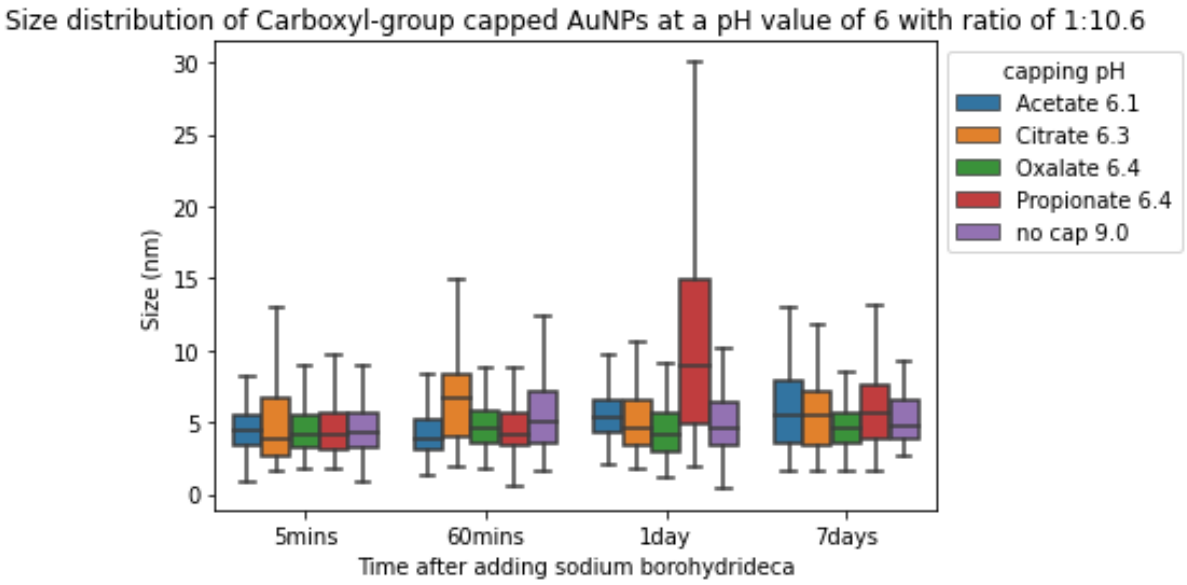


Figure 4. 38 1:10.6 molar ratio of carboxyl group capped AuNPs with pH 6 and aging time. The size distribution is represented using a box-and-whisker plot. The box in the plot represents the interquartile range, indicating the spread of the dataset. The whiskers extend from the box to show the rest of the distribution, excluding outliers.

Interestingly, increasing the amount of capping agent in the solution does not lead to smaller NPs. This highlights the need for further investigation into the role of the capping agent and how it influences the protection of NPs from further growth.

4.13.1 Comparing acetate and propionic acid 1:7 and 1:10.6 at pH 6

Here in Figure 4.39, we compared the effect of capping agent size, with both propionic acid and acetate having the same number of carboxyl groups, pH, and molar ratio. Propionic acid is larger with three carbons in its molecule, while acetate has only two.

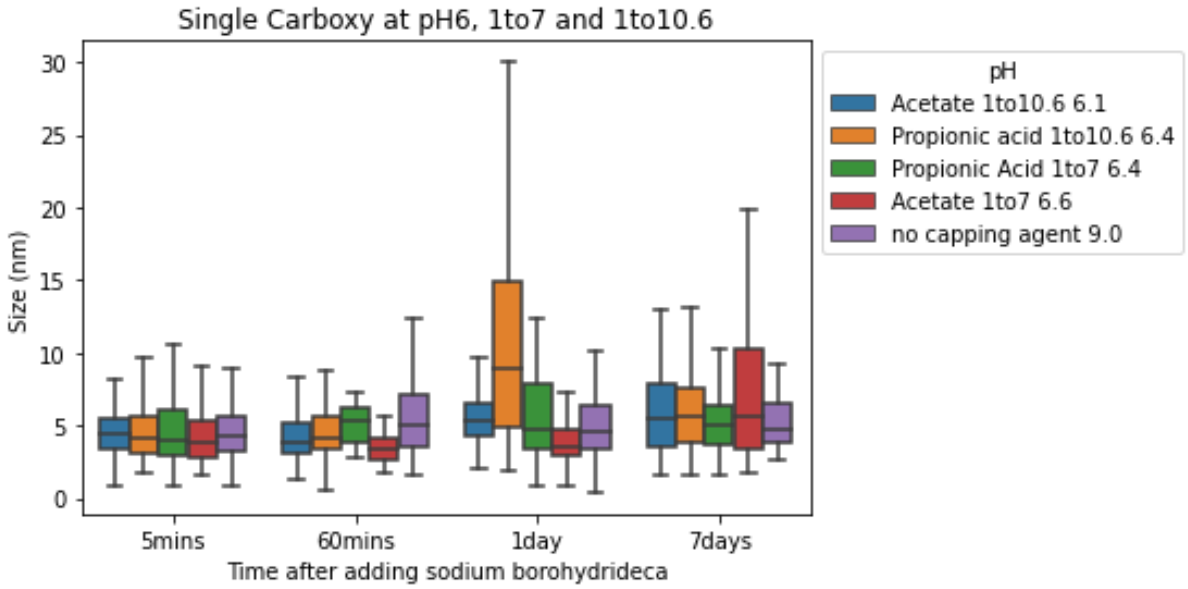


Figure 4. 39. 1:7 and 1:10.6 molar ratio of acetate and propionic acid capped AuNPs with pH 6 and aging time. The size distribution is represented using a box-and-whisker plot. The box in the plot represents the interquartile range, indicating the spread of the dataset. The whiskers extend from the box to show the rest of the distribution, excluding outliers.

In terms of polydispersity, both acetate-capped AuNPs at 1:7 and 1:10.6 molar ratios showed an increase during the 7-day period. Propionic acid-capped AuNPs exhibited similar polydispersity over the 7-day period for both 1:7 and 1:10.6 molar ratios.

Furthermore, acetate-capped AuNPs showed higher polydispersity than propionic acid-capped AuNPs at the 7-day mark with a 1:7 molar ratio. However, at a 1:10.6 molar ratio, polydispersity remained unchanged for both propionic acid and acetate-capped AuNPs.

4.14 Contamination

The energy-dispersive X-ray spectroscopy (EDS) analysis shown in Figure 4.40, indicating the detection of only Au and Cu as the main elements in the core and shell regions of the STEM images above, suggests that there is no evidence of contamination within the solution. This reinforces the idea that the observed structures are primarily composed of AuNPs and their PNCs, without the presence of additional foreign elements.

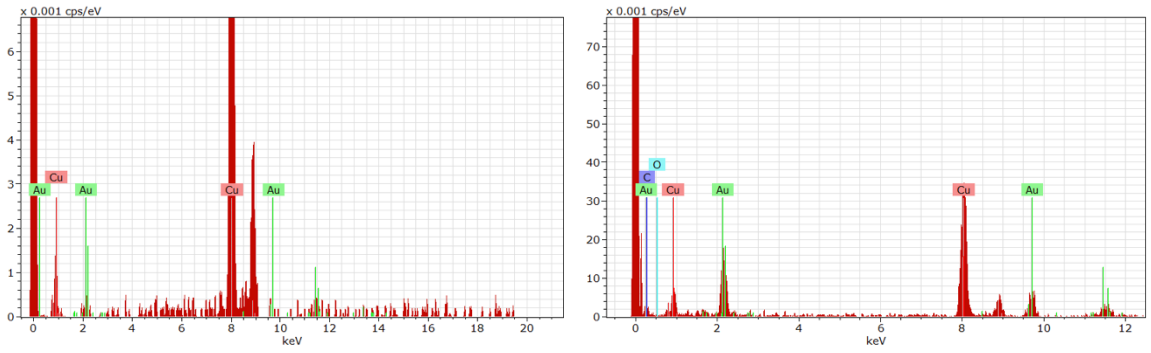


Figure 4. 40 EDS of Core-shell motif. From left to right, Core, and shell EDS from Figure 4. 13 respectively.

4.15 Effect of pH

At pH 6, the speciation of both citrate and chloroauric acid is expected to be optimized for synthesizing AuNPs as indicated by Kettemann et al. (Kettemann et al., 2016). While pH 6 does yield the best size distribution in terms of dispersity compared to other synthesis methods, a lot of the synthesized AuNPs in this experiment still show signs of particle-to-particle adhesiveness and bridging, which eventually lead to the formation of nanowire structures as observed in the STEM images. The possibility of citrate etching adatoms from the surface of AuNPs (Grys et al., 2020) can accelerate the aging process. The presence of terminal carboxylate groups on citrate, which consistently bind with 1 or 2 gold atoms (Monti et al., 2017) on the surface, could provide an explanation for the observed shell formation in previous STEM images.

4.16 Relationship between PNCs and growth kinetics (aging)

In classical nucleation theory and DLVO theory, gold precursors must undergo reduction to Au^0 to initiate nucleation and allow for the growth of AuNPs. This reduction step relies on a supersaturation of Au^0, which triggers nucleation. The size of the resulting particles can be controlled by adjusting the number of nucleation seeds and the nucleation rate (Mozaffari et al., 2017). This theory is well-established and supported by experimental evidence (Chen et al., 2015).

In contrast, non-classical nucleation theory provides an alternative pathway for the formation and growth of metal NPs in chemical reduction synthesis (Leffler et al., 2021, Russo and Tanaka, 2016, Lee et al., 2016, Sahu et al., 2022). According to this theory, PNCs can form before full nucleation occurs (Yildirim et al., 2023) enabling growth from these non-zero-valent atom clusters to larger structures, such as dimers (Ramamoorthy et al., 2020), which is a pair of adatoms.

This implies that nucleation does not always proceed in the discrete steps described by classical nucleation theory. Instead, nucleation and growth may be continuous, with PNCs playing a critical role in shaping the growth kinetics and final morphology of the NPs, which we will discuss in the next chapter.

If PNCs are indeed crucial in governing NP development, it is essential to understand how they interact with one another in solution and how they influence the growth kinetics when interacting with a crystalline NP. In this experiment, PNCs were observed in numerous STEM images (indicated by orange arrows). The persistence of PNCs in the solution, observed up to 7 days, suggests they are stabilized by molecules in their surroundings.

The said PNCs were observed in a lot of the STEM images described previously and marked with orange arrows. The PNCs exist in the solution as an intermediate stage of growth mechanics and the PNCs were stabilized by molecules in the solution because the existence of PNCs was observed up to 7 days in the solution.

The coexistence of PNCs and crystalline NPs can lead to unpredictable morphologies, as the NPs evolve continuously rather than in discrete stages. As seen in supplementary circularity plots, the synthesized NPs in this system are not perfectly spherical, demonstrating the aging process and morphological changes over time. This unpredictable shape evolution (aging) can affect the final NPs' properties, with potential implications for both their functionality and potential toxicity.

4.17 Role of capping agent, reduction mechanics and growth prediction

In the experiments described in this chapter, a rapid reduction method using sodium borohydride as a strong reducing agent was used. Sodium borohydride quickly reduces the gold precursor to Au^0, theoretically initiating nucleation following classical nucleation theory. However, unlike the traditional Turkevich method, which involves boiling, this method does not involve elevated temperature. The absence of boiling may be a critical factor in preventing the formation of small, spherical NPs.

In the Turkevich method, the boiling step typically lasts around 20 minutes. During this period, the elevated temperature enables citrate to act as a weak reducing agent, gradually reducing the gold precursor to Au^0. Pong and colleague (Pong et al., 2007)found that nanowires or gel-like structures exists at the early stage of Turkevich boiling parts, however these structures generally disappear as boiling

continues (Pong et al., 2007), and the additional thermal energy aids in forming thermodynamically stable spherical NPs, usually around 20 nm in size. This larger, spherical morphology results from the increased kinetic energy, which facilitates atomic rearrangements toward a stable, lower-energy configuration.

In contrast, the method used in this experiment, which skips the boiling step, may lack sufficient thermal energy to guide the NPs toward spherical stability. This could explain why the synthesized NPs exhibit irregular shapes and a less predictable morphology, particularly at the smaller sizes targeted in this study. The absence of sustained thermal energy may allow PNCs or fused NPs to persist, preventing the formation of more stable, spherical NPs seen in the Turkevich method (Pong et al., 2007).

4.18 Surface coverage

Traditionally, it is assumed that capping agents like citrate are meant to fully cover the surface of particles and establish an electrical double layer to prevent aggregations. However, this assumption only holds true when citrate provides optimal coverage on the surface. In fact, citrate coverage can be suboptimal (Perfilieva et al., 2019), resulting in a crown-like structure. This type of citrate coverage exposes certain facets on the surface of AuNPs, providing landing sites for additional citrate molecules to enhance coverage or induce aging if they fuse with other particles or capture free adatoms through Ostwald ripening. When

comparing the synthesis method employed in this paper to the Turkevich method, it is observed that smaller-sized AuNPs are more challenging to be fully covered by citrate due to steric hindrance .

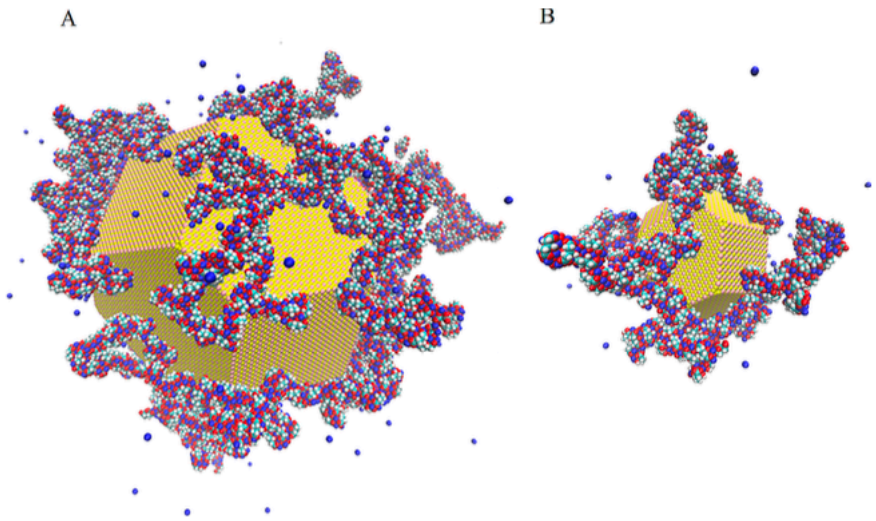


Figure 4. 41. Citrate crown formation on AuNPs of size A) 14nm and B) 6nm (Perfilieva et al., 2019).

4.19 Circularity discussion for carboxyl group

In theory, more spherical NPs should have lower surface energy, making them more stable. However, in this experiment, the irregular structures observed (e.g. Figure 4.20c) show that the particles aged anisotropically and unpredictably. This deviation from spherical morphology is likely due to the role of PNCs in the nucleation and growth processes.

During the growth of NPs, the PNCs can have a size sometimes up to 4 nm and can adhere to the surface of the growing crystalline NPs. This results in surface diffusion from the PNCs, effectively covering the NPs surface. As a result, the NPs can lose their distinct solid facets. In this state, the surface energy of the NPs becomes much more complex and harder to predict. This complexity is influenced by the type of ligand or capping agent present in the solution.

The interaction of PNCs with the capping agent, such as the number of carboxyl or functional groups, adds an additional layer of unpredictability. For example, capping agents with more carboxyl groups can form stronger or more complex interactions with the NP surface. This alters the surface energy and promotes anisotropic growth, as opposed to a predictable, uniform epitaxial growth.

For instance, when a free gold atom adheres to an icosahedral facet, it will favour growth in a symmetric manner, as all facets are energetically favourable. However, when a PNC adheres to the same facet, the morphology changes, disrupting the uniform growth process and leading to more irregular shapes. This mechanism explains why different capping agents, or even the absence of a capping agent, result in varying nanoparticle sizes and shapes, favouring unpredictable, anisotropic growth over the more predictable growth seen in classical nucleation pathways.

4.20 Conclusion

In conclusion, this study utilized sodium borohydride as a strong reducing agent to synthesize sub-10 nm AuNPs and examined the effects of key factors such as pH, molar ratio of capping agent to gold, the number of carboxyl groups in the capping agent, and the size of the capping agent on the growth of the AuNPs. Notably, the study found that increasing the molar ratio of capping agent to gold did not lead to the formation of smaller AuNPs, challenging conventional expectations.

Among the different pH levels tested, pH 6 demonstrated the best dispersity, making it the most stable condition for synthesizing AuNPs. At low pH and low molar ratios of capping agent to gold, acetate and oxalate were less effective at controlling particle size after nucleation compared to citrate and the absence of a capping agent. However, as the molar ratio of capping agents increased, the size discrepancy between AuNPs synthesized with capping agents containing fewer carboxyl groups diminished.

PNCs were observed in nearly all the solutions studied, and their role in nucleation and growth remains a subject requiring further investigation. The study suggests that PNCs may function either as an intermediate stage in the nucleation process or as basic building blocks for subsequent growth. This could lead to the unpredictable morphology of AuNPs. Furthermore, the persistence of PNCs in the solution for up to 7 days indicates their metastable state, which could prolong the processes of nucleation, growth, or aging. Additional research is needed to fully

understand the growth mechanisms involving PNCs and their influence on the final nanoparticle properties.

4.21 Future work

It would be interesting to explore the aging effect of other capping agents like thiol group and study the existence of PNCs. For instance, compounds such as cysteine and glutathione, which possess one thiol group. This could provide further insights into the formation of PNCs and the aging effect on NPs. Further investigation should also be conducted to examine the role of Na+ concentration, considering that both Na and Cl ions have been found to induce undesired aggregation leading to coral-like structures (Zhang et al., 2014). However, Na+ ions also contribute to the

Chapter 5: The properties of prenucleation clusters (PNCs) and the interaction with thiol and carboxyl group capped gold nanoparticles

5.1 Introduction

This chapter aims to study the nucleation stage of AuNPs in the presence of thiol group ligand capping agents namely L-cysteine (Cys) and glutathione (GSH) by using a fast-reducing method with NaBH4. I will also compare with carboxyl-functionalised particles from the previous chapter. Finally, I will attempt to combine all result to develop a model for PNC formation. By gaining a better understanding of the kinetics and formation of PNCs, this chapter seeks to provide deeper insights into nucleation theory and the mechanisms of growth in AuNP synthesis.

5.2 Experiment

The carboxyl group-capped AuNPs were synthesized in the previous chapter. In this chapter, Cys and GSH are used as thiol capping agents to investigate the relationship between ligand mechanisms and the formation of PNCs. For both

Cys and GSH, the molar ratio was maintained at 1:3.5 to compare the influence of thiol and carboxyl groups as well as the effect of ligand size on synthesis under the same reference conditions used in the previous chapter. The pH for Cys was adjusted to 7.5 and 8.4, while the pH for GSH was controlled at 8 (Table 5.1).

During synthesis, Cys solutions gradually changed colour from pink to purple and then to red over a period of 60 minutes. In contrast, GSH solutions remained clear after the addition of NaBH4 and slowly developed a brown colour over time.

Table 5. 1 List of experiments using thiol as capping agent.

pH	Capping agent to gold molar ratio	38.8mM capping agent [mL]	1M NaOH [mL]
7.5	L-Cysteine 3.5	1	0.006
8.4	L-Cysteine 3.5	1	0.007
8.0	GSH 3.5	1	0.01

Additional synthesis using the same protocol with Ag were also conducted as listed in table 5.2. This experiment will serve as a simple comparison for the AuNP nucleation and growth using an alternative element.

Table 5. 2 List of experiments of AgNPs.

pH	Capping agent to gold molar ratio	38.8mM capping agent [mL]	1M NaOH [mL]
6.3	0	0	0
6.9	Citric acid 3.5	1	0

5.3 Aging of different thiol molecule capped AuNPs

This section presents the synthesized AuNPs capped with different thiol molecules at various time intervals (5 minutes, 60 minutes, 1 day, and 7 days) after the addition of sodium borohydride, using the same methodology as described in the previous chapter on carboxyl-capped AuNPs. The results will begin with L-cysteine-capped AuNPs at pH 7.5 and a molar ratio of 1:3.5, followed by pH 7.4, and then glutathione-capped AuNPs at pH 8.0 and a molar ratio of 1:3.5. The objective is to observe differences in size and morphology in the presence of these alternative ligands using HAADF-STEM imaging.

5.3.1 Aging of L-cysteine capped AuNPs in pH 7.5 at molar ratio of 1:3.5

This section presents the results of Cys-capped AuNPs at pH 7.5 with a molar ratio of 1:3.5. Figure 5.1 shows the HAADF-STEM images of Cys-capped AuNPs at 5 minutes, 60 minutes, 1 day, and 7 days. Although the AuNPs primarily shows agglomeration, no significant aggregation or coalescence is observed. Features such as "sticky" behaviour, bridging, and shell motifs commonly found in carboxyl group capped AuNPs are absent in the thiol group capped AuNPs. These motifs will be discussed later in this chapter.

Regarding size and circularity changes over time, there are no significant differences between the images taken at 5 minutes and 7 days.

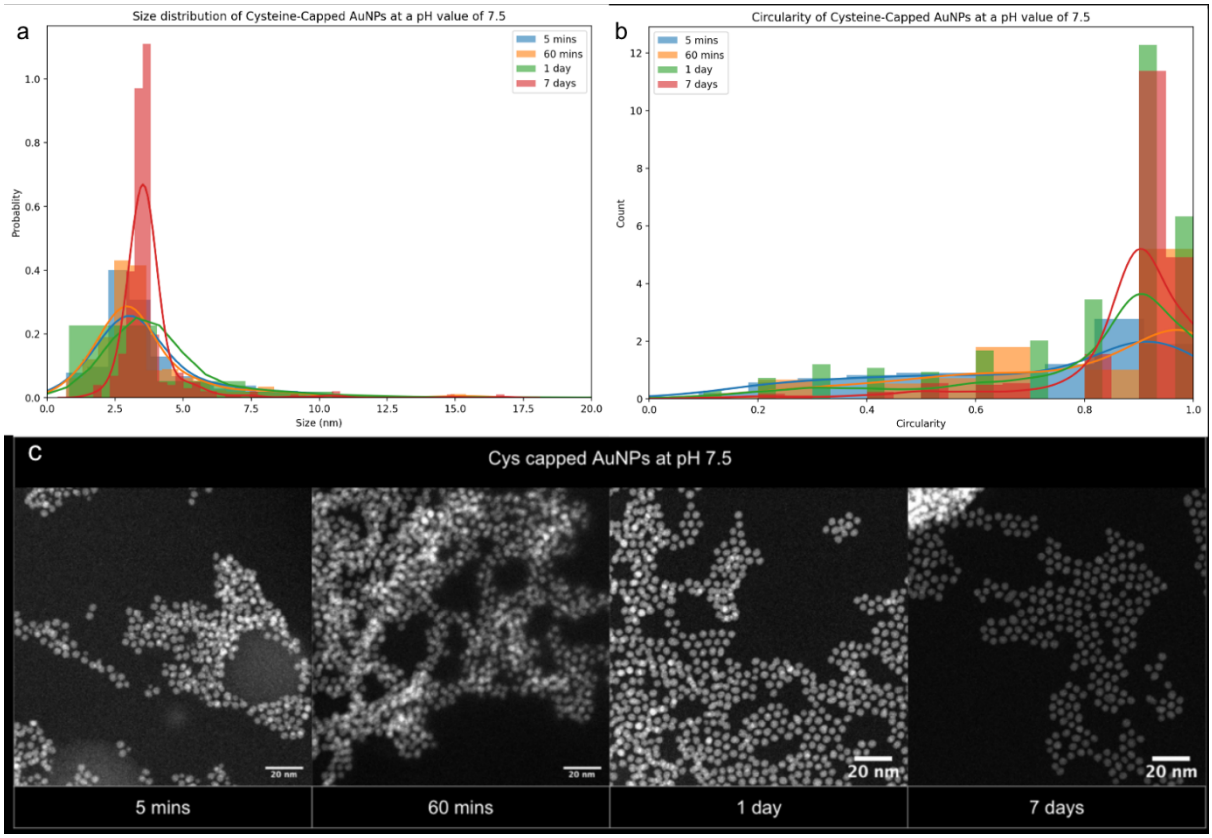


Figure 5. 1. a) top left plot shows the size distribution of L-cysteine capped AuNPs at pH 7.5 with molar ratio 1:3.5. b) top right plot shows the circularity. c) bottom

STEM images of samples collected at different time points, after the start of the experiment: 5 minutes, 60 minutes, 1 day and 7 days.

5.3.2 Aging of L-cysteine capped AuNPs in pH 8.4 at molar ratio of 1:3.5

Similar to the behaviour of Cys-capped AuNPs at pH 7.5, Cys -capped AuNPs at pH 8.4 with the same molar ratio of 1:3.5 also exhibit comparable characteristics, as shown in Figure 5.2. At the 5-minute mark, all AuNPs remain agglomerated. However, by 60 minutes, “blurry clusters” assumed to be PNCs appear around the crystallized AuNPs (same sample also at Figure 5.12). The NPs eventually aggregate and merge after 7 days with the absent of the “blurry clusters”. The possible causes of the entities observed around the crystallized AuNPs at the 60-minute mark will be discussed later in this chapter.

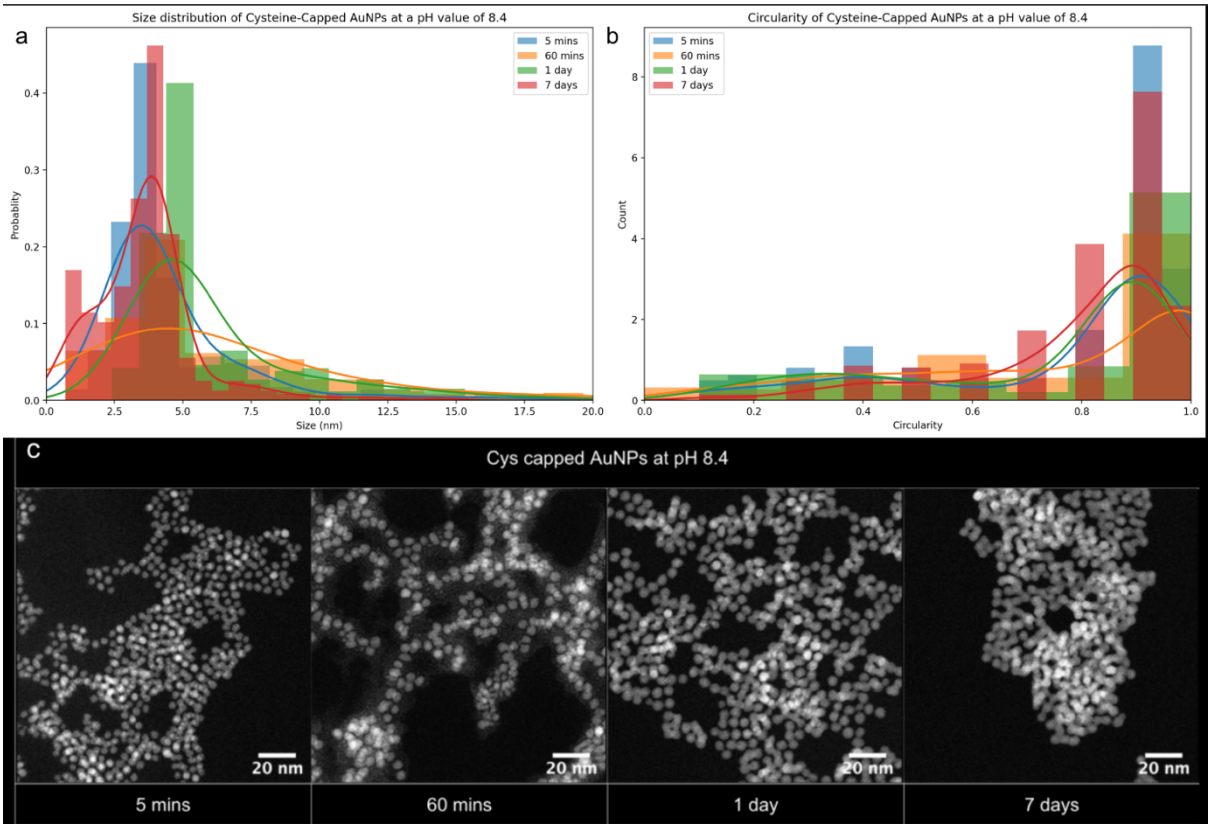


Figure 5. 2. a) top left plot shows the size distribution of L-cysteine capped AuNPs at pH 8.4 with molar ratio 1:3.5. b) top right plot shows the circularity. c) bottom STEM images of samples collected at different time points, after the start of the experiment: 5 minutes, 60 minutes, 1 day and 7 days.

5.3.3 Aging of glutathione capped AuNPs in pH 8.0 at molar ratio of 1:3.5

At the 5-minute and 60-minute marks, AuNPs are visible (2 nm observed at 60 minutes), and crystallized structures are observed, indicating that the clusters can nucleate and grow. However, after 60 minutes, the AuNPs disappear, as observed

in subsequent samples (up to 28 days, shown in Appendix Figure A.2.1 and Figure A.2.2). Instead, numerous single Au atoms are observed. These single Au atoms appear in a patterned structure, as shown in the 1-day image in Figure 5.3. As this synthesis is repeated multiple times with the result of all AuNPs eventually disappeared after 1 day, it is believed that the AuNPs capped with this ligand dissolved.

Although the TEM grid used is not a Holey carbon grid, this patterned structure is observed on a standard copper-carbon TEM grid. The formation of this structure requires further investigation but is assumed to be related to the ligand used in this synthesis as a metal-organic self-assembly structure (Yoneya et al., 2015).

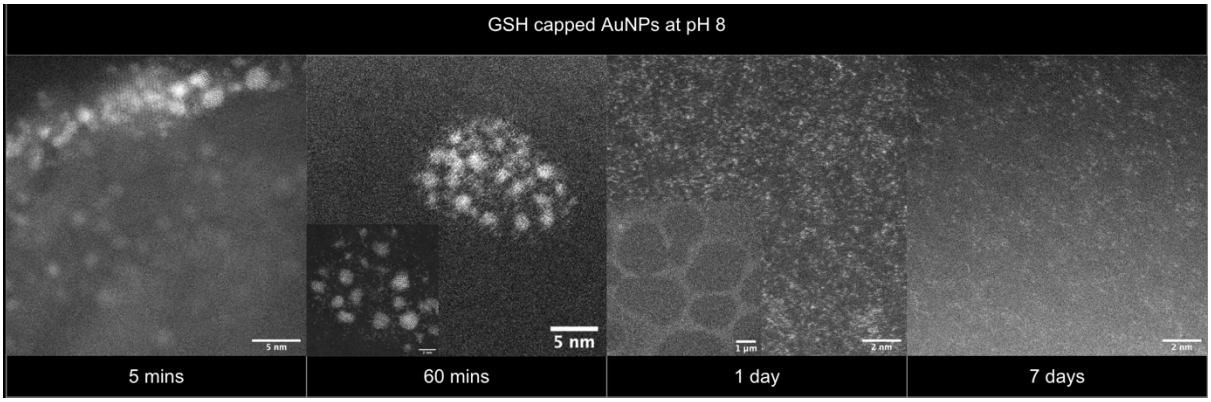


Figure 5. 3 Glutathione capped AuNPs at pH 8 with molar ratio 1:3.5. STEM images of samples collected at different time points, after the start of the experiment: 5 minutes, 60 minutes, 1 day and 7 days.

5.4 Aging of uncapped and citrate capped AgNPs

In this section, silver nanoparticles (AgNPs) without a capping agent and those capped with citrate are presented. AgNPs were chosen because silver belongs to the same group as gold in the periodic table and is also a widely studied material for nanoparticles. Although the synthesis protocol was not optimized for AgNPs, I intentionally made minimal adjustments to the protocol to observe differences when the same method is applied to a different transition metal. Consequently, the AgNPs synthesized in this study are not suitable for providing quantitative data on size and circularity.

5.4.1 Aging of no capped AgNPs in pH 6.3

Here, uncapped AgNPs synthesized at pH 6.3 were imaged using HAADF-STEM. In all samples, entities with weaker intensity were observed. These entities consistently appear near crystallized AgNPs and are assumed to be PNCs, similar to those observed in some of the synthesis experiments involving AuNPs. The morphology of these entities will be discussed later in this chapter.

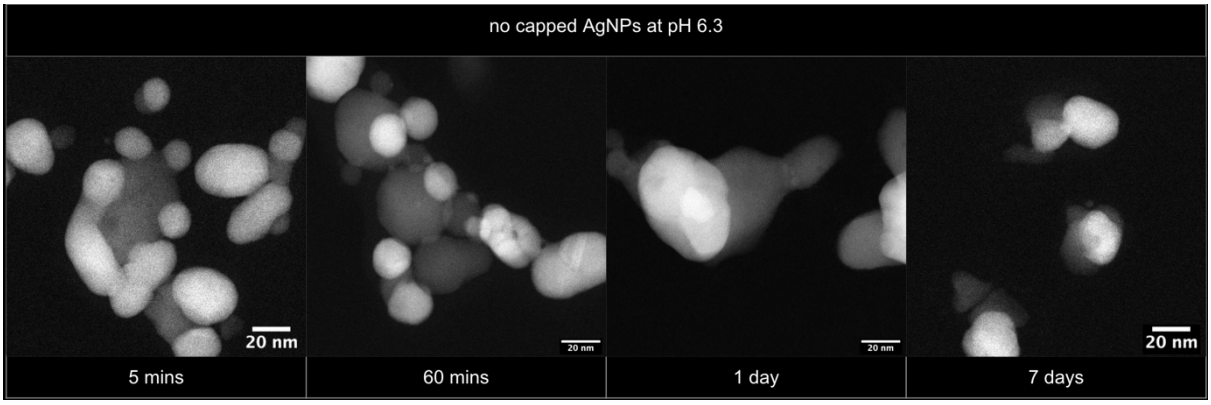


Figure 5. 4 AgNPs with no capping agent added at pH 6.3. STEM images of samples collected at different time points, after the start of the experiment: 5 minutes, 60 minutes, 1 day and 7 days.

5.4.2 Aging of citric acid capped AgNPs in pH 6.9 at molar ratio of 1:3.5

Citric acid-capped AgNPs synthesized at pH 6.9 with a molar ratio of 1:3.5 were also analysed. Entities with weaker intensity were observed in all samples, appearing around crystallized AgNPs. In the 7-day sample, AgNPs were found surrounding another entity with a line structure inside. This formation was also observed in some carboxyl-group-capped AuNPs and will be discussed later in this chapter. The origin of this structure is assumed to be influenced by the ligand used in the synthesis. However, further investigation is required to confirm its formation and determine its role.

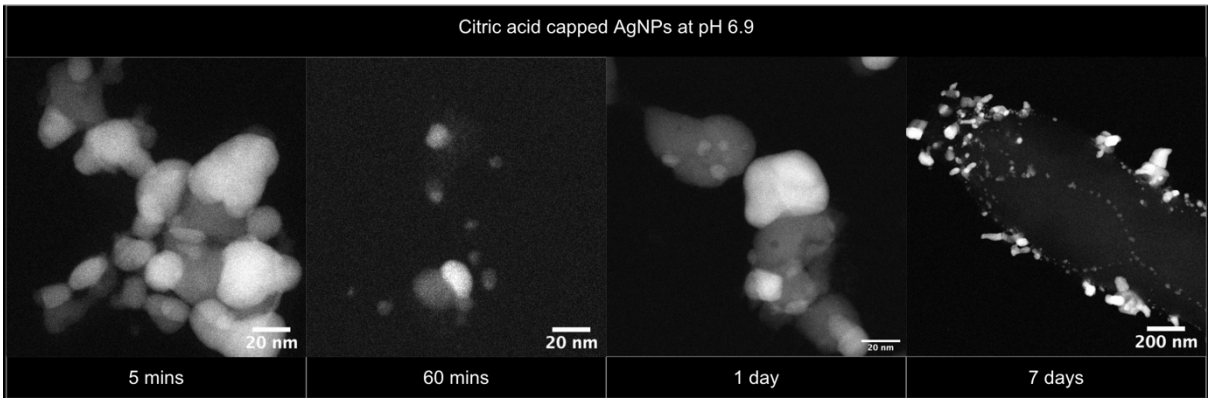


Figure 5. 5 Citric acid capped AgNPs at pH 6.9 with molar ratio of 1:3.5. STEM images of samples collected at different time points, after the start of the experiment: 5 minutes, 60 minutes, 1 day and 7 days.

5.5 Result summary

Sections 5.3 and 5.4 presented HAADF-STEM images of synthesized AuNPs, capped with thiol group bearing ligands and AgNPs with no capping agent or citric acid capping. The purpose of these additional experiments was to compare the effectiveness of an alternative capping molecule, thiol, on AuNPs, as well as that of the synthesis methodology to a closely related to Au chemical element, Ag. Additionally, to use all the information to develop an understanding of the role on PNCs. The results suggest that the formation of nanoparticles and the structures near the crystallized nanoparticles are closely related to the size and shape transformations of the nanoparticles. The formation and interaction of PNCs will be discussed in the next section, with a focus on understanding their role, kinetics, and influence on morphological transformations over time (aging).

5.6 Properties of PNCs under STEM imaging

According to the Gibbs free energy plot in classical nucleation theory, there is a critical radius that governs the stability of particles. However, with the existence of pre-nucleation clusters (PNCs), it becomes essential to determine the size of PNCs to modify the Gibbs free energy curve. The Gibbs free energy indicates the particle size at which stability can be achieved, represented as a trough in the energy plot. However, the exact size range of this trough remains unknown. Additionally, multiple troughs may exist, corresponding to multiple energy minima influenced by the interaction of ligands during PNC formation. Therefore, it is important to investigate the location of the energy minima and identify whether multiple local minima exist by observing the size of PNCs.

To start, understanding the fundamental properties of PNCs such as their size and stability is critical for understanding their role in nanoparticle systems. The size of PNCs was found to range from approximately 1.2 nm (Figure 5.6a) to 5 nm (Figure 5.7b) with methods mentioned in chapter 3 section 3.5.2. PNCs were observed across all samples regardless of pH range or capping agent, with no apparent trend of disappearing over time as shown in Figure 5.6b, PNCs were detected in a sample that had been synthesized 28 days prior.

Since different size of PNCs exists and observed in multiple sample (Figure 5.6a and Figure 5.6b), It is hypothesized that the size of PNCs may vary significantly

and is likely determined by the metastable Gibbs free energy curve. Therefore, these PNCs are expected to remain in solution if they exist at an energy local minimum. This highlights the necessity of further investigation into the metastable states associated with PNCs to refine our understanding of nucleation and growth processes.

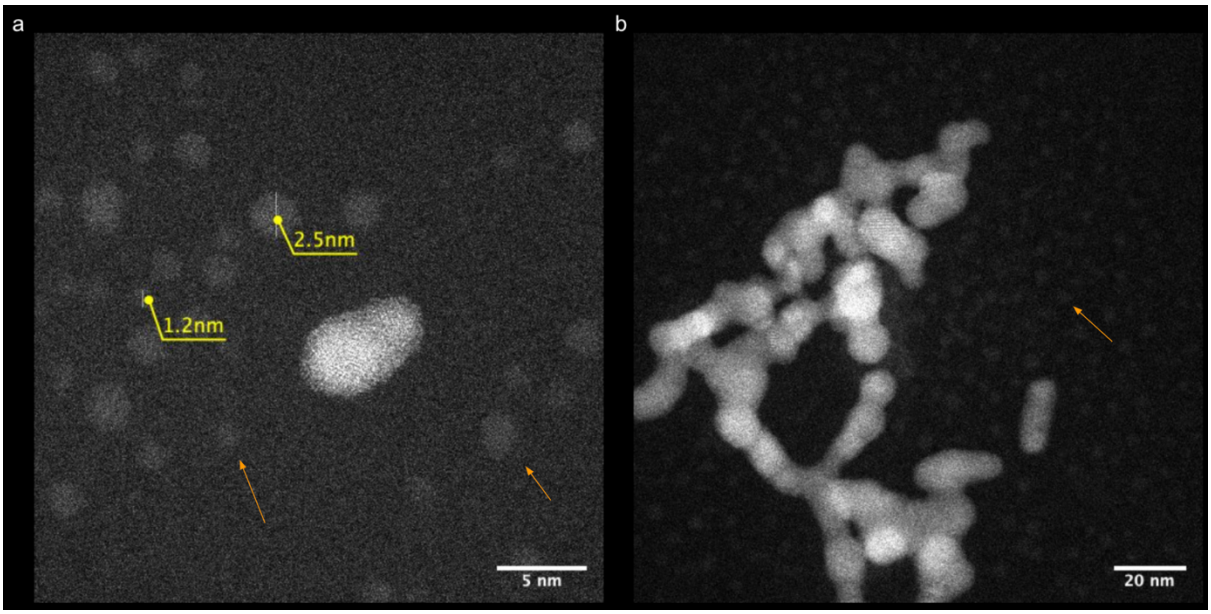


Figure 5. 6. a) PNCs with acetate capped AuNPs on pH 6.1 at 5 minutes with molar ratio 1:3.5. b) PNCs found inside citrate capped AuNPs on pH 6.7 28 days with molar ratio 1:3.5. Orange arrows indicate presumed pre-nucleation clusters.

Core-shell AuNPs were also observed. In Figure 5.7a, the central particle is a crystalline AuNP surrounded by a less dense structural layer. The distance between the surface of the core AuNP and the shell is measured to be approximately 1 nm, as shown in Figure 5.7b. This distance is significantly larger than the lattice constant of gold, which is 0.408 nm (Uddin, 2018).

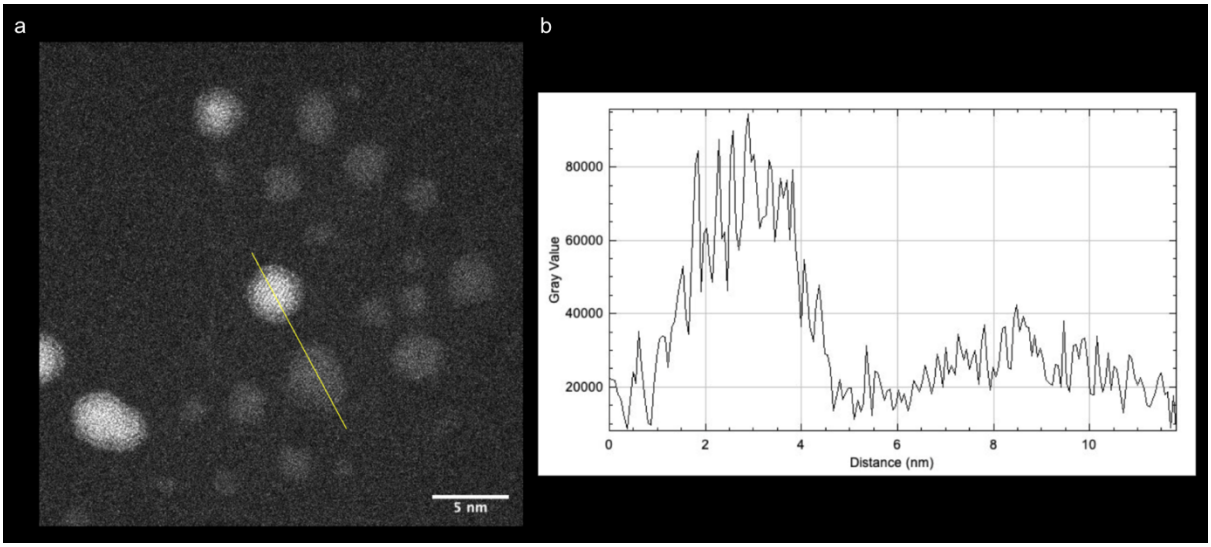


Figure 5. 7. a) STEM image of PNC with acetate capped AuNPs on pH 5.3 60 minutes. b) intensity vs distance along the yellow line indicator on the STEM image.

When comparing the intensity magnitude under STEM, the intensity of the shell is notably weaker than that of the core AuNP. In Figure 5.7b, the left intensity group corresponds to the central AuNP shown in Figure 5.7a. The surface of this AuNP is located at approximately 1.75 nm and 4.5 nm, as indicated by the intensity plot, while the shell motif is positioned at 0.75 nm and 5.5 nm, respectively. Figure 5.7b also provides an example of the intensity profile of a PNC. The size of this PNC was measured to be 5 nm, which exceeds the size of some crystallised AuNPs. The structure of the PNC remains amorphous and less dense, resulting in much weaker intensity compared to a crystalline AuNP.

5.7 Formation and structural dynamics of PNCs in liquid media

Having established the foundational properties of PNCs, we now examine their structural dynamics during formation in liquid media. Superlattices of PNCs were observed in some samples, suggesting that these assemblies of aligned PNCs could serve as precursors to the formation of fused particles strings.

Figure 5.8 highlights the superlattices of PNCs along with some crystalline AuNPs. The crystalline AuNPs in Figure 5.8b exhibit a core-shell motif, where a crystalline AuNP serves as the core, while amorphous PNCs form the shell. However, this is not the case of a not-yet fully crystallised shell. A not-yet fully crystallised shell should show as a very clear atoms on the surface of the AuNPs in this range of size. The adatom should be easily visible compared to what is observed here. The weak lattice structure visible in the bright field image indicates that the PNCs are beginning to crystallize, transitioning to a lower-energy state.

Line patterns, consisting of numerous PNCs and some crystalline AuNPs (distinguished by their intensity differences), were observed in acetate-capped AuNPs with a 1:10.6 molar ratio after one day (Figure 5.8c). Such line formations were observed in all carboxyl- and thiol-capped AuNP samples. For example, Figure 5.9a shows a relatively thin PNC line structure, while Figure 5.8c and Figure 5.8d display denser line formations.

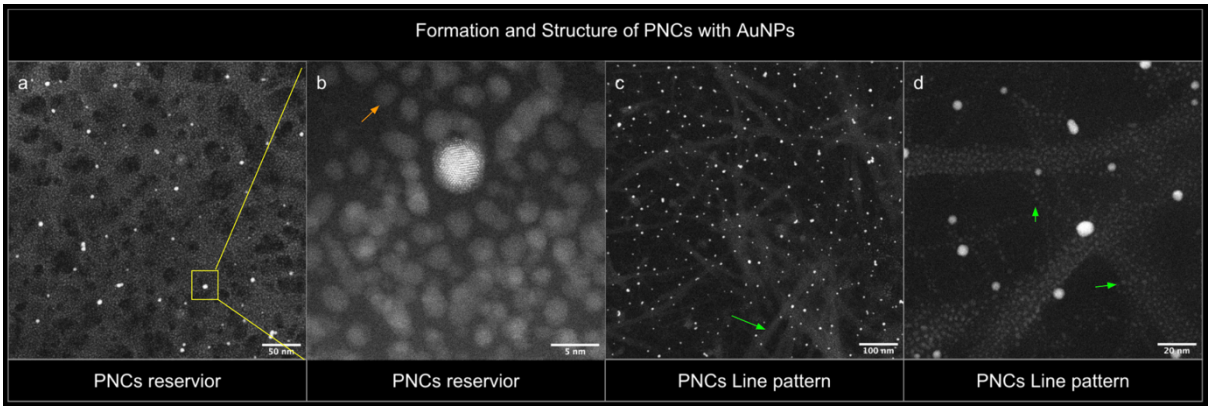


Figure 5. 8. STEM images of a) PNCs group and a crystalline AuNPs from acetate capped AuNPs on pH 6.1 with 1:10.6 molar ratio at 60 minutes. b) magnified image of the core-shell AuNPs PNCs of 5.8a. c) line pattern of PNCs with crystalline AuNPs from acetic capped AuNPs on pH 6.1 with molar ratio 1:10.6 at 1 day. d) magnified image of the line pattern on 5.8c. Orange arrows indicate presumed pre-nucleation clusters. Green arrows indicate PNCs in a line formation.

In Figure 5.9b, AuNPs surrounded by a PNC cloud align along the line pattern. Figure 5.9c illustrates a crystalline AuNP line structure, in which no PNCs remain visible in the solution. It is plausible to hypothesize that the PNCs in this sample have transformed into material supporting the crystalline AuNP formation. Additionally, Figure 5.9d reveals PNC clouds surrounding L-cysteine-capped AuNPs.

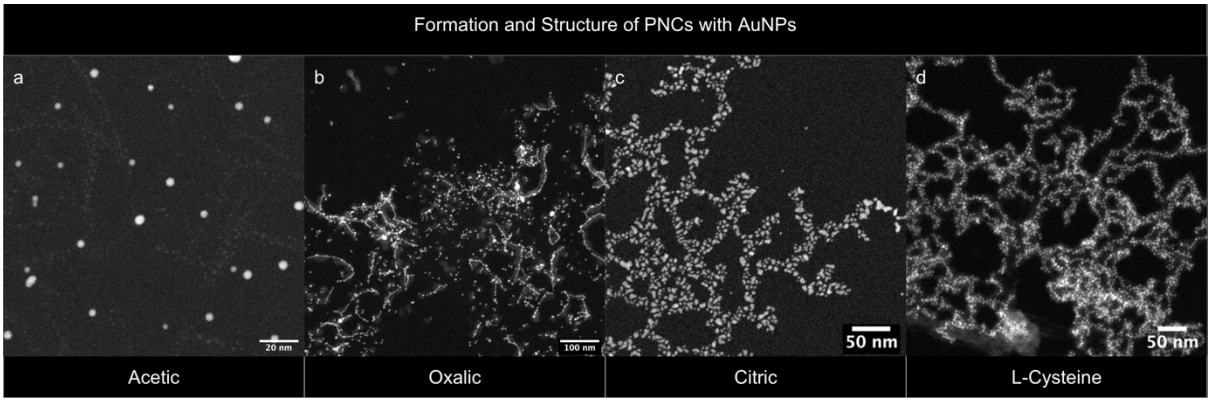


Figure 5. 9. STEM images of a) acetic capped AuNPs on pH 6.1 at 1 day with molar ratio 1:10.6. b) oxalic capped AuNPs with 1:1.5 on pH 3 at 7 days. c) citric capped AuNPs on pH 6.2 at 5 minutes. d) L-cysteine capped AuNPs on pH 8.4 at 60 minutes.

A comparison between Figures 5.8 and 5.9 shows variations in material density. Figure 5.9a demonstrates the lowest amount of material, while Figure 5.8a and Figure 5.8c reveal a significant reservoir of PNCs. The presence of excess PNC material could serve as a reservoir, potentially fuelling further growth or nucleation events.

5.8 Origins of PNCs around AuNPs and AgNPs

Beyond their formation, it is essential to investigate the origins of PNCs around AuNPs and AgNPs to better understand their role and how they influence growth mechanisms.

Figure 5.10 presents a high magnification image of the sample introduced in Figure 5.9b. Crystalline AuNPs along the observed line pattern are accompanied by a cloud of PNCs, as indicated by yellow arrows in Figures 5.10b. Figure 5.10c displays the Fast Fourier Transform (FFT) of the cloud structure highlighted by the yellow square in the top-right corner of Figure 5.10b. The lattice spacing measured at 0.23 nm corresponds to the gold (111) lattice structure (Nakamura et al., 2011), confirming that the cloud is composed of PNCs.

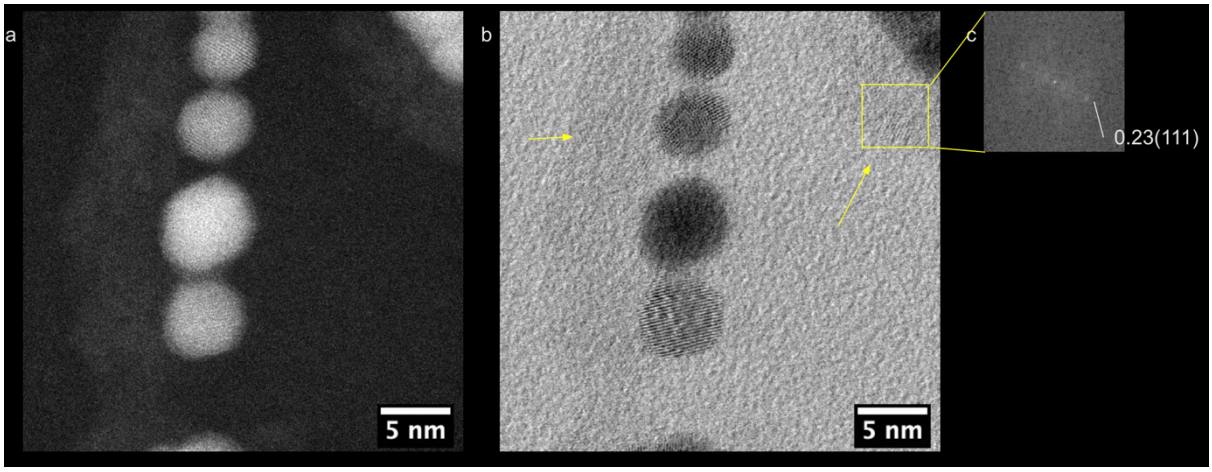


Figure 5. 10. STEM images of a) oxalic capped AuNPs with 1:1.5 pH 3 7 days. b) BF image of 5.10a with a yellow arrow indicates the cloud structure PNC. c) FFT of 5.10b cloud structure indicated by yellow square.

To better understand the origins of this cloud formation, a single AuNP with a cloud structure was isolated for further analysis. Figure 5.11a shows the AuNP highlighted by a yellow box in the bright-field (BF) image in Figure 5.11b. FFT analysis of this section identified lattice spacings of 0.23 nm and 0.20 nm, corresponding to the gold (111) and (200) planes, respectively. This confirms that the cloud structure surrounding the AuNP is indeed composed of PNCs, providing

further evidence that the clouds observed in Figures 5.8 and 5.9a–c are also PNCs. However, not all PNCs will show crystal lattices because some of them are still in amorphous state, which also observed in other liquid-cell TEM experiment (Dachraoui et al., 2021b).

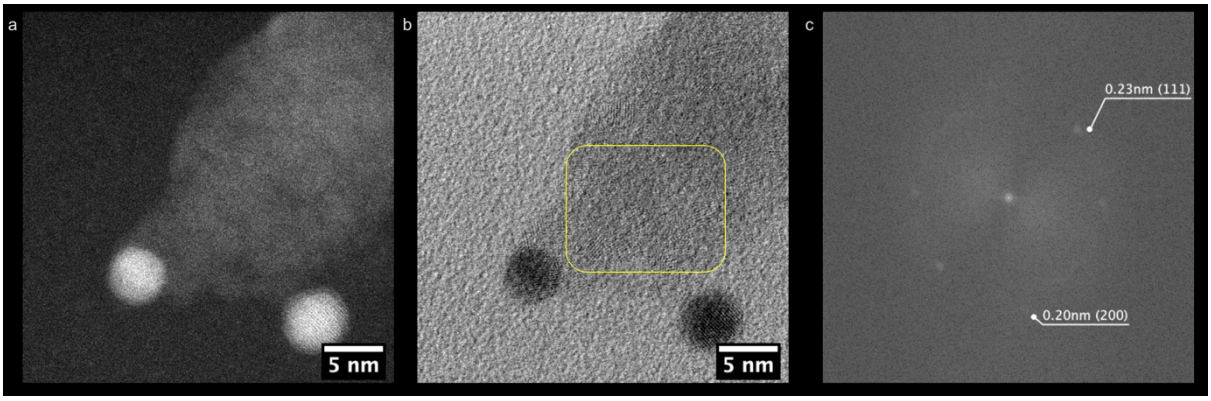


Figure 5. 11. STEM images of a) oxalic capped AuNPs with 1:1.5 at 7 days. b) BF image of 5.11a. c) FFT of 5.11b cloud structure indicated by yellow square.

As carboxyl group-capped AuNPs exhibited cloud structures assumed to be PNCs, it was equally important to investigate whether this phenomenon occurred with other capping agents. A similar PNC cloud was observed in a sample of L-cysteine-capped AuNPs (Figure 5.9d). In Figure 5.12, an amorphous structure is seen covering crystalline AuNPs, suggesting that the cloud formation mechanism is comparable to that in carboxyl group-capped AuNPs.

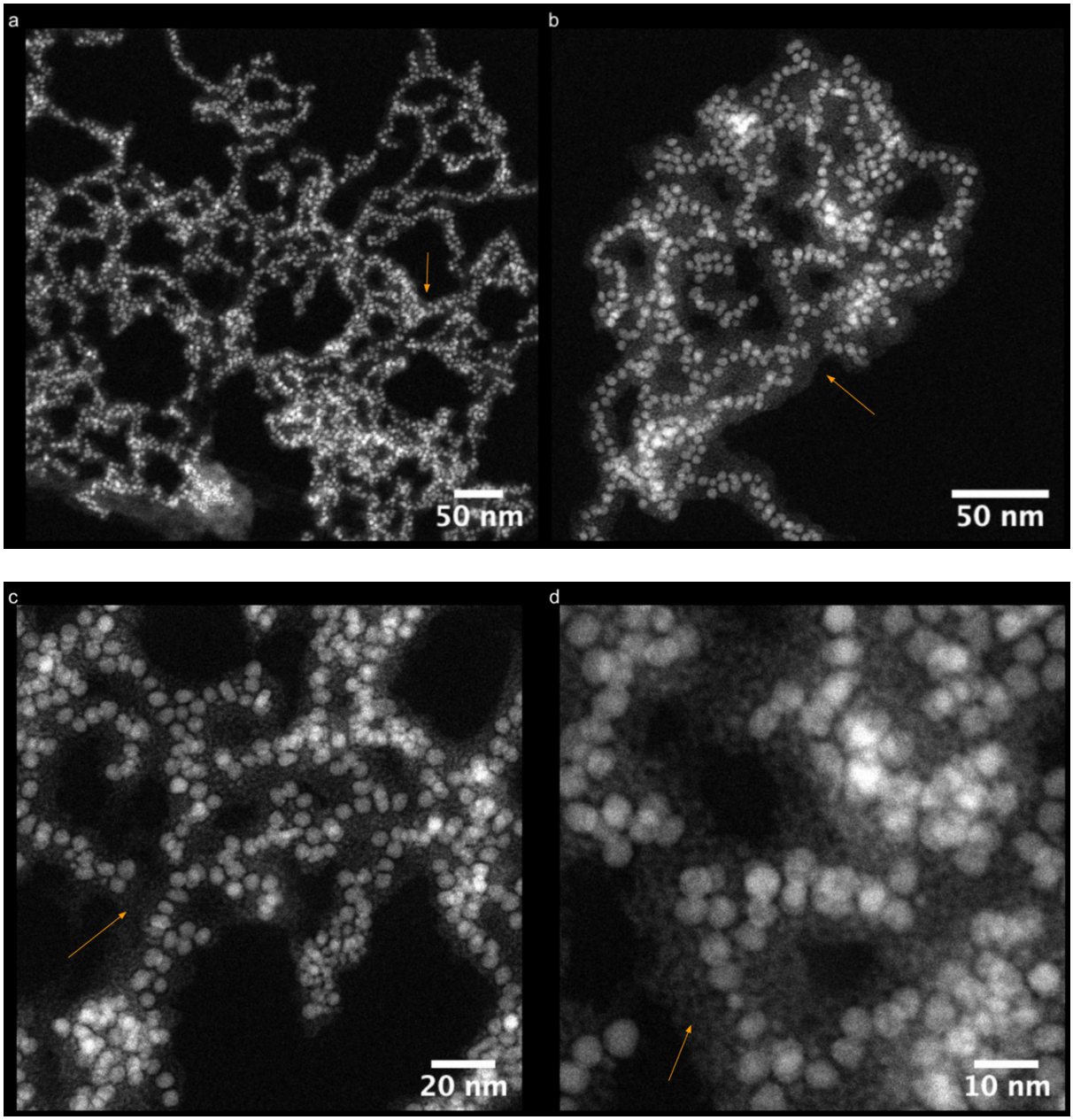


Figure 5. 12. Magnification of Figure 5.9d, L-cysteine capped AuNPs on pH 8.4 at 60 minutes, with PNCs cloud around the AuNPs core at magnification of a) x300k, b) x600k, c) x1M, d) x2M. Orange arrows indicate presumed pre-nucleation clusters.

However, the amorphous cloud structure in Figure 5.12 differs from the PNC clouds in Figure 5.11. For carboxyl group-capped AuNPs, the PNCs in the solution

appear blurry in imaging, indicating that the gold atoms are bonded with organic molecules such as ligands that exists in the solution (Gebauer et al., 2014). This results in an “blurry” appearance under STEM imaging , lacking sharp intensity peaks despite being composed of gold atoms (Dachraoui et al., 2021b).

In contrast, the L-cysteine-capped AuNPs in Figure 5.13c exhibit distinct intensity peaks under STEM imaging. This suggests that the gold atoms in these reservoirs are in a zero-valence state, remaining as a reservoir of gold atoms rather than nucleating to form crystalline AuNPs. These observations suggest that such reservoirs of gold atoms may act as PNCs, as seen in the carboxyl group-capped AuNPs (Figures 5.10 and 5.11) and GSH-capped AuNPs (Figure 5.14).

The PNCs appear spontaneously and are observed with every ligand. However, their appearance differs between ligand types. In carboxyl ligands, they exhibit a more amorphous structure under STEM, appearing as cluster-cloud. In contrast, PNCs in thiol ligands are observed as distinct intensity spikes, corresponding to gold atoms under STEM.

Figure 5.14a displays a similar cloud formation around crystalline AuNPs, identified by bright spots. However, Figure 5.14b reveals no crystalline structure in these bright spots. FFT of the yellow square in Figure 5.14b confirms a lattice spacing of 0.24 nm, consistent with the gold (111) plane. This indicates that the blurry features in Figure 5.14a and the fringes in Figure 5.14b are PNCs, suggesting that GSH-capped AuNPs exhibit cloud structures resembling those of carboxyl group-capped AuNPs.

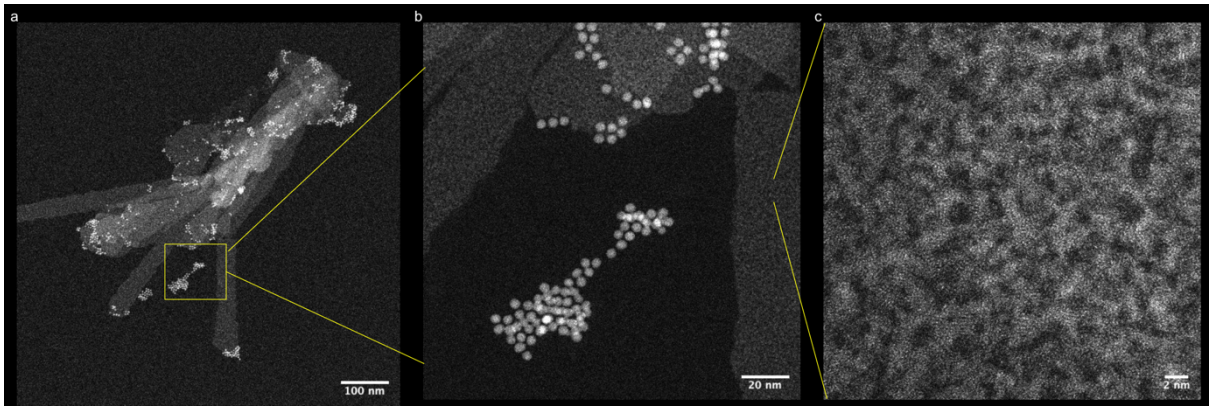


Figure 5. 13. STEM images of a) cysteine capped AuNPs with pH 8 at 1 day. b,c) are the magnified images of the yellow square section in 5.13a.

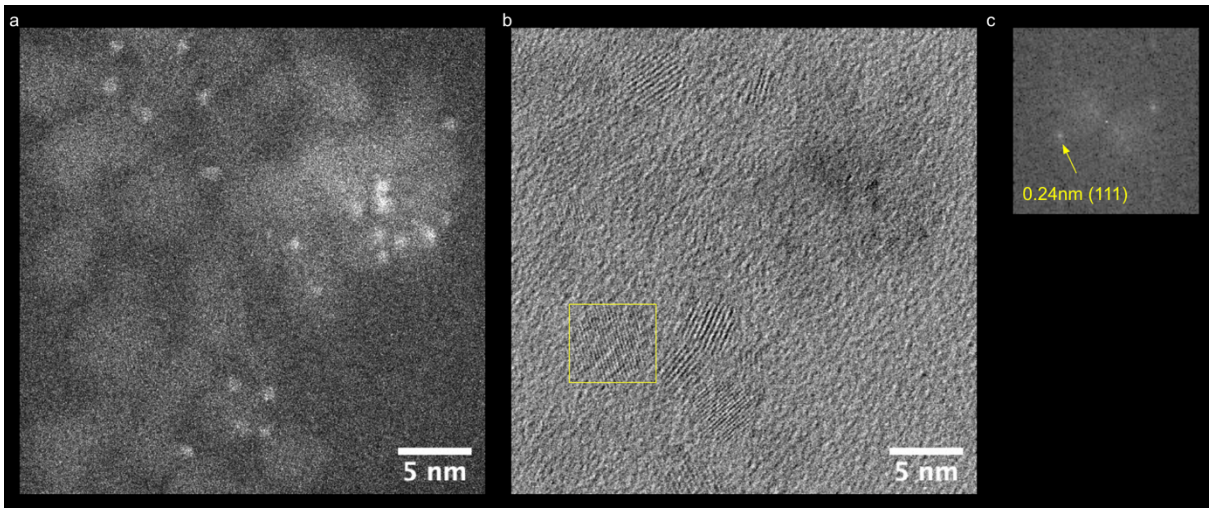


Figure 5. 14. STEM images of a) GSH capped AuNPs on pH 8 at 5 minutes. 5.14b, BF image of 5.14a. 5.14c, FFT of the yellow square section indicated in 5.14b.

PNCs are also of interest in the synthesis of AgNPs. As shown in Figure 5.15, PNCs were observed alongside crystalline AgNPs. Figure 5.15a identifies a crystallized AgNPs (#1) and AgPNCs (#2, #3, and #4). While AgPNCs #2 and #3 exhibit amorphous structures, AgPNCs #4 shows a crystalline lattice. Similar to

AuPNCs, AgPNCs display lower STEM intensity than crystallized AgNPs, indicating a lower density. This formation persisted after one day, as shown in Figure 5.16.

The lattice distance of AgPNCs #4 in Figure 5.15a was measured at 0.21 nm, corresponding to the Ag (200) lattice plane. FFT analysis in Figure 5.15d confirmed lattice spacings of 0.23 nm and 0.21 nm, corresponding to the Ag (111) and (200) planes, respectively.

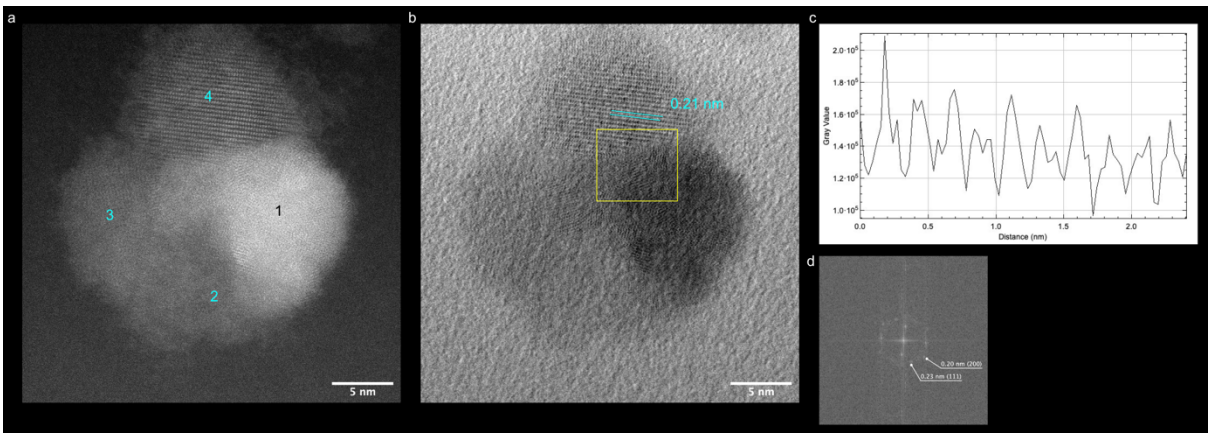


Figure 5. 15. Citric capped AgNPs on pH 6.9 at 60 minutes. a) DF images showing crystallized AgNPs indicated by number 1, amorphous AgPNCs indicated by blue number 2 and 3, PNCs showing lattice structure indicated by blue number 4. b) BF images of a. c) intensity plot of the lattice structure indicated by the blue line in 5.15b. d) FFT of the yellow square indicated in 5.15b.

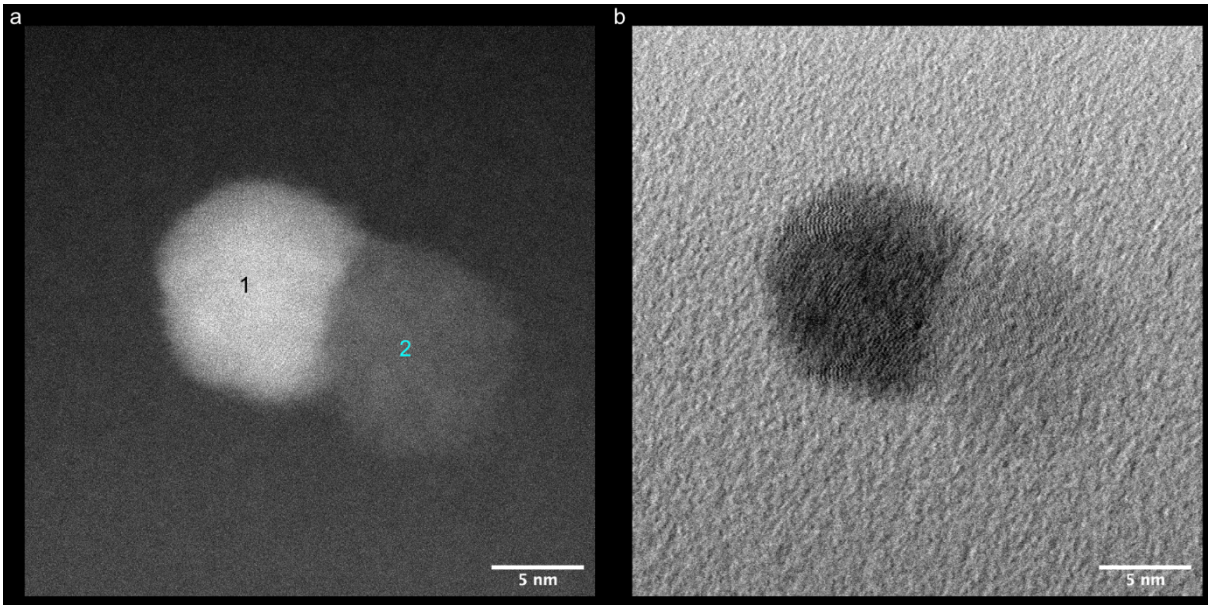


Figure 5. 16. a) citrate capped AgNPs on pH 6.9 at 1 day. Crystallized AgNPs were indicated by black number 1, AgPNCs were indicated by blue number 2. B) BF of image 5.16a.

5.9 Core crystalline AuNPs and shell PNCs

From the above samples, it is essential to investigate the formation of the shell motif around the core crystalline AuNPs. Understanding this phenomenon is critical for strengthening the fundamental knowledge of the nucleation process in nanoparticles (NPs) and other nanostructures. Here, the term "core-shell NPs" does not imply the presence of different elements within the nanoparticle. Instead, the "core" refers to the crystallized, higher-density region of the NP, while the "shell" refers to the surrounding pre-nucleation shell (PNSs), identified by their

lower-density structure. Thus, these core-shell NPs represent a hybrid of crystalline and amorphous material.

In classical nucleation theory, a precursor (e.g., $HAuCl_4$ or chloroauric acid) is reduced to its zero-valent form, Au(0). Due to local supersaturation, nucleation begins around a seed nucleus, initiating the growth process. This classical pathway, depicted on the bottom-left side of Figure 5.17, explains the formation of crystalline AuNPs under conditions where external factors do not interfere with the particle growth kinetics, such as in a vacuum or noble gas environment.

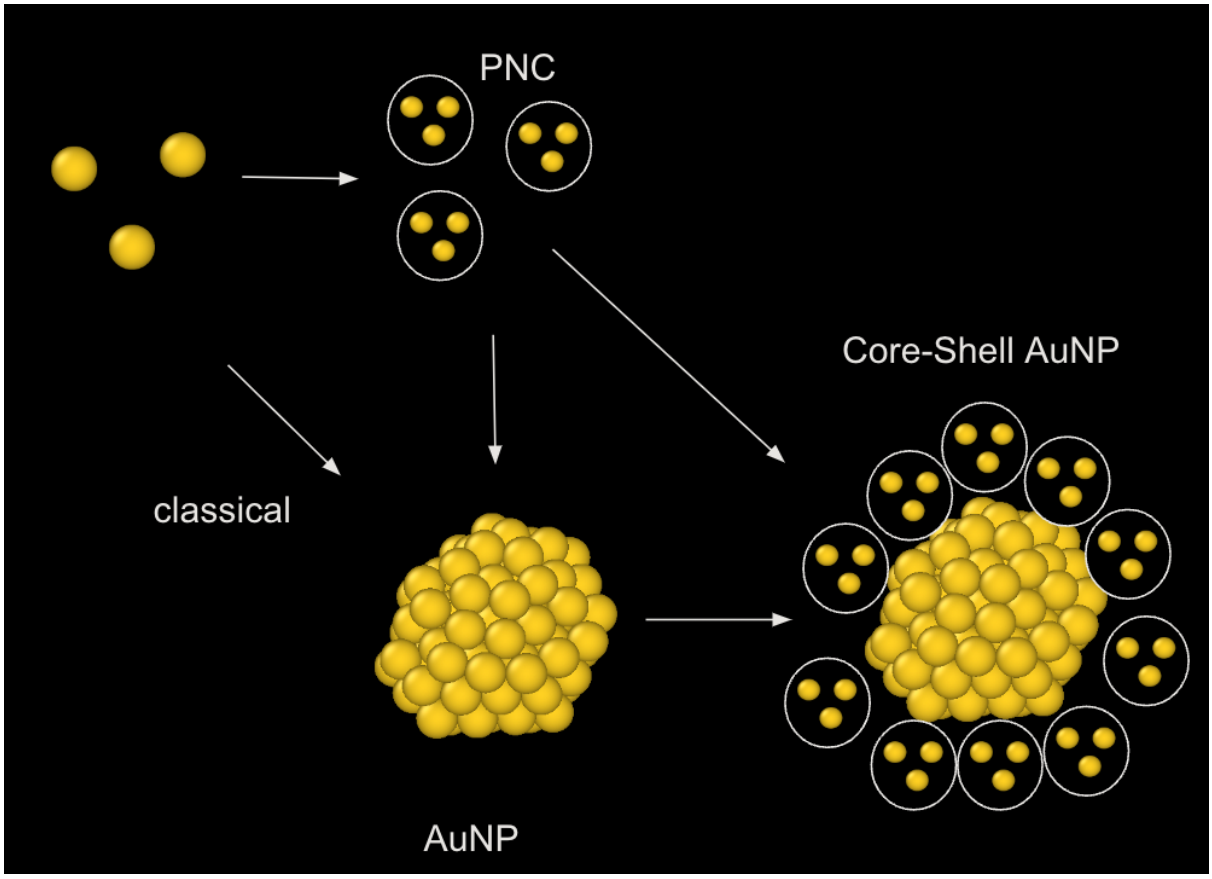


Figure 5. 17 Schematic of nucleation of classical path and non-classical nucleation path with PNCs and the formation of core shell AuNPs.

Alternatively, nucleation can proceed via a non-classical pathway, leading to the formation of PNCs. In this pathway, shown at the top of Figure 5.17, the precursor does not need to be fully reduced to Au(0). Instead, clusters of atoms form pre-nucleation regions that are subsequently reduced as a group to create crystalline nanoparticles.

For core-shell NPs, the process combines both pathways. Some of the precursor is reduced to Au(0), forming a crystalline AuNP core. Meanwhile, the remaining precursor remains as metastable PNCs, which adsorb onto the surface of the crystalline AuNPs. This adsorption minimizes surface area, stabilizing the particle and leading to the formation of a core-shell structure.

Core-shell motifs were observed during nucleation in several syntheses. Figure 5.18 highlights four AuNPs with significant differences in intensity between their core and shell regions, consistent with the density disparity between the crystalline core and the amorphous shell. These intermediate species are consistently accompanied by PNCs, as indicated by orange arrows in Figure 5.18. When the PNCs are not fully crystallized but are adsorbed onto the surface of an already crystallized AuNP, a core-shell structure is formed. This structure is evident in STEM images due to the intensity contrast between the dense core and the less dense surface region of the NPs.

5.10 Bridging of PNCs between AuNPs and AgNPs

The origins of PNCs also influence their interactions, including the formation of bridges between AuNPs and AgNPs, which will be explored further. During the formation of core-shell particles, if the PNCs come into proximity with other NPs, they can adsorb to the surfaces of multiple particles, as indicated by the green arrow in Figure 5.18. These bridges do not resemble typical crystallized NP aggregation, agglomeration, or coalescence. Instead, they result from the adsorption of multiple PNCs onto the surface of crystallized NPs. This helps explain the "stickiness" of the bridges and the abnormal surface density observed, as shown by the white arrow in Figure 5.18.

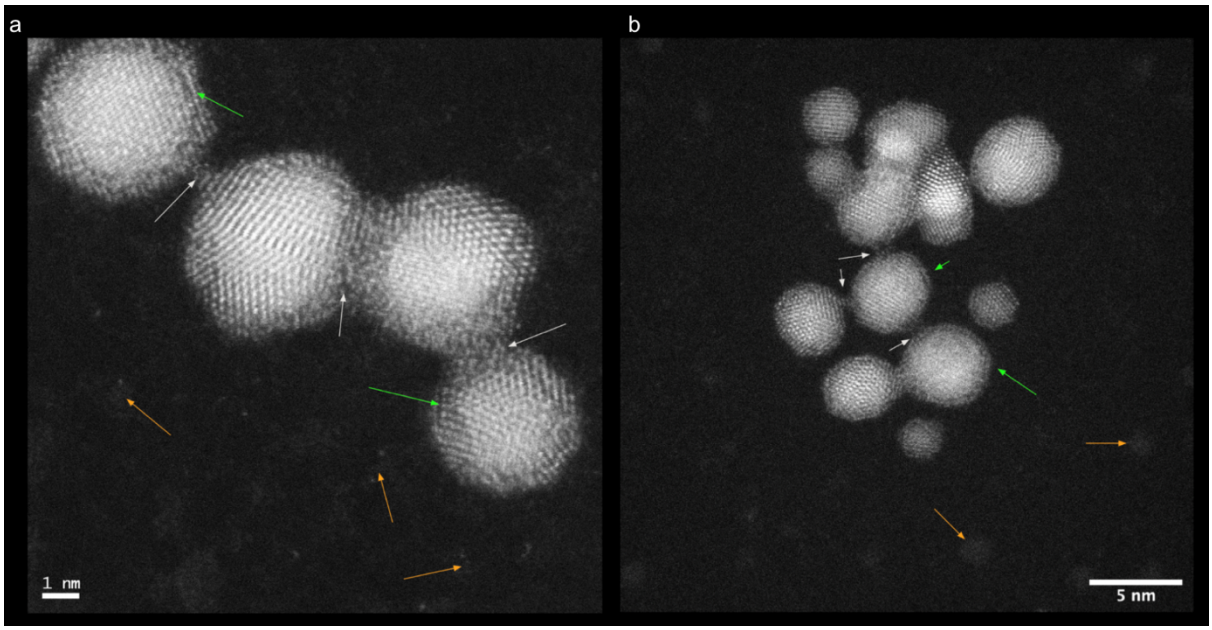


Figure 5. 18. STEM images of a,b) citrate capped AuNPs at pH 6.3 with 1:7 molar ratio at 5 minutes. White arrow indicates the bridges formation. Green arrow indicates shell motif. Orange arrow indicates PNCs.

This bridging phenomenon was also observed in the synthesis of AgNPs. Figure 5.19 shows a bridge structure connecting three crystallized AgNPs, marked as yellow numbers 1, 2, and 3 in Figure 5.19c, with the bridge structure highlighted by a blue arrow and square. The bridge structure in Figure 5.19c shows a crystallized lattice, while the bridges in Figure 5.18, indicated by the white arrow, display an amorphous structure. It is reasonable to assume that the bridge formation in AgNPs, as shown in Figure 5.19c, represents a later stage, where the amorphous structure is undergoing recrystallization into a lower-energy state by overcoming stacking fault energy. The lattice distance in the blue arrow section was measured to be 0.26 nm, which is larger than the crystal plane (111) of AgNPs (Chen et al., 2008).

This bridging formation can also act as a "glue". As the amorphous bridge structure crystallizes into a lattice, it merges the neighbouring NPs into a single nanostructure. Therefore, PNCs play a crucial role in shaping NPs into non-spherical forms with unpredictable morphologies. These interactions set the stage for subsequent transformations, such as the crystallization of PNCs, which leads to the development of solid nanoparticles.

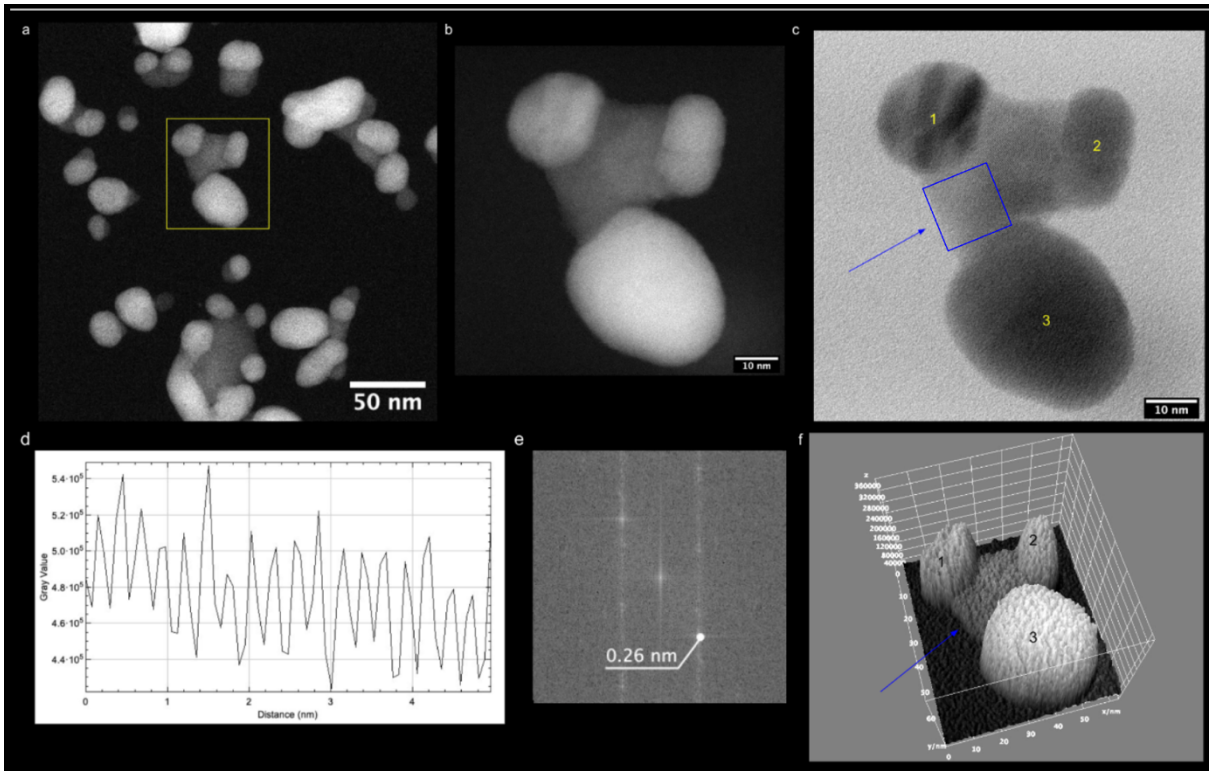


Figure 5. 19 STEM images of a) No capping agent of AgNPs with pH 6.3 at 5 minutes. b) magnified image of 5.19a yellow square section. c) BF image of 5.19b. d) is the intensity plot of the blue arrow indicated in 5.19c for calculating the lattice distance of the substance between AgNPs 1, 2, 3. e) FFT of the area indicated by blue arrow and square in 5.19c. 5.19f, the surface plot of the region indicated by yellow square in 5.19a.

5.11 Crystallization of amorphous PNCs into solid NPs

The formation of PNCs adsorbed on the surface of crystallized NPs can occur in multiple stages. First, the PNCs land on the surface of the crystallized NPs. Since PNCs consist of multiple gold atoms and have a disordered structure, the shell

initially forms as a soft, amorphous layer, as shown in Figure 5.20a and Figure 5.20b illustrates a later stage of PNC adsorption on the surface of the crystallized NPs. This phenomenon cannot be attributed to an atom-by-atom growth mechanism, as individual adatoms would be clearly visible on the surface of AuNPs in this size range. The presence of crystallized AuNPs covered by a shell suggests that growth does not occur atom by atom. Instead, it points to a sudden surplus of atoms on the surface, along with ligands. This rapid accumulation of atoms in the presence of ligands is a likely mechanism for the formation of stable PNCs.

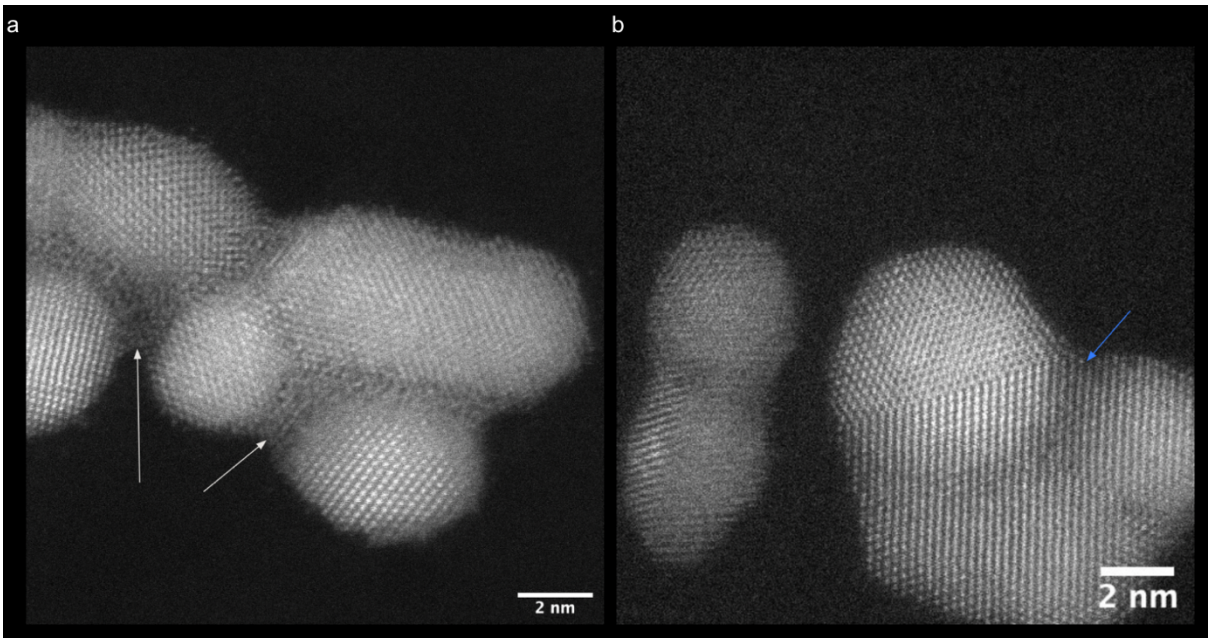


Figure 5. 20. STEM images of a) citrate capped AuNPs with pH 6 at 5 minutes, soft shell indicated by white arrow on the left image. b) citrate capped AuNPs with pH 4.8 at 60 minutes, hard shell indicated by blue arrow on the right image.

Once the PNCs cover the NPs, normal diffusion processes apply. The random atomic arrangement in the PNCs acts as a fault, requiring adjustment to reach a

lower-energy state, i.e., the preferred crystalline structure. The blue arrow in Figure 5.20b indicates the formation of a hard-shell motif. The difference in intensity between the shell and the original crystallized NPs further illustrates the transition from a soft-shell to a more ordered crystalline structure. This diffusion process transforms the soft-shell structure in Figure 5.20a into a crystallized form, as seen in Figure 5.20b. Although Figure 5.20a and Figure 5.20b depict different AuNPs, it is reasonable to conclude that the transition from soft shell to hard shell results from multiple faults in the crystal structure of the PNCs shell, which adjust into a crystalline lattice.

5.12 Adhesion of PNCs on solid AuNPs

A crystallized AuNPs capped with acetate adsorbing a PNC was captured in the early stage of synthesis. The intensity along the yellow indicator in Figure 5.21a is shown in Figure 5.21b. The intensity of the crystallized AuNPs is significantly higher, measured at 25k in the centre. The intensity of the crystallized AuNPs and the PNCs shell starts at 10k and gradually decreases to 5k, which represents background noise. A similar intensity transition is also observed in Figure 5.7. The transition from the surface of the crystallized AuNPs to the PNCs shell is gradual, distinguishing it from the typical aggregation and agglomeration of NPs, which will be discussed later in this chapter.

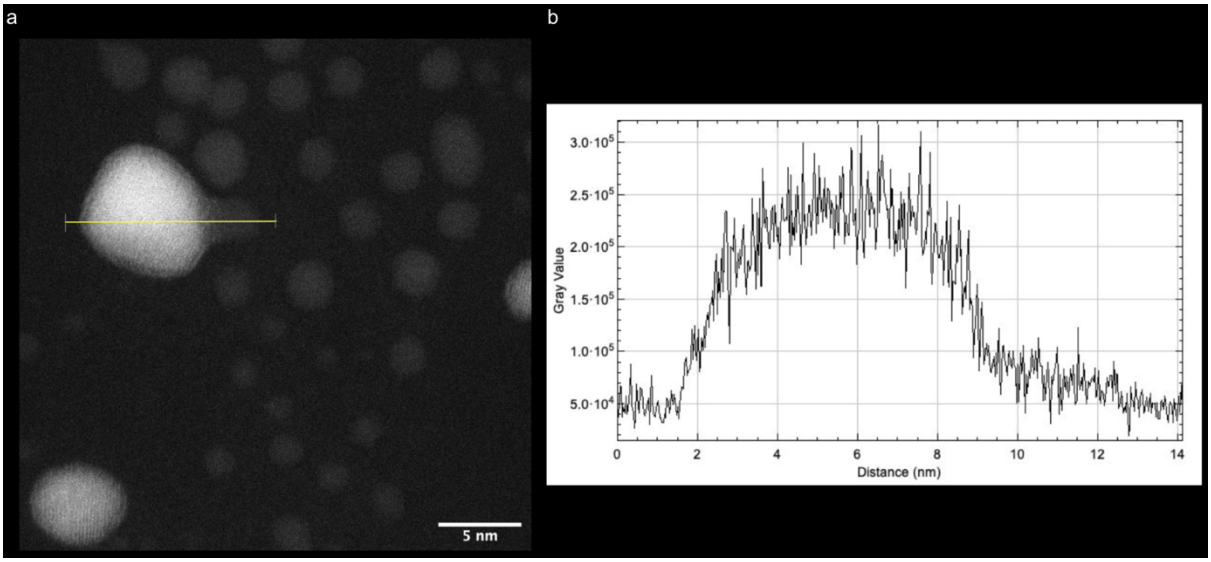


Figure 5. 21. STEM image of a) acetic capped AuNPs with 1:7 at pH 6.6 5 minutes. b) intensity plot along the yellow indicator on Figure 5.21a.

At a later stage, if the surface energy favours a transition from PNCs to crystalline NPs, it is possible that the PNCs will begin to crystallize themselves. Figure 5.22 shows multiple PNCs at 60 minutes starting to crystallize into a structure during an acetate-capped AuNPs synthesis. Based on the crystal structure, the large central particles consist of two regions: the upper structure and the bottom structure. The blurred region in between represents the remaining PNCs awaiting crystallization.

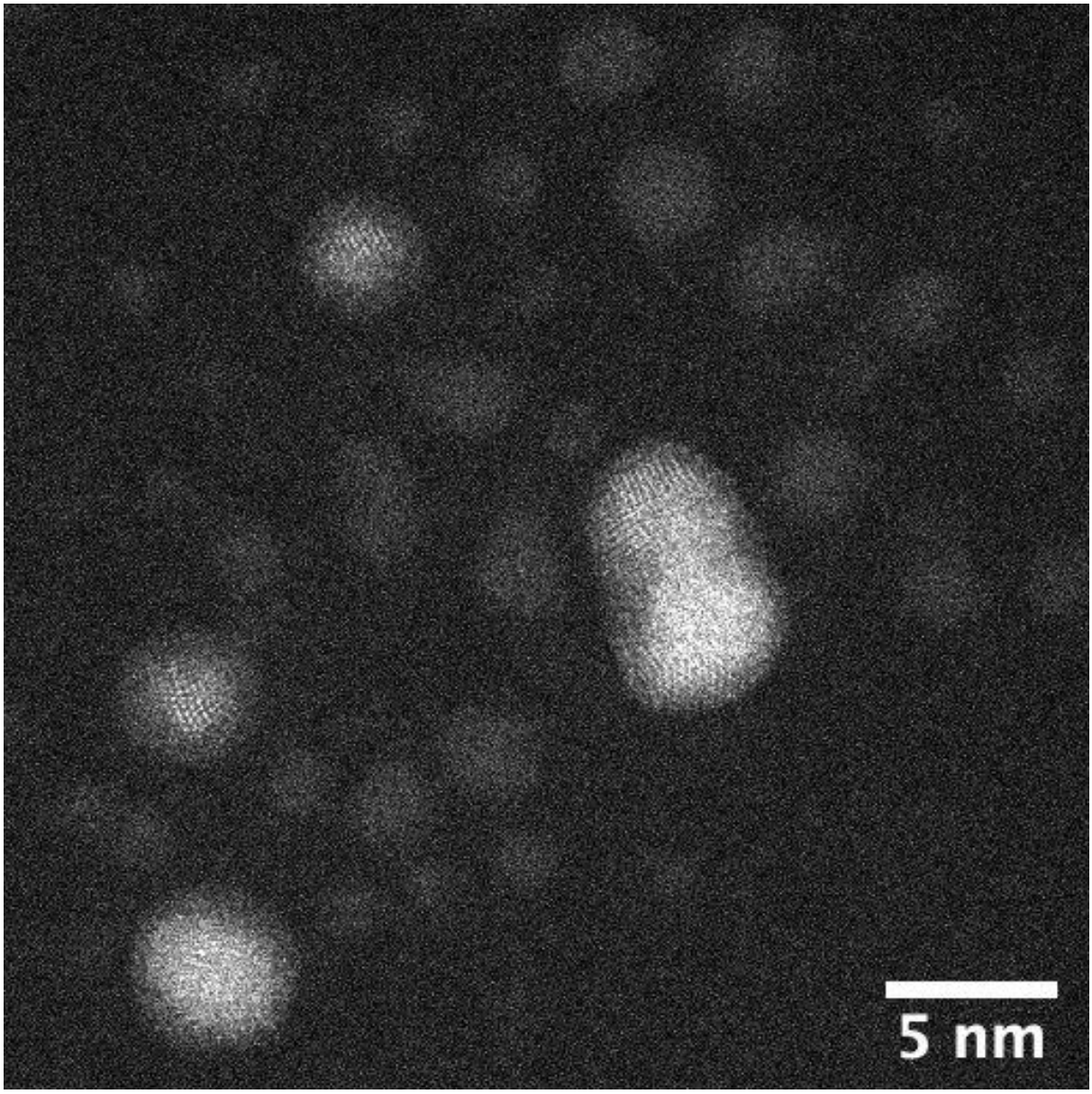


Figure 5. 22 STEM image of acetic capped AuNPs at pH 5.3 at 60 minutes.

5.13 PNCs-induced aging vs classical growth mechanisms

As PNCs evolve, their role in nanoparticle growth mechanisms diverges significantly from classical processes such as agglomeration or Ostwald ripening.

As mentioned earlier, the mechanism of PNCs covering multiple crystallized NPs' surfaces induces a spread and redistribute of atoms and ligands from the PNCs "wrapping", as shown in Figure 5.18 (indicated by the green arrow). This "wrapping" effect also generates a "stickiness" around the surface, leading to the formation of bridges, as indicated by the white arrow in Figure 5.18. This mechanism differs greatly from crystallized NPs' aggregation and agglomeration.

In the aggregation process, crystallized NPs undergo an irreversible transformation when two NPs' surfaces approach and bond together permanently. This is a one-way process, typically occurring when the NP surfaces are exposed due to the lack of a surfactant or capping agent. A typical aggregation formation is shown in Figure 5.23.

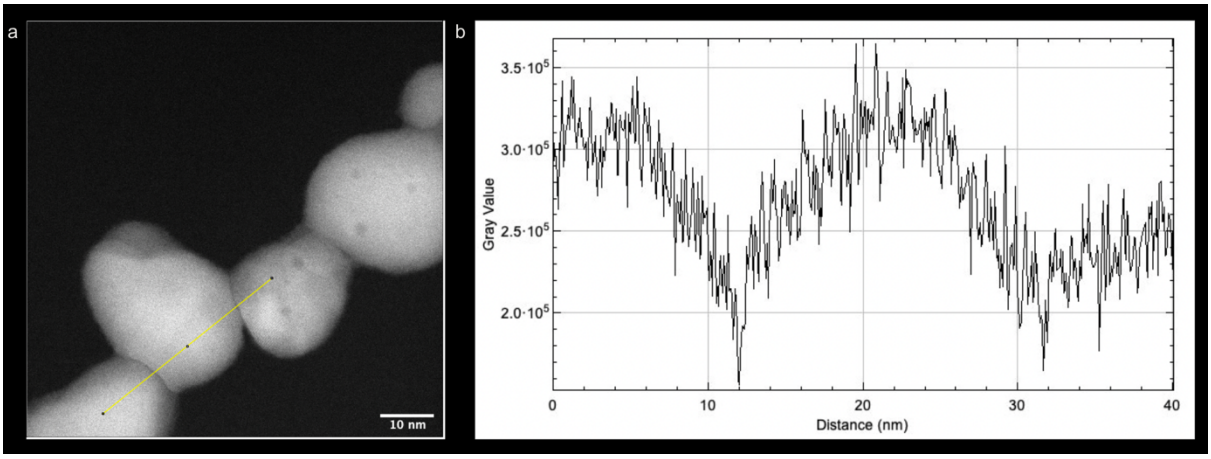


Figure 5. 23. a) AgNPs with no capping agent at 60 minutes. b) intensity plot along the yellow indicator in Figure 5.23a.

In Figure 5.23a, AgNPs are synthesized without a capping agent. The absence of a protective capping agent causes multiple AgNPs to aggregate, forming a chain-

like structure of AgNPs. Figure 5.23b shows the intensity along the yellow indicator in Figure 5.23a. The intensity transition between the bridges of these aggregated AgNPs is very sharp and visually distinguishable in Figure 5.23a. This drastic change in intensity is due to the aggregation of crystallized NPs without the presence of PNCs on their surface.

Agglomeration, on the other hand, is a reversible process where a group of NPs stack together without their surfaces touching. This occurs when sufficient capping agent prevents “aging” or stops further NP growth, assuming the capping agent fully covers the particles. For example, Figure 5.24 shows a group of AuNPs capped with L-cysteine. These AuNPs exhibit a relatively consistent separation between their surfaces. Compared to Figure 5.23, where aggregation occurs, agglomeration involves a loose grouping driven by a favourable lower surface energy state, without forming a permanent bond between the NPs.

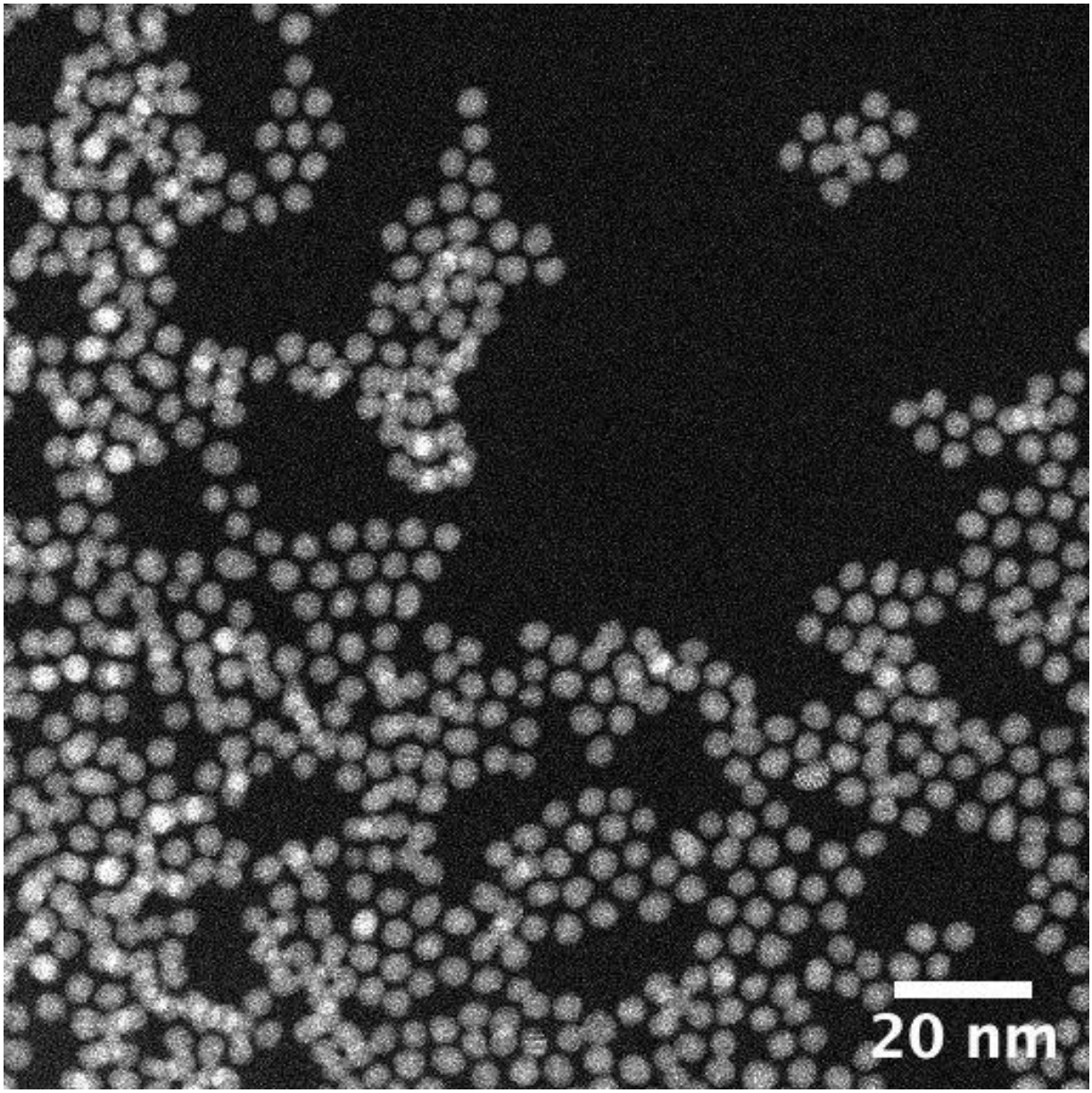


Figure 5. 24 STEM image of AuNPs capped with L-cysteine at pH 7.5 at molar ratio 1:3.5 at 1 day.

Figure 5.24 also highlights the difference between stacking and sticking. Stacking, visible in the top left corner of Figure 5.24, is characterized by a sudden spike in intensity, indicating stacked NPs. This effect could result from drying or a dumbbell-shaped nanostructure along the axis perpendicular to the screen (out of focus). Sticking, on the other hand, as shown in Figures 5.18 and 5.19, involves a

gradual and steady change in intensity. This is due to the redistribution of surface atoms with ligands from the adhesion of PNCs. After surface diffusion, the structure eventually crystallizes, creating a naturally irreversible configuration, as shown in Figure 5.20.

5.14 PNC-induced nano-string formation

The mechanisms of nanoparticle agglomeration and aggregation, as discussed earlier, are well-established. However, the role of PNCs in driving nanoparticle growth or aging remains somewhat ambiguous. One striking outcome of PNC-induced shape transformation is the possible formation of nano-string, a phenomenon explored in detail below. If a PNC cloud is near a cluster of crystallized NPs, it is possible for multiples PNCs to adhere to the surface and redistribute it's Au atoms with ligand original from the PNCs, subsequently also detach original surface atom from the AuNPs (Dachraoui et al., 2021b). These reconfiguration process bridge these NPs as mentioned in section 5.10 and 5.11, resulting in a crystalline nano-string, as seen in Figure 5.25 and Figure 5.26.

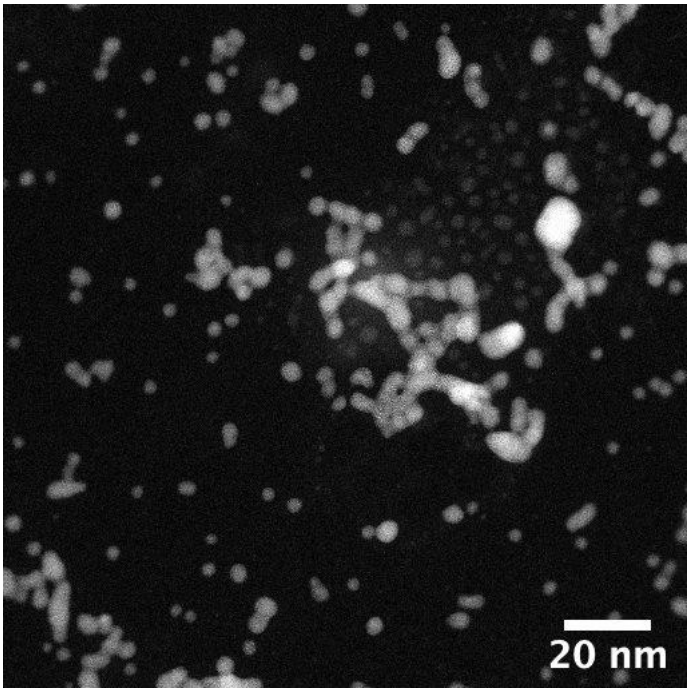


Figure 5. 25 STEM image of citric capped AuNPs with 1:3.5 at pH 6.3 at 5 minutes.

Nano-string can form through several mechanisms, including nanoparticle assembly via oriented attachment and particle dissolution followed by re-nucleation, as seen in Ostwald Ripening.

Coalescence and oriented attachment are the two primary mechanisms by which NPs evolve into nanowires. Although they both lead to nanowire formation, they are fundamentally different processes. Coalescence involves the merging of NPs without the formation of a common crystal plane, whereas oriented attachment leads particles to align along a shared crystalline plane. The particles aggregated in Figure 5.23 are the product of coalescence.

Ostwald ripening, another growth mechanism, involves the growth of larger particles at the expense of smaller ones. However, this process does not typically result in multiple-domain nanowires like the one shown in Figure 5.27.

Figure 5.26a shows the early stages of nanowire formation, with a shell of PNCs surrounding the solid core NPs. This process is similar to the schematic in Figure 5.17, but with more core NPs involved. The white arrow in Figure 5.26a indicates the bridging of PNCs between the core NPs, while the green arrow points to the wrapping of PNCs around the NPs, like the mechanism shown in Figure 5.18. The orange arrows highlight the presence of PNCs surrounding the core NPs and suggest that the nanowire forms via the wrapping of PNCs, driven by an excess of PNCs in the system.

In Figure 21b, the intensity profile along the cross-section of the forming nanowire is shown. The smooth transition in intensity between the core and the PNC-wrapped shell (or bridging formation) mirrors the situation seen in Figure 5.21b. This intensity transition differs significantly from that in Figure 5.23, where aggregation and coalescence are at play.

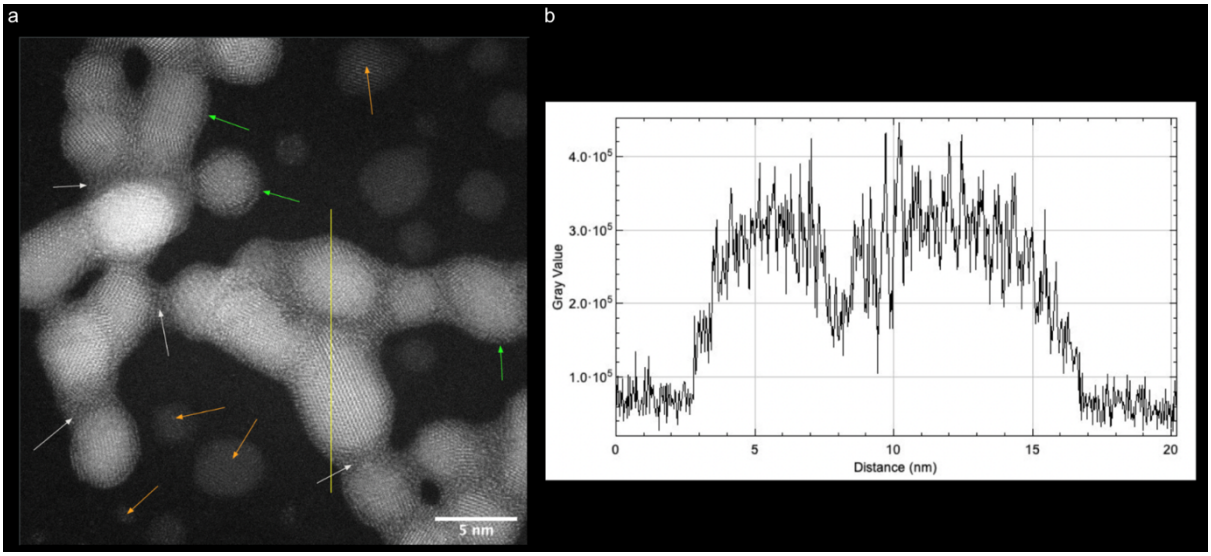


Figure 5. 26. STEM image of c) citric capped AuNPs with 1:3.5 on pH 6.3 at 5 minutes, shell structure indicated by green arrow, bridge structure indicated by white arrow, PNCs indicated by orange arrow. b) intensity plot alone the yellow indicator in 5.26a.

Figure 5.27 presents a nanowire with multiple domains, marked by the blue arrows. This structure lacks a common crystalline plane, ruling out oriented attachment as the formation mechanism. It also cannot be attributed to coalescence, as the bridging indicated by the white arrow shows a stretching motif. This suggests that the formation of a nanowire by PNCs wrapping around a group of NPs is a plausible mechanism.

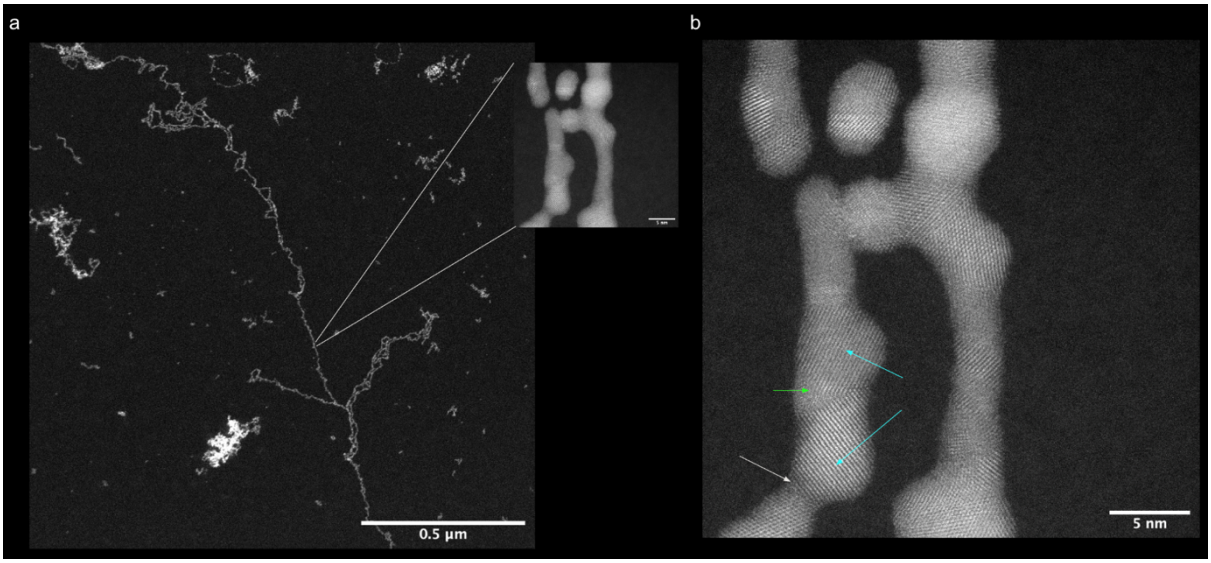


Figure 5. 27. STEM images of a) citric capped AuNPs with 1:1 at pH 4.4 at 60 minutes. b) magnified image on the top right corner of 5.27a.

If the process of PNCs redistributing atoms around a group of crystalline NPs coincides with the soft-to-hard shell transition, a nanowire without a defined facet can form. Figure 5.27b illustrates a crystalline nanowire with uneven density throughout, resembling the structure seen in Figure 5.26a.

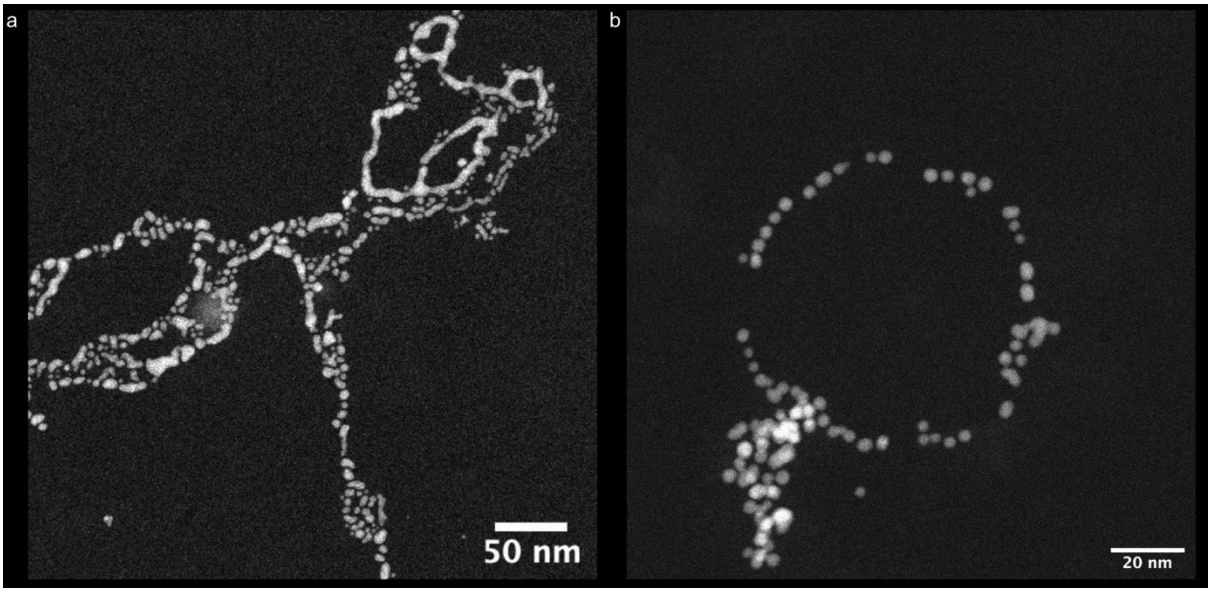


Figure 5. 28. STEM images of a) citric capped AuNPs with molar ratio 1:1 on pH 4.4 at 60 minutes as an unpredictable morphology of nano-string. b) NPs with circle formation that potentially will evolve into a nano-string.

The nanowire in Figure 5.27b consists of different NP domains that are bonded together by PNCs through the soft-to-hard shell process, as described in Figure 5.20. This results in the transformation from a single crystallized NP (or a group of NPs) to a core-shell structure, with different densities covered by PNCs. This process leads to an unpredictable nanowire morphology, as seen in Figure 5.28a and Figure 5.28b.

5.15 Impact of functional groups on PNCs behaviour

The functional group of capping agents plays a crucial role in PNC-driven transformations. As discussed earlier in this chapter, when the synthesis involves a carboxyl group capping agent, the resulting PNCs tend to remain in a diffused atom form, as seen in Section 5.8, Figures 5.10 and 5.11. In contrast, when a thiol group capping agent is used, the PNCs are reduced to a zero-valent form, as shown in Figure 8.

The differing nature of the PNCs in solution significantly influences the further growth of nanoparticles. PNCs can act as a material source for growth when they

adhere to the surface of existing nanoparticles. This interaction can impact the stability, size, and shape predictability of the nanoparticles.

Figure 5.29 presents the size distribution of AuNPs capped with acetic, oxalic, citric, and cysteine ligands after 7 days in solution. All carboxyl group-capped AuNPs show signs of aging, evident from their growth into larger sizes (shown in Figure 5.29a) and unpredictable shapes (shown in Figure 5.29b). In contrast, cysteine-capped AuNPs remain monodisperse and spherical. This difference is due to the nature of the PNCs formed with carboxyl group ligands, which typically exhibit a sticky motif, as demonstrated in Figure 5.18. In contrast, PNCs formed with thiol group ligands are reduced to zero-valent gold atoms, as shown in Figure 5.13.

The absence of the "stickiness" observed in carboxyl group-capped PNCs allows cysteine-capped AuNPs to maintain their spherical shape, preventing further aggregation or irregular growth.

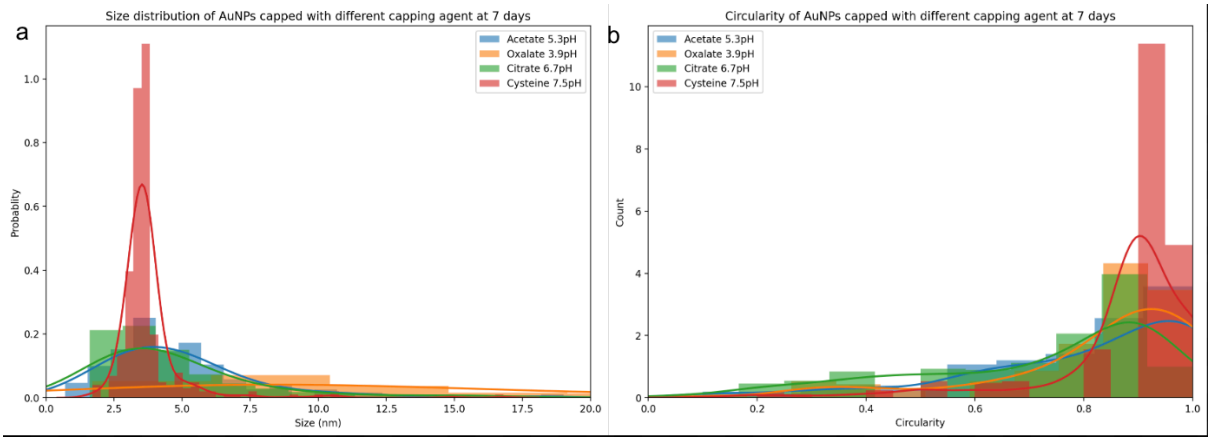


Figure 5. 29. a) size distribution after 7 days of the synthesis. Acetate capped AuNPs indicated by blue colour, oxalate capped AuNPs indicated by yellow colour,

citrate capped AuNPs indicated by green colour, and cysteine capped AuNPs indicated by red colour. c) the circularity of the AuNPs with different capping agents in 5.29a.

5.16 Beam induced growth with PNC to core NPs

As most of the characterization of the AuNPs in this chapter utilizes STEM imaging, it is essential to understand how the electron beam can affect the morphology of the AuNPs during imaging. It has been observed that the electron beam can induce growth in AuNPs when focused on a specific area of interest with the setting mentioned in chapter 3. For example, a sequence of images shown in Figure 5.31 illustrates this effect.

Figure 5.31a shows the initial state (t = 0) of the AuNPs, where the shell motif, PNCs, bridges, and free gold atoms are indicated by green, orange, white, and blue arrows, respectively. At t = 0, the thickness of the bridges was measured to be 1.2 nm. After 20 seconds, the bridge thickness increased to 1.4 nm in Figure 5.31b and further grew to 1.8 nm in Figure 5.31d. The growth becomes particularly significant after 1 minute of electron beam exposure. Additionally, the electron beam provides enough energy to trigger nucleation, resulting in further NP growth, as seen in Figure 5.32.

This observation highlights the importance of carefully considering experimental setups and in situ characterization techniques. In liquid-cell TEM experiments, for instance, excessive material may be provided for nucleation, and the electron beam could facilitate NP growth, potentially bypassing the PNCs stage.

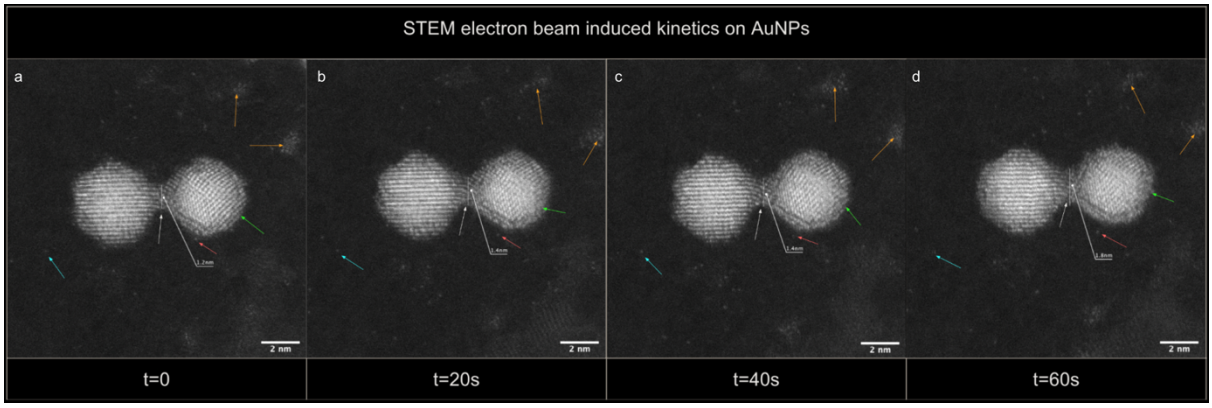


Figure 5. 30 STEM electrons beam induced growth on AuNPs on timestamp of a) t = 0 s, b) t = 20 s, c) t = 40 s, d) t = 60 s. Blue arrow indicate single gold atom. Green arrows indicate the shell formation. White arrows indicate the neck formation between two AuNPs. Orange arrows indicate PNCs.

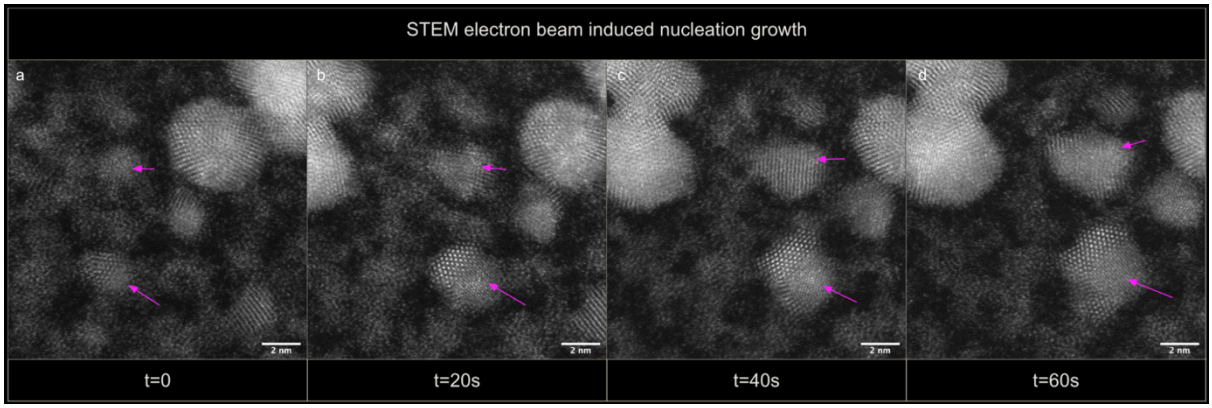


Figure 5. 31 STEM electrons beam induced nucleation and growth on AuNPs on timestamp of a) t = 0 s, b) t = 20 s, c) t = 40 s, d) t = 60 s. Purple arrow indicates the nucleation of AuNPs.

5.17 Conclusion

This chapter provides an in-depth analysis of PNCs, uncovering their pivotal role in shaping the physicochemical properties of NPs, the formation pathways and the effect of long-term stability. Through detailed exploration, several key insights are detailed below.

First, the properties and stability of PNCs were investigated. PNCs exhibit a size range up to 5 nm and a shell thickness of approximately 1 nm on the NPs surfaces. They demonstrate remarkable stability in solution, remaining present for up to 28 days. These properties highlight their structure as metastable in the solution, making them critical as an intermediate in NPs nucleation and growth. PNCs also act as a reservoir in the synthesis medium, influencing Np formation. Consistent line patterns observed in different ligand-capped AuNPs (acetic, oxalic, citric, and cysteine) suggest a universal mechanism dictating PNCs arrangement and interaction with NPs and ligands.

The origins of the cloud structure around AuNPs and AgNPs were also studied, the PNCs surrounding AuNPs and AgNPs exhibit lattice spacings of 0.23 nm and 0.20 nm, corresponding to gold (111) and (200) planes, and 0.23 nm and 0.21 nm for silver (111) and (200) planes, respectively. PNCs formed with carboxyl group ligands display a “sticky” nature, contrasting with the non-sticky behaviour

observed in thiol-based PNCs, emphasizing the role of ligand chemistry in PNC properties.

The formation of the core-shell AuNPs were also suggested alongside with the bridging formation caused by the PNCs bridging between NPs, effectively “gluing” them together. This bridging drives the aging process, leading to non-spherical shapes and unpredictable morphologies, emphasizing the role of PNCs in structural transformations when co-exist with NPs in the medium.

The crystallization dynamics of the amorphous PNCs were also suggested to be an irreversible transformation highlighting the dynamics of amorphous PNCs and the crystalline phase in NPs growth.

The sequence and combination of mechanisms like PNCs adhesion, core-shell sticky nature, bridging, and eventually crystallization, highlights the possibility of PNCs-induced nanowire formation. These structures arise from PNCs-mediated interaction, deviating from classical growth pathways.
Finally, the unpredictable shapes of NPs driven by PNCs, and the properties of the “stickiness” of carboxyl-based PNCs contrasting with the behaviour of thiol-based PNCs influencing the predictability of the NPs.

5.19 Future work

This chapter establishes the foundational understanding of PNC properties, mechanisms, and impacts on nanoparticle synthesis. By bridging classical and non-classical growth paradigms, PNCs present new opportunities for designing nanomaterials with tailored properties. Future research should focus on studying the nature of PNCs in reduction and early-stage nucleation. Because of the challenging nature of observing these PNCs, simulation and modelling might be favourable when studying the creation of PNCs and the interaction between PNCs and NPs.

Chapter 6: Molecular Dynamics of Gold Nanoparticle Nucleation and Growth with Ligands in Aqueous Media

6.1 Introduction

In Chapter 4, we investigated the influence of the number of carboxyl groups in capping agents on the morphology of AuNPs. Chapter 5 highlighted the pivotal role of PNCs during synthesis in determining the evolution of AuNP morphology. This chapter aims to bridge these findings by employing molecular dynamics (MD) simulations to provide an atomistic view of the nucleation and growth mechanisms of AuNPs, focusing on the role of ligands in non-classical nucleation.

MD simulations offer a unique opportunity to study atomistic interactions and processes such as nucleation and growth, which are otherwise challenging to observe experimentally. Importantly, MD simulations eliminate observer-induced artifacts, such as the potential nucleation triggered by the electron beam in STEM imaging, as discussed in Chapter 4. By integrating MD simulations with experimental observations, we aim to construct a comprehensive framework describing the evolution of AuNP size and morphology, eventually predicting changes in their properties resulting from interactions with surrounding molecules.

6.1.1 Advancing nucleation studies through MD simulations

Historically, classical MD simulations have relied on traditional force fields like the Lennard-Jones (LJ) potential, which assumes fixed bonds and cannot model chemical reactions. While suitable for studying non-reactive environments or growth under vacuum or a non-reactive media (Wang et al., 2016, Brault et al., 2019, Desgranges and Delhommelle, 2009, Grochola et al., 2007, Martin et al., 2019, Zhu et al., 2020), these methods fall short for systems involving dynamic bond-breaking and formation during nucleation. Recent advancements, however, have introduced semi-empirical potentials that approximate limited chemical reactions. These potentials have facilitated studies of annealing (Essajai et al., 2018, Essajai and Hassanain, 2018), solvent interactions (Chang et al., 2008, Martin et al., 2019, Wright et al., 2014), bond energy and formation (Meena and Sulpizi, 2016), and the stabilisation of NPs by ligand (Monego et al., 2020, Monego et al., 2018, Kister et al., 2018). . Despite these advancements, they remain insufficient for studying the complexities of non-classical nucleation.

The meso-molecular model used by Suarez-Lopez et al. (Suarez-Lopez et al., 2022). addressed some of these limitations by grouping multiple atoms into single entities (beads), reducing computational costs while simulating ligand effects in aqueous media. While insightful, this approach cannot reveal the chemical reactions critical to understanding PNC formation in non-classical nucleation.

6.1.2 Breakthrough in modelling chemical reactions via ReaxFF

To overcome these challenges, the Reactive Force Field (ReaxFF) was developed (Liang et al., 2013, Duin et al., 2001, Chenoweth et al., 2008, Senftle et al., 2016) Unlike traditional force fields, ReaxFF allows dynamic adjustment of bond orders, enabling the simulation of chemical reactions in MD while maintaining computational efficiency. This positions ReaxFF as a bridge between classical MD, which is computationally light but chemically limited, and quantum mechanical methods such as DFT, which are highly accurate but computationally intensive.

ReaxFF has been employed to study ligand-binding mechanisms on NPs, such as cysteine (Monti et al., 2016b, Monti et al., 2016a) and citric acid (Monti et al., 2017, Perfilieva et al., 2019). This capability makes it possible to model the complex chemical interactions involved in PNC-driven transformations and predict NP crystal structures (Carpenter and Grunwald, 2021).

6.1.3 Objectives of this chapter

This chapter utilizes ReaxFF simulations to study the nucleation of AuNPs in the presence of different carboxyl and thiol ligands in aqueous media. Our goal is to connect the findings of Chapters 3 and 4 by exploring how ligand chemistry influences NP formation under non-classical nucleation conditions. This integrated

approach, combining experimental observations with computational modelling, provides valuable insights into the evolution of NP morphology and physicochemical properties. Ultimately, this work aims to enhance our understanding of ligand effects on NP growth, offering predictive tools for tailoring NP properties for specific applications.

6.2.1 Role of ligands in nucleation: carboxyl and thiol functional groups

Ligands significantly influence the nucleation of AuNPs by mediating the interactions between Au atoms. In this study, the ligands are categorized into two groups: carboxyl-containing and thiol-containing ligands.

The carboxyl group ligands used in these simulations include acetic acid, oxalic acid, citric acid, and propionic acid. These ligands stabilize AuNPs through coordination of their carboxyl functional groups to the surface of AuNPs or free Au atom. The number of carboxyl groups in each ligand is hypothesized to directly affect the stability and nucleation rate of AuNPs. An additional carboxyl-containing ligand, propionic acid, also has a single carboxyl functional group but it has a longer carbon chain than acetic acid, therefore the surface coordination can be different from acetic acid to AuNPs. This ligand is included to study the potential effects of steric hindrance on nucleation. Figures 6.1 and 6.2 depict the structures

of the selected carboxyl-containing ligands, highlighting their functional groups and relative sizes.

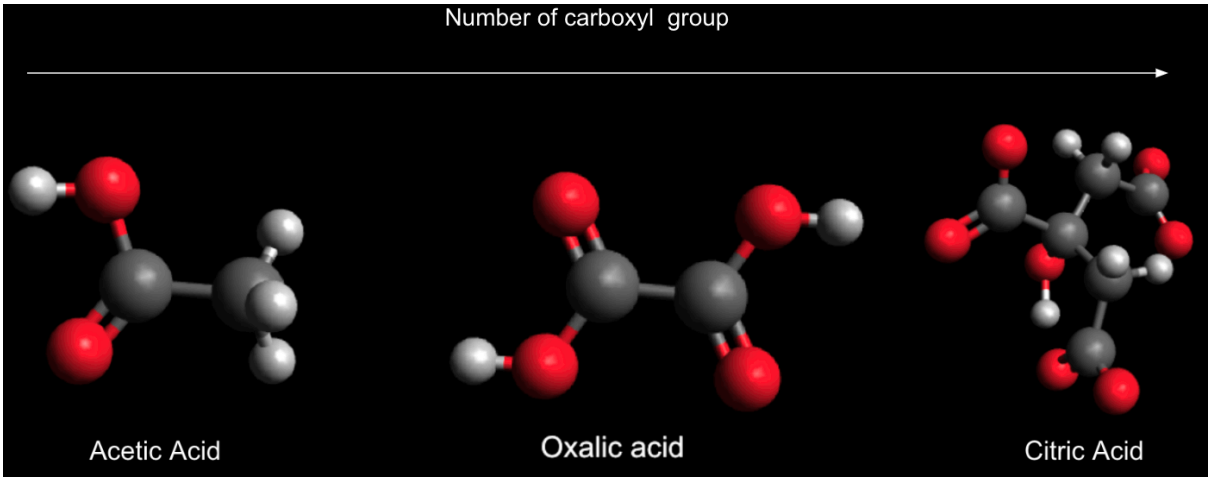


Figure 6. 1 Ball and stick style illustration of the atomic arrangement of three carboxyl group ligands, acetate, oxalate, citrate, used in the simulations. Dark grey: carbon atoms, red: oxygen atoms, light gray: hydrogen atoms.

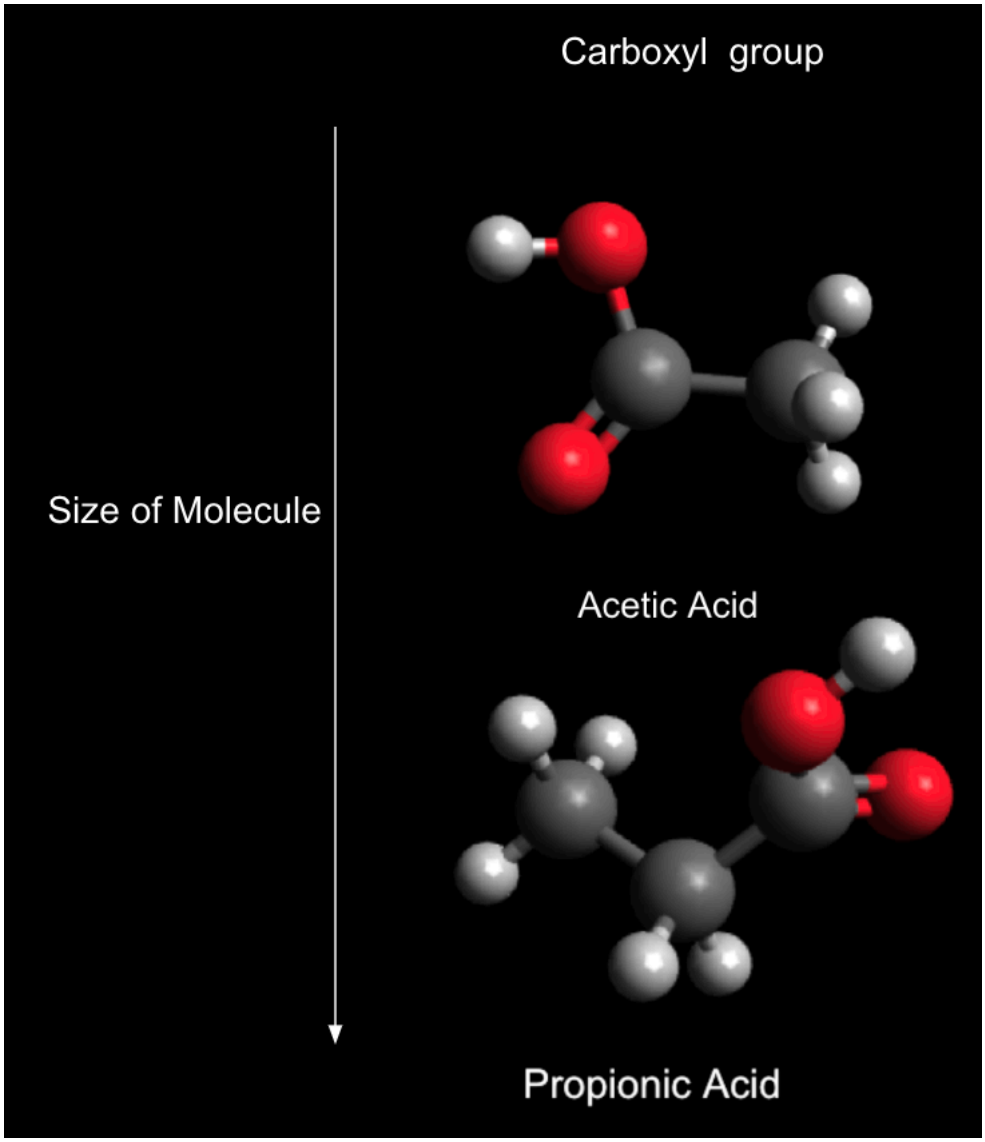


Figure 6. 2 Ball and stick style illustration of the atomic arrangement of two carboxyl group ligands, acetate and propionate, used in the simulations. Dark grey: carbon atoms, red: oxygen atoms, light gray: hydrogen atoms.

Thiol-containing ligands, such as L-cysteine (L-cys) and glutathione (GSH), form strong covalent bonds with Au atoms, creating a stable "staple layer" around AuNPs. GSH, being larger than L-cys, is included to evaluate the impact of ligand size on the nucleation rate. Figure 6.3 shows the structures of these thiol ligands, emphasizing their thiol groups and molecular size differences.

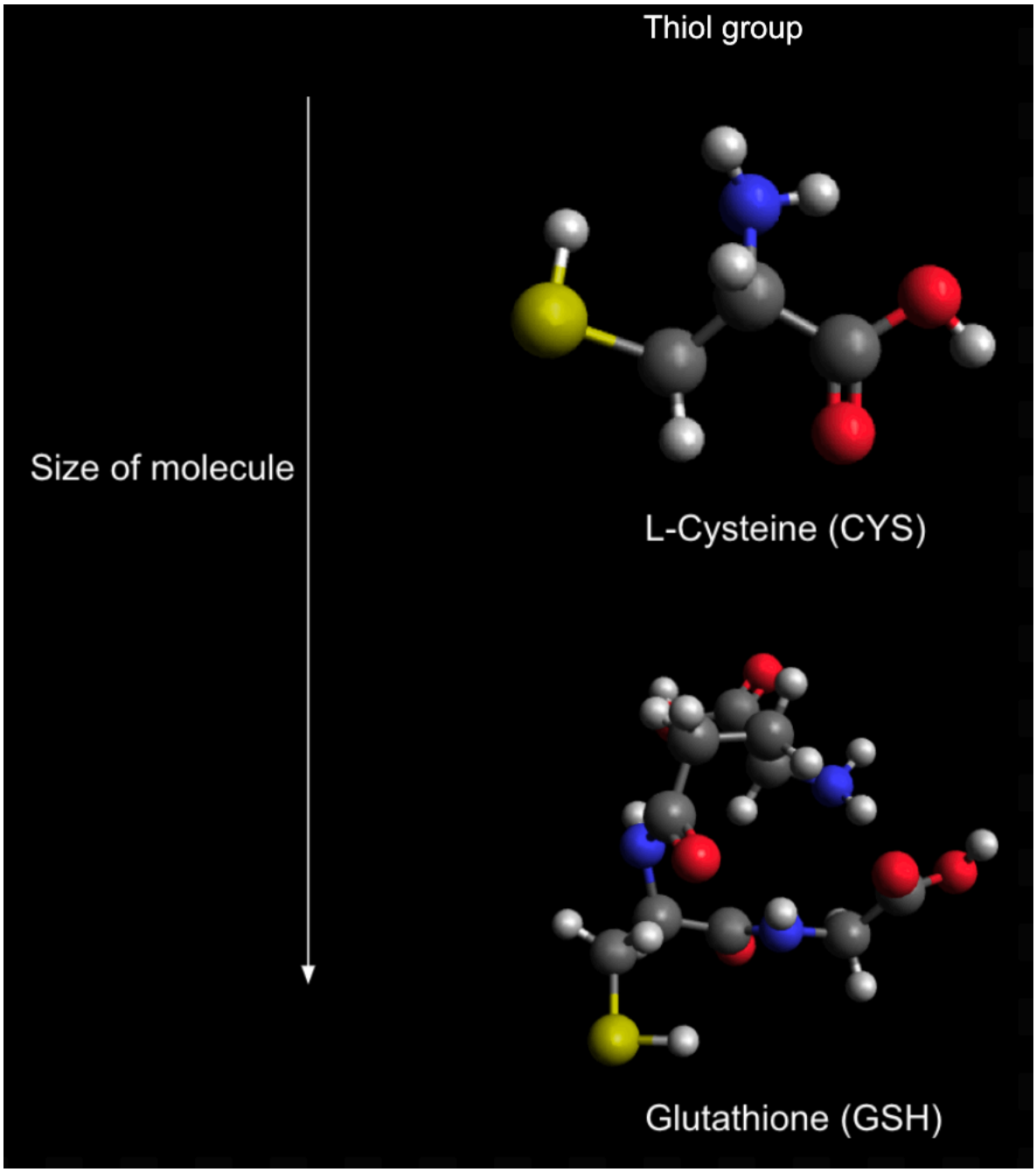


Figure 6. 3 Ball and stick style illustration of the atomic arrangement of two thiol group ligands, L-Cysteine (CYS) and Glutathione (GSH), used in the simulations. Dark grey: carbon atoms, red: oxygen atoms, light gray: hydrogen atoms, blue: nitrogen, yellow: sulphur.

In this chapter, all ReaxFF simulations contain 1000 water molecules, 100 free gold atoms for nucleation simulation and a respective number of free gold atoms (30, 60, 90) for growth simulation.

The chosen number of water molecules ensures computational efficiency while facilitating the nucleation process by increasing the likelihood of Au atom interactions. Although this water-to-gold molar ratio (10:1) is significantly smaller than the experimental ratio (~20,000:1, as described in Chapter 3), it allows for effective simulation within computational constraints mentioned in Chapter 3. Detailed simulation parameters and procedures also included in chapter 3 section 3.9.

To simplify the simulation, the Au atoms are assumed to be in their reduced Au(0) state, corresponding to experimental conditions achieved with sodium borohydride ($NaBH_4$) as a reducing agent. Therefore, the reduction process is not explicitly modelled.

6.2.2 Crystallographic considerations for Au

Gold adopts an FCC (face-centered cubic) structure, with a lattice parameter of 4.08 Å at room temperature (Uddin, 2018). The coordination environments are described as follows:

First nearest neighbour: Located at the face diagonal (2.88 Å), with a coordination number of 12.

Second nearest neighbour: At the lattice parameter (4.08 Å), with a coordination number of 6.

Third nearest neighbour: At 5.00 Å, with a coordination number of 24.

Fourth nearest neighbour: At 5.77 Å, with a coordination number of 12.

Fifth nearest neighbour: At 6.45 Å, with a coordination number of 24.

6.2.3 Radial distribution function (RDF) analysis

To quantify nucleation rates, the radial distribution function (RDF) is employed as mentioned in the methodology chapter. By monitoring changes in the RDF increments, it is possible to evaluate the influence of different ligands during the nucleation stage. This analysis provides insights into how ligands stabilize Au atoms, drive their organization into crystalline structures, and affect nucleation kinetics.

6.3 Nucleation with free gold atoms in water without ligands

To understand the baseline nucleation behaviour, it is essential to study how free gold atoms interact and nucleate in water without any capping agents. This

provides a reference for assessing the impact of ligands in subsequent simulations.

Figure 6.4a shows the initial state of the simulation involving 100 Au atoms in a system with 1,000 water molecules. At 200k steps (50 ps of simulation time), nuclei formation is evident. This is indicated by the peak at approximately 0.29 Å in the RDF, corresponding to the first nearest neighbour, as shown by the blue curve in Figure 6.4c. Notably, at this stage, no significant peak is visible around 5 Å, which would represent the third nearest neighbour.

Figure 6.4b shows the final nucleation stages at 3.8M steps (950 ps of simulation time). The first nearest neighbour count increases to around 700, signalling the continued addition of Au atoms to the structure. In addition, a peak around 5 Å becomes visible, representing the third nearest neighbour. Also, another peak around 5.7 Å corresponding to the fourth nearest neighbour starting to emerge. However, there is no visible peak at 4.08 Å, the second nearest neighbour, which corresponds to the lattice constant for FCC gold.

This simulation performed without any ligands in the aqueous medium, highlights a scenario where nucleation continues without any capping agent in present. The absence of ligands means there are no stabilizing interactions to moderate the growth rate of Au nuclei. Instead, the addition of Au atoms to the structure remains in an intermediate state. Consequently, the system demonstrates a high nucleation rate, as evident from the rapid increase in the first nearest neighbour count and the distinct peaks appearing at higher coordination distances. The

absence of a peak at 4.08 Å throughout the simulation suggests that the nucleated clusters do not yet adopt an FCC structure.

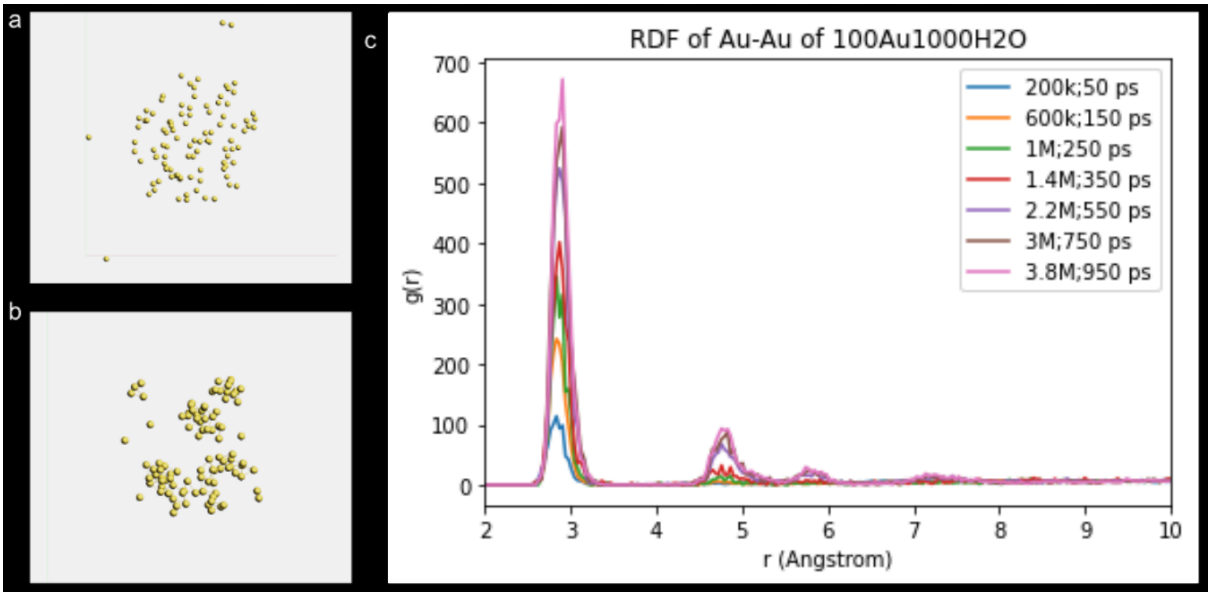


Figure 6. 4 Snapshot of 100 free gold atoms with 1000 water molecules at: a) 200k step, 50 ps. b) 3.8M step, 950 ps. c) RDF of all the calculated snapshots combined.

This analysis establishes a critical baseline for comparing the effects of carboxyl and thiol ligands on nucleation rates and structural evolution in subsequent simulations.

6.4.1 Nucleation with carboxyl group ligand in water (acetic acid)

When acetic acid is added to the simulation as a capping agent, the nucleation rate of AuNPs decreases. Figure 6.5 shows the simulation with only 10 acetic acid

molecules added to the simulation box. The nucleation rate is significantly slower compared to nucleation without any capping agent. At 200k steps, the first nearest-neighbour peak does not reach 100 counts, whereas nucleation without a capping agent already exceeds this value. This indicates that the early stages of nucleation are affected by the addition of acetic acid molecules. The subsequent RDF counts at each step also show a slower rate. However, the peak at the third nearest neighbour remains similar after 3.8M steps when compared to nucleation without any capping agent. Additionally, this simulation does not show any peak at the second nearest neighbour around 4.07. This suggests that acetic acid, as a mono-carboxyl group capping agent, exhibits weak coordination and has a moderate influence on the nucleation rate.

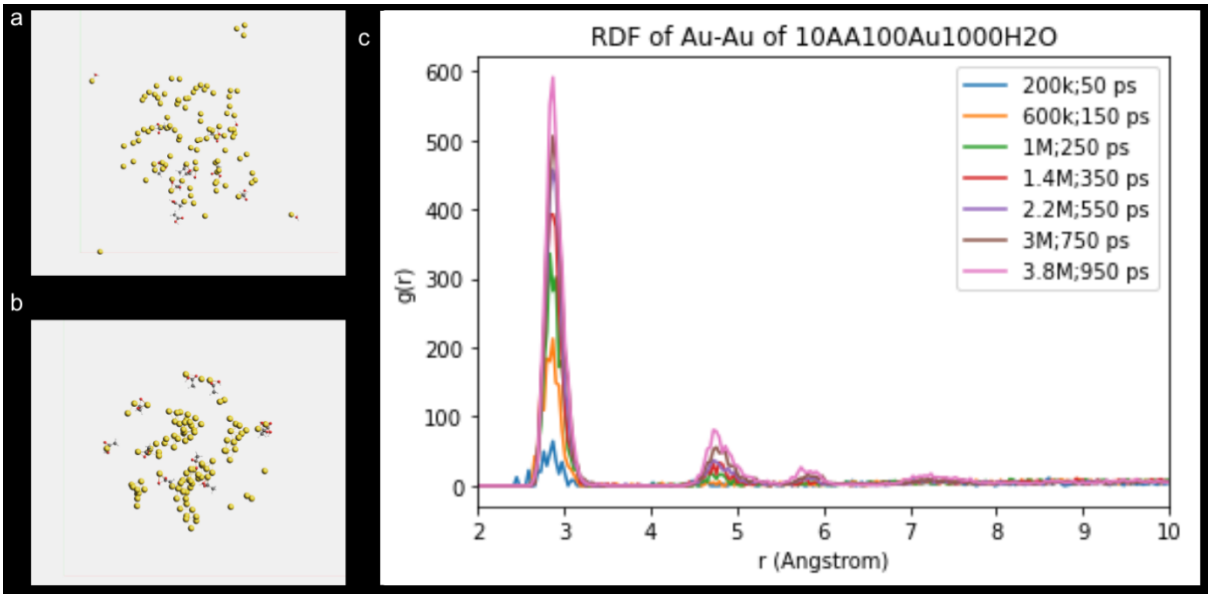


Figure 6. 5 Snapshot of 10 acetic acid and 100 free gold atoms with 1000 water molecules at a) 200k step, 50 ps. b) 3.8M step, 950 ps. c) RDF of all the calculated snapshots combined.

6.4.2 Nucleation with carboxyl group ligand in water (oxalic acid)

The nucleation rate decreases further when the capping agent is changed to 10 oxalic acid molecules, which contain two carboxyl groups per molecule. From Figure 6.6, the pink curve representing the 3.8M step or 950 ps shows that the count at the first nearest neighbour and the count at the third nearest neighbour do not reach 500 and 100, respectively. Although the AuNPs in this simulation are still nucleating, the nucleation rate is slower compared to that observed with acetic acid. This suggests that oxalic acid, as a di-carboxyl group ligand, has stronger coordination, slowing the nucleation rate by occupying more free Au atoms.

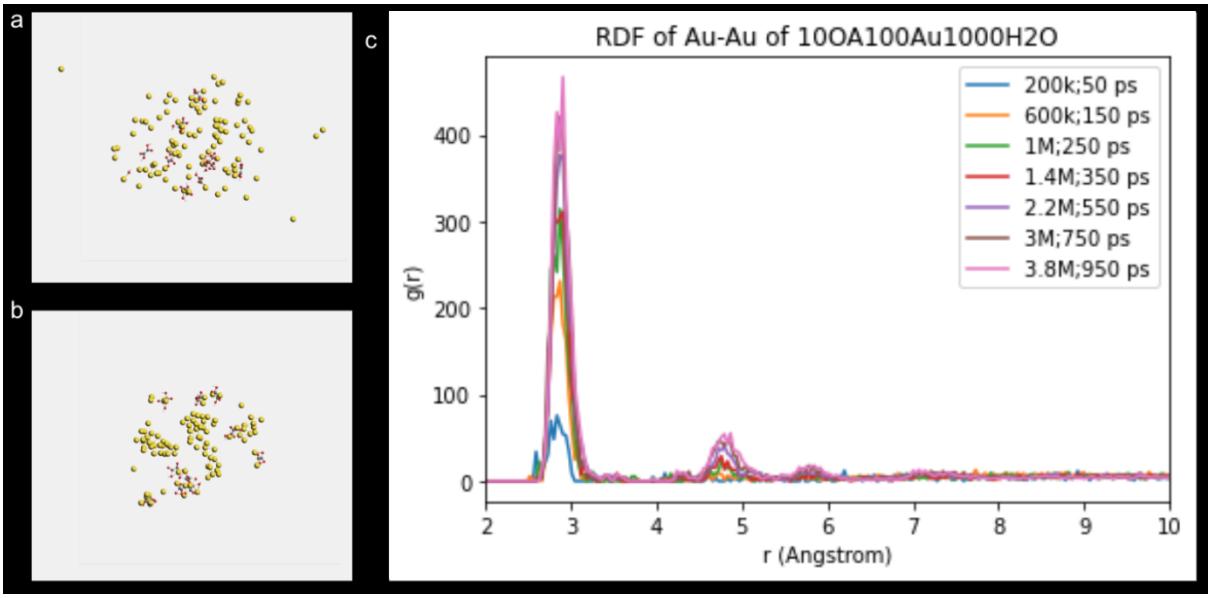


Figure 6. 6 Snapshot of 10 oxalic acid and 100 free gold atoms with 1000 water molecules at a) 200k step, 50 ps. b) 3.8M step, 950 ps. c) RDF of all the calculated snapshots combined.

6.4.3 Nucleation with carboxyl group ligand in water (citric acid)

The nucleation rate is the slowest among the carboxyl group simulations when 10 citric acid molecules are added to the simulation box. At 200k steps, as shown in Figures 6.7a and 6.7c, the first nearest-neighbour count reaches only 50 (indicated by the blue curve) and increases to only 350 at 3.8M steps. The peak at the third nearest neighbour also reaches only 50, as expected. In terms of nucleation rate, citric acid demonstrates the slowest nucleation across all simulation steps in Figure 6.7c. This is because citric acid, as a tri-carboxyl capping agent, stabilizes the nucleation by occupying more free Au atoms in the solution. This provides more controlled growth for the AuNPs compared to oxalic and acetic acid molecules.

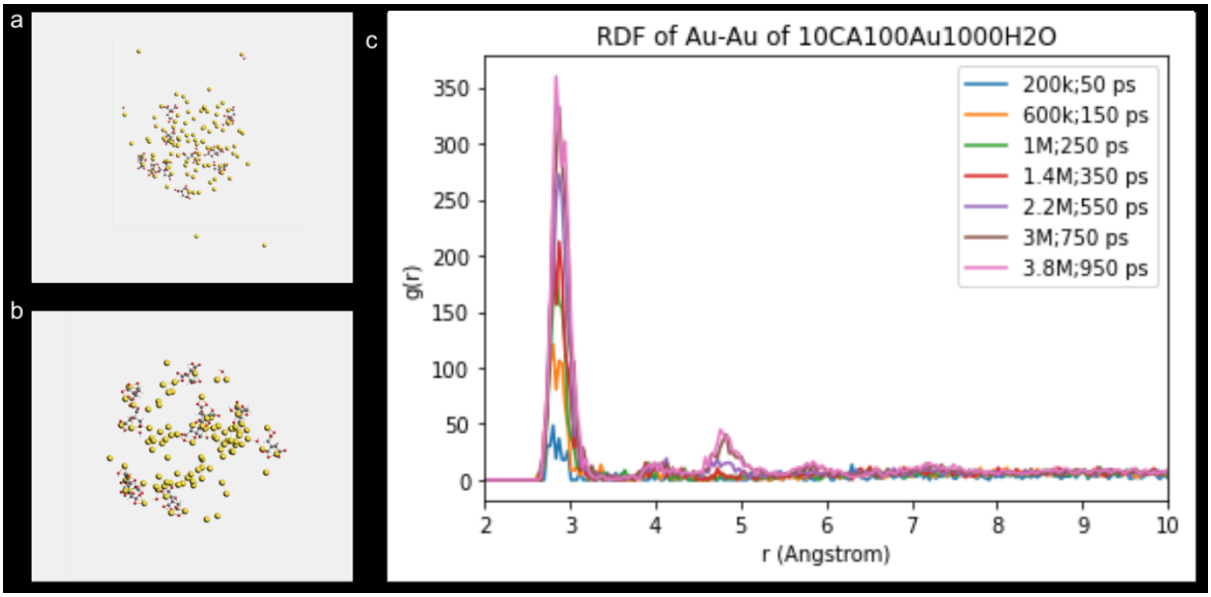


Figure 6. 7 Snapshot of 10 citric acid and 100 free gold atoms with 1000 water molecules at a) 200k step, 50 ps. b) 3.8M step, 950 ps. c) RDF of all the calculated snapshots combined.

6.4.4 Nucleation with carboxyl group ligand in water (propionic acid)

When the capping agent is replaced with 10 propionic acid molecules, the nucleation rate is similar to that observed with 10 acetic acid molecules. This indicates that the steric hindrance effect is not significant when the capping agent has a slightly longer carbon chain (Figure 6.8). On the other hand, the number of carboxyl groups plays a more pronounced role in influencing the nucleation rate when comparing carboxyl group ligands.

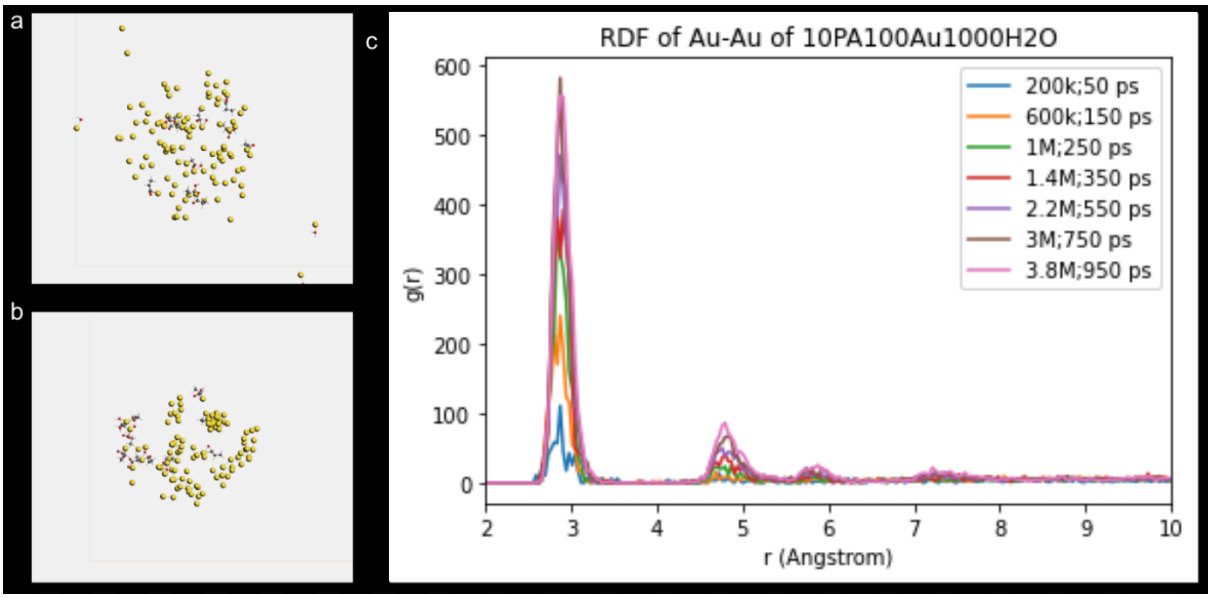


Figure 6. 8 Snapshot of 10 propionic acid and 100 free gold atoms with 1000 water molecules at a) 200k step, 50 ps. b) 3.8M step, 950 ps. c) RDF of all the calculated snapshots combined.

The number of carboxyl groups in the capping agent has a significant effect on the nucleation rate of the AuNPs in the simulation. As the number of carboxyl groups increases, the nucleation rate decreases significantly. Acetic and propionic acids exhibit the fastest nucleation rates, citric acid exhibits the slowest, and oxalic acid falls in between. This is because the additional carboxyl groups can coordinate with more free Au atoms, effectively slowing down nucleation or controlling the growth process.

6.5 Nucleation with citric acid pre-bound to 3 Au atoms

It is interesting to observe such an effect on the nucleation rate based on the number of carboxyl groups on a ligand, even with a molar ratio of 1 capping molecule to 10 Au atoms. However, the molar ratio of capping agent to gold atoms is much higher in experiments. It would be intriguing to explore what happens if all the carboxyl groups in a citric acid molecule occupy gold atoms. In experiments, the molar ratio of capping agent to gold ranges from 3.5:1 to 10.5:1, which is 100 times more capping molecules than in the simulation.

If the citric acid molecules each occupy 3 Au atoms, nucleation is completely prevented. Figure 6.9 shows the nucleation with 33 citric molecules, where each carboxyl functional group binds to one gold atom (i.e., three carboxyl groups coordinate with three Au atoms). At 200k steps, the RDF in Figure 6.9c shows the same peak as at 3.8M steps. Additionally, no visible nuclei are observed in Figures 6.9a and 6.9b. This indicates that nucleation does not occur if all the free gold atoms are captured by citric acid molecules.

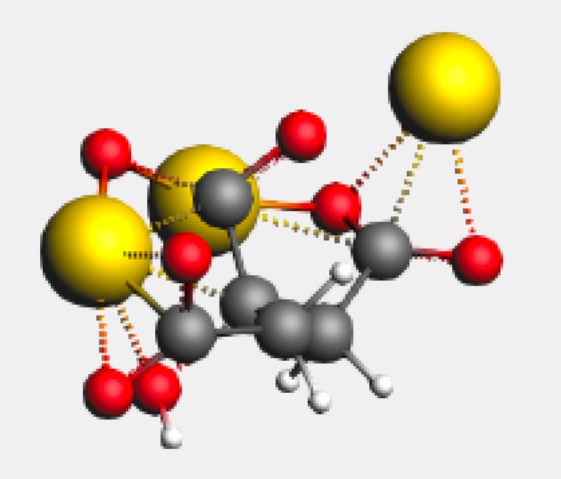


Figure 6. 9 Molecules consists of 1 citric acid with 3 gold atoms attached. This hybrid molecules were simulated as mentioned in Chapter 3 section 3.9.2.

Although the formation of well-defined nuclei of AuNPs is not observed, clustering of the citric–gold hybrid molecules occur. At 200k steps, the separation between the hybrid molecules is generally larger, as indicated by the blue curve in Figures 6.10a and 6.10c. However, by 3.8M steps (as seen in Figures 6.10b and 6.10c), the hybrid molecules are closer together, evidenced by the higher pink curve compared to the blue curve. Both the initial and final curves show peaks at approximately 4 Å and around 7 Å. While this distance is very close to the lattice

constant of FCC gold (4 Å), it is highly unlikely that nucleation occurred during this simulation.

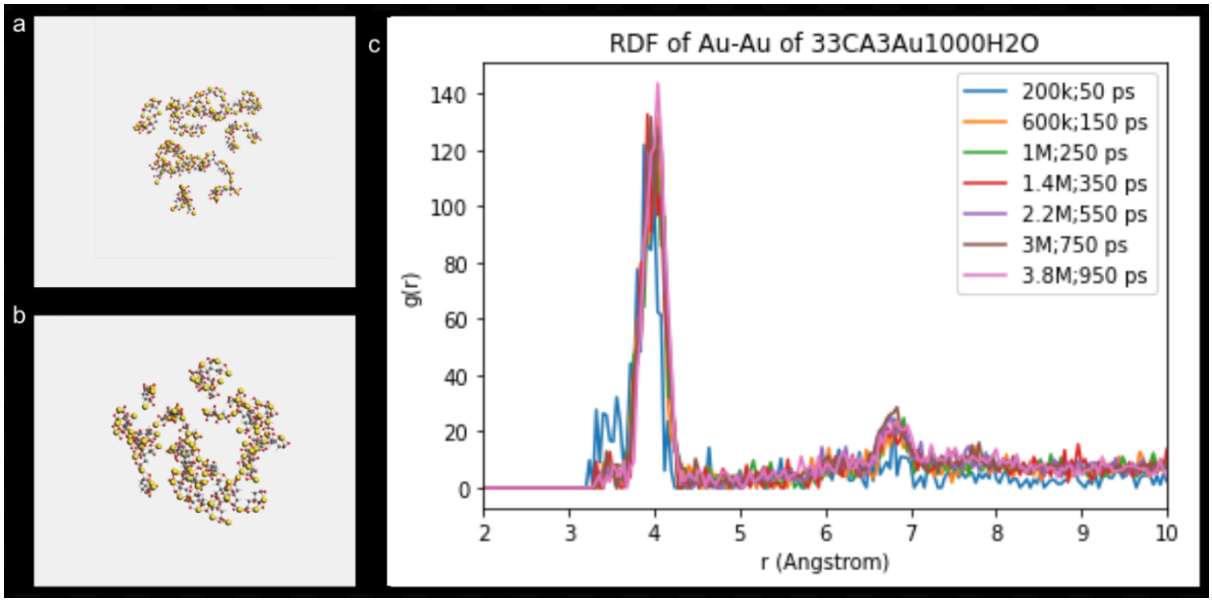


Figure 6. 10 Snapshot of 33 citric acid already bonded with 3 Au atoms with 1000 water molecules at a) 200k step, 50 ps. b) 3.8M step, 950 ps. c) RDF of all the calculated snapshots combined.

When comparing the RDF of the hybrid molecules of citric acid with 3 Au atoms to the nucleation simulations without citric acid, the simulation with hybrid molecules does not nucleate, as the yellow curve representing the RDF of the hybrid molecules never peaks at the first nearest neighbour distance of 2.88 Å (Figure 6.11). In contrast, both the 100-Au pre-made cluster (Appendix III, Figure A.3.1) mentioned in Chapter 3 section 3.9.1, and the 100 free Au atoms nucleation simulations show peaks at this distance, as well as at approximately 5 Å and 5.7 Å, like the 100-Au pre-made cluster (Figure 6.11). The absence of a peak at 4 Å in the simulation with 100 free Au atoms suggests that the peak original should exist

at 5 Å is now located at a closer location (4.75 A from Figure 6.11), differing from the 100-Au pre-made cluster. If the positions of the gold atoms are disordered, as in the 100 free Au atoms nucleation simulation, it may not be favourable for the Au atoms to align in the lattice at 4 Å, completing the second nearest-neighbour lattice distance.

It is also assumed that if the simulation continues, the nucleation of 100 free Au atoms will eventually occur and grow into a crystal structure similar to the 100-Au pre-made cluster (Appendix III, Figure A.3.1). However, the final size may differ because the surface energy of the 100-Au cluster in vacuum differs from that of the 100 free Au atoms in the presence of water molecules.

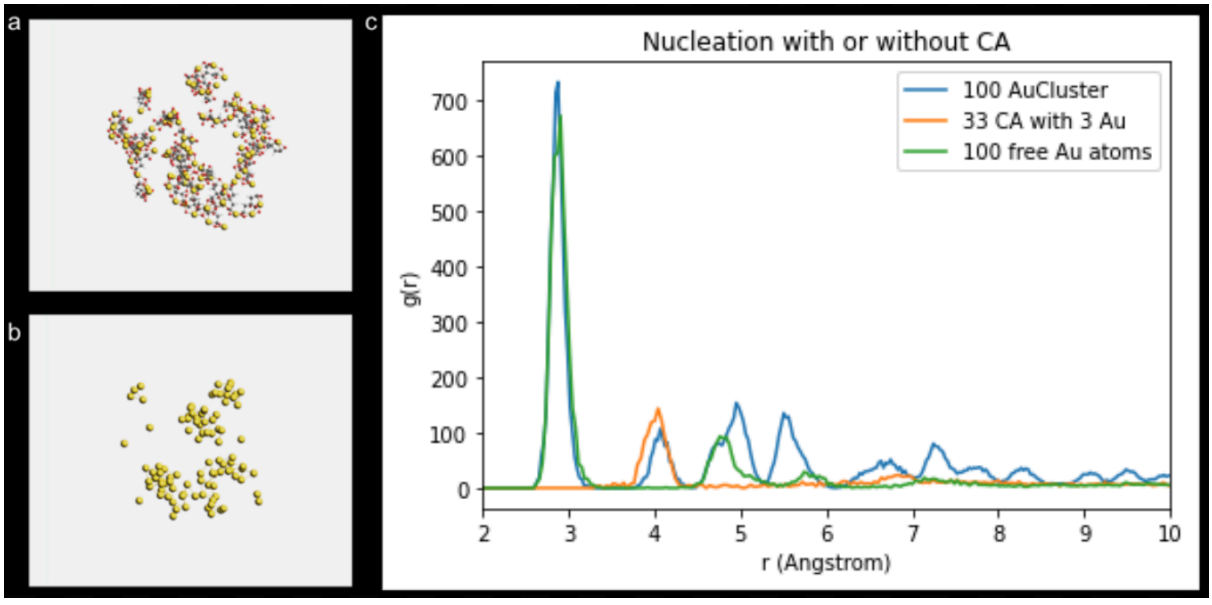


Figure 6. 11 Snapshot of a) 33 citric acids already bonded with 3 Au atoms with 1000 water molecules at 3.8M step, 950 ps. b) 100 Au atoms with 1000 water molecules at 3.8M step, 950 ps. c) RDF of 6.11a and 6.11b at 3.8M step, 950 ps.

6.6.1 Nucleation with thiol group ligands (L-Cysteine)

When a thiol group ligand is used in nucleation simulations, the nucleation rate is generally slower compared to carboxyl group ligands. In this study, 10 cysteine (Cys) molecules were used for the nucleation of 100 Au atoms in 1000 water molecules. At 200k steps, the first nearest-neighbour peak reaches around 50, as indicated by the blue curve in Figures 6.12a and 6.12c, but there is no peak at the third nearest neighbour. By 3.8M steps, the first nearest-neighbour peak reaches 500, and a peak at the third nearest neighbour appears, reaching almost 100, as shown by the pink curve. The nucleation rate of L-cysteine falls between that of acetic and oxalic molecules. This is because the strong Au–S bonds (Burgi, 2015) dominate the stabilization ability during nucleation.

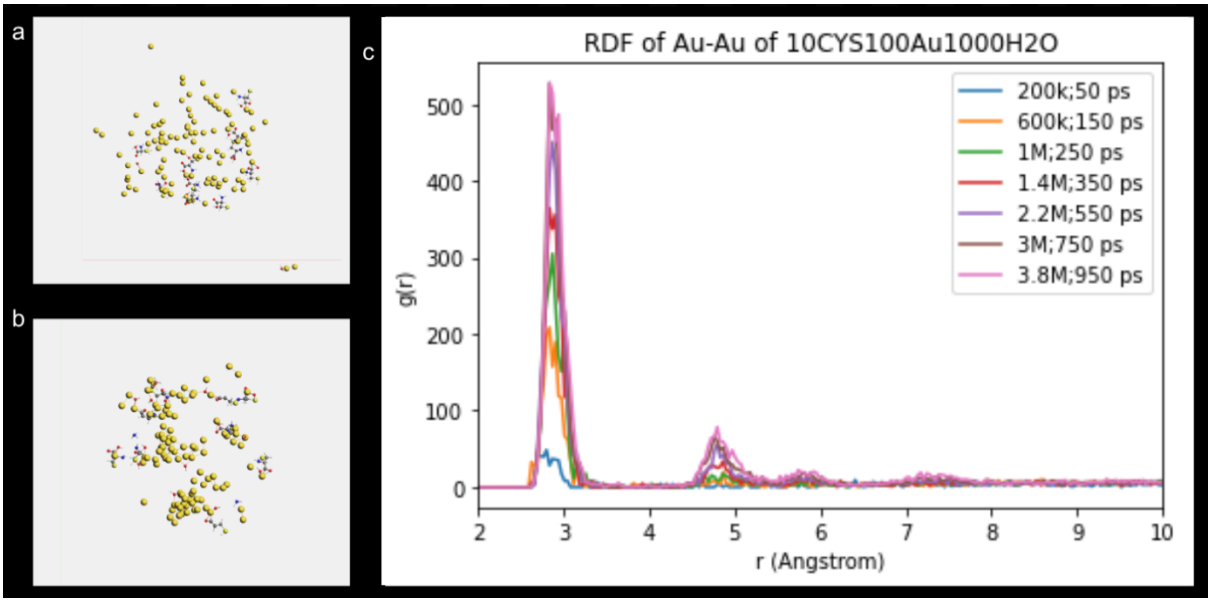


Figure 6. 12 Snapshot of 10 L-cysteine with 100 Au atoms with 1000 water molecules at a) 200k step, 50 ps. b) 3.8M step, 950 ps. c) RDF of all the calculated snapshots combined.

6.6.2 Nucleation with thiol group ligands (glutathione)

When a much larger molecule with a thiol functional group is used, the nucleation rate slows down significantly. In this case, 10 glutathione (GSH) molecules were added as the capping agent, replacing cysteine. At 200k steps, the first nearest-neighbour peak reaches 100, as indicated by the blue curve in Figures 6.13a and 6.13c and eventually reaches 400 at 3.8M steps. Comparing the nucleation rates of Cys and GSH in Figures 6.12c and 6.13c, the initial nucleation rate with GSH is higher than with Cys. Although the size of GSH is much larger than Cys, it is more challenging for GSH to move and capture free Au atoms. Cys, on the other hand, is smaller and experiences less resistance when moving through the medium, including interactions with other Cys and water molecules. As a result, the nucleation rate of GSH is initially higher than that of Cys. However, GSH should eventually captures more free Au atoms due to its multidentate nature as a capping agent.

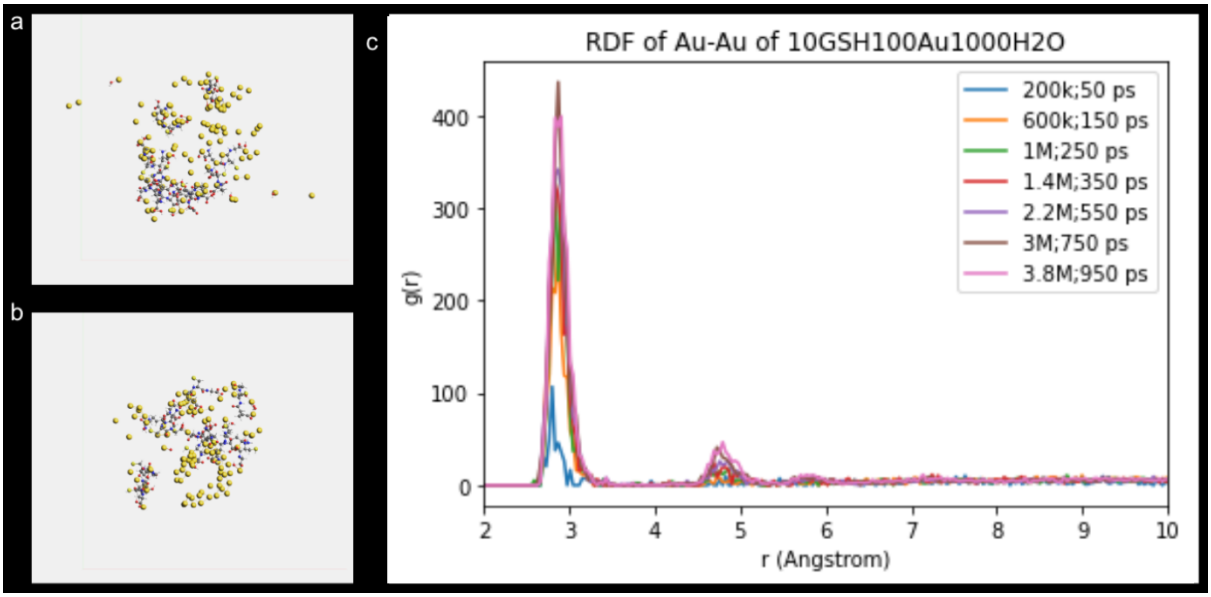


Figure 6. 13 Snapshot of 10 GSH with 100 Au atoms with 1000 water molecules at a) 200k step, 50 ps. b) 3.8M step, 950 ps. c) RDF of all the calculated snapshots combined.

Thiol-containing ligands generally provide stronger stabilization compared to carboxyl group ligands because of the strong covalent bonds between Au and S, which are advantageous for producing smaller, monodisperse AuNPs. Carboxyl group ligands, on the other hand, offer a simpler solution for slowing nucleation by reducing surface energy without forming strong bonds between the AuNP surface and the capping agent. This allows easier further treatment of AuNPs for various applications.

6.7 Comparison of nucleation rates

This section will compare the nucleation rates of all capping agents used in the simulation. Figure 6.14 shows the nucleation rates with different ligands at 3.8M steps, 950 ps. The nucleation rate at the first nearest neighbour distance of 2.8 Å, from fastest to slowest, is as follows: no capping, acetic, propionic, cysteine (Cys), oxalic, glutathione (GSH), and citric. It is interesting that citric acid has the slowest nucleation rate, even when compared to GSH, which is a much larger molecule with a thiol group.

Compared to the 100-Au cluster in vacuum (Appendix 3 Figure A.3.1), there is no visible peak at the second nearest neighbour distance, which corresponds to the lattice distance of FCC gold at 4 Å. All the aqueous nucleation simulations, with or without a capping agent, show a left-shifted peak at the third nearest neighbour distance, ranging from 5 Å to 4.75 Å. This left-shifted peak indicates that the positions of the gold atoms are misaligned compared to the 100-Au cluster in vacuum, which follows the crystal structure. The gold atoms located on the left-shifted peak location prevents another Au atom from fitting into the second nearest neighbour position, hindering the formation of a lower-energy crystal structure.

However, if the simulation runs long enough, the Au atoms might eventually restructure themselves to adopt the lowest energy crystal structure, favouring the FCC gold structure, with a peak at the second nearest neighbour distance of 4 Å, which is the lattice constant of gold. On the other hand, it is also possible for the Au atoms to form a “magic number” (Zeng et al., 2016) structure and exist as a stable nanocluster. The “magic number” structure usually refers to a very small AuNPs (usually refers to nanocluster if the size is small enough <200 gold atoms.)

that are capped with thiol ligands (Zeng et al., 2014, Li et al., 2014). This structure is a stable configuration as in the ligands are part of the nanocluster forming an Au-S-Au-S-Au staple motif on the surface of the nanocluster (Goswami et al., 2016).

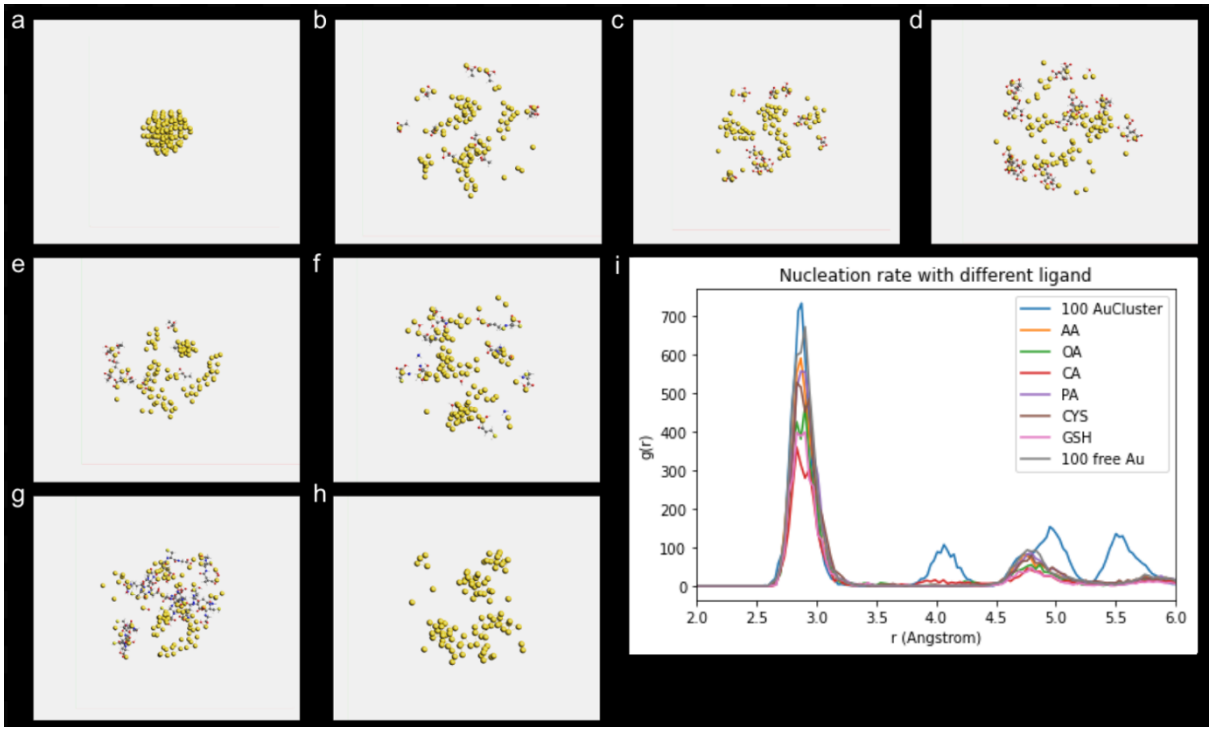


Figure 6. 14 Snapshot of the nucleation with different ligands at 3.8M step, 950 ps. a) 100-Au Cluster in vacuum (also shown on Appendix 3 Figure A.3.1). b) acetic acid. c) oxalic acid. d) citric acid. e) propionic acid. f) L-Cys. g) GSH. h) 100 free gold atoms in water. i) RDF of all the different ligands at 3.8M step, 950 ps.

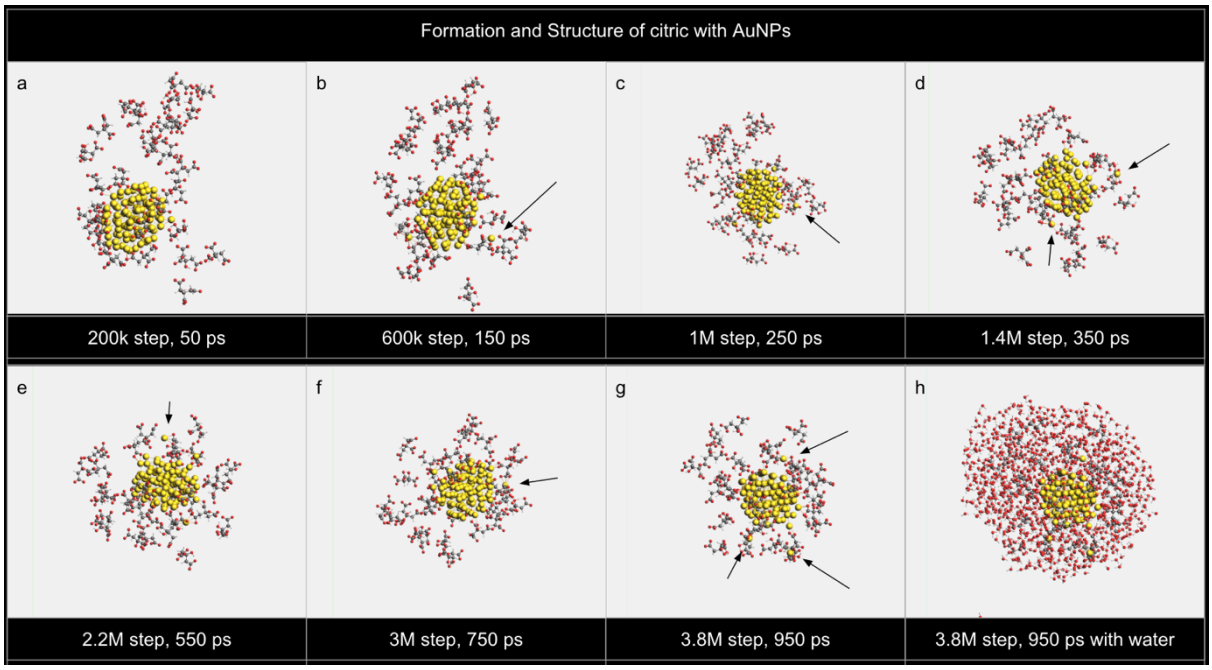
6.8 Citric acid with 100Au NPs

After studying the effect of the functional group on a ligand's influence on the nucleation rate of AuNPs, it is important to understand the morphology of the capping agent around already formed AuNP surfaces. In this section, a simulation with a pre-made 100-Au cluster in vacuum (Appendix III Figure A.3.1) with method mentioned in Chapter 3 section 3.9.1, was added to the simulation box, along with 1000 water molecules and 30 citric acid molecules, to investigate the structure of citric acid around the surface of the 100-Au cluster.

Initially, at 200k steps, the citric molecules are unevenly distributed, as shown in Figure 6.15a. However, over time, the citric molecules become more evenly distributed around the surface of the 100-Au cluster, as seen in Figure 6.15g. Although the citric molecules are evenly distributed after 3.8M steps, they do not fully cover the surface of the 100-Au cluster. A similar citric crown motif was also observed in another study (Perfilieva et al., 2019), where citric acid molecules did not provide full surface coverage of the AuNPs, leaving areas exposed for adatoms to adhere to.

From Figure 6.15b, an etched Au atom was found in the middle of the citric molecule chain, leaving the Au cluster at 600 k steps. This etched Au atom was also observed later in the simulation, as indicated by the black arrow in Figures 6.15b to 6.15g. This suggests that the size of this AuNP, combined with the citric acid molecules on the surface, is not stable. The citric molecules can etch Au atoms from the surface of the Au cluster, resulting in a decrease in the first nearest neighbour count, as shown in Figure 6.15i.

It is possible that the 100-Au cluster could completely dissolve into a hybrid structure, as described in Section 6.5. On the other hand, it is also possible that the 100-Au cluster will reach a lower surface energy state by restructuring the unstable surface adatoms and binding with additional citric molecules (Dachraoui et al., 2021b), making the cluster more stable. This could lead to a size selection approach (Hussain et al., 2020).



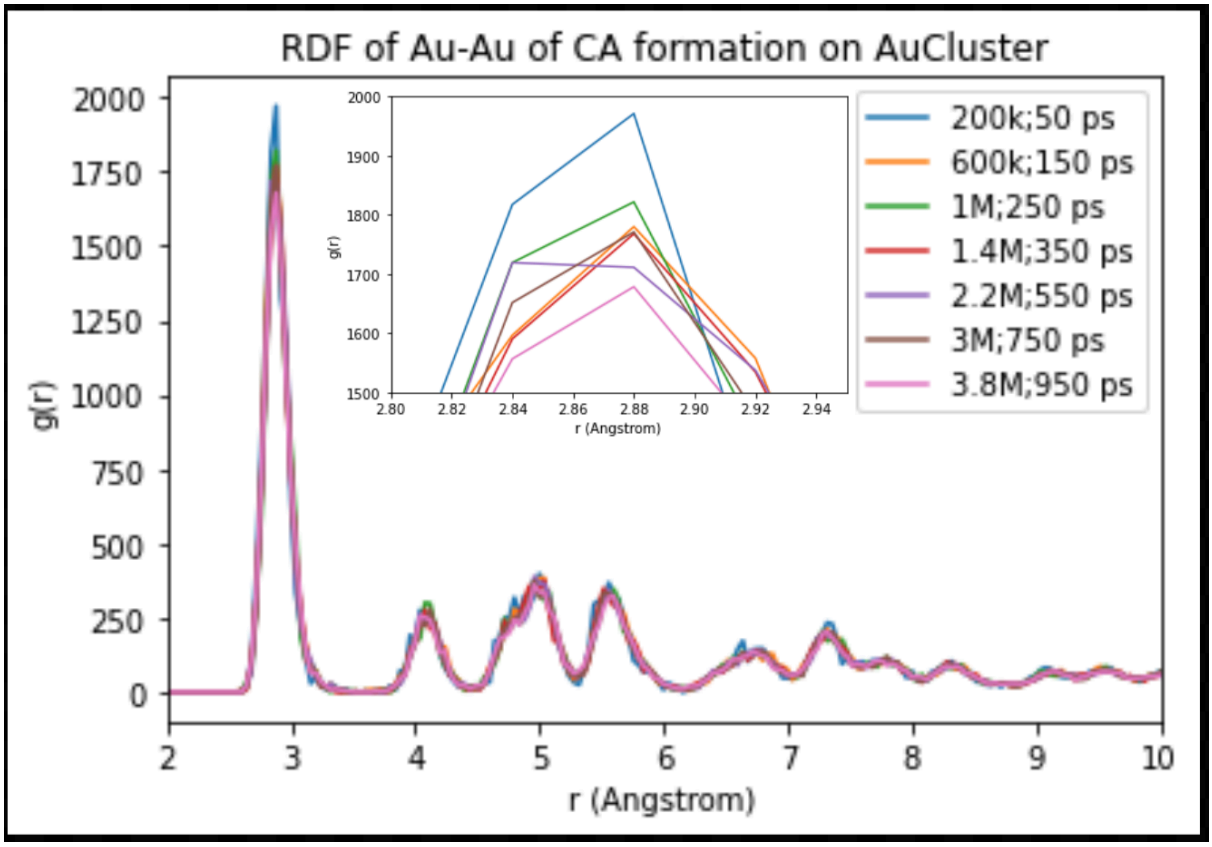


Figure 6. 15 Snapshot of 30 citric acid with 100-Au Cluster with 1000 water molecules. Arrow indicates an etched Au atom. a) 200k step, 50 ps. b) 600k step, 150 ps. c) 1M step, 250 ps. d) 1.4M step, 350 ps. e) 2.2M step, 550 ps. f) 3M step, 750 ps. g) 3.8M step, 950 ps. h) 6.14g with water molecules. i) RDF of all the snapshot combined.

6.9 Growth of citrate-capped AuNPs with free gold atoms

After studying the possibility of ligand etching atoms from the surface of the 100-Au cluster, it is important to examine how this influences the growth of the cluster when more free Au atoms are available. In this study, we compared the growth

rate in two scenarios: one with 30 citric acid molecules and 90 free gold atoms, and another where 30 citric acid molecules are already bonded with 3 gold atoms each.

From Figures 6.16 and 6.17, it is observed that both scenarios, whether free gold atoms are present in the simulation or not, result in a similar structure, judging by the height of the first nearest-neighbour peak. However, both scenarios end up with a lower first nearest-neighbour peak compared to the 100-Au cluster (Appendix III, Figure A.3.1). This suggests that the addition of citric molecules, even with free gold, does not induce further growth or nucleation in the system. Instead, the addition of citric acid causes the crystal structure to develop defects or become amorphous, thereby destabilizing the 100-Au cluster. This results in a lower coordination compared to a perfect FCC gold crystal structure, as shown in Figure 6.17c.

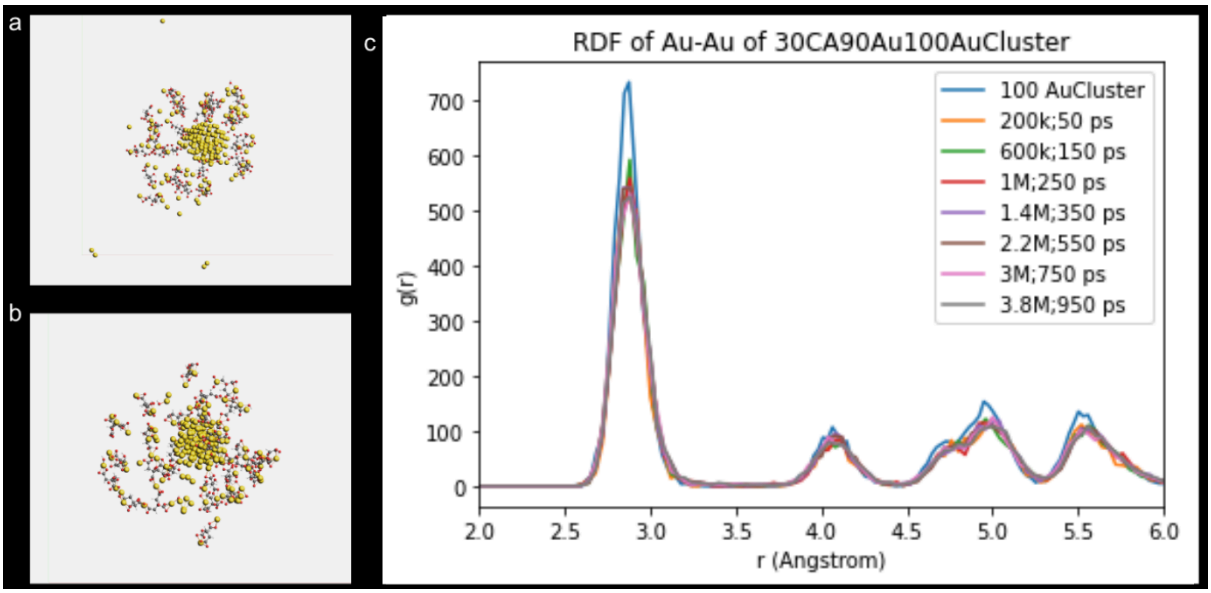


Figure 6. 16 Snapshot of 30 citric acid with 90 free Au atoms and 100 Au cluster with 1000 water molecules at a) 200k step, 50 ps. b) 3.8M step, 950 ps. c) RDF of all the snapshots combined.

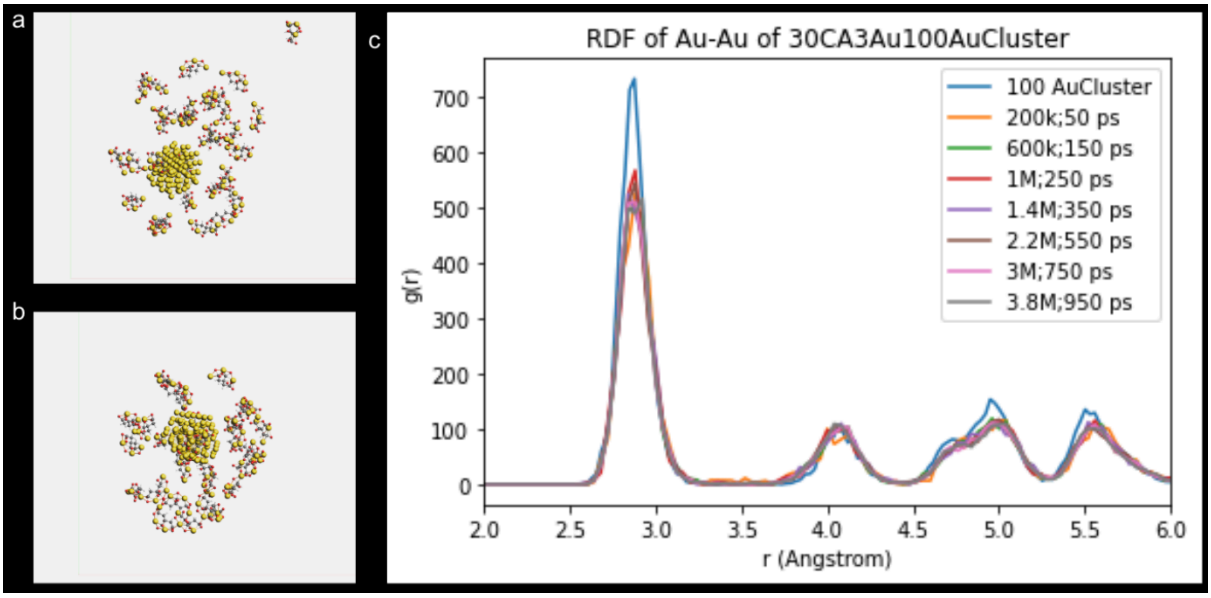


Figure 6. 17 Snapshot of 30 citric acid already bonded with 3 Au atoms and 100 Au Cluster with 1000 water molecules at a) 200k step, 50 ps. b) 3.8M step, 950 ps. c) RDF of all the snapshots combined.

6.10.1 Growth with carboxyl group ligands (acetic acid)

To further investigate the effect of carboxyl group ligands on growth and stability in the medium, we start with a ligand containing one carboxyl group, acetic acid. Here, we compare the growth and stability when the molar ratio of acetic acid to gold is the same, with 90 free gold atoms and 30 acetic acid molecules, as in the

previous case with citric acid. Citric acid was chosen as the base for comparison because it is commonly used as a capping agent.

When a molar ratio of 1:1 is chosen for acetic acid to gold (e.g., 30 acetic acid molecules to 30 free gold atoms), significant nucleation (as seen in the first nearest-neighbour peak) and growth (observed in the second, third, and fourth nearest-neighbour peaks) were noted, as shown by the blue and yellow curves in Figures 6.18a and 6.18c. Interestingly, when the number of free gold atoms is increased to 90 (a molar ratio of 1 acetic molecule to 3 gold atoms), there is no increase in the RDF, indicating no nucleation or growth. This suggests that the combination of 30 acetic molecules, 30 free gold atoms, and a 100-Au cluster does not reach a lower energy level, as in the "magic number" state (Cowan and Mpourmpakis, 2019).

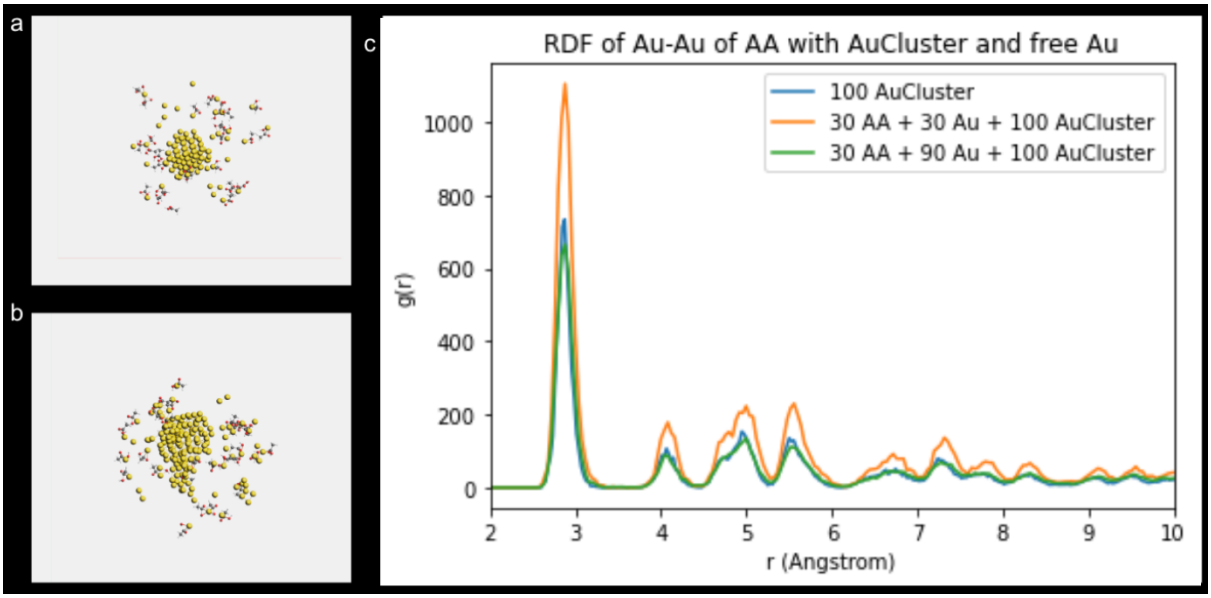


Figure 6. 18 Snapshot of a) 30 acetic acids with 30 Au atoms and 100-Au Cluster with 1000 water molecules at 3.8M step, 950 ps. b) 30 acetic acids with 90 Au

atoms and 100-Au Cluster with 1000 water molecules at 3.8M step, 950 ps. c) RDF of 6.18a and 6.18b at 3.8M step, 950 ps.

6.10.2 Growth with carboxyl group ligands (oxalic acid)

When acetic molecules are replaced by oxalic acid molecules, the phenomenon of the capping agent destabilizing the 100-Au cluster still occurs. With 30 oxalic molecules and 60 free gold atoms added to the 100-Au cluster, the first nearest-neighbour peak is higher than in the 100-Au cluster alone. This suggests that the combination of 30 oxalic acid molecules and 60 gold atoms favours nucleation, as indicated by the first nearest-neighbour peak in Figure 6.19c. The increase in the second, third, and fourth nearest-neighbour peaks also indicates the growth of the crystal structure. However, when the number of free gold atoms is increased to 90, the cluster destabilizes, as evidenced by the lower first nearest-neighbour peak. Additionally, the decrease in the second, third, and fourth nearest-neighbour peaks suggests that this combination of capping agent and free gold atoms does not favour crystal growth. It is unclear why, despite the presence of free gold atoms, growth does not occur, and the cluster instead dissolves.

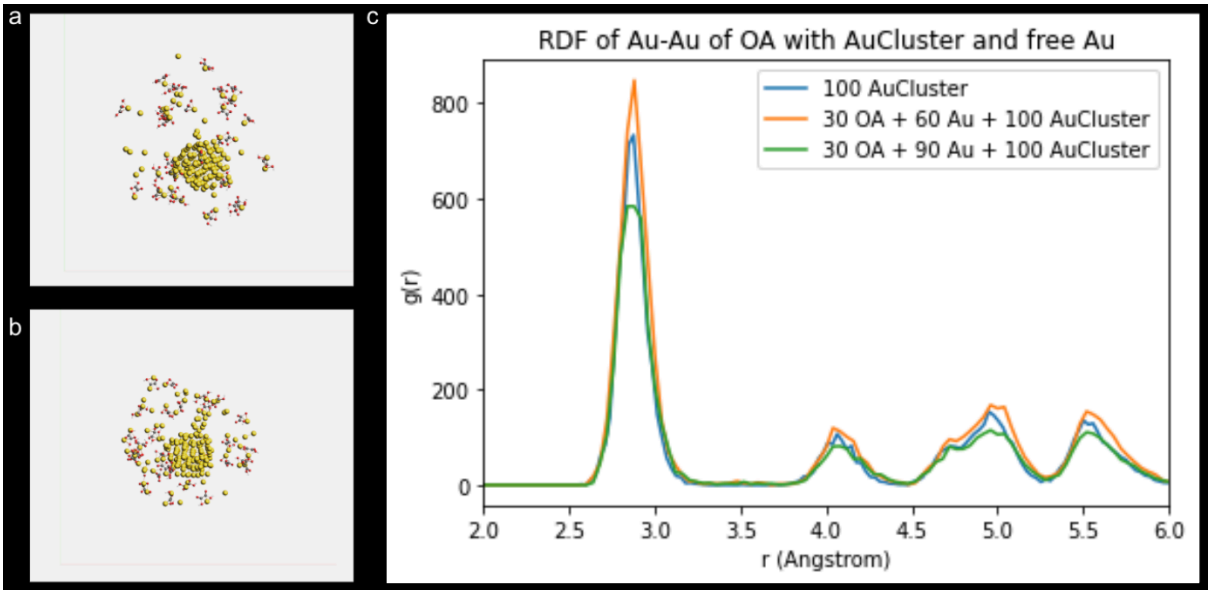


Figure 6. 19 Snapshot of a) 30 oxalic acids with 60 Au atoms and 100-Au Cluster with 1000 water molecules at 3.8M step, 950 ps. b) 30 oxalic acids with 90 Au atoms and 100-Au Cluster with 1000 water molecules at 3.8M step, 950 ps. c) RDF of 6.19a and 6.19b at 3.8M step, 950 ps.

6.11 Comparison of growth rate of carboxyl ligand capped AuNPs

After comparing the nucleation and growth rates of individual carboxyl group-capped AuNPs, this section will compare the growth rate of carboxyl ligand-capped AuNPs with 90 free Au atoms and a 100-Au cluster. From Figure 6.20e, propionic acid and acetic acid both show a similar effect on the growth rate of the AuNPs and do not destabilize the 100-Au cluster significantly. However, citric acid destabilizes the 100-Au cluster, as indicated by the lowest first nearest-neighbour count.

With an excess of 90 free Au atoms, all carboxyl group ligands demonstrate the ability to control the nucleation rate of the excessive free Au atoms, as the blue curve remains the highest in Figure 6.20e. However, the possibility of nucleation with a destabilized core cannot be ignored. Hence, even though the blue curves remain the highest, the dropping of other curves can be attributed to the dissolution of the 100-Au cluster, resulting in a lower first nearest-neighbour count. Regarding the crystal structure, the 100-Au cluster remains in a relatively fault-free crystal structure, as the second, third, and fourth nearest-neighbour peaks remain relatively the same.

In the same manner as the results from the nucleation rate of different ligand-capped AuNPs in section 1.5, the growth rate follows a similar pattern in terms of the speed or dissolution rate of the ligand with free Au atoms and the 100-Au cluster. From fast to slow, the order is acetic acid = propionic acid > oxalic acid > citric acid. Acetic and propionic acid show the least effect on destabilizing the 100-Au cluster, while citric acid shows a significantly lower first nearest-neighbour count, indicating a more destabilized cluster. Oxalic acid falls in the middle.

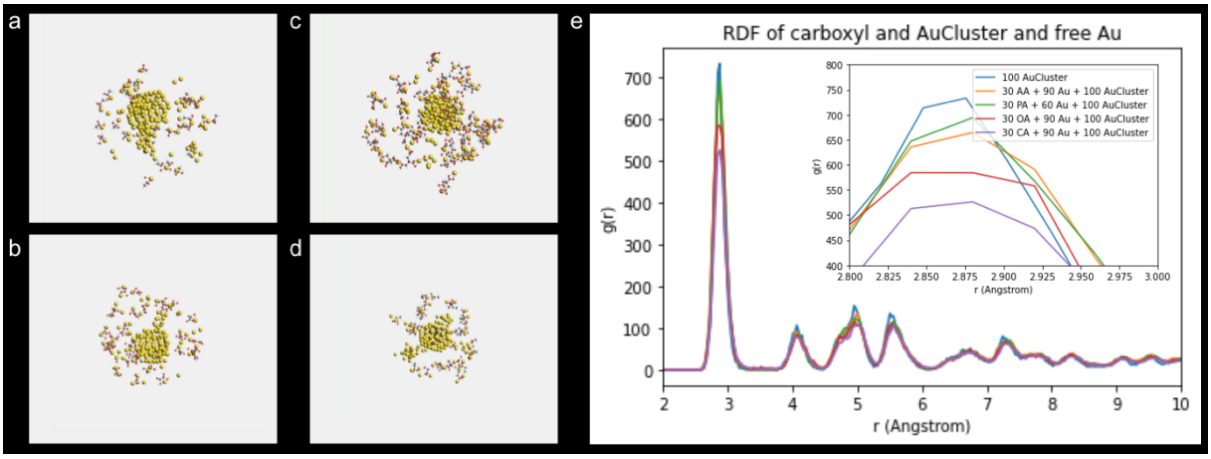


Figure 6. 20 Snapshot of a) 30 acetic acids with 90 free gold atoms and 100-Au Cluster with 1000 water molecules at 3.8M step, 950 ps. b) 30 oxalic acids with 90 free gold atoms and 100-Au Cluster with 1000 water molecules at 3.8M step, 950 ps. c) 30 citric acids with 90 Au atoms and 100-Au Cluster with 1000 water molecules at 3.8M step, 950 ps. d) 30 propionic acids with 90 Au atoms and 100-Au Cluster with 1000 water molecules at 3.8M step, 950 ps. e) RDF of 6.20a, 6.20b, 6.20c and 6.20d at 3.8M step, 950 ps.

6.12 Correlation between growth rates and carboxyl group numbers

After observing the unusual pattern where citric acid is the most destabilizing ligand among the carboxyl group ligands, it is important to investigate whether the number of carboxyl groups in a ligand also affects the growth rate. This section will compare the carboxyl ligands with the same number of free Au atoms to their respective number of carboxyl groups.

From Figures 6.21a and 6.21d, 30 acetic acid molecules and 30 free Au atoms show the highest amount of growth and nucleation compared to 30 oxalic acid molecules with 60 free Au atoms and 30 citric acid molecules with 90 free Au atoms. This suggests that even when the number of free Au atoms matches the number of carboxyl groups in the capping ligands, acetic and oxalic acid still fail to stabilize nucleation and growth in the simulation. Additionally, 30 citric acid

molecules with 90 free Au atoms destabilize the 100-Au cluster, as indicated by the lower RDF count. Eventually, the AuNPs in acetic and oxalic acid should grow with some small nuclei present in the media, while the AuNPs in citric acid will redistribute into a preferred size with multiple AuNPs.

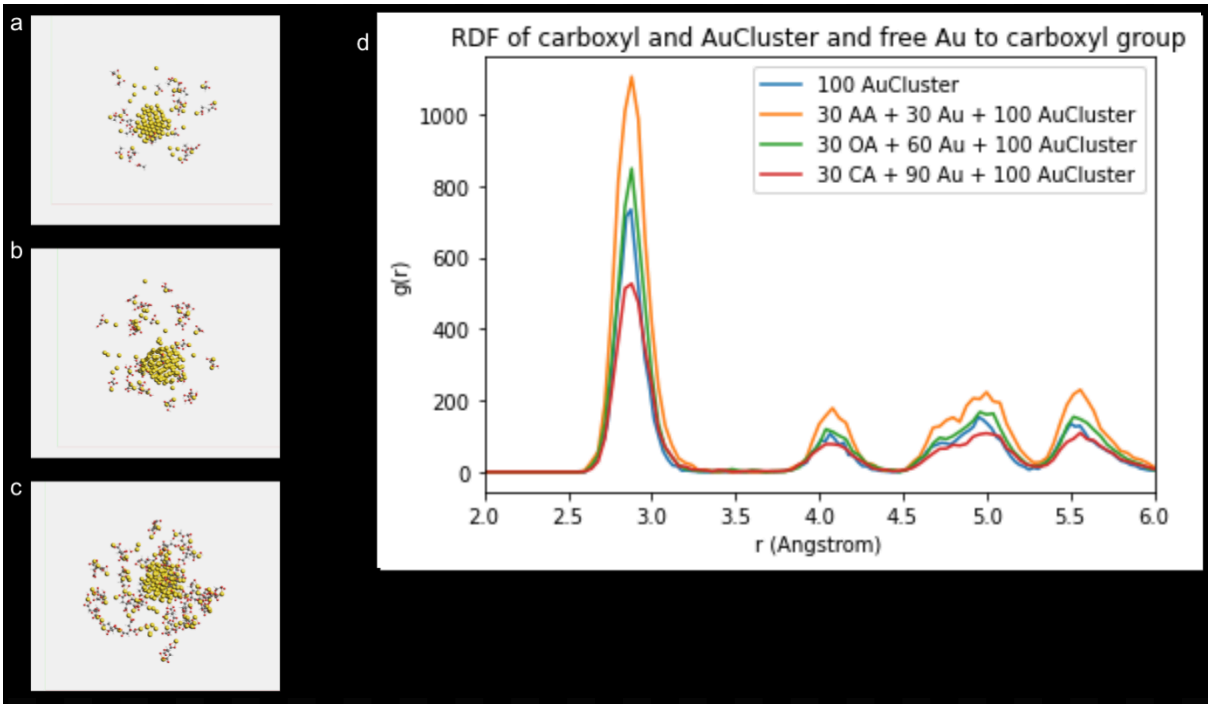


Figure 6. 21 Snapshot of a) 30 acetic acids with 30 free gold atoms and 100-Au Cluster with 1000 water molecules at 3.8M step, 950 ps. b) 30 oxalic acids with 60 free gold atoms and 100-Au Cluster with 1000 water molecules at 3.8M step, 950 ps. c) 30 citric acids with 90 Au atoms and 100-Au Cluster with 1000 water molecules at 3.8M step, 950 ps. d) RDF of 6.21a, 6.21b and 6.21c at 3.8M step, 950 ps.

6.13 Comparison of single carboxyl group ligands (acetic acid vs propionic acid)

After studying the correlation between the number of carboxyl groups in a ligand and the growth rate, it is also important to examine how the size of the ligand affects the growth rate of the AuNPs. This section will compare the growth rate of 30 acetic acid molecules with 90 free Au atoms to 30 propionic acid molecules with 90 free Au atoms. Both acetic and propionic acids contain a single carboxyl group, but propionic acid has a longer carbon chain. This provides an opportunity to compare the effect of steric hindrance on the growth rate.

From Figure 6.22c, there is no significant difference in the steric effect of a longer carbon chain in terms of the growth rate of the AuNPs. However, the acetic acid simulation shows a lower first nearest neighbour peak compared to propionic acid. Although both cases show that the 100-Au cluster is restructuring or destabilizing, a carboxyl group with a longer carbon chain, like in propionic acid, provides better stability to the cluster, as evidenced by the slightly higher first nearest neighbour peak.

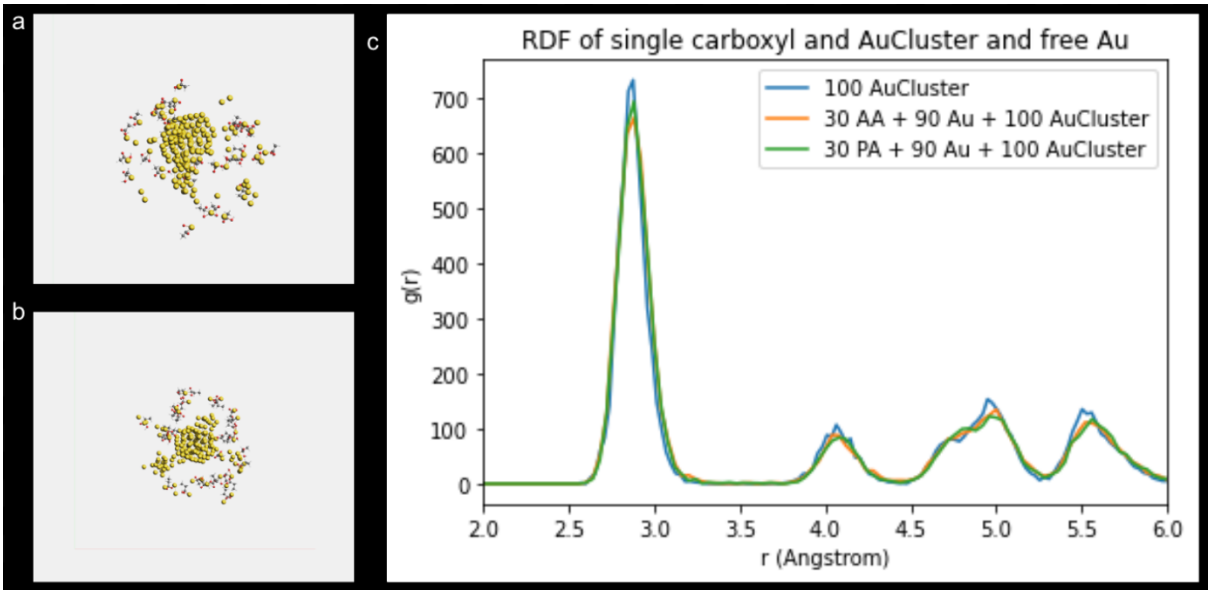


Figure 6. 22 Snapshot of a) 30 acetic acids with 90 free gold atoms and 100-Au Cluster with 1000 water molecules at 3.8M step, 950 ps. b) 30 propionic acids with 90 free gold atoms and 100-Au Cluster with 1000 water molecules at 3.8M step, 950 ps. c) RDF of 6.22a and 6.22b at 3.8M step, 950 ps.

6.14 Comparison of thiol ligands (L-cys, GSH) with citric acid

As the steric effect of carboxyl group ligands shows a small impact, this section will investigate the steric effect of thiol group ligands, such as L-cysteine (Cys) and glutathione (GSH). From Figure 6.23d, all capping agents (Cys, GSH, and citric acid) show signs of destabilizing the 100-Au cluster, with citric acid having the most significant effect on the crystal structure of the 100-Au cluster. GSH shows a similar peak to citric acid, suggesting it has a comparable potential for destabilizing the 100-Au cluster. In contrast, cysteine has a higher peak, which may indicate

that individual atoms, as observed in Chapter 6, are clusters that are dissolving and stabilizing due to the ligand used in the experiment.

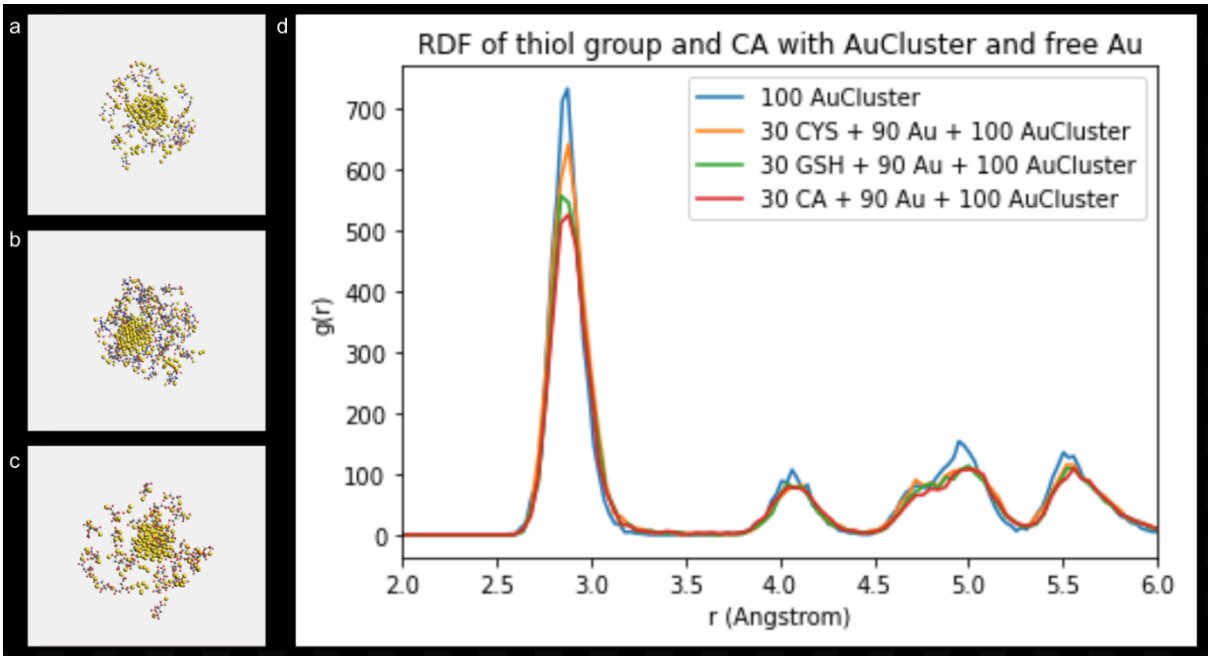


Figure 6. 23 Snapshot of a) 30 Cys with 90 free gold atoms and 100-Au Cluster with 1000 water molecules at 3.8M step, 950 ps. b) 30 GSH with 90 free gold atoms and 100-Au Cluster with 1000 water molecules at 3.8M step, 950 ps. c) 30 citric acids with 90 Au atoms and 100-Au Cluster with 1000 water molecules at 3.8M step, 950 ps. d) RDF of 6.23a, 6.23 and 6.23c at 3.8M step, 950 ps.

6.15 Conclusion

This chapter examines the early nucleation stage of AuNPs using reactive molecular dynamics with a reactive force field. This approach allows for the study

of the formation and interaction of nuclei, as well as the adatom growth of AuNPs, in the presence of carboxyl and thiol capping agents in aqueous media.

Regarding carboxyl group capping agents, acetic, oxalic, citric, and propionic acids stabilize AuNPs by coordinating through their carboxyl groups. Their influence on nucleation and growth rates depends significantly on the number of carboxyl groups in the ligand. For instance, ligands with a single carboxyl group, such as acetic and propionic acids, exhibit less stabilization power compared to citric acid, which contains three carboxyl groups.

In contrast, thiol groups stabilize AuNPs by forming strong covalent bonds with the Au atoms at the nanoparticle surface, creating a robust ligand layer that prevents further growth. However, the phenomenon of ligands destabilizing AuNPs was observed in multiple simulations, as discussed in Section 6.8. This observation provides valuable insights into the possible formation mechanisms of pre-nucleation clusters during nucleation and offers a solid foundation for understanding the long-term stability of PNCs during aging.

Table 6. 1 Influence on nucleation and growth rate with respect to Ligand type.

Ligand	Stabilization mechanism	Nucleation rate	Growth rate
Acetic acid	Mono-carboxyl	Fast	fast

Propionic acid	Mono-carboxyl, bigger than acetic	Fast	fast
Oxalic acid	di-carboxyl, stronger coordination	Moderate	Moderate
Citric acid	Tri-carboxyl, strong network	Slow	Controlled growth
L-Cysteine	Strong thiol Au-S bond	Moderate	Controlled growth
Glutathione	Multidentate thiol	slow	Controlled growth

The study of gold nanoparticle nucleation and growth through molecular dynamics using reactive force fields enhances our understanding by integrating the chemistry of ligand interactions with the physics of cluster formation. Reactive force fields enable accurate simulations of dynamic processes such as bond formation, ligand binding, and solvent effects, making them essential tools for exploring ligand-mediated mechanisms. Carboxyl and thiol groups play distinct yet complementary roles in stabilizing and guiding nanoparticle formation, offering important implications for the design of ligands for targeted nanoparticle synthesis.

6.16 Future work

Further studies should focus on developing a ReaxFF potential that incorporates elements such as boron, sodium, chloride, and other species that may be present during the synthesis of AuNPs. This would help investigate the reduction mechanisms involved in AuNP synthesis. Such advancements would provide a solid foundation for understanding non-classical nucleation pathways and offer a robust method for using molecular dynamics to study the formation and interactions of pre-nucleation clusters (PNCs).

Chapter 7: Conclusions and Future Work

The primary aim of this thesis was to investigate the growth and stability of sub-10 nm AuNPs in aqueous media with different carboxyl and thiol based capping agents. To study the mechanisms of early nucleation stage and initial growth, different pH, molar ratio with different capping agent namely acetic acid, oxalic acid, citric acid, propionic acid, L-cysteine, glutathione was used in the synthesis of AuNPs. With the help of atomic resolution HAADF-STEM and reactive molecular dynamics, an understanding on classical and non-classical nucleation pathways with an emphasis on the existence and role of PNCs can be developed.

The aim of the first research chapter was also to investigate the size and shape changes with respect to time of AuNPs in aqueous media. This sub-10 nm AuNPs were synthesized using sodium borohydride as a reducing agent, this chapter focus on the impact of key factors such as pH, molar ratio of capping agent to gold, the number of carboxyl groups in the capping agent, and the size of the capping agent on the growth behaviour of AuNPs with HAADF-STEM.

The first research chapter shows that contrary to conventional expectations, increasing the molar ratio of capping agent to gold did not result in smaller AuNPs. Among the conditions tested, pH 6 provided optimal dispersity and stability, showing the least changes as a function of aging. At lower pH levels and low molar ratios, acetic and oxalic acid were less effective in controlling particle size compared to citric or the absence of a capping agent, though this size variation

diminished at higher molar ratios. The study also found pre-nucleation clusters (PNCs) in most suspensions, whose exact role in nucleation and growth remains unclear in this chapter. However, the presence of PNCs in nearly all systems studied suggested their metastable nature and potential role in mediating particle morphology and growth, particularly during the early nucleation stages.

The aim of the second research chapter was to investigate the size and morphology changes of L-cysteine and glutathione capped AuNPs and citric, L-cysteine capped AgNPs with respect to time. Comparing the difference in nucleation and growth between carboxyl group capped AuNPs and thiol group capped AuNPs and understanding the nature of PNCs.

The second research chapter provided an in-depth characterization of PNCs, highlighting their metastable properties, with persistence in solution for up to 28 days and a size range of up to 5 nm. The study revealed distinct ligand-dependent behaviours: carboxyl-based PNCs exhibited a “sticky” nature, facilitating core-shell formation, bridging between nanoparticles, and structural transformations, while thiol-based PNCs displayed non-sticky behaviour. The bridging and adhesive nature of PNCs drove unpredictable aging processes, including the formation of non-spherical structures and nano-string morphologies, deviating from classical growth pathways. Additionally, the study suggested that amorphous PNCs undergo irreversible crystallization, further influencing the structural evolution of AuNPs.

The aim of the third chapter was to utilize the reactive molecular dynamics to bridge the gap between the findings observed in first two chapters by simulating the atomistic view of the early nucleation stages and initial growth of AuNPs in the presence of carboxyl and thiol capping agents.

The third research chapter successfully compared the nucleation and initial growth of AuNPs with ligands used in the carboxyl capped AuNPs chapter and the thiol capped AuNPs chapter. Carboxyl groups stabilized AuNPs through coordination interactions, with their stabilizing power dependent on the number of carboxyl groups in the ligand. Conversely, thiol groups stabilized AuNPs through strong covalent bonds, creating a robust ligand layer that hindered growth but occasionally led to destabilization. The simulations provided valuable insights into ligand-mediated nucleation mechanisms and the role of PNCs in early-stage growth dynamics, emphasizing the complementarity of carboxyl and thiol groups in guiding nanoparticle formation.

Combining all findings in research chapters, this thesis shows the correlation of classical and non-classical nucleation pathways by highlighting the critical role of PNCs as intermediates in the formation and growth of sub-10 nm AuNPs with the present of ligands.

These intermediate PNCs exist in AuNP synthesis using sodium borohydride as a strong reducing agent, along with commonly used capping agents such as citrate and other carboxyl-based ligands, including acetate, oxalate, and propionate, as well as thiol-based ligands like L-cysteine and glutathione.

Given their presence as stable entities in almost all solutions, it is highly likely that PNCs persist in solution for extended periods and act as mediators, facilitating structural transformations of the initial AuNPs. These transformations occur through mechanisms such as core-shell formation, bridging, and crystallization. PNCs redistribute additional atoms from nearby clusters and reorganize surface atoms of the original nanoparticles (NPs), enhancing the formation of nano-string structures in solution. This process ultimately leads to irreversible changes in the size and shape of the original NPs, resulting in aging into unpredictable morphologies with potential shifts in surface chemistry.

The recurring nature of these cluster-cloud PNCs has also been demonstrated in studies using liquid-cell STEM without any capping agent on PdNPs (Dachraoui and Erni, 2023), alloy (Dachraoui et al., 2022, Sun et al., 2023).

Ligand chemistry plays a significant role in determining the properties of PNCs, which directly influence the stability of NPs and their growth pathways, as demonstrated in this project.

The predictability of NP morphology evolution over time is heavily impacted by PNC-mediated interactions mentioned in chapter 5, often leading to unpredictable morphologies and properties that deviate from classical nucleation and growth pathways. For instance, differences between carboxyl group PNCs and thiol group PNCs were observed in STEM, as discussed in Chapter 5.

The nucleation and growth simulations presented in Chapter 6 provide a solid foundation for studying PNCs using reactive molecular dynamics (r-MD). Dachraoui and colleagues (Dachraoui et al., 2021a, Dachraoui et al., 2021b) observed the possibility of surface reconfiguration in the absence of capping agents. Similarly, in Chapters 4 and 5, this project demonstrated the recrystallization process of PNCs, revealing that it is possible to retain core density while facilitating surface crystallization into a favorable lattice structure, as discussed in Section 5.11.

These findings, complemented by the insights from Chapter 6, highlight the strong tendency for reconfiguration of NP surfaces. This phenomenon is further amplified by the potential etching of surface atoms by capping agents, particularly in the case of citrate coordination (Grys et al., 2020).

Additionally, it is possible that the sodium borohydride reduction method creates a more heterogeneous nucleation system. In the Turkevich method, the capping agent (citric acid) molecules are evenly distributed in the solution along with chloroauric acid. Nucleation is then initiated by elevating the temperature to boiling, allowing for more homogeneous nucleation throughout the aqueous medium. On the other hand, the sodium borohydride reduction method used in Chapters 4 and 5 involves adding the reducing agent to the solution after mixing the capping agent and chloroauric acid. This process may create a slightly heterogeneous nucleation system, where the reducing agent reacts with the gold precursor it first encounters. This could result in uneven reduction across the medium, leading to a heterogeneous nucleation system.

However, there are differences between experiment and simulation. Comparing the observational results from the synthesis chapter and the molecular dynamics chapter, nucleation is completely stopped by citric acid molecules if all citric acid molecules bond with three gold atoms. In the simulation, the molar ratio is approximately one citric acid molecule to three gold atoms (0.33:1), which is lower than the ratios used in the synthesis experiments conducted in this thesis.

Unfortunately, simulating conditions identical to the experiments is currently unfeasible due to the rare nature of nucleation (Finney and Salvalaglio, 2023) and computational limitations. For example, the synthesis protocol mentioned in chapter 3 and conducted in chapter 4 and chapter 5 are using a molar ratio of water to gold of 200k:1. To simulate 1 gold atom is physically not possible.

Classical MD simulations have been performed on systems such as calcium sulfate (Li et al., 2017) and calcium phosphate (Garcia et al., 2019) to study the nature of PNCs (Zhang et al., 2024). Building on this approach, the present work successfully explores the early stages of nucleation with various ligands present in an aqueous environment, as discussed in Chapter 6. Additionally, by complementing studies on the self-assembly of metal-organic frameworks (Yoneya et al., 2015), this research provides valuable insights into the formation of super-lattice structures (Figure 7.1) observed in Chapter 5, Section 5.7 and in the universe (Sousbie et al., 2011).

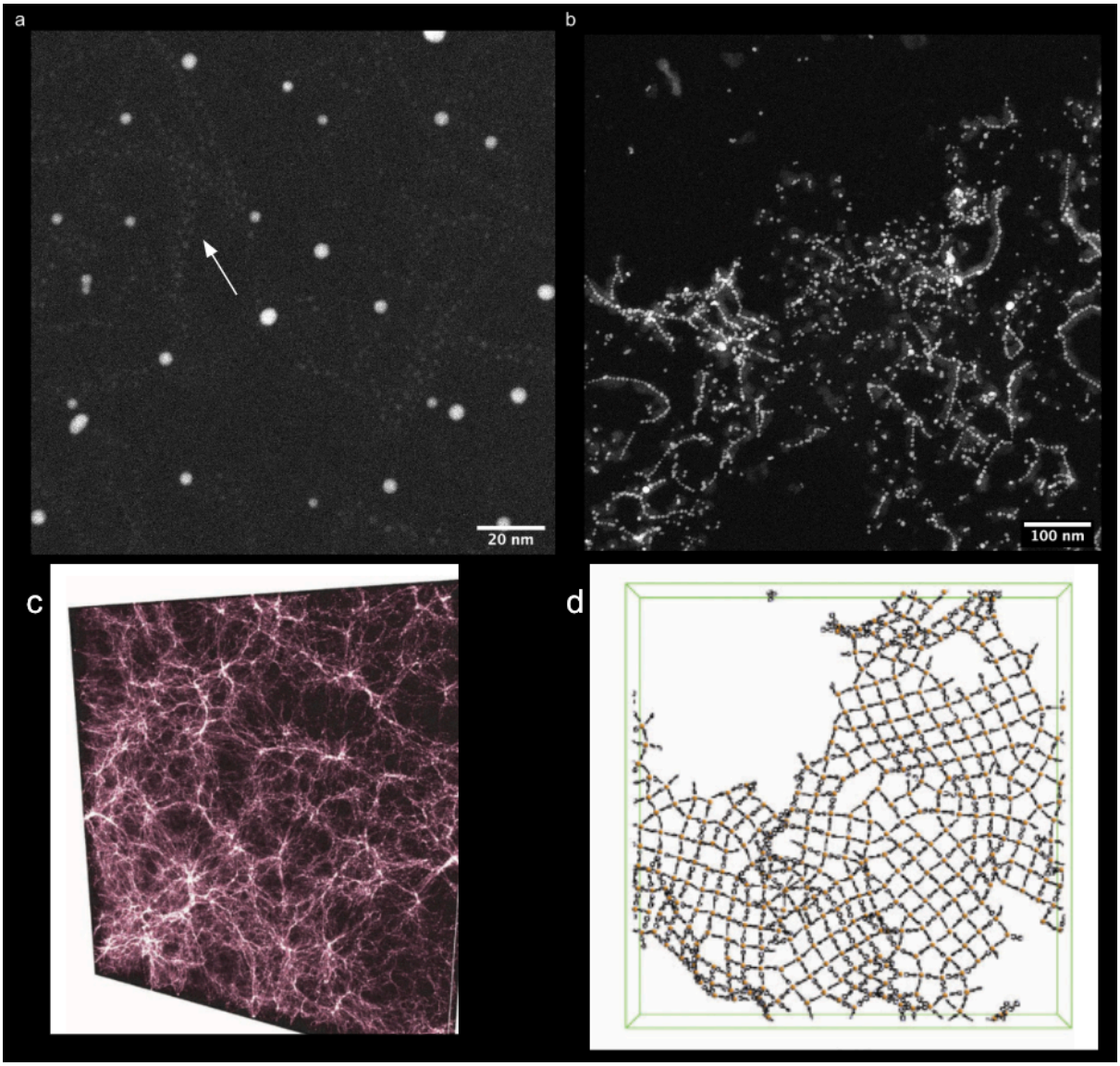


Figure 7. 1. Super-lattice structure observed in STEM images of a) acetate capped AuNPs on pH 6.1 at 1 day with molar ratio 1:10.6. b) oxalate capped AuNPs with 1:1.5 on pH 3 at 7 days. c) Simulation of cosmic web with dark matter (Sousbie et al., 2011). d) Simulation of self-assembly metal-organic framework (Yoneya et al., 2015).

In theory, if the simulation adopted the same molar ratio as the synthesis, no nucleation should occur in experiments because the excess carboxyl groups in the citric acid molecules would capture all free gold atoms and prevent nucleation.

However, this was not the case as nucleation and growth was observed with molar ratio of gold to capping agents up to 1:10.5 as presented in chapter 4. This discrepancy between experimental and simulation results highlights critical gaps in understanding the interactions between precursors and ligands in solution. Further investigation into the reduction mechanisms and the initial growth processes of AuNPs is necessary to bridge this gap.

New frameworks should be developed to include the dynamics nature of nucleation (Jia et al., 2023) integrating elements of classical nucleation theory with non-classical nucleation theory (Fu et al., 2021). These frameworks should also account for ligand interactions and the potential roles of intermediate species and structural transformations, tracing the progression from monomers to PNCs, "magic-sized" nanoclusters, and eventually fully grown NPs.

The combination of experimental observation and nucleation simulation provides a robust approach to overcoming the limitations inherent in direct observation techniques.

While the advancements in in-situ liquid-cell STEM characterization techniques (Lv et al., 2025, Liu et al., 2021) have offered fascinating insights into the study of PNCs, these methods still face significant challenges. One such challenge is the difficulty in modifying experimental parameters to comprehensively study the dynamic nature and behaviour of PNCs using these techniques.

This thesis demonstrated the multiple pathway nucleation also observable using traditional STEM characterisation technique and still able to observe and characterise the PNCs as an ex-situ technique. This indicates the existence of non-classical nucleation pathways and PNCs in real synthesis processes, particularly when capping agents like carboxyl and thiol group ligands are present in the solution. While the observation is indirect compared to liquid-cell STEM, the experimental setup and characterization are much easier to conduct, enabling more extensive studies on PNCs. The study on PNCs is not limited to in-situ liquid-cell STEM (Dachraoui et al., 2021b). With a careful consideration of beam current and electron dose (Li et al., 2021), which can indued growth on the NPs (Loh et al., 2017) as mentioned in Chapter 5, the ex-situ method adopted in this thesis provides an alternative approach with the added benefit of allowing manipulation of experimental parameters.

Chapter 8: Future Directions

This work highlights the complex nature of nanoparticle nucleation and growth. By carefully selecting characterization techniques and simulation approaches, it becomes possible to study the nucleation and growth mechanisms of AuNPs, complemented by ReaxFF molecular dynamics modelling to overcome challenges faced during experimental observations.

In the future, the study of nucleation, growth, and aging presented in Chapter 4 could be extended to include different ligands, such as PVP or amine groups. Additionally, the synthesis of other transition metal nanoparticles could be optimized to investigate their effects on nucleation and growth. Ideally, further research could deepen the understanding of the role of PNCs during nucleation, growth, and aging. Ultimately, a comprehensive synthesis approach could be developed, ensuring the availability of nanoparticles of all sizes with well-understood properties.

To achieve this, future research should also focus on advancing reactive molecular dynamics simulations to include additional elements (e.g., boron, sodium, and chloride) involved in AuNP synthesis. This will enable a deeper exploration of reduction mechanisms and ligand-mediated pathways. Additionally, simulations involving a greater number of ligands could be conducted to test the hypotheses presented in Chapter 6. Section 6.8 discusses the potential for ligands to dissolve crystallized NPs, while Section 6.5 explores the possibility of ligands

completely inhibiting nucleation. However, a boundary where PNCs transition into nanoclusters should exist. Studying this transformation through molecular dynamics simulations would be a fascinating topic for future research.

Furthermore, simulation and modelling approaches are essential for addressing challenges in directly observing PNCs, as the process of observing PNCs may introduce biases in the results, as noted at the end of the chapter 5. These approaches can provide a robust understanding of the dynamic interactions between PNCs and NPs.

Additionally, the relationship between PNCs and "magic number" nanoclusters should be investigated. Given their relatively similar size, this could provide valuable insights into the boundary conditions between nanoclusters and PNCs, further enhancing our understanding of PNCs. Furthermore, these "magic number" nanoclusters could potentially explain the pre-nucleation cluster-cloud observed in many synthesis processes including carboxyl group capped AuNPs.

To conduct this investigation, a general approach using liquid-cell STEM could be adopted (Dachraoui et al., 2021b) with capping agents such as carboxyl or thiol group ligands. However, introducing a reducing agent for the gold precursor poses a challenge, as there is currently no external method to add a reducing agent directly into the microscope.

By integrating experimental observations with computational simulations, this work offers valuable insights for designing tailored ligands and optimizing nanoparticle

synthesis processes. Ultimately, it contributes to advancing the field of nanomaterials by enabling precise control over nanoparticle size, shape, and stability. Once a well-established approach for all nanomaterials is achieved, a comprehensive theory encompassing their behaviours, properties, and toxicity can be developed.

References

ABID, N., KHAN, A. M., SHUJAIT, S., CHAUDHARY, K., IKRAM, M., IMRAN, M., HAIDER, J., KHAN, M., KHAN, Q. & MAQBOOL, M. 2022. Synthesis of nanomaterials using various top-down and bottom-up approaches, influencing factors, advantages, and disadvantages: A review. Adv Colloid Interface Sci, 300, 102597.

AGMO HERNÁNDEZ, V. 2023. An overview of surface forces and the DLVO theory. ChemTexts, 9.

AGRAWAL, S., MYSKO, R. A., NIGRA, M. M., MOHANTY, S. K. & HOEPFNER, M. P. 2021. Plasmonic Photocatalytic Enhancement of L-Cysteine SelfAssembled Gold Nanoparticle Clusters for Fenton Reaction Catalysis.pdf. Langmuir, 37, 3281-3287.

AL-JOHANI, H., ABOU-HAMAD, E., JEDIDI, A., WIDDIFIELD, C. M., VIGER-GRAVEL, J., SANGARU, S. S., GAJAN, D., ANJUM, D. H., OULD-CHIKH, S., HEDHILI, M. N., GURINOV, A., KELLY, M. J., EL ETER, M., CAVALLO, L., EMSLEY, L. & BASSET, J. M. 2017. The structure and binding mode of citrate in the stabilization of gold nanoparticles. Nat Chem, 9, 890-895.

AMINA, S. J. & GUO, B. 2020. A Review on the Synthesis and Functionalization of Gold Nanoparticles as a Drug Delivery Vehicle. Int J Nanomedicine, 15, 9823-9857.

AN, D., SU, J., WEBER, J. K., GAO, X., ZHOU, R. & LI, J. 2015. A Peptide-Coated Gold Nanocluster Exhibits Unique Behavior in Protein Activity Inhibition. J Am Chem Soc, 137, 8412-8.

BALFOURIER, A., LUCIANI, N., WANG, G., LELONG, G., ERSEN, O., KHELFA, A., ALLOYEAU, D., GAZEAU, F. & CARN, F. 2020. Unexpected intracellular biodegradation and recrystallization of gold nanoparticles. Proc Natl Acad Sci U S A, 117, 103-113.

BERENDSEN, H. J. C., POSTMA, J. P. M., VAN GUNSTEREN, W. F., DINOLA, A. & HAAK, J. R. 1984. Molecular dynamics with coupling to an external bath. The Journal of Chemical Physics, 81, 3684-3690.

BEURTON, J., LAVALLE, P., PALLOTTA, A., CHAIGNEAU, T., CLAROT, I. & BOUDIER, A. 2020. Design of surface ligands for blood compatible gold nanoparticles: Effect of charge and binding energy. Int J Pharm, 580, 119244.

BHASKAR, S. P., VIJAYAN, M. & JAGIRDAR, B. R. 2014. Size Modulation of Colloidal Au Nanoparticles via Digestive Ripening in Conjunction with a Solvated Metal Atom Dispersion Method: An Insight Into Mechanism. The Journal of Physical Chemistry C, 118, 18214-18225.

BISWAS, A., BAYER, I. S., BIRIS, A. S., WANG, T., DERVISHI, E. & FAUPEL, F. 2012. Advances in top-down and bottom-up surface nanofabrication: techniques, applications & future prospects. Adv Colloid Interface Sci, 170, 2-27.

BRAULT, P., CHAMORRO-CORAL, W., CHUON, S., CAILLARD, A., BAUCHIRE, J.-M., BARANTON, S., COUTANCEAU, C. & NEYTS, E. 2019. Molecular dynamics simulations of initial Pd and PdO nanocluster growth in a magnetron gas aggregation source. Frontiers of Chemical Science and Engineering, 13, 324-329.

BRUST, M., WALKER, M., BETHELL, D., SCHIFFRIN, D. J. & WHYMAN, R. 1994. Synthesis of thiol-derivatised gold nanoparticles in a two-phase Liquid–Liquid system.pdf. J. Chem. Soc. Chem. Commun., 7, 801-802.

BURGI, T. 2015. Properties of the gold-sulphur interface: from self-assembled monolayers to clusters. Nanoscale, 7, 15553-67.

CARPENTER, J. E. & GRUNWALD, M. 2021. Pre-Nucleation Clusters Predict Crystal Structures in Models of Chiral Molecules. J Am Chem Soc, 143, 21580-21593.

CHA, E., CHUNG, H., JANG, J., LEE, J., LEE, E. & YE, J. C. 2022. Low-Dose Sparse-View HAADF-STEM-EDX Tomography of Nanocrystals Using Unsupervised Deep Learning. ACS Nano, 16, 10314-10326.

CHANG, C. I., LEE, W. J., YOUNG, T. F., JU, S. P., CHANG, C. W., CHEN, H. L. & CHANG, J. G. 2008. Adsorption mechanism of water molecules surrounding Au nanoparticles of different sizes. J Chem Phys, 128, 154703.

CHEN, R., NUHFER, N. T., MOUSSA, L., MORRIS, H. R. & WHITMORE, P. M. 2008. Silver sulfide nanoparticle assembly obtained by reacting an assembled silver nanoparticle template with hydrogen sulfide gas. Nanotechnology, 19, 455604.

CHEN, X., SCHRODER, J., HAUSCHILD, S., ROSENFELDT, S., DULLE, M. & FORSTER, S. 2015. Simultaneous SAXS/WAXS/UV-Vis Study of the Nucleation and Growth of Nanoparticles: A Test of Classical Nucleation Theory. Langmuir, 31, 11678-91.

CHEN, Y., XIANYU, Y. & JIANG, X. 2017. Surface Modification of Gold Nanoparticles with Small Molecules for Biochemical Analysis. Acc Chem Res, 50, 310-319.

CHENOWETH, K., DUIN, A. C. T. V. & GODDARD, W. A. 2008. ReaxFF Reactive Force Field for Molecular Dynamics Simulations of HydrocarbonOxidation.pdf. J. Phys. Chem. A, 112, 1040-1053.

CHOI, Y., CHO, B. K., SEOK, S. H., KIM, C., RYU, J. H. & KWON, I. C. 2023. Controlled spatial characteristics of ligands on nanoparticles: Determinant of cellular functions. J Control Release, 360, 672-686.

COWAN, M. J. & MPOURMPAKIS, G. 2019. Structure-property relationships on thiolate-protected gold nanoclusters. Nanoscale Adv, 1, 184-188.

DACHRAOUI, W. & ERNI, R. 2023. Nonclassical Nucleation and Growth of Pd Nanocrystals from Aqueous Solution Studied by In Situ Liquid Transmission Electron Microscopy. Chemistry of Materials, 35, 1201-1208.

DACHRAOUI, W., BODNARCHUK, M. I. & ERNI, R. 2022. Direct Imaging of the Atomic Mechanisms Governing the Growth and Shape of Bimetallic Pt-Pd Nanocrystals by In Situ Liquid Cell STEM. ACS Nano, 16, 14198-14209.

DACHRAOUI, W., HENNINEN, T. R., KELLER, D. & ERNI, R. 2021a. Multi-step atomic mechanism of platinum nanocrystals nucleation and growth revealed by in-situ liquid cell STEM. Sci Rep, 11, 23965.

DACHRAOUI, W., KELLER, D., HENNINEN, T. R., ASHTON, O. J. & ERNI, R. 2021b. Atomic Mechanisms of Nanocrystallization via Cluster-Clouds in Solution Studied by Liquid-Phase Scanning Transmission Electron Microscopy. Nano Lett, 21, 2861-2869.

DARUICH DE SOUZA, C., RIBEIRO NOGUEIRA, B. & ROSTELATO, M. E. C. M. 2019. Review of the methodologies used in the synthesis gold nanoparticles by chemical reduction. Journal of Alloys and Compounds, 798, 714-740.

DEL RÍO, E., HUNGRÍA, A. B., TINOCO, M., MANZORRO, R., CAUQUI, M. A., CALVINO, J. J. & PÉREZ-OMIL, J. A. 2016. CeO2-modified Au/TiO2 catalysts with outstanding stability under harsh CO oxidation conditions. Applied Catalysis B: Environmental, 197, 86-94.

DESGRANGES, C. & DELHOMMELLE, J. 2009. Molecular simulation of the nucleation and growth of gold nanoparticles.pdf. J. Phys. Chem. C, 113, 3607-3611.

DONG, J., CARPINONE, P. L., PYRGIOTAKIS, G., DEMOKRITOU, P. & MOUDGIL, B. M. 2020. Synthesis of Precision Gold Nanoparticles Using Turkevich Method. Kona, 37, 224-232.

D. Li, M. H. Nielsen, J. R. I. Lee, C. Frandsen, J. F. Banfield and J. J. D. Yoreo. 2012. Direction-Specific Interactions Control Crystal Growth by Oriented Attachment. Science Vol. 336 Pages 1014-1018.

DREADEN, E. C., ALKILANY, A. M., HUANG, X., MURPHY, C. J. & EL-SAYED, M. A. 2012. The golden age: gold nanoparticles for biomedicine. Chem Soc Rev, 41, 2740-79.

DUIN, A. C. T. V., DASGUPTA, S., LORANT, F. & GODDARD, W. A. 2001. ReaxFF: A Reactive Force Field for Hydrocarbons. J. Phys. Chem. A, 105, 9396-9409.

ESSAJAI, R. & HASSANAIN, N. 2018. Molecular dynamics study of melting properties of gold nanorods. Journal of Molecular Liquids, 261, 402-410.

ESSAJAI, R., RACHADI, A., FEDDI, E. & HASSANAIN, N. 2018. MD simulation-based study on the thermodynamic, structural and liquid properties of gold nanostructures. Materials Chemistry and Physics, 218, 116-121.

EYVAZZADEH, N., SHAKERI-ZADEH, A., FEKRAZAD, R., AMINI, E., GHAZNAVI, H. & KAMRAN KAMRAVA, S. 2017. Gold-coated magnetic nanoparticle as a nanotheranostic agent for magnetic resonance imaging and photothermal therapy of cancer. Lasers Med Sci, 32, 1469-1477.

FINNEY, A. R. & SALVALAGLIO, M. 2023. Molecular simulation approaches to study crystal nucleation from solutions: Theoretical considerations and computational challenges. WIREs Computational Molecular Science, 14.

FLEURY, B., CORTES-HUERTO, R., TACHE, O., TESTARD, F., MENGUY, N. & SPALLA, O. 2015. Gold Nanoparticle Internal Structure and Symmetry Probed by Unified Small-Angle X-ray Scattering and X-ray Diffraction Coupled with Molecular Dynamics Analysis. Nano Lett, 15, 6088-94.

FRENS, G. 1972. Controlled Nucleation For Regulation Of Particle-Size In Monodisperse Gold Suspensions.pdf. Nature, 241, 20-22.

FU, H., GAO, X., ZHANG, X. & LING, L. 2021. Recent Advances in Nonclassical Crystallization: Fundamentals, Applications, and Challenges. Crystal Growth & Design, 22, 1476-1499.

GARCIA, N. A., MALINI, R. I., FREEMAN, C. L., DEMICHELIS, R., RAITERI, P., SOMMERDIJK, N., HARDING, J. H. & GALE, J. D. 2019. Simulation of Calcium Phosphate Prenucleation Clusters in Aqueous Solution: Association beyond Ion Pairing. Cryst Growth Des, 19, 6422-6430.

GEBAUER, D., KELLERMEIER, M., GALE, J. D., BERGSTROM, L. & COLFEN, H. 2014. Pre-nucleation clusters as solute precursors in crystallisation. Chem Soc Rev, 43, 2348-71.

GHARATAPE, A., DAVARAN, S., SALEHI, R. & HAMISHEHKAR, H. 2016. Engineered gold nanoparticles for photothermal cancer therapy and bacteria killing. RSC Advances, 6, 111482-111516.

GHOBASHY, M. M., ALKHURSANI, S. A., ALQAHTANI, H. A., EL-DAMHOUGY, T. K. & MADANI, M. 2024. Gold nanoparticles in microelectronics advancements and biomedical applications. Materials Science and Engineering: B, 301.

GOSWAMI, N., YAO, Q., CHEN, T. & XIE, J. 2016. Mechanistic exploration and controlled synthesis of precise thiolate-gold nanoclusters. Coordination Chemistry Reviews, 329, 1-15.

GROCHOLA, G., RUSSO, S. P. & SNOOK, I. K. 2007. On morphologies of gold nanoparticles grown from molecular dynamics simulation. J Chem Phys, 126, 164707.

GRYS, D. B., DE NIJS, B., SALMON, A. R., HUANG, J., WANG, W., CHEN, W. H., SCHERMAN, O. A. & BAUMBERG, J. J. 2020. Citrate Coordination and Bridging of Gold Nanoparticles: The Role of Gold Adatoms in AuNP Aging. ACS Nano, 14, 8689-8696.

GUBICZA, J., LÁBÁR, J. L., QUYNH, L. M., NAM, N. H. & LUONG, N. H. 2013. Evolution of size and shape of gold nanoparticles during long-time aging. Materials Chemistry and Physics, 138, 449-453.

GUO, Z., WAN, Y., WANG, M., XU, L., LU, X., YANG, G., FANG, K. & GU, N. 2012. High-purity gold nanobipyramids can be obtained by an electrolyte-assisted and functionalization-free separation route. Colloids and Surfaces A: Physicochemical and Engineering Aspects, 414, 492-497.

HABIBA, K., MAKAROV, V. I., WEINER, B. R. & MORELL, G. 2014. Fabrication of Nanomaterials by Pulsed Laser Synthesis. In: A, W. & N, A. (eds.). one central press.

HABRAKEN, W. J., TAO, J., BRYLKA, L. J., FRIEDRICH, H., BERTINETTI, L., SCHENK, A. S., VERCH, A., DMITROVIC, V., BOMANS, P. H., FREDERIK, P. M., LAVEN, J., VAN DER SCHOOT, P., AICHMAYER, B., DE WITH, G., DEYOREO,

J. J. & SOMMERDIJK, N. A. 2013. Ion-association complexes unite classical and non-classical theories for the biomimetic nucleation of calcium phosphate. Nat Commun, 4, 1507.

HAISS, W., THANH, N. T. K., AVEYARD, J. & FERNIG, D. G. 2007. Determination of Size and Concentration of Gold Nanoparticles from UV-Vis Spectra.pdf. Analytical Chemistry, 79, 4215-4221.

HAKKINEN, H. 2012. The gold-sulfur interface at the nanoscale. Nat Chem, 4, 443-55.

HARO-GONZÁLEZ, P. G., RAMÍREZ-RICO, D. S. & LARIOS-DURÁN, E. R. 2019. Synthesis of Gold Nanoparticles in Aqueous Solutions by Electrochemical Reduction Using poly(ethylen glicol) as Stabilizer. International Journal of Electrochemical Science, 14, 9704-9710.

HARUTA, M. 2004. Gold as a Novel Catalyst in the 21st Century: Preparation, Working Mechanism and Applications. Gold Bulletin, 37/1-2.
HARUTA, M., KOBAYASHI, T., SANO, H. & YAMADA, N. 1987. Novel Gold Catalysts for the Oxidation of Carbon Monoxide at a Temperature far Below 0 °C.pdf. Chemistry Letters, 405-408.

HARUTA, M., YAMADA, N., KOBAYASHI, T. & IIJIMA, S. 1989. Gold catalysts prepared by coprecipitation for low-temperature oxidation of hydrogen and of carbon monoxide.pdf. Journal of Catalysis, 115, 301-309.

HEUER-JUNGEMANN, A., FELIU, N., BAKAIMI, I., HAMALY, M., ALKILANY, A., CHAKRABORTY, I., MASOOD, A., CASULA, M. F., KOSTOPOULOU, A., OH, E., SUSUMU, K., STEWART, M. H., MEDINTZ, I. L., STRATAKIS, E., PARAK, W. J. & KANARAS, A. G. 2019. The Role of Ligands in the Chemical Synthesis and Applications of Inorganic Nanoparticles. Chem Rev, 119, 4819-4880.

HIGUCHI, E., OKADA, K., CHIKU, M. & INOUE, H. 2015. Electrocatalytic Activity for Oxygen Reduction Reaction of Au Core/Pt Shell Nanoparticle-Loaded Carbon Black Catalyst with Different Core Sizes. Electrochimica Acta, 179, 100-107.

HONG, J. W., LEE, S. U., LEE, Y. W. & HAN, S. W. 2012. Hexoctahedral Au nanocrystals with high-index facets and their optical and surface-enhanced Raman scattering properties. J Am Chem Soc, 134, 4565-8.

HOSSEINI, S., ALSIRAEY, N., RILEY, A. J., ZUBKOV, T., CLOSSON, T., TYE, J., BODAPPA, N. & LI, Z. 2018. Variable Growth and Characterizations of Monolayer-Protected Gold Nanoparticles Based on Molar Ratio of Gold and Capping Ligands. Langmuir, 34, 15517-15525.

HUANG, M., XIONG, E., WANG, Y., HU, M., YUE, H., TIAN, T., ZHU, D., LIU, H. & ZHOU, X. 2022. Fast microwave heating-based one-step synthesis of DNA and RNA modified gold nanoparticles. Nat Commun, 13, 968.

HUSSAIN, M. H., ABU BAKAR, N. F., MUSTAPA, A. N., LOW, K. F., OTHMAN, N. H. & ADAM, F. 2020. Synthesis of Various Size Gold Nanoparticles by Chemical Reduction Method with Different Solvent Polarity. Nanoscale Res Lett, 15, 140.

ISHIDA, T., MURAYAMA, T., TAKETOSHI, A. & HARUTA, M. 2020. Importance of Size and Contact Structure of Gold Nanoparticles for the Genesis of Unique Catalytic Processes. Chem Rev, 120, 464-525.

JANG, E., LIM, E.-K., CHOI, J., PARK, J., HUH, Y.-J., SUH, J.-S., HUH, Y.-M. & HAAM, S. 2011. Br-Assisted Ostwald Ripening of Au Nanoparticles under H2O2 Redox. Crystal Growth & Design, 12, 37-39.

JI, X., SONG, X., LI, J., BAI, Y., YANG, W. & PENG, X. 2007. Size Control of Gold Nanocrystals in Citrate Reduction- The Third Role of Citrate.pdf. J. Am. Chem. Soc, 129, 13939-13948.

JIA, C., XIAO, A., ZHAO, J., WANG, P., FANG, X., ZHANG, H. & GUAN, B. 2023. A New Perspective on Crystal Nucleation: A Classical View on Non-Classical Nucleation. Crystal Growth & Design, 24, 601-612.

JIANG, Y., SALLEY, D., SHARMA, A., KEENAN, G., MULLIN, M. & CRONIN, L. 2022. An artificial intelligence enabled chemical synthesisrobot for exploration and optimization of nanomaterials. SCIENCE ADVANCES, 8.

JIN, B., SUSHKO, M. L., LIU, Z., JIN, C. & TANG, R. 2018. In Situ Liquid Cell TEM Reveals Bridge-Induced Contact and Fusion of Au Nanocrystals in Aqueous Solution. Nano Lett, 18, 6551-6556.

JIN, R., ZENG, C., ZHOU, M. & CHEN, Y. 2016. Atomically Precise Colloidal Metal Nanoclusters and Nanoparticles: Fundamentals and Opportunities. Chem Rev, 116, 10346-413.

KANG, H., BUCHMAN, J. T., RODRIGUEZ, R. S., RING, H. L., HE, J., BANTZ, K. C. & HAYNES, C. L. 2019. Stabilization of Silver and Gold Nanoparticles: Preservation and Improvement of Plasmonic Functionalities. Chem Rev, 119, 664-699.

KAPIL, N., CARDINALE, F., WEISSENBERGER, T., TROGADAS, P., NIJHUIS, T. A., NIGRA, M. M. & COPPENS, M. O. 2021. Gold nanoparticles with tailored size through ligand modification for catalytic applications. Chem Commun (Camb), 57, 10775-10778.

KARIMI, S., MOSHAII, A. & NIKKHAH, M. 2019. Controlled synthesis of colloidal monodisperse gold nanoparticles in a wide range of sizes; investigating the effect of reducing agent. Materials Research Express, 6.

KARTHIKA, S., RADHAKRISHNAN, T. K. & KALAICHELVI, P. 2016. A Review of Classical and Nonclassical Nucleation Theories. Crystal Growth & Design, 16, 6663-6681.

KASHIWAYA, S., SHI, Y., LU, J., SANGIOVANNI, D. G., GRECZYNSKI, G., MAGNUSON, M., ANDERSSON, M., ROSEN, J. & HULTMAN, L. 2024. Synthesis of goldene comprising single-atom layer gold. Nature Synthesis, 3, 744-751.

KATIYAR, R. S. & JHA, P. K. 2018. Molecular simulations in drug delivery: Opportunities and challenges. WIREs Computational Molecular Science, 8.

KESHARWANI, P., MA, R., SANG, L., FATIMA, M., SHEIKH, A., ABOUREHAB, M. A. S., GUPTA, N., CHEN, Z. S. & ZHOU, Y. 2023. Gold nanoparticles and gold nanorods in the landscape of cancer therapy. Mol Cancer, 22, 98.

KETTEMANN, F., BIRNBAUM, A., WITTE, S., WUITHSCHICK, M., PINNA, N., KRAEHNERT, R., RADEMANN, K. & POLTE, J. 2016. Missing Piece of the Mechanism of the Turkevich Method: The Critical Role of Citrate Protonation. Chemistry of Materials, 28, 4072-4081.

KHAN, I., SAEED, K. & KHAN, I. 2019. Nanoparticles: Properties, applications and toxicities. Arabian Journal of Chemistry, 12, 908-931.

KISTER, T., MONEGO, D., MULVANEY, P., WIDMER-COOPER, A. & KRAUS, T. 2018. Colloidal Stability of Apolar Nanoparticles: The Role of Particle Size and Ligand Shell Structure. ACS Nano, 12, 5969-5977.

KROMMENHOEK, P. J., WANG, J., HENTZ, N., JOHNSTON-PECK, A. C., KOZEK, K. A., KALYUZHNY, G. & TRACY, J. B. 2012. Bulky Adamantanethiolate

and Cyclohexanethiolate Ligands Favor Smaller Gold Nanoparticles with Altered Discrete Sizes.pdf. ACS Nano, 6, 4903-4911.

KUO, C. H., YANG, Y. C., GWO, S. & HUANG, M. H. 2011. Facet-dependent and au nanocrystal-enhanced electrical and photocatalytic properties of Au-Cu2O core-shell heterostructures. J Am Chem Soc, 133, 1052-7.

KUS-LISKIEWICZ, M., FICKERS, P. & BEN TAHAR, I. 2021. Biocompatibility and Cytotoxicity of Gold Nanoparticles: Recent Advances in Methodologies and Regulations. Int J Mol Sci, 22.

LACAVA, J., WEBER, A. & KRAUS, T. 2015. Ageing of Alkylthiol-Stabilized Gold Nanoparticles. Particle & Particle Systems Characterization, 32, 458-466.

LAMER, V. K. & DINEGAR, R. H. 1950. Theory,ProductionandMechanismofFormationofMonodispersedHydrosols. J. Am. Chem. Soc, 72, 4847-4854.

LE GOAS, M., SABER, J., BOLÍVAR, S. G., RABANEL, J.-M., AWOGNI, J.-M., BOFFITO, D. C. & BANQUY, X. 2022. (In)stability of ligands at the surface of inorganic nanoparticles: A forgotten question in nanomedicine? Nano Today, 45.

LEE, D., PARK, S., LEE, J. & HWANG, N. 2007. A theoretical model for digestive ripening. Acta Materialia, 55, 5281-5288.

LEE, H. E., AHN, H. Y., MUN, J., LEE, Y. Y., KIM, M., CHO, N. H., CHANG, K., KIM, W. S., RHO, J. & NAM, K. T. 2018. Amino-acid- and peptide-directed synthesis of chiral plasmonic gold nanoparticles. Nature, 556, 360-365.

LEE, J., YANG, J., KWON, S. G. & HYEON, T. 2016. Nonclassical nucleation and growth of inorganic nanoparticles. Nature Reviews Materials, 1.

LEFFLER, V., EHLERT, S., FORSTER, B., DULLE, M. & FORSTER, S. 2021. Nanoparticle Heat-Up Synthesis: In Situ X-ray Diffraction and Extension from Classical to Nonclassical Nucleation and Growth Theory. ACS Nano, 15, 840-856.

LEMAK, A. S. & BALABAEV, N. K. 1994. On The Berendsen Thermostat. Molecular Simulation, 13, 177-187.

LI, D., CHEN, Q., CHUN, J., FICHTHORN, K., DE YOREO, J. & ZHENG, H. 2023. Nanoparticle Assembly and Oriented Attachment: Correlating Controlling Factors to the Resulting Structures. Chem Rev, 123, 3127-3159.

LI, G., HE, N., DENG, J., LIU, J., SUN, Y., QU, M., JIANG, Y., ZHAO, T., ZHOU, S.-Y., ZENG, H., ZHENG, Q., LIAO, H.-G. & SUN, S.-G. 2021. Observations of Dense Liquid Phase-Assisted Nanocrystal Growth and Coalescence. Crystal Growth & Design, 21, 6025-6030.

LI, G., ZENG, C. & JIN, R. 2014. Thermally robust Au99(SPh)42 nanoclusters for chemoselective hydrogenation of nitrobenzaldehyde derivatives in water. J Am Chem Soc, 136, 3673-9.

LI, H. J., YAN, D., CAI, H. Q., YI, H. B., MIN, X. B. & XIA, F. F. 2017. Insights into water-mediated ion clustering in aqueous CaSO(4) solutions: pre-nucleation cluster characteristics studied by ab initio calculations and molecular dynamics simulations. Phys Chem Chem Phys, 19, 11390-11403.

LI, Q., PAN, Y., CHEN, T., DU, Y., GE, H., ZHANG, B., XIE, J., YU, H. & ZHU, M. 2018. Design and mechanistic study of a novel gold nanocluster-based drug delivery system. Nanoscale, 10, 10166-10172.

LI, X., JIANG, L., ZHAN, Q., QIAN, J. & HE, S. 2009. Localized surface plasmon resonance (LSPR) of polyelectrolyte-functionalized gold-nanoparticles for bio-sensing. Colloids and Surfaces A: Physicochemical and Engineering Aspects, 332, 172-179.

LIANG, T., SHIN, Y. K., CHENG, Y.-T., YILMAZ, D. E., VISHNU, K. G., VERNERS, O., ZOU, C., PHILLPOT, S. R., SINNOTT, S. B. & VAN DUIN, A. C. T. 2013. Reactive Potentials for Advanced Atomistic Simulations. Annual Review of Materials Research, 43, 109-129.

LIFSHITZ, I. M. & SLYOZOV, V. V. 1961. The kinetics of precipitation from supersaturated solid solutions.pdf. J Phys Chem Solids, 19(1-2), 35-50.

LIN, K. & WANG, Z. 2023. Multiscale mechanics and molecular dynamics simulations of the durability of fiber-reinforced polymer composites. Communications Materials, 4.

LIU, M., TANG, F., YANG, Z., XU, J. & YANG, X. 2019a. Recent Progress on Gold-Nanocluster-Based Fluorescent Probe for Environmental Analysis and Biological Sensing. J Anal Methods Chem, 2019, 1095148.

LIU, Y., GENG, H., QIN, X., YANG, Y., ZENG, Z., CHEN, S., LIN, Y., XIN, H., SONG, C., ZHU, X., LI, D., ZHANG, J., SONG, L., DAI, Z. & KAWAZOE, Y. 2019b. Oriented Attachment Revisited: Does a Chemical Reaction Occur? Matter, 1, 690-704.

LIU, Z., CAO, Z., HE, J., ZHANG, H., GE, Y. & CHEN, B. 2021. Versatile Printing of Substantial Liquid Cells for Efficiently Imaging In Situ Liquid-Phase Dynamics. Nano Lett, 21, 6882-6890.

LOH, N. D., SEN, S., BOSMAN, M., TAN, S. F., ZHONG, J., NIJHUIS, C. A., KRAL, P., MATSUDAIRA, P. & MIRSAIDOV, U. 2017. Multistep nucleation of nanocrystals in aqueous solution. Nat Chem, 9, 77-82.

LONG, J., NAND, A. & RAY, S. 2021. Application of Spectroscopy in Additive Manufacturing. Materials (Basel), 14.

LOVE, O., GALINDO-MURILLO, R., ZGARBOVA, M., SPONER, J., JURECKA, P. & CHEATHAM, T. E., 3RD 2023. Assessing the Current State of Amber Force Field Modifications for DNA horizontal line 2023 Edition. J Chem Theory Comput, 19, 4299-4307.

LV, H., SI, W., SHA, J., CHEN, Y. & ZHANG, Y. 2025. Strategies for high performance characterization of nanomaterials using in situ liquid cell transmission electron microscopy. Next Nanotechnology, 7.

MARTIN, P., ZHANG, P., RODGER, P. M. & VALSAMI-JONES, E. 2019. Simulations of morphological transformation in silver nanoparticles as a tool for assessing their reactivity and potential toxicity. NanoImpact, 14.

MARTINEZ, L., ANDRADE, R., BIRGIN, E. G. & MARTINEZ, J. M. 2009. PACKMOL: a package for building initial configurations for molecular dynamics simulations. J Comput Chem, 30, 2157-64.

MEENA, S. K. & SULPIZI, M. 2016. From Gold Nanoseeds to Nanorods: The Microscopic Origin of the Anisotropic Growth. Angew Chem Int Ed Engl, 55, 11960-4.

MENDEZ, E., FAGUNDEZ, P., SOSA, P., GUTIERREZ, M. V. & BOTASINI, S. 2021. Experimental evidences support the existence of an aggregation/disaggregation step in the Turkevich synthesis of gold nanoparticles. Nanotechnology, 32, 045603.

MONEGO, D., KISTER, T., KIRKWOOD, N., DOBLAS, D., MULVANEY, P., KRAUS, T. & WIDMER-COOPER, A. 2020. When Like Destabilizes Like: Inverted Solvent Effects in Apolar Nanoparticle Dispersions. ACS Nano, 14, 5278-5287.

MONEGO, D., KISTER, T., KIRKWOOD, N., MULVANEY, P., WIDMER-COOPER, A. & KRAUS, T. 2018. Colloidal Stability of Apolar Nanoparticles: Role of Ligand Length. Langmuir, 34, 12982-12989.

MONTI, S., BARCARO, G., SEMENTA, L., CARRAVETTA, V. & ÅGREN, H. 2017. Characterization of the adsorption dynamics of trisodium citrate on gold in water solution. RSC Adv., 7, 49655-49663.

MONTI, S., CARRAVETTA, V. & AGREN, H. 2016a. Decoration of gold nanoparticles with cysteine in solution: reactive molecular dynamics simulations. Nanoscale, 8, 12929-38.

MONTI, S., CARRAVETTA, V. & AGREN, H. 2016b. Simulation of Gold Functionalization with Cysteine by Reactive Molecular Dynamics. J Phys Chem Lett, 7, 272-6.

MOURDIKOUDIS, S., PALLARES, R. M. & THANH, N. T. K. 2018. Characterization techniques for nanoparticles: comparison and complementarity upon studying nanoparticle properties. Nanoscale, 10, 12871-12934.

MOZAFFARI, S., LI, W., THOMPSON, C., IVANOV, S., SEIFERT, S., LEE, B., KOVARIK, L. & KARIM, A. M. 2017. Colloidal nanoparticle size control: experimental and kinetic modeling investigation of the ligand-metal binding role in controlling the nucleation and growth kinetics. Nanoscale, 9, 13772-13785.

NAM, J. M., OWEN, J. S. & TALAPIN, D. V. 2023. The Ligand-Surface Interface and Its Influence on Nanoparticle Properties. Acc Chem Res, 56, 2265-2266.

NEGISHI, Y., NAKAZAKI, T., MALOLA, S., TAKANO, S., NIIHORI, Y., KURASHIGE, W., YAMAZOE, S., TSUKUDA, T. & HAKKINEN, H. 2015. A critical size for emergence of nonbulk electronic and geometric structures in dodecanethiolate-protected Au clusters. J Am Chem Soc, 137, 1206-12.

´NEZ, J. M. M. &´NEZ, L. M. 2003. Packing Optimization for Automated Generation of Complex System's Initial Configurations for Molecular Dynamics and Docking.pdf. J Compu Chem, 24, 819-825.

NISHIGAKI, J., TSUNOYAMA, R., TSUNOYAMA, H., ICHIKUNI, N., YAMAZOE, S., NEGISHI, Y., ITO, M., MATSUO, T., TAMAO, K. & TSUKUDA, T. 2012. A new binding motif of sterically demanding thiolates on a gold cluster. J Am Chem Soc, 134, 14295-7.

NOSÉ, S. 1984. A unified formulation of the constant temperature molecular dynamics methods. The Journal of Chemical Physics, 81, 511-519.

OJEA-JIMÉNEZ, I., BASTÚS, N. G. & PUNTES, V. 2011. Influence of the Sequence of the Reagents Addition in the Citrate-Mediated Synthesis of Gold Nanoparticles. The Journal of Physical Chemistry C, 115, 15752-15757.

OLIVEIRA, A. E. F., PEREIRA, A. C., RESENDE, M. A. C. & FERREIRA, L. F. 2023. Gold Nanoparticles: A Didactic Step-by-Step of the Synthesis Using the Turkevich Method, Mechanisms, and Characterizations. Analytica, 4, 250-263.

OSTWALD, W. 1897. Studien über die Bildung und Umwandlung fester Körper. 1. Abhandlung: Übersättigung und Überkaltung, 22U, 289-330.

OU, X., SIETSMA, J. & SANTOFIMIA, M. J. 2022. Fundamental study of nonclassical nucleation mechanisms in iron. Acta Materialia, 226.

PAL, J. & PAL, T. 2015. Faceted metal and metal oxide nanoparticles: design, fabrication and catalysis. Nanoscale, 7, 14159-90.

PAN, J. A., RONG, Z., WANG, Y., CHO, H., COROPCEANU, I., WU, H. & TALAPIN, D. V. 2021. Direct Optical Lithography of Colloidal Metal Oxide Nanomaterials for Diffractive Optical Elements with 2pi Phase Control. J Am Chem Soc, 143, 2372-2383.

PARK, J. W. & SHUMAKER-PARRY, J. S. 2014. Structural study of citrate layers on gold nanoparticles: role of intermolecular interactions in stabilizing nanoparticles. J Am Chem Soc, 136, 1907-21.

PATIL, T., GAMBHIR, R., VIBHUTE, A. & TIWARI, A. P. 2022. Gold Nanoparticles: Synthesis Methods, Functionalization and Biological Applications. Journal of Cluster Science, 34, 705-725.

PATTADAR, D. K. & ZAMBORINI, F. P. 2019. Effect of Size, Coverage, and Dispersity on the Potential-Controlled Ostwald Ripening of Metal Nanoparticles. Langmuir, 35, 16416-16426.

PATTADAR, D. K., SHARMA, J. N., MAINALI, B. P. & ZAMBORINI, F. P. 2019. Impact of the Assembly Method on the Surface Area-to-Volume Ratio and Electrochemical Oxidation Potential of Metal Nanospheres. The Journal of Physical Chemistry C, 123, 24304-24312.

PAUW, B. R., KASTNER, C. & THUNEMANN, A. F. 2017. Nanoparticle size distribution quantification: results of a small-angle X-ray scattering inter-laboratory comparison. J Appl Crystallogr, 50, 1280-1288.

PAUW, B. R., SMITH, A. J., SNOW, T., SHEBANOVA, O., SUTTER, J. P., ILAVSKY, J., HERMIDA-MERINO, D., SMALES, G. J., TERRILL, N. J., THUNEMANN, A. F. & BRAS, W. 2021. Extending synchrotron SAXS instrument ranges through addition of a portable, inexpensive USAXS module with vertical rotation axes. J Synchrotron Radiat, 28, 824-833.

PENG, C., YU, M. & ZHENG, J. 2020. In Situ Ligand-Directed Growth of Gold Nanoparticles in Biological Tissues. Nano Lett, 20, 1378-1382.

PERALA, S. R. & KUMAR, S. 2013. On the mechanism of metal nanoparticle synthesis in the Brust-Schiffrin method. Langmuir, 29, 9863-73.

PERFILIEVA, O. A., PYSHNYI, D. V. & LOMZOV, A. A. 2019. Molecular Dynamics Simulation of Polarizable Gold Nanoparticles Interacting with Sodium Citrate. J Chem Theory Comput, 15, 1278-1292.

PFEIFFER, C., REHBOCK, C., HUHN, D., CARRILLO-CARRION, C., DE ABERASTURI, D. J., MERK, V., BARCIKOWSKI, S. & PARAK, W. J. 2014. Interaction of colloidal nanoparticles with their local environment: the (ionic) nanoenvironment around nanoparticles is different from bulk and determines the physico-chemical properties of the nanoparticles. J R Soc Interface, 11, 20130931.

PIELLA, J., BASTÚS, N. G. & PUNTES, V. 2016. Size-Controlled Synthesis of Sub-10-nanometer Citrate-Stabilized Gold Nanoparticles and Related Optical Properties. Chemistry of Materials, 28, 1066-1075.

PISSUWAN, D., VALENZUELA, S. M., MILLER, C. M. & CORTIE, M. B. 2007. A Golden Bullet? Selective Targeting of Toxoplasma gondii Tachyzoites Using Antibody-Functionalized Gold Nanorods.pdf. Nano Lett, 7, 3808-3812.

POLTE, J. R., ERLER, R., ̈NEMANN, A. F. T., SOKOLOV, S., AHNER, T. T., RADEMANN, K., EMMERLING, F. & KRAEHNERT, R. 2010. Nucleation and Growth of GoldNanoparticles Studiedvia in situSmallAngle X-ray Scattering at MillisecondTime Resolution. ACS Nano, 4, 1076-1082.

PONCE, A., MEJIA-ROSALES, S. & JOSE-YACAMAN, M. 2012. Scanning transmission electron microscopy methods for the analysis of nanoparticles. Methods Mol Biol, 906, 453-71.

PONG, B.-K., ELIM, H. I., CHONG, J.-X., JI, W., TROUT, B. L. & LEE, J.-Y. 2007. New Insights on the Nanoparticle Growth Mechanism in the Citrate Reduction of Gold(III)Salt Formation of the Au Nanowire Intermediate and Its Nonlinear Optical Properties. J. Phys. Chem. C, 111, 6281-6287.

PRASAD, B. L. V., STOEVA, S. I., SORENSEN, C. M. & KLABUNDE, K. J. 2002. Digestive ripening of thiolated gold nanoparticles- the effect of alkyl chain length..pdf. Langmuir, 18, 7515-7520.

QIAN, H., ZHU, M., WU, Z. & JIN, R. 2012. Quantum Sized Gold Nanoclusters with Atomic Precision.pdf. Accounts of chemical research, 45, 1470-1479.

RAMAMOORTHY, R. K., YILDIRIM, E., BARBA, E., ROBLIN, P., VARGAS, J. A., LACROIX, L. M., RODRIGUEZ-RUIZ, I., DECORSE, P., PETKOV, V., TEYCHENE, S. & VIAU, G. 2020. The role of pre-nucleation clusters in the crystallization of gold nanoparticles. Nanoscale, 12, 16173-16188.

RAPAPORT, D. C. 2004. The Art of Molecular Dynamics Simulation, Cambridge.

REEVES, A. 2008. Optimized Fast Hartley Transform for the MC68000 with applications in image processing.

ROMAIN, M., ROMAN, P., SAVIOT, L., MILLOT, N. & BOIREAU, W. 2023. Inferring the Interfacial Reactivity of Gold Nanoparticles by Surface Plasmon Resonance Measurements. Langmuir, 39, 13058-13067.

RUSSO, J. & TANAKA, H. 2016. Nonclassical pathways of crystallization in colloidal systems. MRS Bulletin, 41, 369-374.

SAHU, J. K., LONE, S. A. & SADHU, K. K. 2022. Methionine-Controlled Impediment of Secondary Nucleation Leading to Nonclassical Growth within Self-Assembled De Novo Gold Nanoparticles. Langmuir, 38, 5865-5873.

SAHU, P. & PRASAD, B. L. 2014. Time and temperature effects on the digestive ripening of gold nanoparticles: is there a crossover from digestive ripening to Ostwald ripening? Langmuir, 30, 10143-50.

SAHU, P. & PRASAD, B. L. V. 2012. Effect of digestive ripening agent on nanoparticle size in the digestive ripening process. Chemical Physics Letters, 525-526, 101-104.

SAHU, P., SHIMPI, J., LEE, H. J., LEE, T. R. & PRASAD, B. L. 2017. Digestive Ripening of Au Nanoparticles Using Multidentate Ligands. Langmuir, 33, 1943-1950.

SANTHOSH, P. B., GENOVA, J. & CHAMATI, H. 2022. Green Synthesis of Gold Nanoparticles: An Eco-Friendly Approach. Chemistry, 4, 345-369.

SARDAR, R. & SHUMAKER-PARRY, J. S. 2011. Spectroscopic and microscopic investigation of gold nanoparticle formation: ligand and temperature effects on rate and particle size. J Am Chem Soc, 133, 8179-90.

SCHNEIDER, C. A., RASBAND, W. S. & ELICEIRI, K. W. 2012. NIH Image to ImageJ: 25 years of image analysis. Nat Methods, 9, 671-5.

SCHULZ, F., DAHL, G. T., BESZTEJAN, S., SCHROER, M. A., LEHMKUHLER, F., GRUBEL, G., VOSSMEYER, T. & LANGE, H. 2016. Ligand Layer Engineering To Control Stability and Interfacial Properties of Nanoparticles. Langmuir, 32, 7897-907.

SCHULZ, F., HOMOLKA, T., BASTUS, N. G., PUNTES, V., WELLER, H. & VOSSMEYER, T. 2014. Little adjustments significantly improve the Turkevich synthesis of gold nanoparticles. Langmuir, 30, 10779-84.

SENFTLE, T. P., HONG, S., ISLAM, M. M., KYLASA, S. B., ZHENG, Y., SHIN, Y. K., JUNKERMEIER, C., ENGEL-HERBERT, R., JANIK, M. J., AKTULGA, H. M.,

VERSTRAELEN, T., GRAMA, A. & VAN DUIN, A. C. T. 2016. The ReaxFF reactive force-field: development, applications and future directions. npj Computational Materials, 2.

SHARMA, S., KUMAR, P. & CHANDRA, R. 2019. Introduction to Molecular Dynamics. Molecular Dynamics Simulation of Nanocomposites Using BIOVIA Materials Studio, Lammps and Gromacs.

SHIMPI, J. R., SIDHAYE, D. S. & PRASAD, B. L. V. 2017. Digestive Ripening: A Fine Chemical Machining Process on the Nanoscale. Langmuir, 33, 9491-9507.
SIDLER, D. & RINIKER, S. 2019. Fast Nose-Hoover thermostat: molecular dynamics in quasi-thermodynamic equilibrium. Phys Chem Chem Phys, 21, 6059-6070.

SONNICHSEN, C., FRANZL, T., WILK, T., VON PLESSEN, G., FELDMANN, J., WILSON, O. & MULVANEY, P. 2002. Drastic reduction of plasmon damping in gold nanorods. Phys Rev Lett, 88, 077402.

SOUSBIE, T., PICHON, C. & KAWAHARA, H. 2011. The persistent cosmic web and its filamentary structure - II. Illustrations. Monthly Notices of the Royal Astronomical Society, 414, 384-403.

STOEVA, S. I., ZAIKOVSKI, V., PRASAD, B. L. V., STOIMENOV, P. K., SORENSEN, C. M. & KLABUNDE, K. J. 2005. Reversible Transformations of Gold Nanoparticle Morphology.pdf. Langmuir, 21, 10280-10283.

SUAREZ-LOPEZ, R., PUNTES, V. F., BASTUS, N. G., HERVES, C. & JAIME, C. 2022. Nucleation and growth of gold nanoparticles in the presence of different surfactants. A dissipative particle dynamics study. Sci Rep, 12, 13926.

SUN, J., LEFF, A., LI, Y. & WOEHL, T. J. 2023. Visualizing formation of high entropy alloy nanoparticles with liquid phase transmission electron microscopy. Nanoscale, 15, 10447-10457.

THAI, V. P., NGUYEN, H. D., SAITO, N., TAKAHASHI, K., SASAKI, T. & KIKUCHI, T. 2022. Precise size-control and functionalization of gold nanoparticles synthesized by plasma-liquid interactions: using carboxylic, amino, and thiol ligands. Nanoscale Adv, 4, 4490-4501.

THANH, N. T., MACLEAN, N. & MAHIDDINE, S. 2014. Mechanisms of nucleation and growth of nanoparticles in solution. Chem Rev, 114, 7610-30.

THOMPSON, A. P., AKTULGA, H. M., BERGER, R., BOLINTINEANU, D. S., BROWN, W. M., CROZIER, P. S., IN 'T VELD, P. J., KOHLMEYER, A., MOORE, S. G., NGUYEN, T. D., SHAN, R., STEVENS, M. J., TRANCHIDA, J., TROTT, C. & PLIMPTON, S. J. 2022. LAMMPS - a flexible simulation tool for particle-based materials modeling at the atomic, meso, and continuum scales. Computer Physics Communications, 271.

TRAN, M., DEPENNING, R., TURNER, M. & PADALKAR, S. 2016. Effect of citrate ratio and temperature on gold nanoparticle size and morphology. Materials Research Express, 3.

TURAN, N. B., ERKAN, H. S., ENGIN, G. O. & BILGILI, M. S. 2019. Nanoparticles in the aquatic environment: Usage, properties, transformation and toxicity—A review. Process Safety and Environmental Protection, 130, 238-249.

TURKEVICH, J., STEVENSON, P. C. & HILLIER, J. 1951. A STUDY OF THE NUCLEATION AND GROWTH PROCESSES IN THE SYNTHESIS OF COLLOIDAL GOLD .pdf. Discussions of the Faraday Society, 11, 55-75.

TURPIN, E. R., MULHOLLAND, S., TEALE, A. M., BONEV, B. B. & HIRST, J. D. 2014. New CHARMM force field parameters for dehydrated amino acid residues, the key to lantibiotic molecular dynamics simulations. RSC Adv., 4, 48621-48631.

UDDIN, J. 2018. Terahertz multispectral imaging for the analysis of gold nanoparticles' size and the number of unit cells in comparison with other techniques. International Journal of Biosensors & Bioelectronics, 4.

USTARROZ, J., HAMMONS, J. A., ALTANTZIS, T., HUBIN, A., BALS, S. & TERRYN, H. 2013. A generalized electrochemical aggregative growth mechanism. J Am Chem Soc, 135, 11550-61.

VAN DUIN, A. C. T., GODDARD, W. A., SCHOOT, H. & YAKOVLEV, A. L. 2024. SCM. theoretical Chemistry, Vrije Universiteit Amsterdam, the Netherlands.

WAGNER, C. 1961. Theorie der alterung von niederschlagen durch Umlosen (Ostwald-reifung). Zeitschrift Fur Elektrochemie, 65(7-8), 581-591.

WANG, J., CHEN, S., CUI, K., LI, D. & CHEN, D. 2016. Approach and Coalescence of Gold Nanoparticles Driven by Surface Thermodynamic Fluctuations and Atomic Interaction Forces. ACS Nano, 10, 2893-902.

WANG, X., RAMIREZ-HINESTROSA, S., DOBNIKAR, J. & FRENKEL, D. 2020. The Lennard-Jones potential: when (not) to use it. Phys Chem Chem Phys, 22, 10624-10633.

WANG, Y., ZEIRI, O., NEYMAN, A., STELLACCI, F. & WEINSTOCK, I. A. 2011. Nucleation and Island Growth of Alkanethiolate Ligand Domains on Gold Nanoparticles.pdf. ACS Nano, 6, 629-640.

WEN, T., BRUSH, L. N. & KRISHNAN, K. M. 2014. A generalized diffusion model for growth of nanoparticles synthesized by colloidal methods. J Colloid Interface Sci, 419, 79-85.

WRIGHT, L. B., RODGER, P. M. & WALSH, T. R. 2014. Structure and properties of citrate overlayers adsorbed at the aqueous Au(111) interface. Langmuir, 30, 15171-80.

WUITHSCHICK, M., BIRNBAUM, A., WITTE, S., SZTUCKI, M., VAINIO, U., PINNA, N., RADEMANN, K., EMMERLING, F., KRAEHNERT, R. & POLTE, J. R.

2015. Turkevich in New Robes- Key Questions Answered for the Most Common Gold Nanoparticle Synthesis.pdf. ACS Nano, 9, 7052-7071.

XIA, H., XIAHOU, Y., ZHANG, P., DING, W. & WANG, D. 2016. Revitalizing the Frens Method To Synthesize Uniform, Quasi-Spherical Gold Nanoparticles with Deliberately Regulated Sizes from 2 to 330 nm. Langmuir, 32, 5870-80.

XIA, K., YATABE, T., YONESATO, K., KIKKAWA, S., YAMAZOE, S., NAKATA, A., ISHIKAWA, R., SHIBATA, N., IKUHARA, Y., YAMAGUCHI, K. & SUZUKI, K. 2024. Ultra-stable and highly reactive colloidal gold nanoparticle catalysts protected using multi-dentate metal oxide nanoclusters. Nat Commun, 15, 851.

XING, T., SUNARSO, J., YANG, W., YIN, Y., GLUSHENKOV, A. M., LI, L. H., HOWLETT, P. C. & CHEN, Y. 2013. Ball milling: a green mechanochemical approach for synthesis of nitrogen doped carbon nanoparticles. Nanoscale, 5, 7970-6.

YAZDANI, S., DANESHKHAH, A., DIWATE, A., PATEL, H., SMITH, J., REUL, O., CHENG, R., IZADIAN, A. & HAJRASOULIHA, A. R. 2021. Model for Gold Nanoparticle Synthesis: Effect of pH and Reaction Time. ACS Omega, 6, 16847-16853.

YILDIRIM, E., RAMAMOORTHY, R. K., PARMAR, R., ROBLIN, P., VARGAS, J. A., PETKOV, V., DIAZ, A., CHECCHIA, S., RUIZ, I. R., TEYCHENÉ, S., LACROIX, L.-M. & VIAU, G. 2023. Simple Synthesis of Monodisperse Ultrasmall

Au Icosahedral Nanoparticles. The Journal of Physical Chemistry C, 127, 3047-3058.

YONEYA, M., TSUZUKI, S. & AOYAGI, M. 2015. Simulation of metal-organic framework self-assembly. Phys Chem Chem Phys, 17, 8649-52.

YU, J., BECKER, M. L. & CARRI, G. A. 2010. A molecular dynamics simulation of the stability-limited growth mechanism of peptide-mediated gold-nanoparticle synthesis. Small, 6, 2242-5.

ZENG, C., CHEN, Y., IIDA, K., NOBUSADA, K., KIRSCHBAUM, K., LAMBRIGHT, K. J. & JIN, R. 2016. Gold Quantum Boxes: On the Periodicities and the Quantum Confinement in the Au(2)(8), Au(3)(6), Au(4)(4) , and Au(5)(2) Magic Series. J Am Chem Soc, 138, 3950-3.

ZENG, C., CHEN, Y., LI, G. & JIN, R. 2014. Magic Size Au64(S-c-C6H11)32 Nanocluster Protected by Cyclohexanethiolate. Chemistry of Materials, 26, 2635-2641.

ZHANG, J., MOU, L. & JIANG, X. 2020. Surface chemistry of gold nanoparticles for health-related applications. Chem Sci, 11, 923-936.

ZHANG, M., SHAO, S., YUE, H., WANG, X., ZHANG, W., CHEN, F., ZHENG, L., XING, J. & QIN, Y. 2021. High Stability Au NPs: From Design to Application in Nanomedicine. Int J Nanomedicine, 16, 6067-6094.

ZHANG, Q. & WANG, H. 2014. Facet-Dependent Catalytic Activities of Au Nanoparticles Enclosed by High-Index Facets. ACS Catalysis, 4, 4027-4033.

ZHANG, Q., ZHOU, Y., VILLARREAL, E., LIN, Y., ZOU, S. & WANG, H. 2015. Faceted Gold Nanorods: Nanocuboids, Convex Nanocuboids, and Concave Nanocuboids. Nano Lett, 15, 4161-9.

ZHANG, Y., YANG, X., ZHAO, S. N., ZHAI, Y., PANG, X. & LIN, J. 2022. Recent Developments of Microscopic Study for Lanthanide and Manganese Doped Luminescent Materials. Small, 18, e2205014.

ZHANG, Z., HU, Z., XING, J. & LI, Q. 2024. Transient and elusive intermediate states in self-assembly processes: An overview. Responsive Materials, 2.

ZHANG, Z., LI, H., ZHANG, F., WU, Y., GUO, Z., ZHOU, L. & LI, J. 2014. Investigation of halide-induced aggregation of Au nanoparticles into spongelike gold. Langmuir, 30, 2648-59.

ZHOU, W., HU, K., KWEE, S., TANG, L., WANG, Z., XIA, J. & LI, X. 2020. Gold Nanoparticle Aggregation-Induced Quantitative Photothermal Biosensing Using a Thermometer: A Simple and Universal Biosensing Platform. Anal Chem, 92, 2739-2747.

ZHU, B., QI, R., YUAN, L. & GAO, Y. 2020. Real-time atomistic simulation of the Ostwald ripening of TiO2 supported Au nanoparticles. Nanoscale, 12, 19142-19148.

Appendix I

This appendix is for chapter 4, which includes all circularity plot for all synthesis as to study the shape changes in terms of aging time.

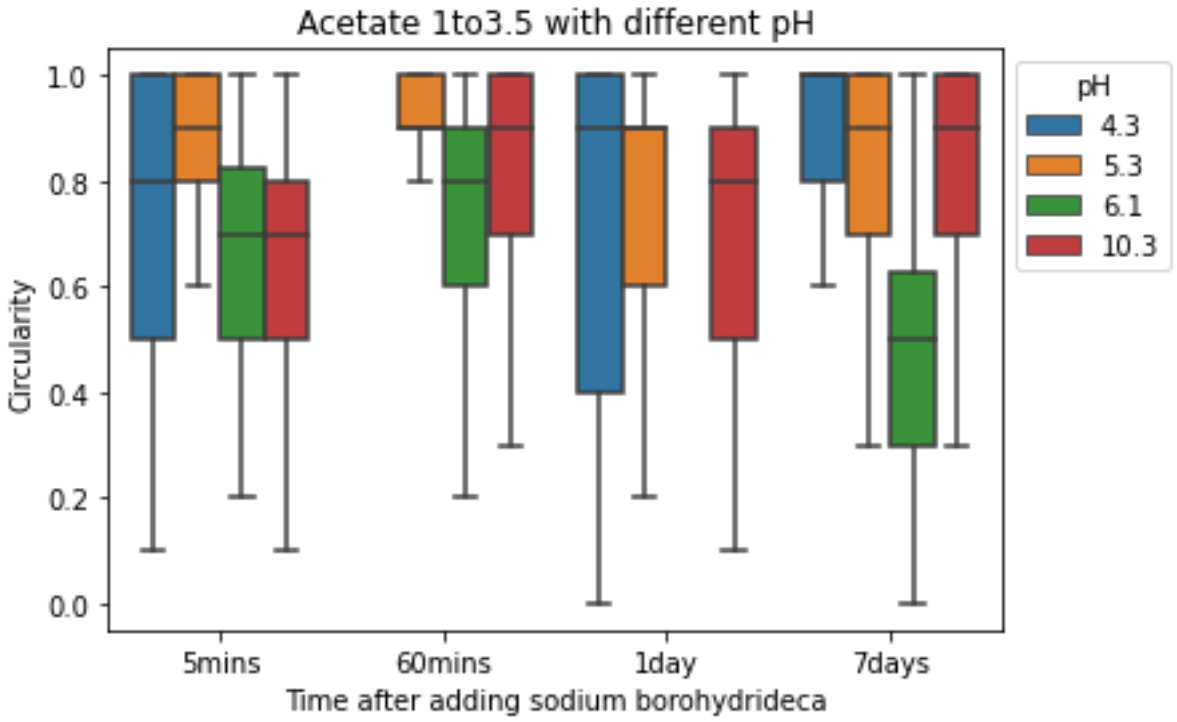


Figure A.1.1 Circularity plot for Acetic acid capped AuNPs with molar ratio 1 : 3.5 with different pH

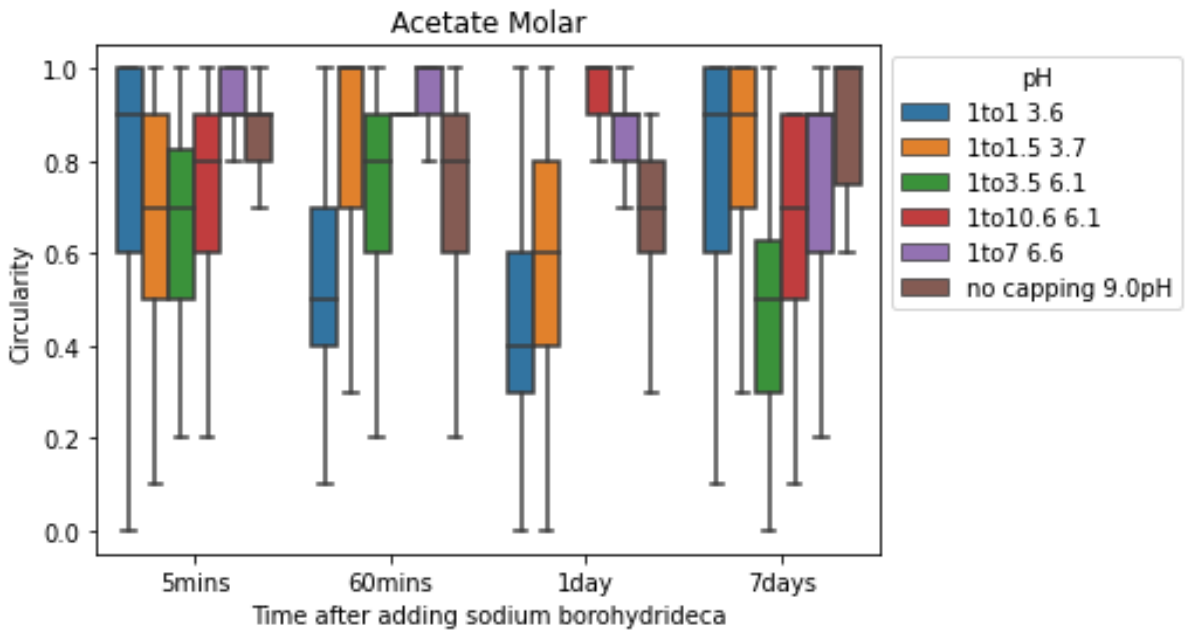


Figure A.1.2 Circularity plot for Acetic acid capped AuNPs with different molar ratio and different pH

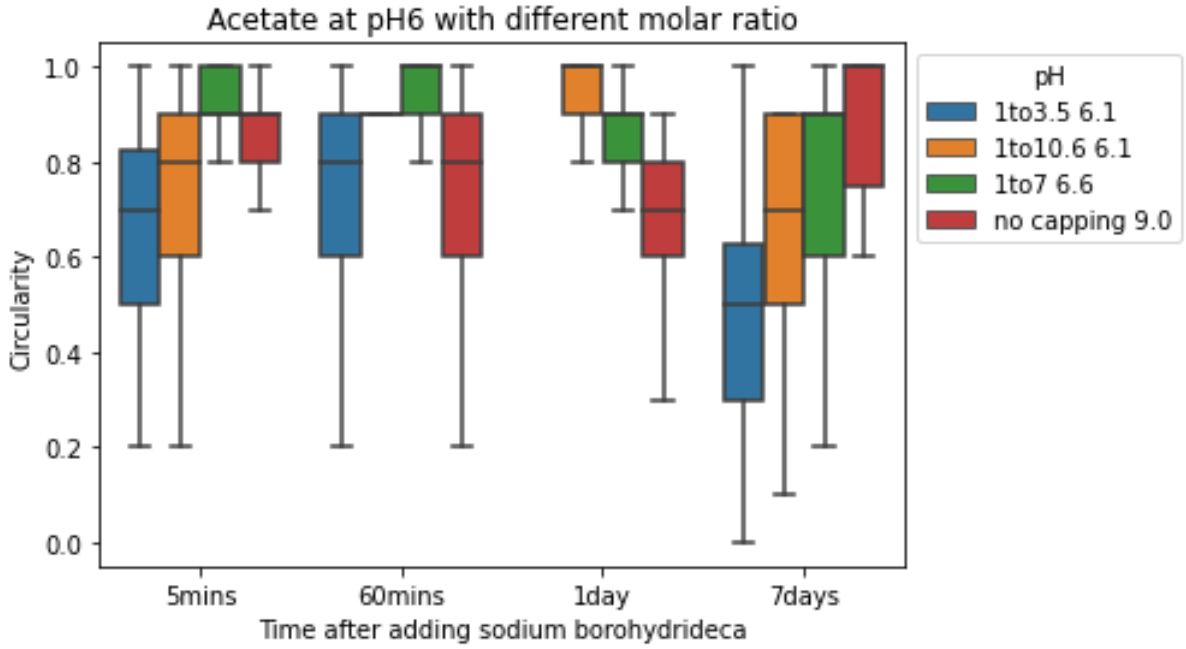


Figure A.1.3 Circularity plot for Acetic acid capped AuNPs with different molar ratio with pH6

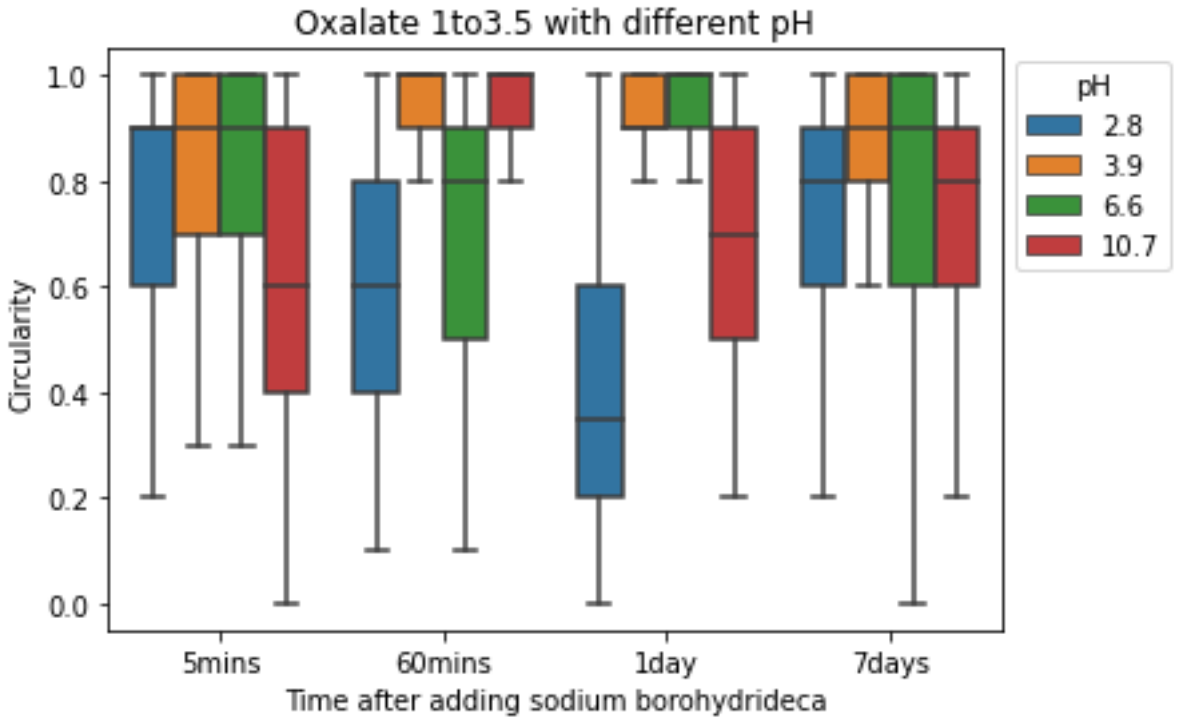


Figure A.1.4 Circularity plot for Oxalic acid capped AuNPs with molar ratio 1 : 3.5 with different pH

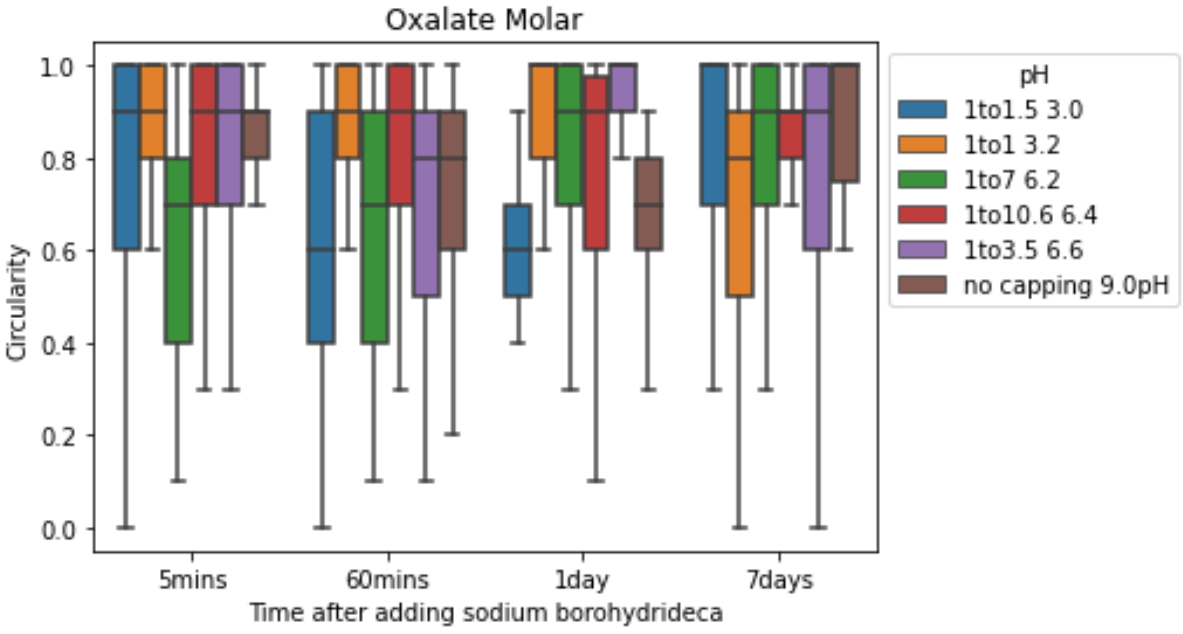


Figure A.1.5 Circularity plot for Oxalic acid capped AuNPs with different molar ratio and different pH

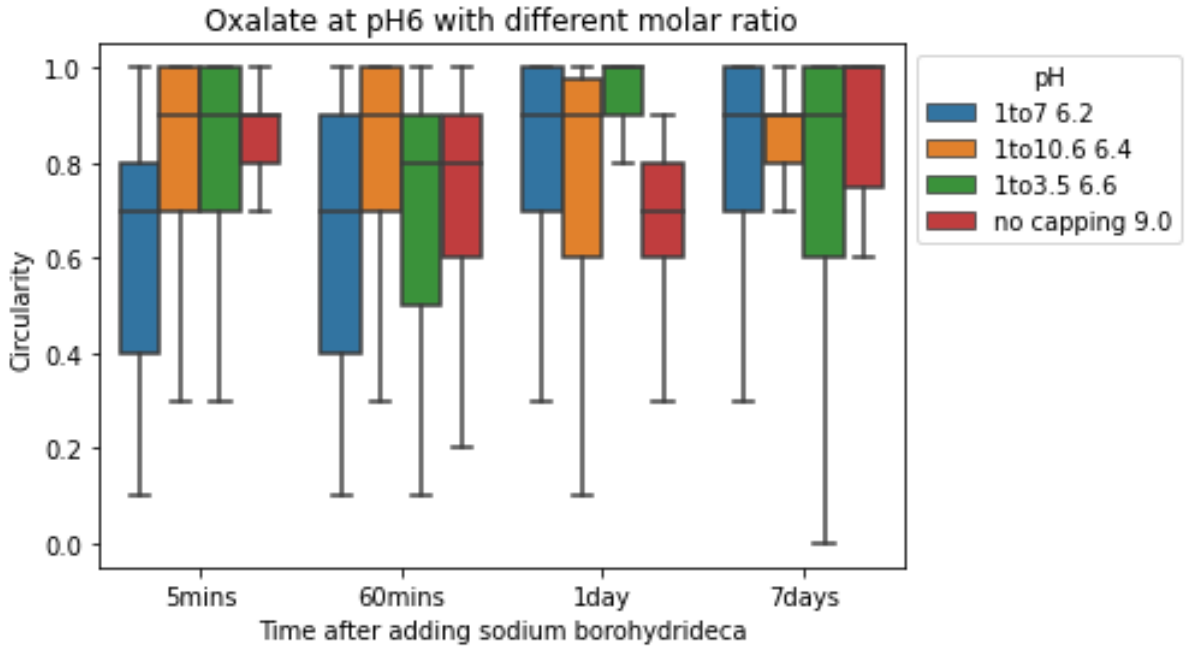


Figure A.1.6 Circularity plot for Oxalic acid capped AuNPs with different molar ratio with pH6

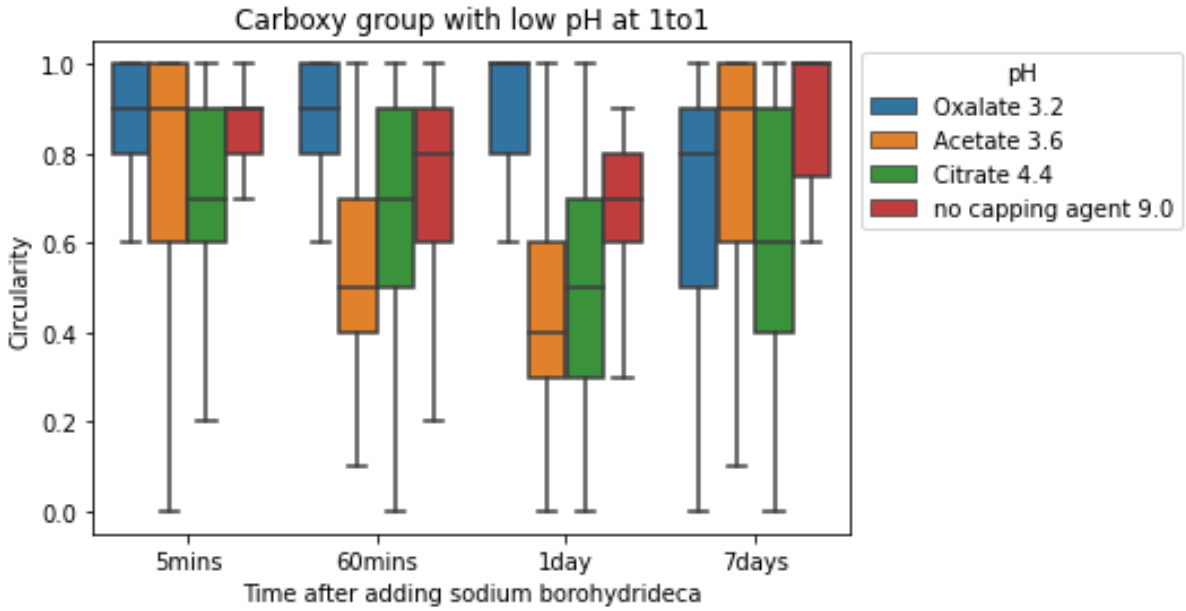


Figure A.1.7 Circularity plot for Carboxyl group ligand capped AuNPs with molar ratio 1 : 1 with low pH

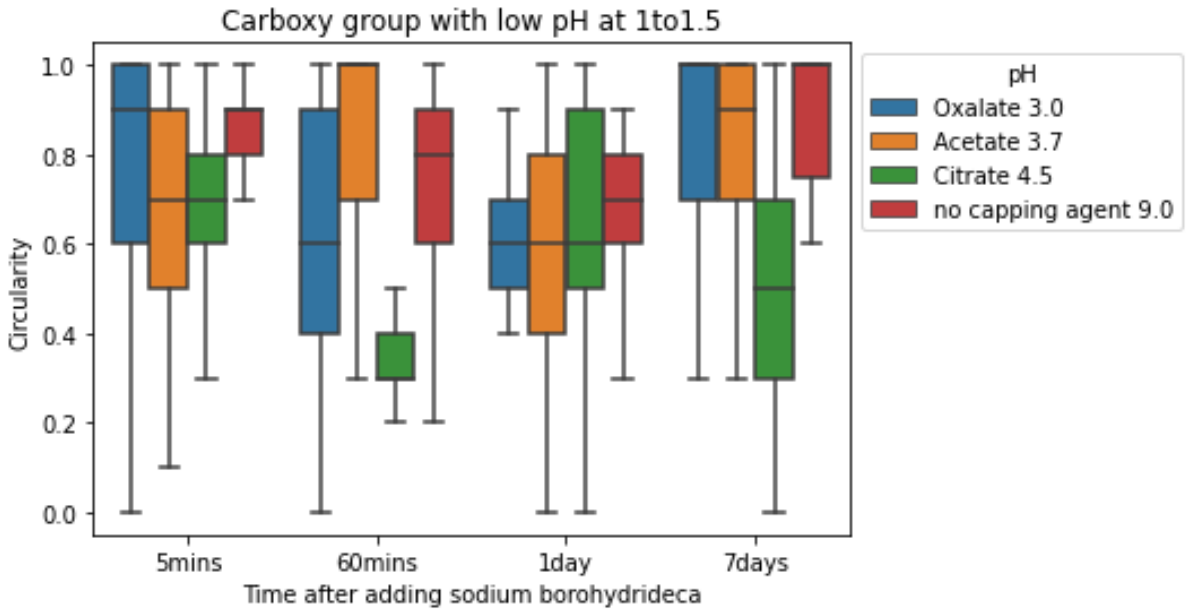


Figure A.1.8 Circularity plot for Carboxyl group ligand capped AuNPs with molar ratio 1 : 1.5 with low pH

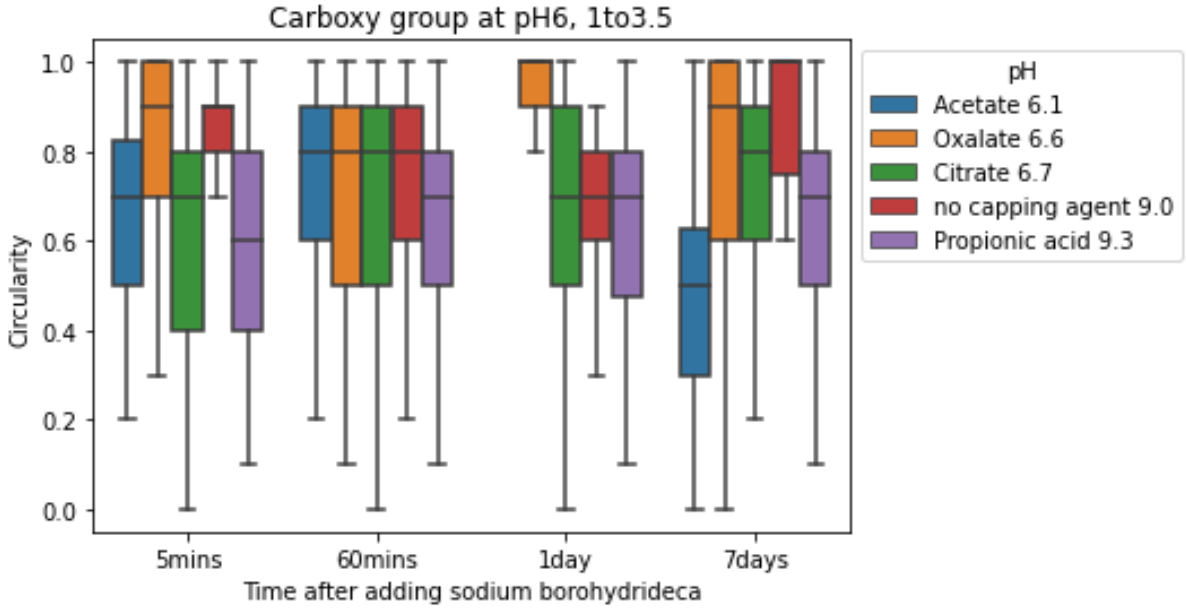


Figure A.1.9 Circularity plot for Carboxyl group ligand capped AuNPs with molar ratio 1 : 3.5 with pH6

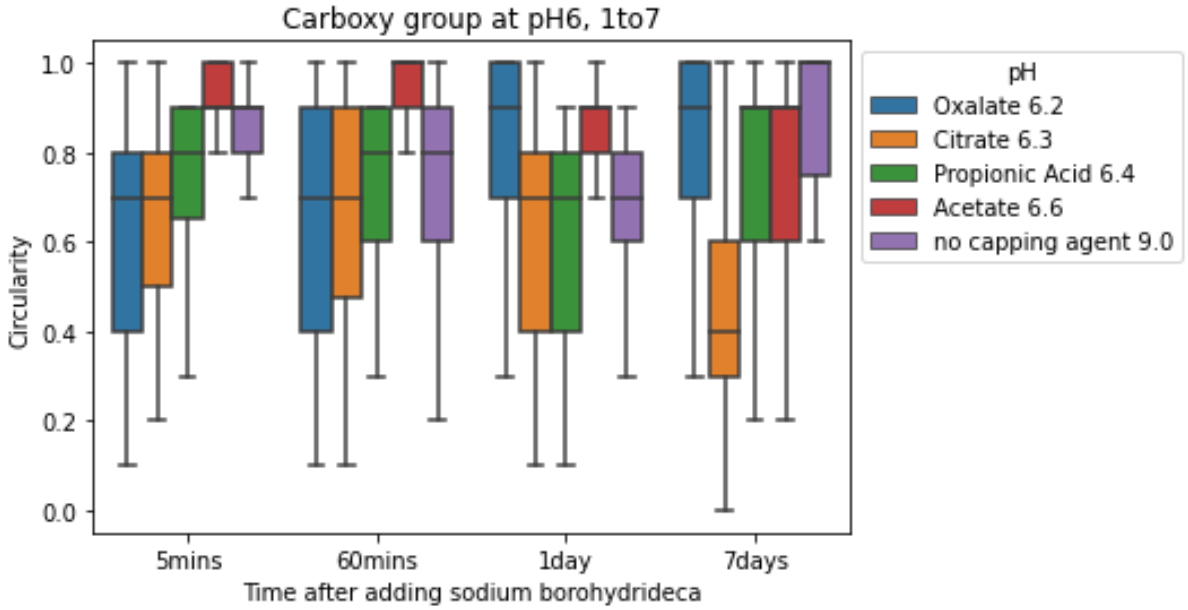


Figure A.1.10 Circularity plot for Carboxyl group ligand capped AuNPs with molar ratio 1 : 7 with pH6

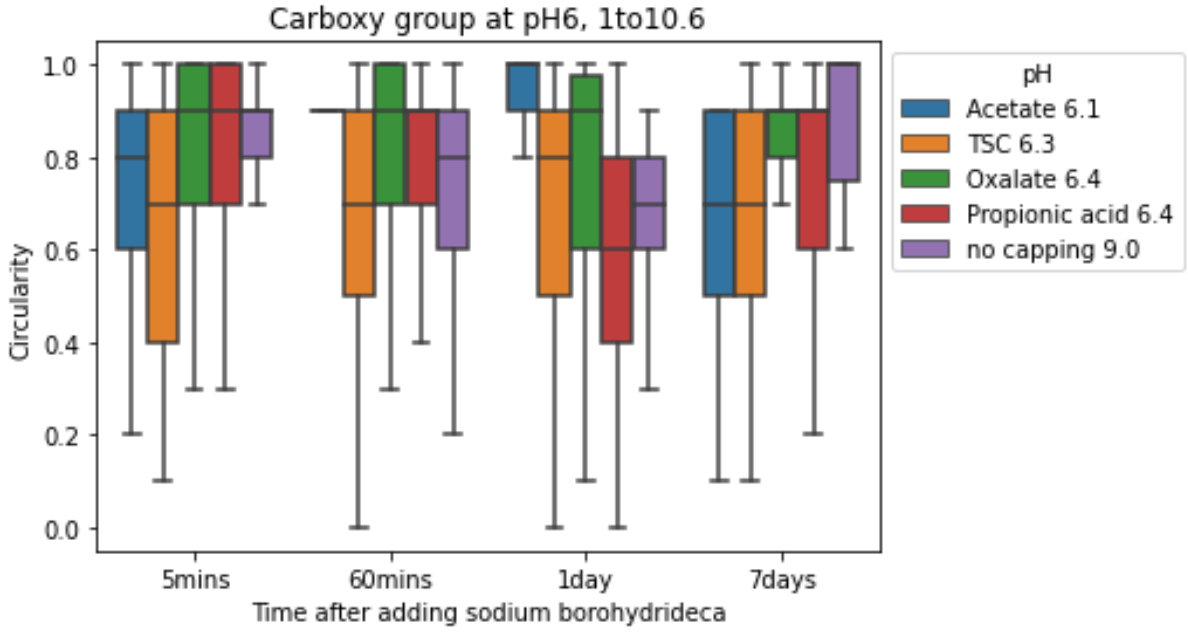


Figure A.1.11 Circularity plot for Carboxyl group ligand capped AuNPs with molar ratio 1 : 10.6 with pH6

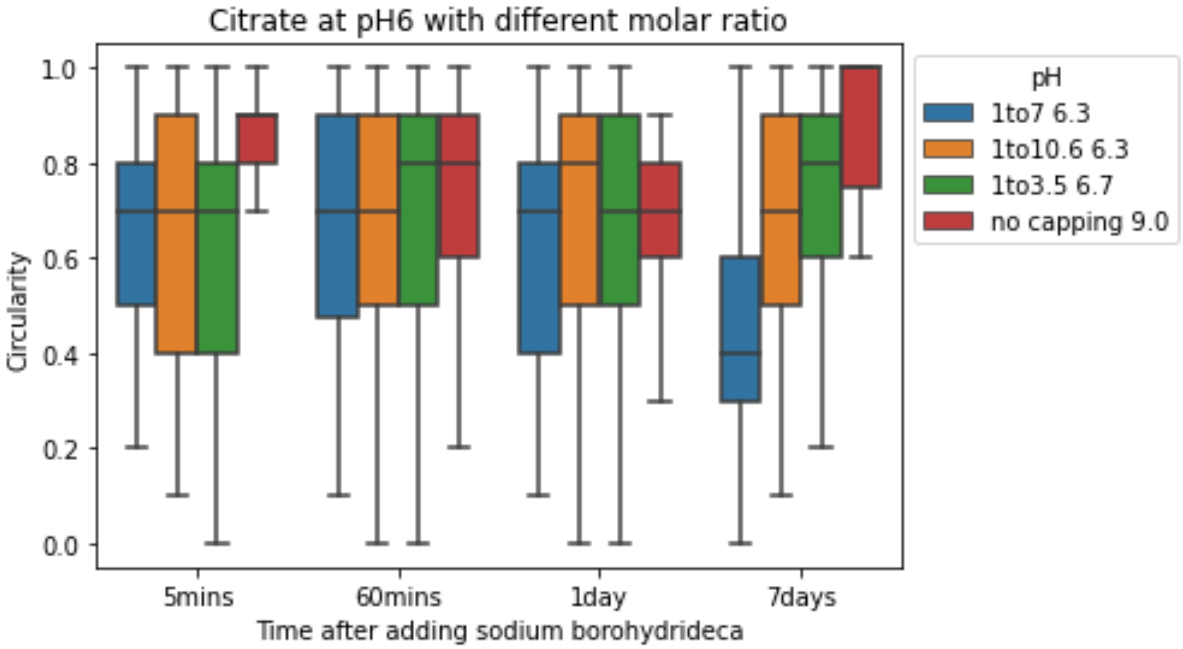


Figure A.1.12 Circularity plot for Carboxyl group ligand capped AuNPs with different molar ratio with pH6

Appendix II

This appendix is for chapter 5, this includes some STEM images for the thiol capped AuNPs and AgNPs.

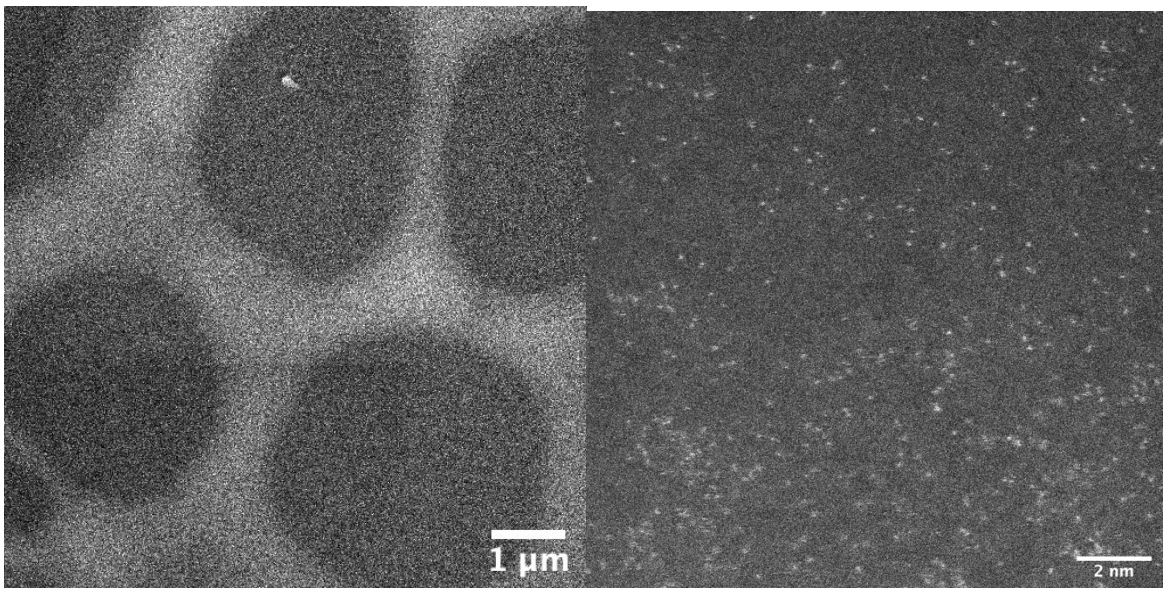


Figure A.2.1 STEM images of GSH capped AuNPs synthesis at 14 days

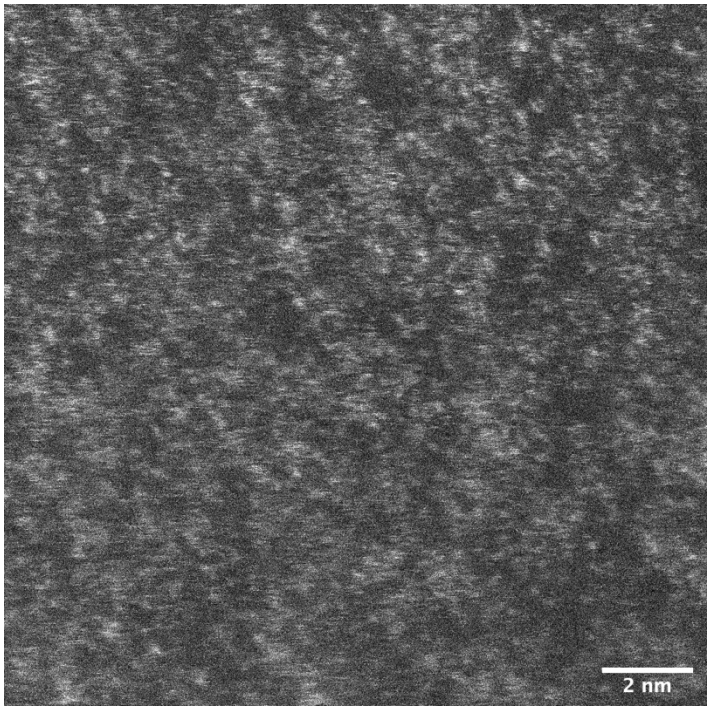


Figure A.2.2 STEM image of GSH capped AuNPs synthesis at 28days.

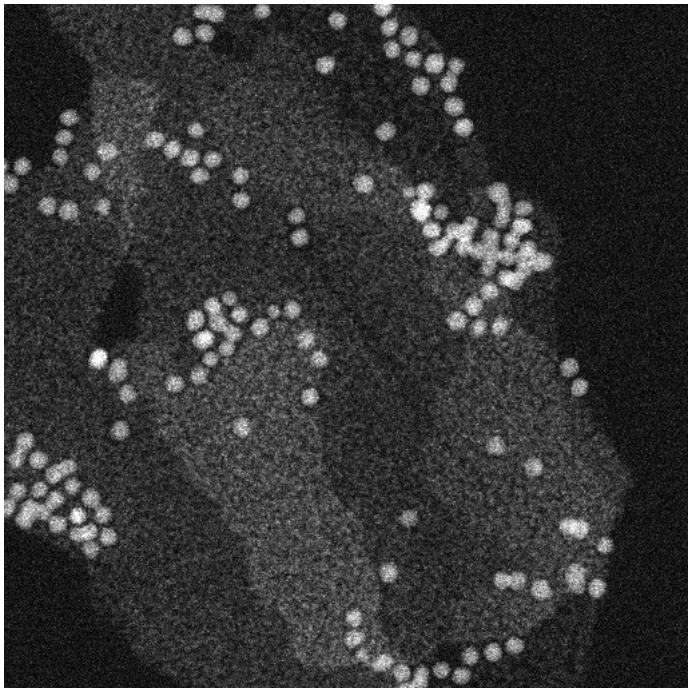


Figure A.2.3 STEM image of Cys capped AuNPs at pH 7.5 with molar ratio 1 : 3.5 at 14 days.

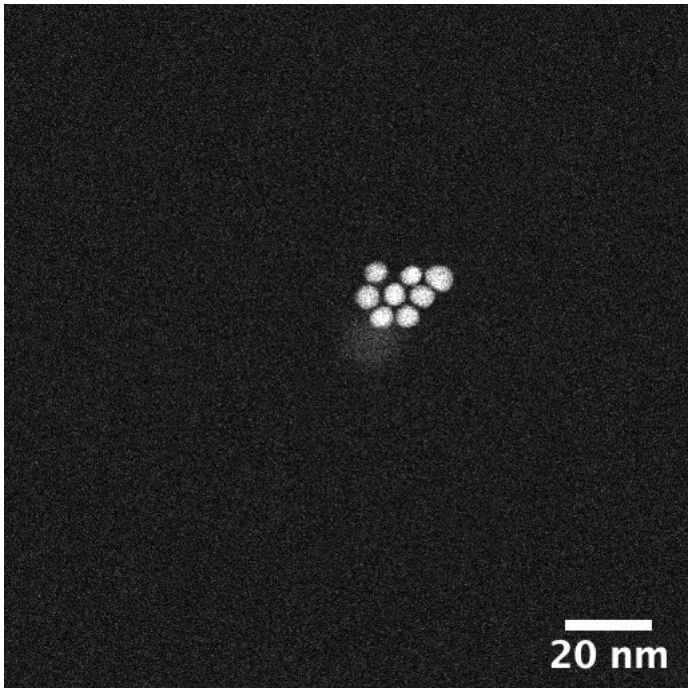


Figure A.2.4 Cys capped AuNPs at pH 8.4 with molar ratio 1 : 3.5 at 14 days.

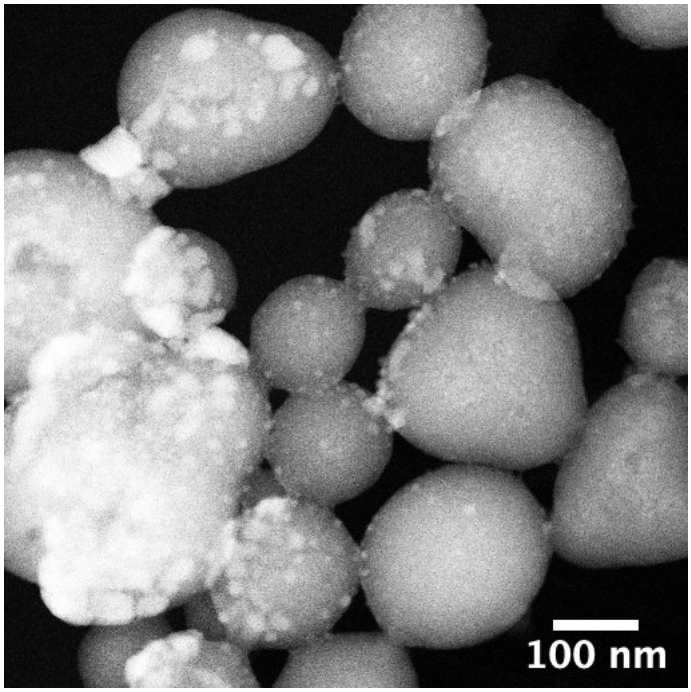


Figure A.2.5 STEM image of Cys capped AgNPs at pH 6.8 with molar ratio 1 : 3.5 at 5 minutes.

Appendix III

This appendix is for chapter 5, this includes all screen shot with water molecules and RDF of all simulation and timestep.

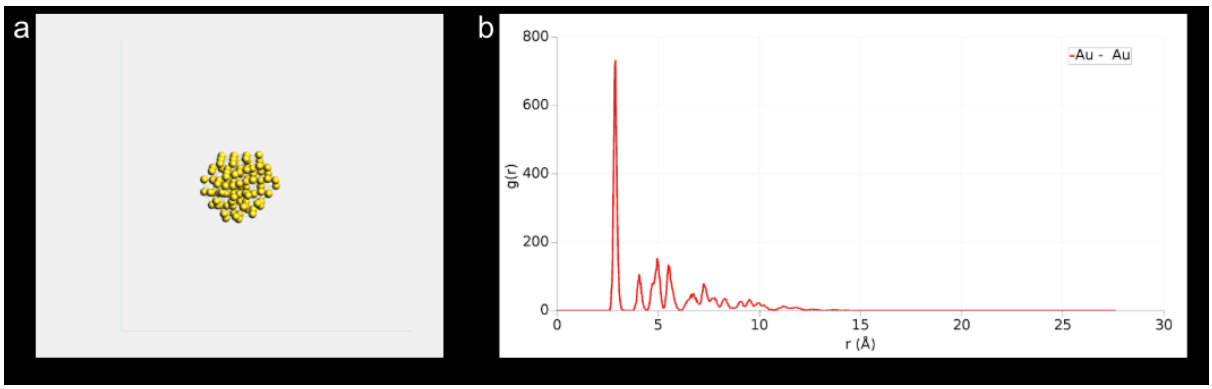


Figure A.3.1 RDF of 100-Au cluster in vacuum.

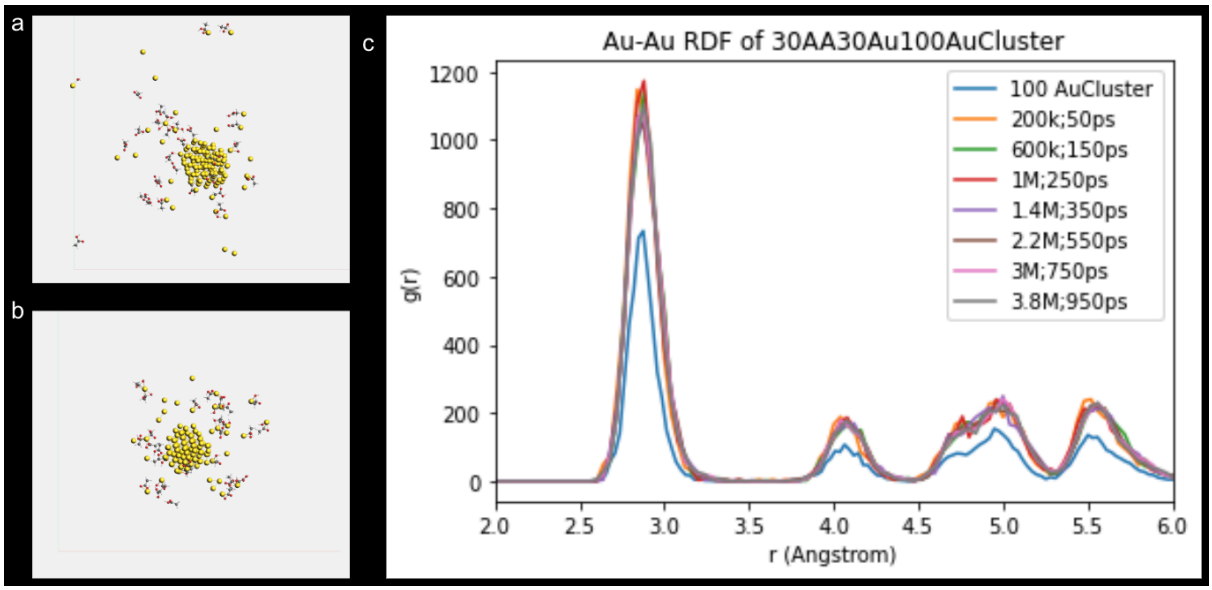


Figure A.3.2 RDF of 30 acetic acids with 30 free Au atoms and 100-Au cluster.

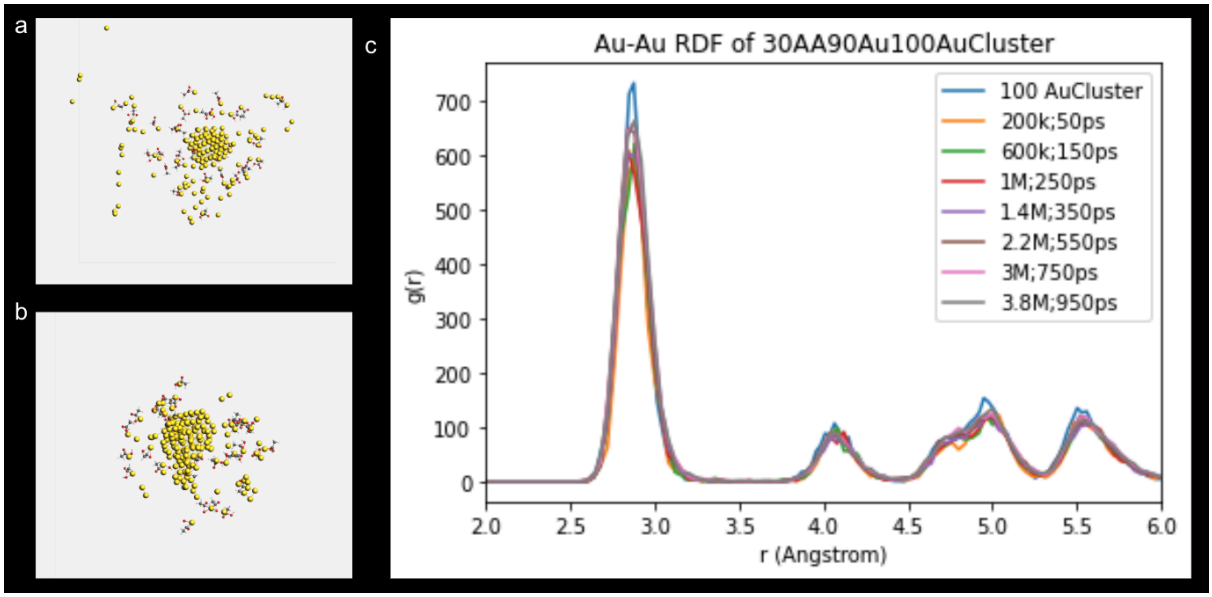


Figure A.3.3 RDF of 30 acetic acids with 90 free Au atoms and 100 Au cluster.

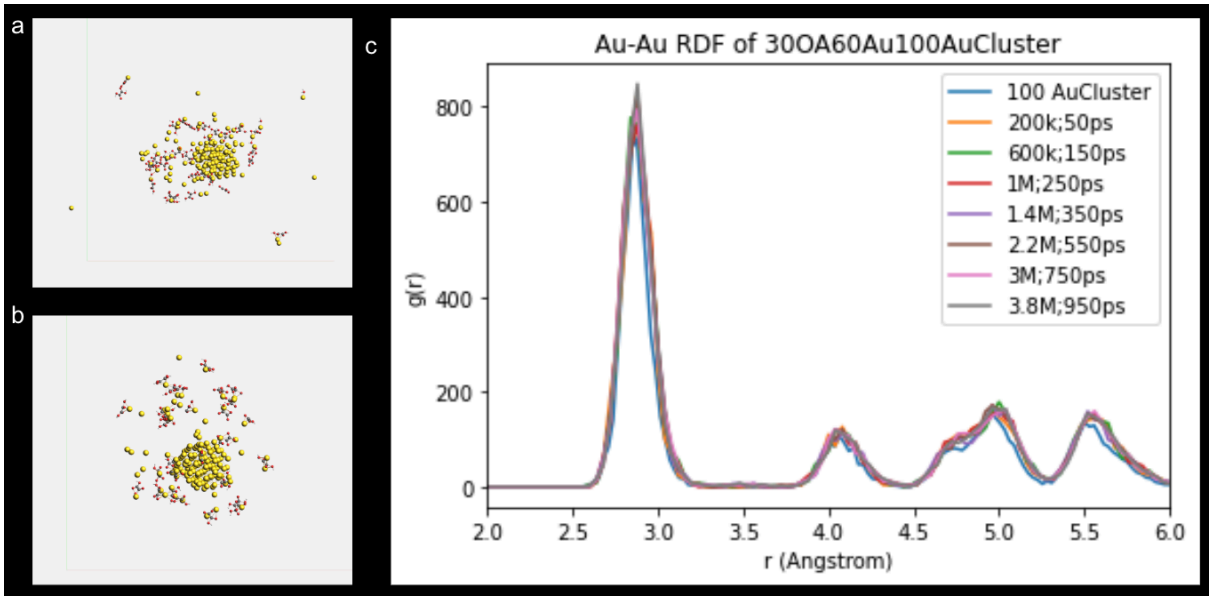


Figure A.3.4 RDF of 30 oxalic acids with 60 free Au atoms and 100 Au cluster

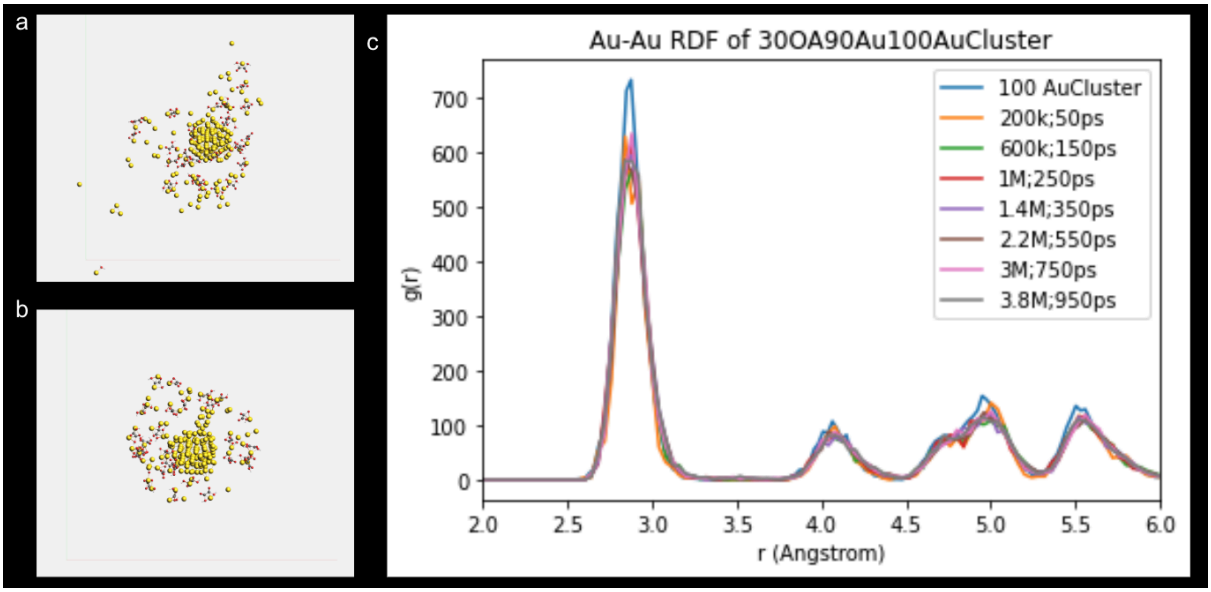


Figure A.3.5 RDF of 30 oxalic acids with 90 free Au atoms and 100 Au cluster.

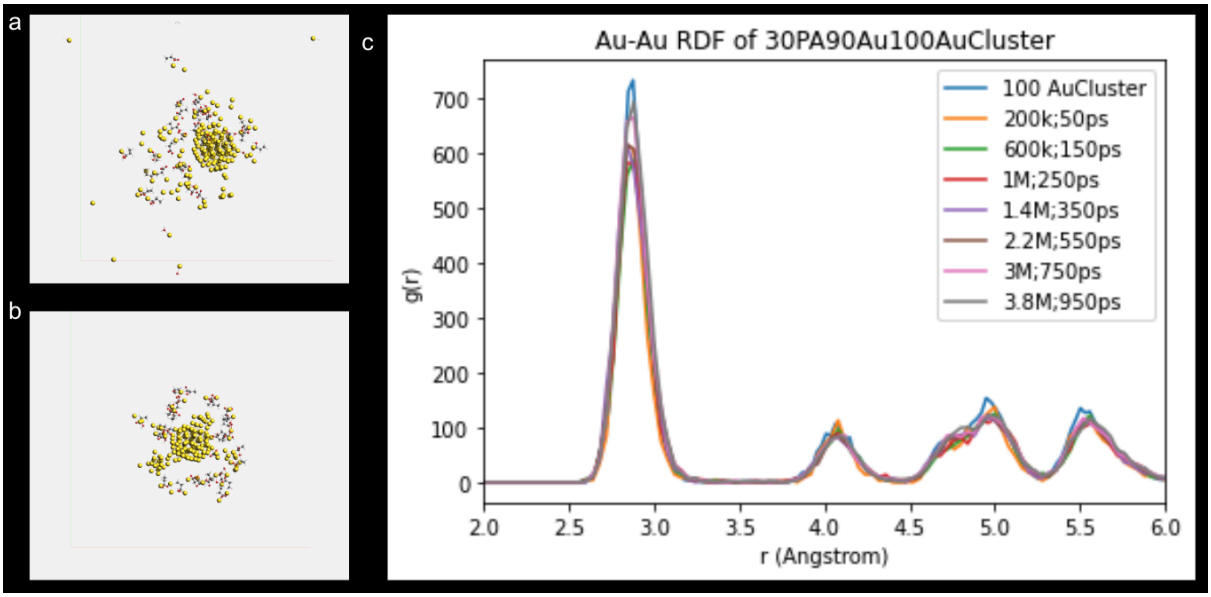


Figure A.3.6 RDF of 30 propionic acids with 90 free Au atoms and 100 Au cluster

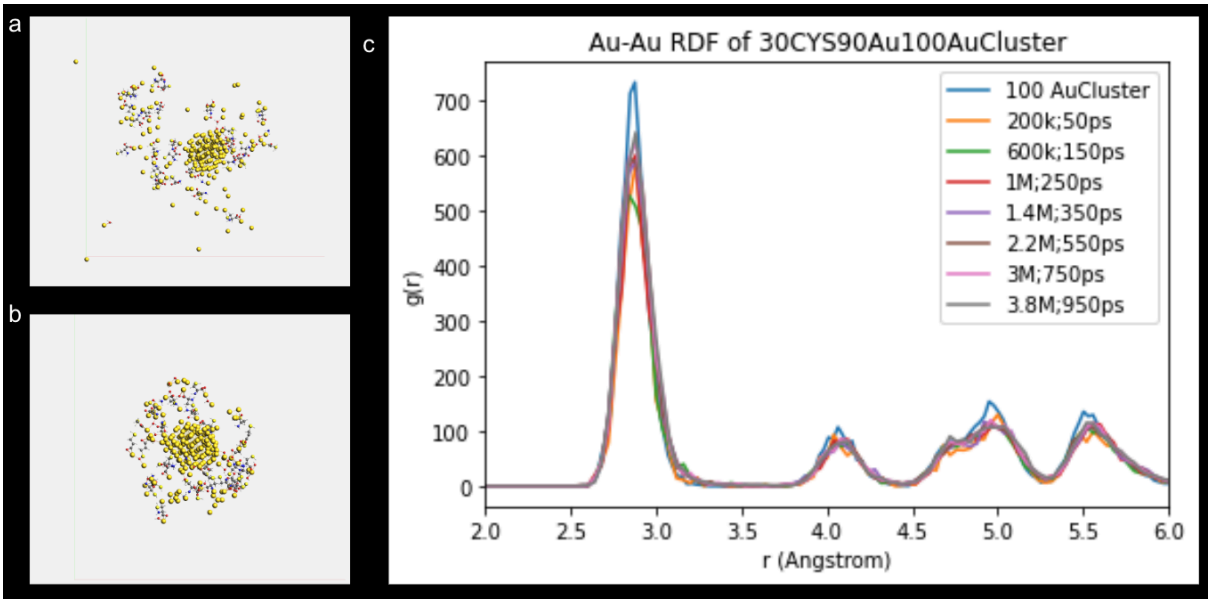


Figure A.3.7 RDF of 30 L-Cysteine with 90 free Au atoms and 100 Au cluster

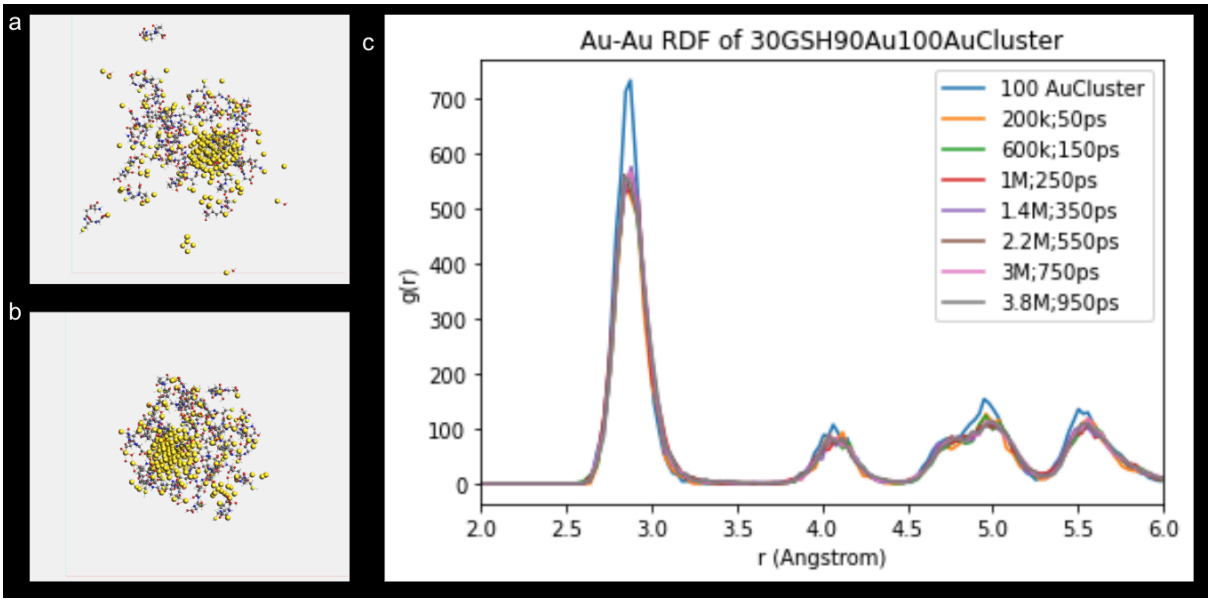


Figure A.3.8 RDF of 30 glutathione with 90 free Au atoms and 100 Au cluster

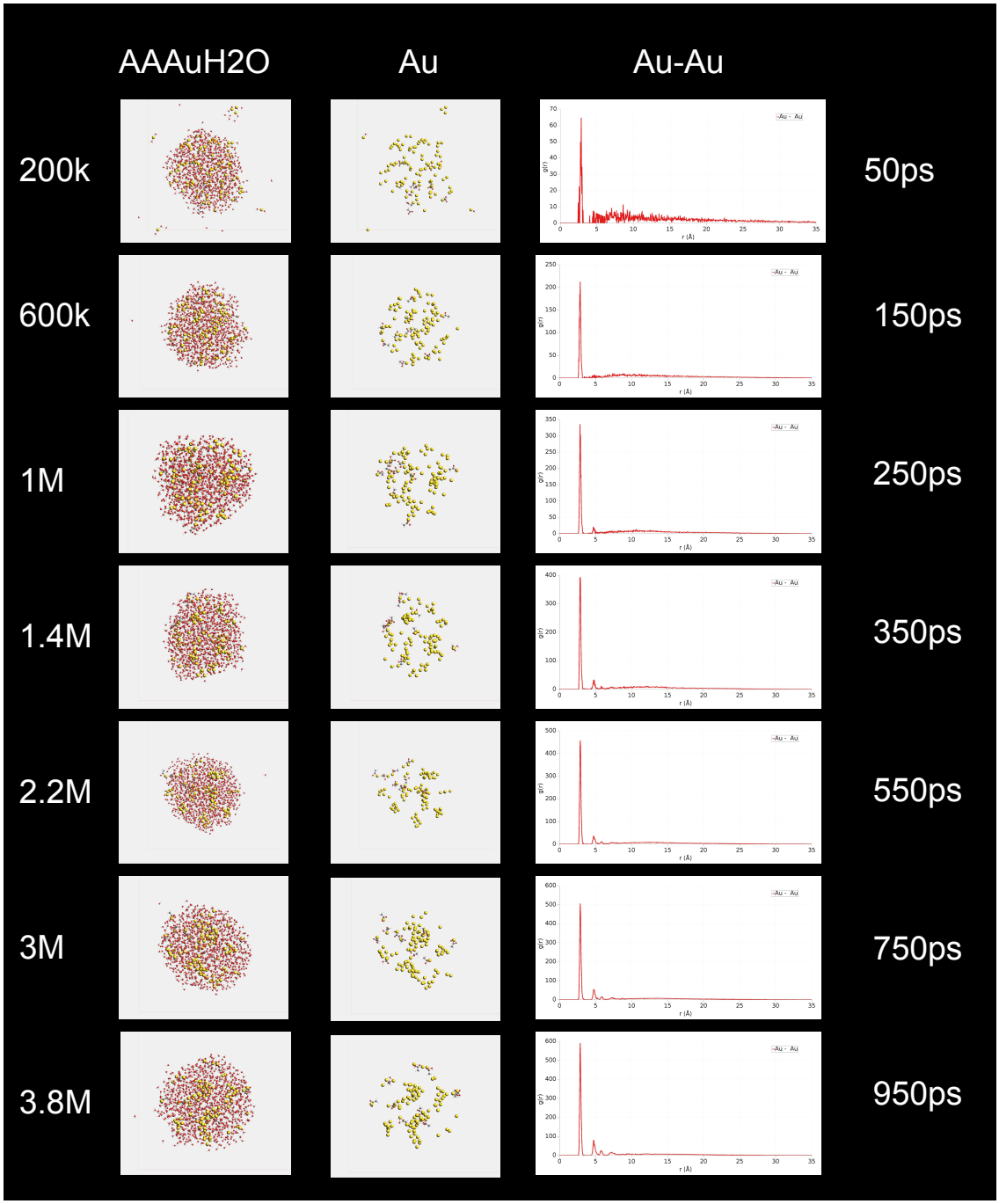


Figure A.3.9 Snapshot of the simulation box with RDF on all timestep for 10 acetic acid, 100 free Au atoms, 1000 water molecules

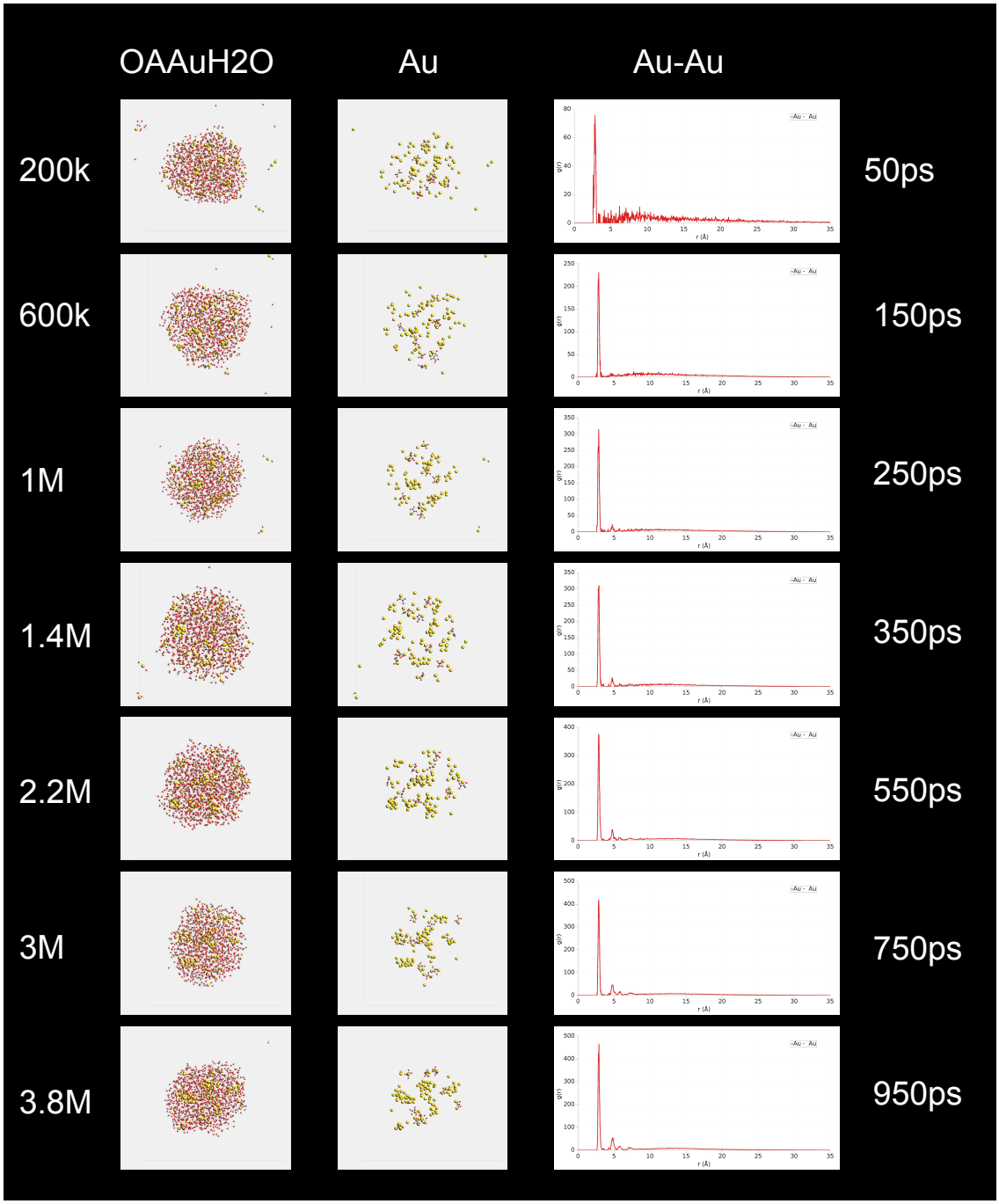


Figure A.3.10 Snapshot of the simulation box with RDF on all timestep for 10 oxalic acid, 100 free Au atoms, 1000 water molecules

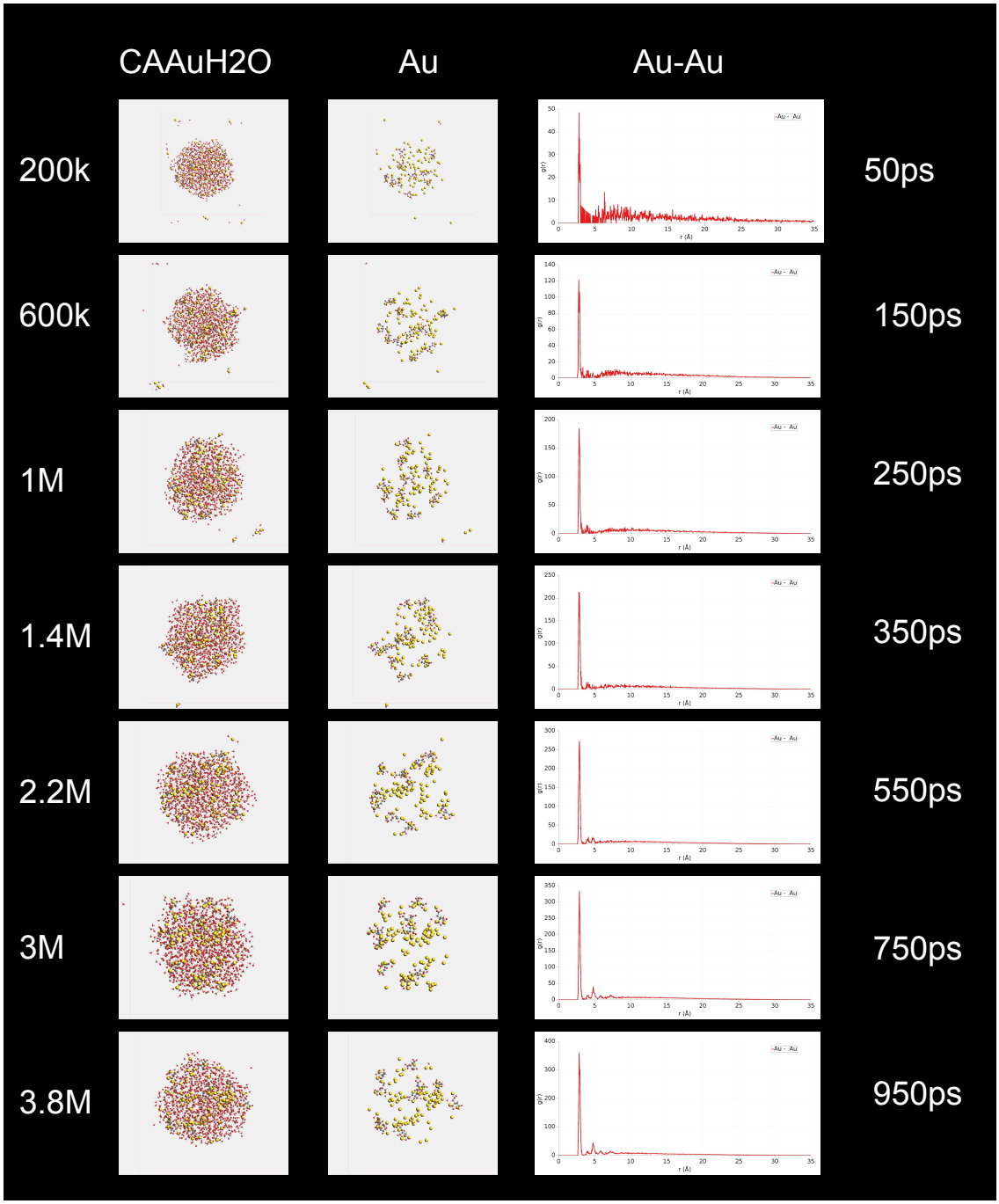


Figure A.3.11 Snapshot of the simulation box with RDF on all timestep for 10 citric acid, 100 free Au atoms, 1000 water molecules

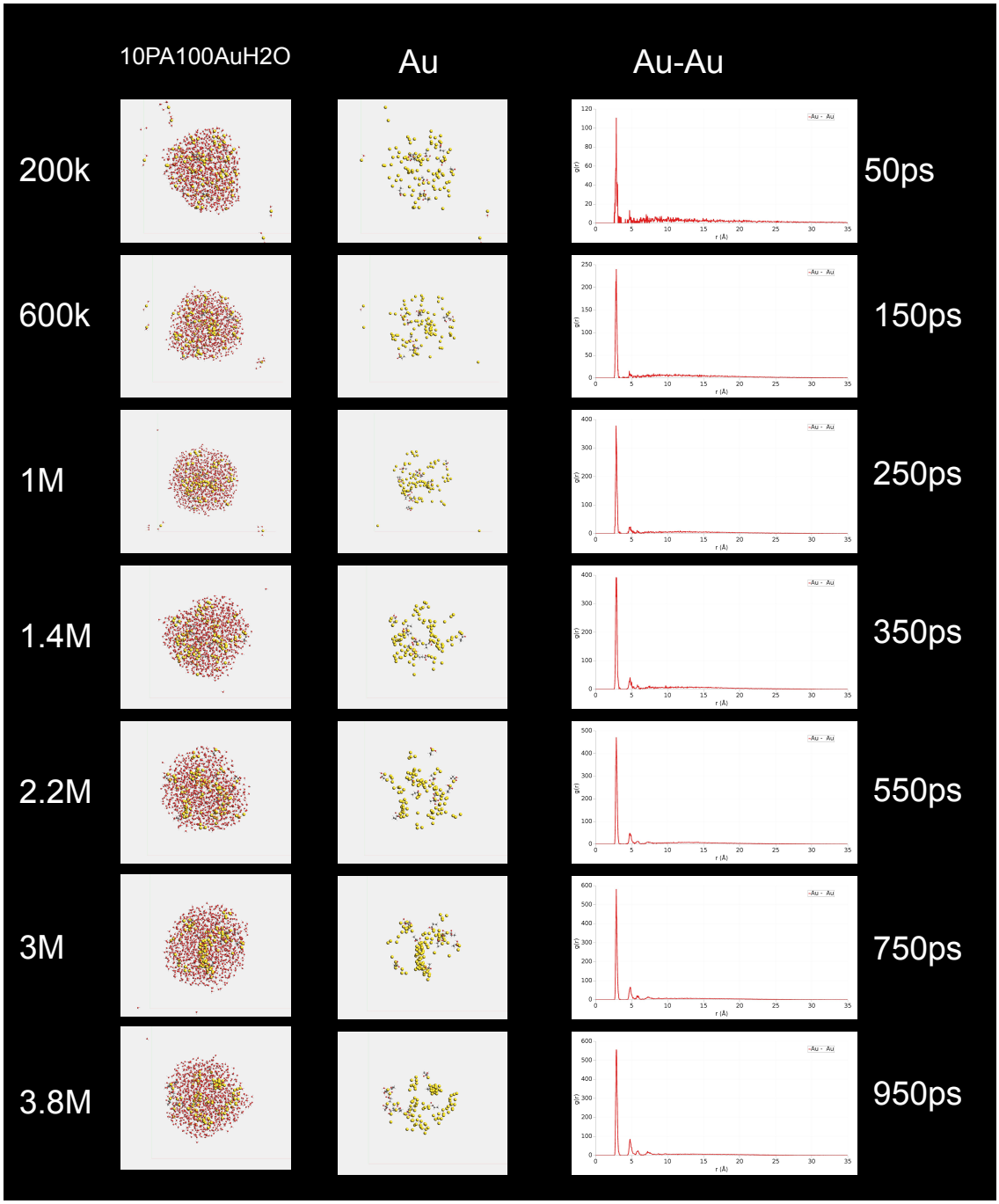


Figure A.3.12 Snapshot of the simulation box with RDF on all timestep for 10 propionic acid, 100 free Au atoms, 1000 water molecules

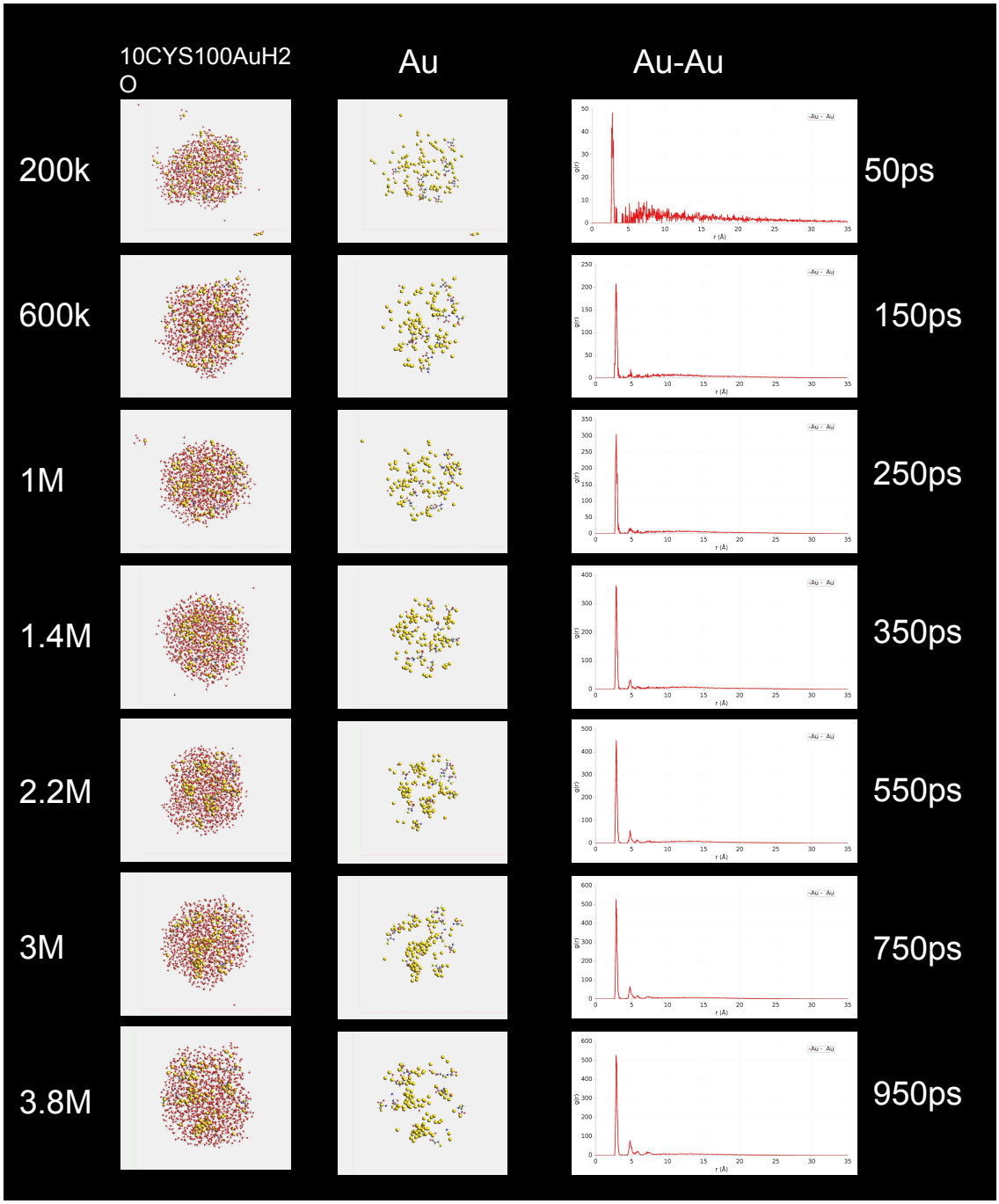


Figure A.3.13 Snapshot of the simulation box with RDF on all timestep for 10 L-cysteine, 100 free Au atoms, 1000 water molecules

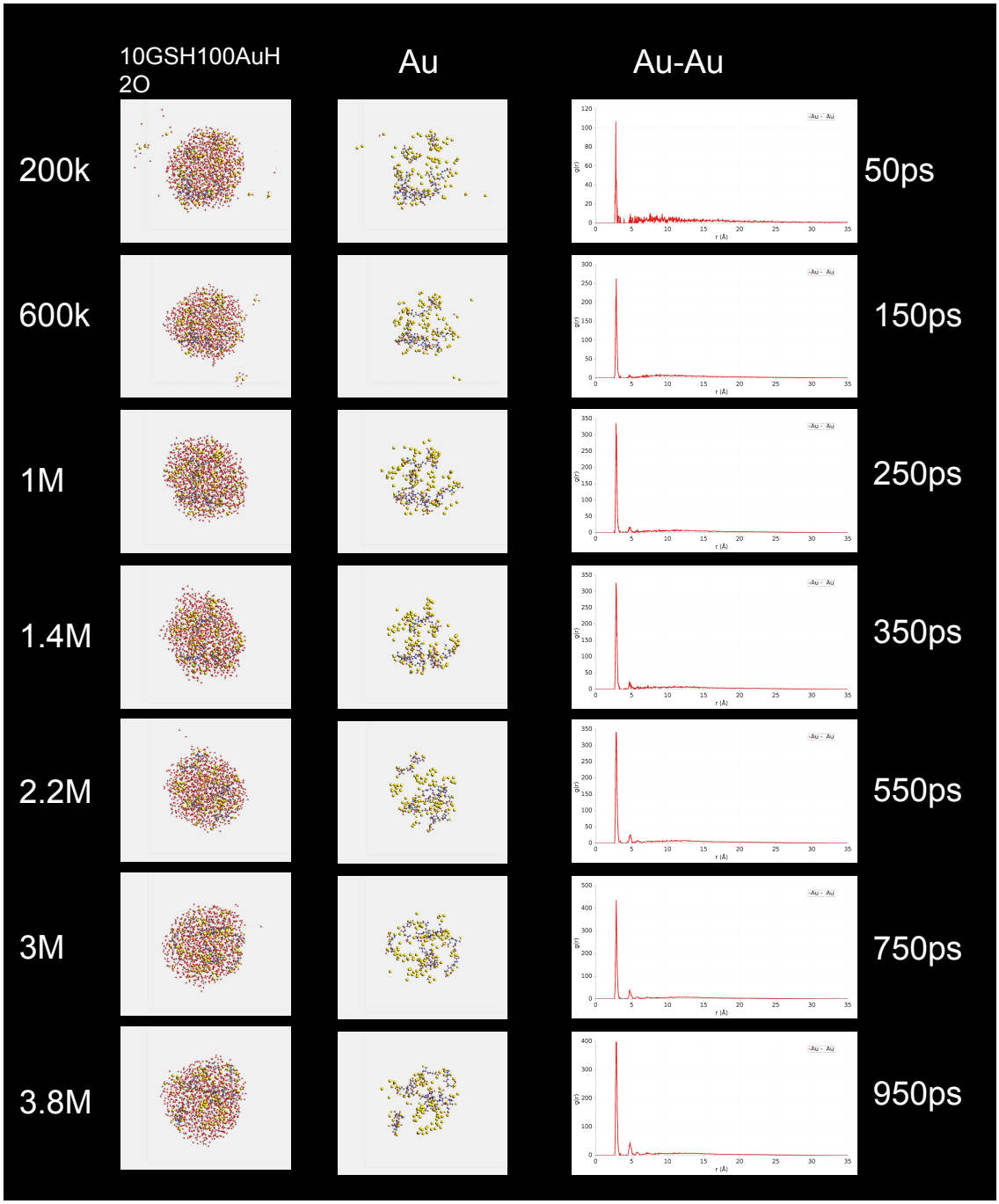


Figure A.3.14 Snapshot of the simulation box with RDF on all timestep for 10 glutathione, 100 free Au atoms, 1000 water molecules

Core with capping agent 90 free gold atom

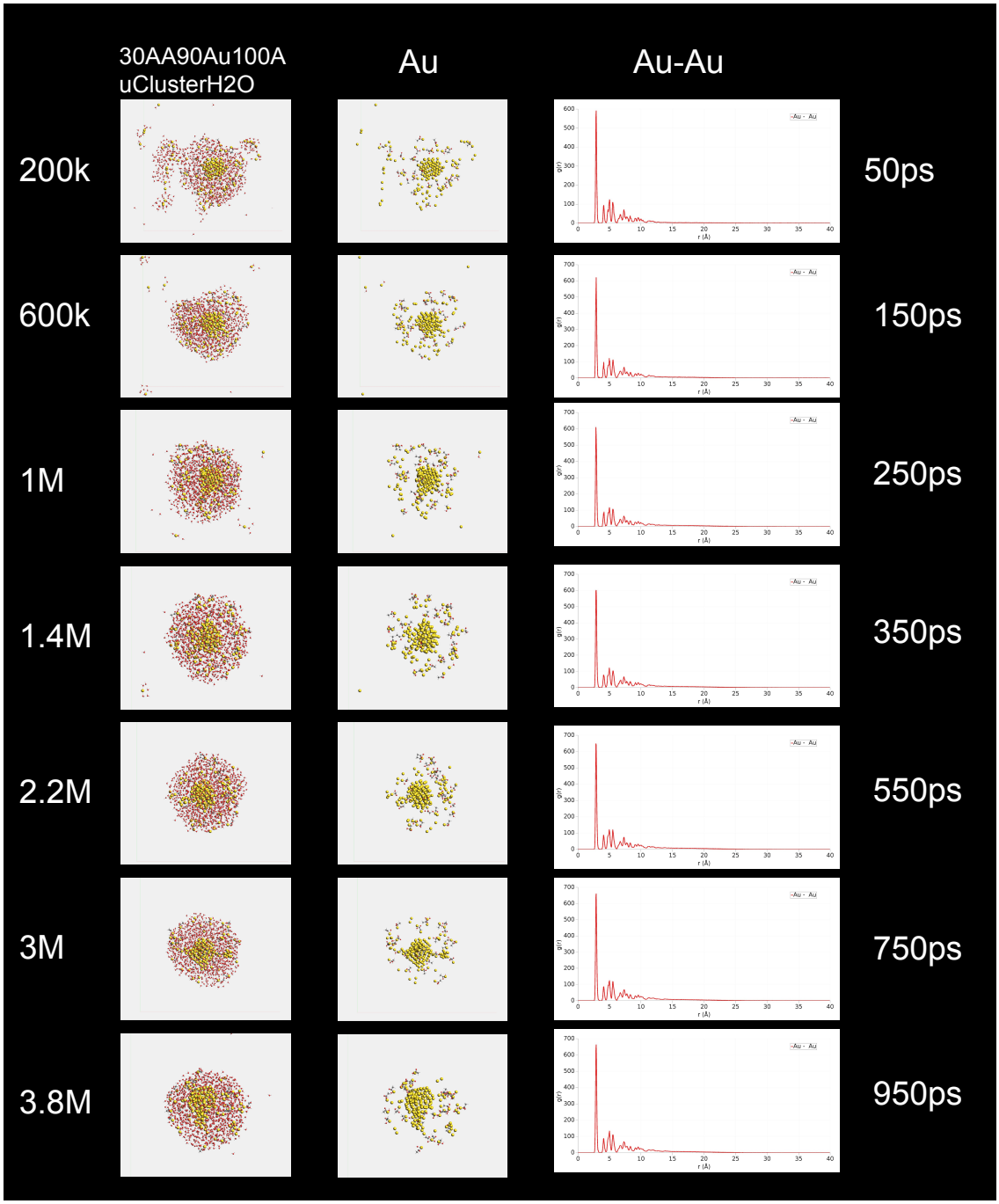


Figure A.3.15 Snapshot of the simulation box with RDF on all timestep for 30 acetic acid, 90 free Au atoms, 100-Au cluster, 1000 water molecules

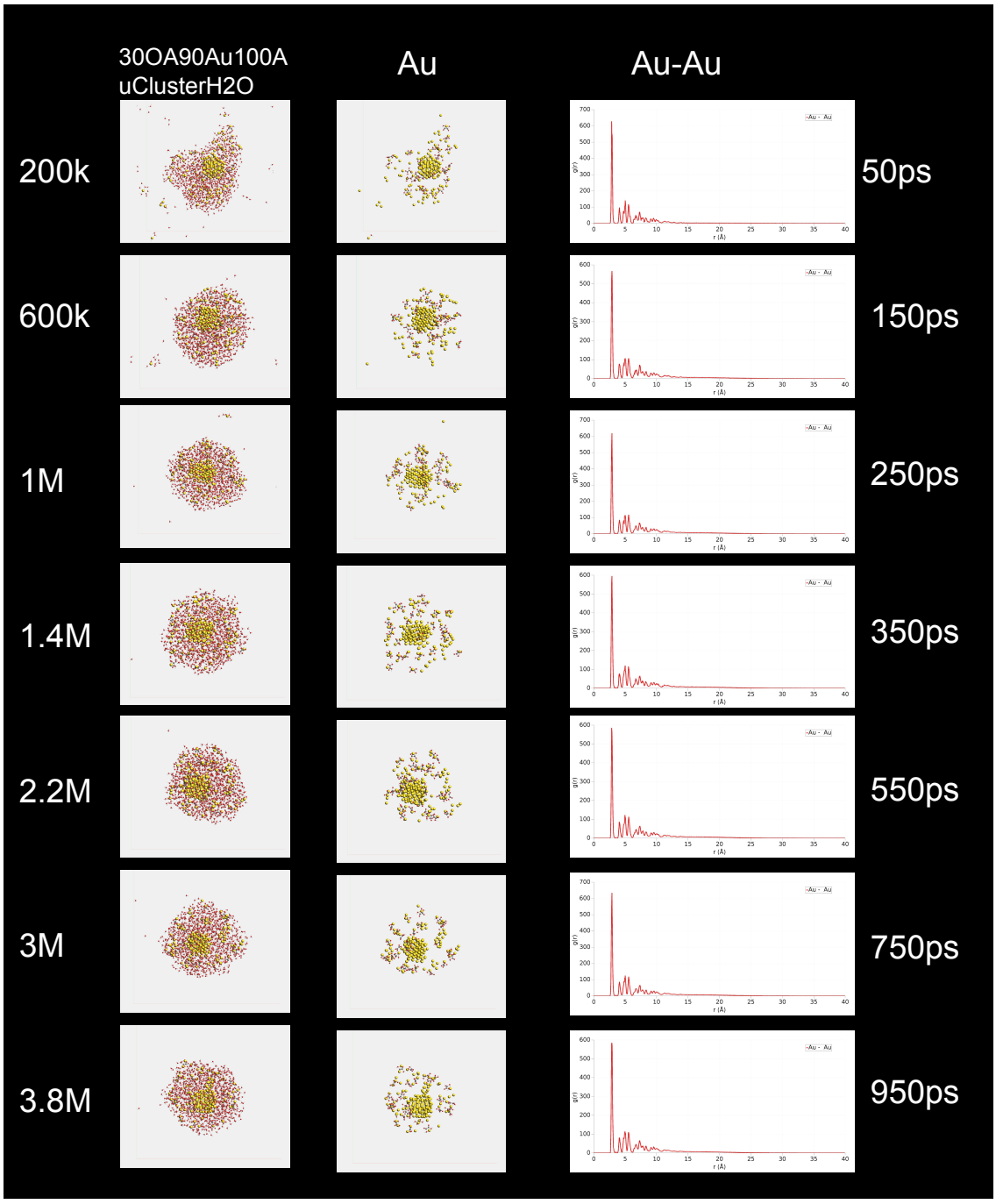


Figure A.3.16 Snapshot of the simulation box with RDF on all timestep for 30 oxalic acid, 90 free Au atoms, 100-Au cluster, 1000 water molecules

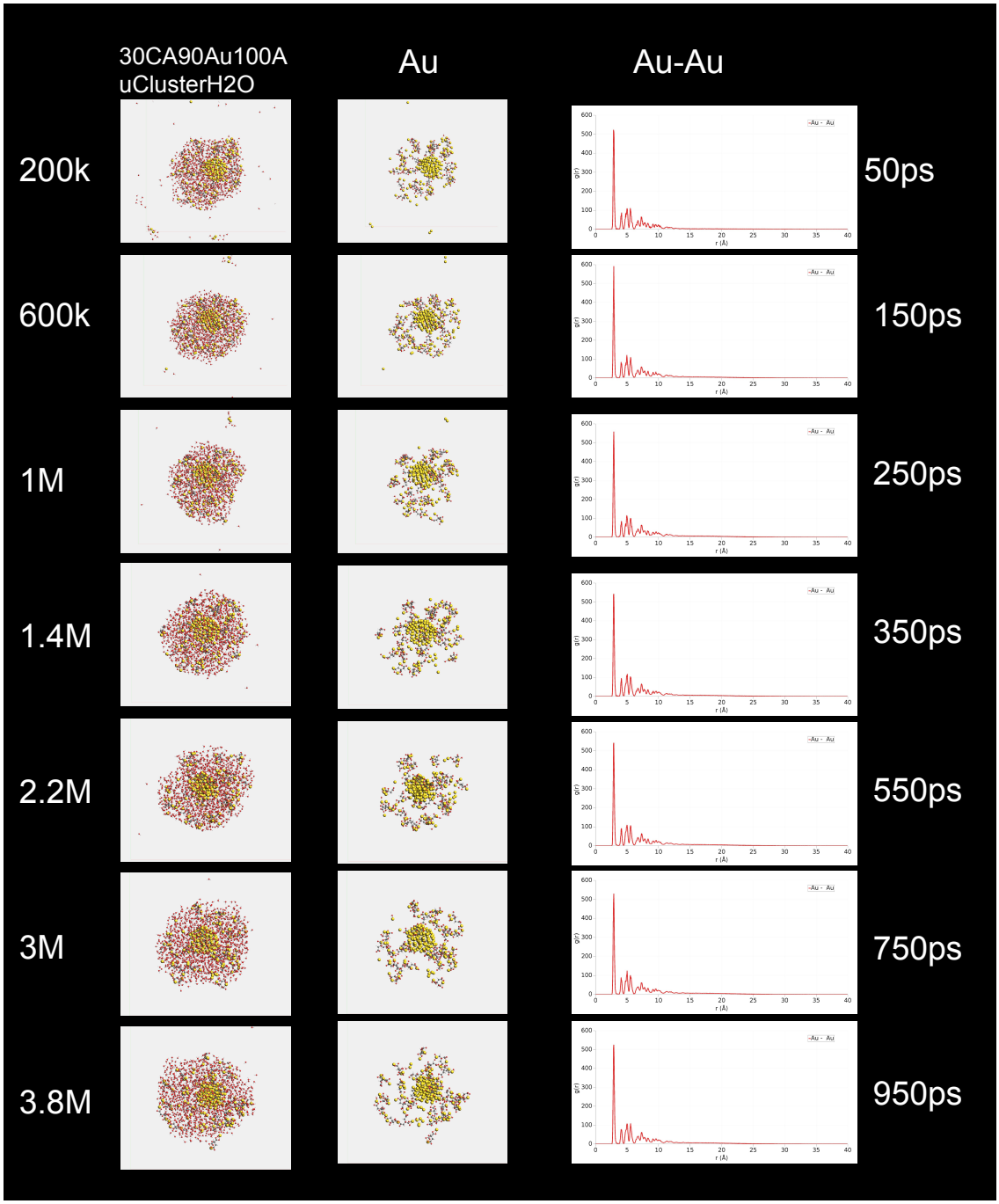


Figure A.3.17 Snapshot of the simulation box with RDF on all timestep for 30 citric acid, 90 free Au atoms, 100-Au cluster, 1000 water molecules

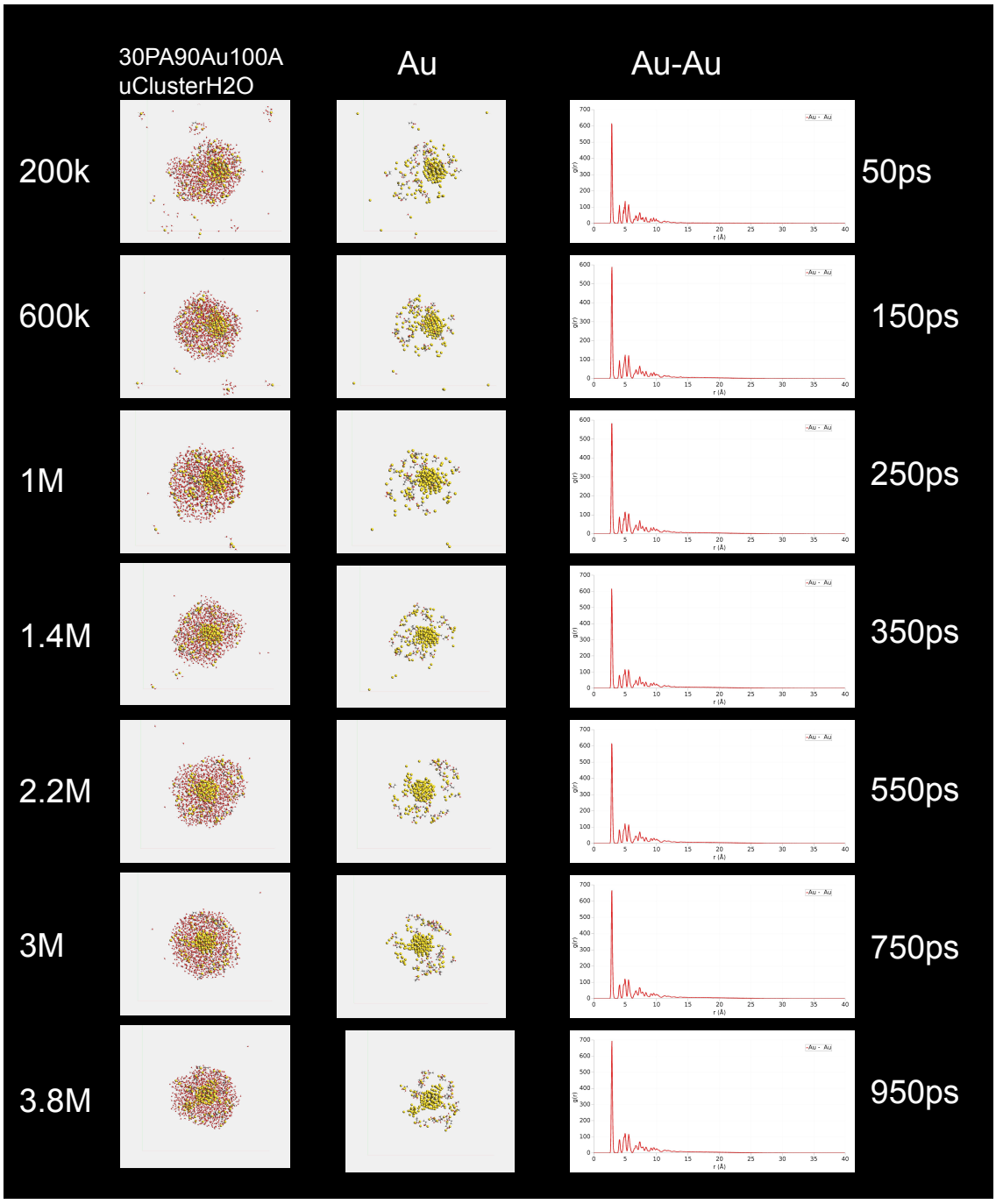


Figure A.3.18 Snapshot of the simulation box with RDF on all timestep for 30 propionic acid, 90 free Au atoms, 100-Au cluster, 1000 water molecules

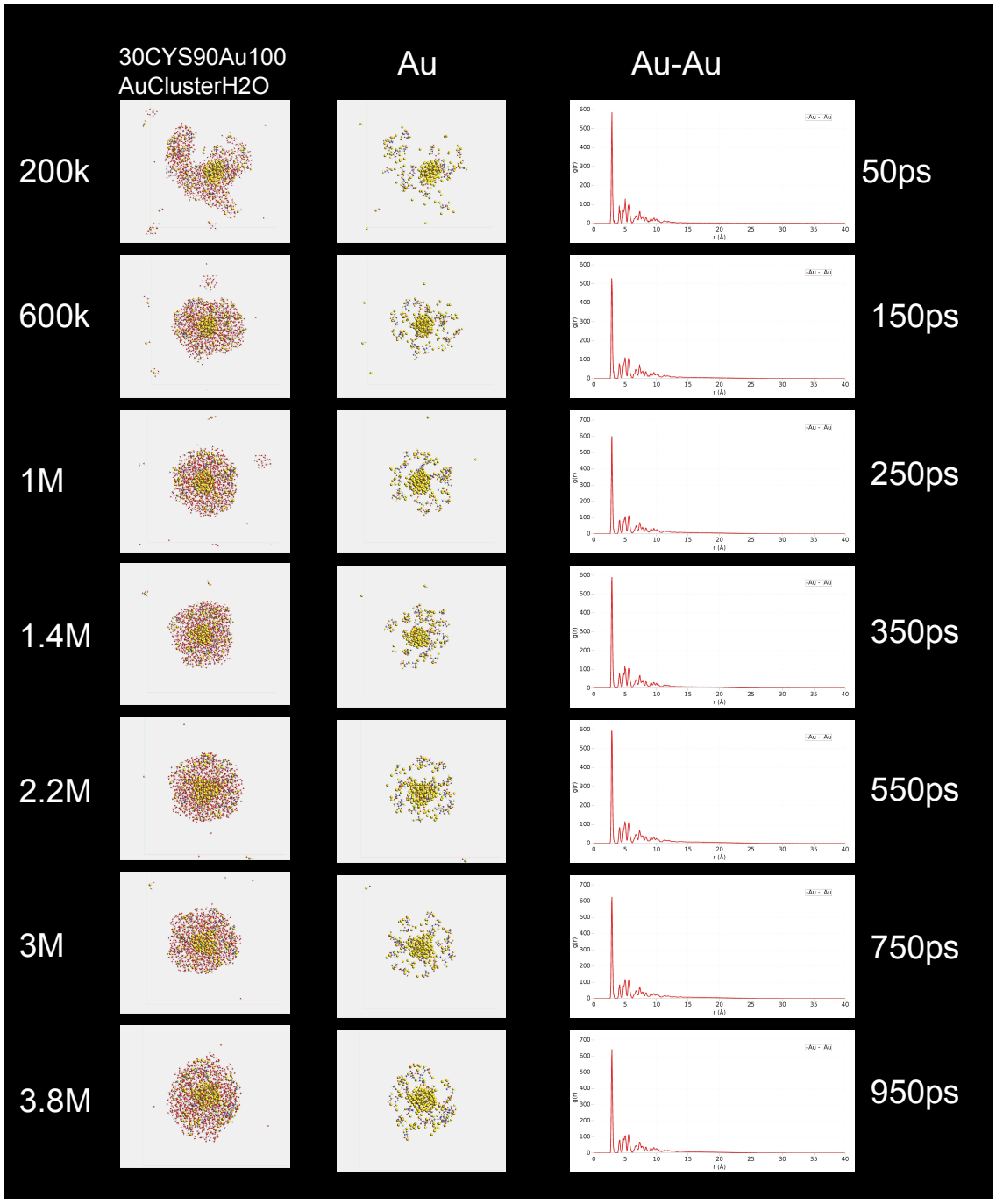


Figure A.3.19 Snapshot of the simulation box with RDF on all timestep for 30 L-cysteine, 90 free Au atoms, 100-Au cluster, 1000 water molecules

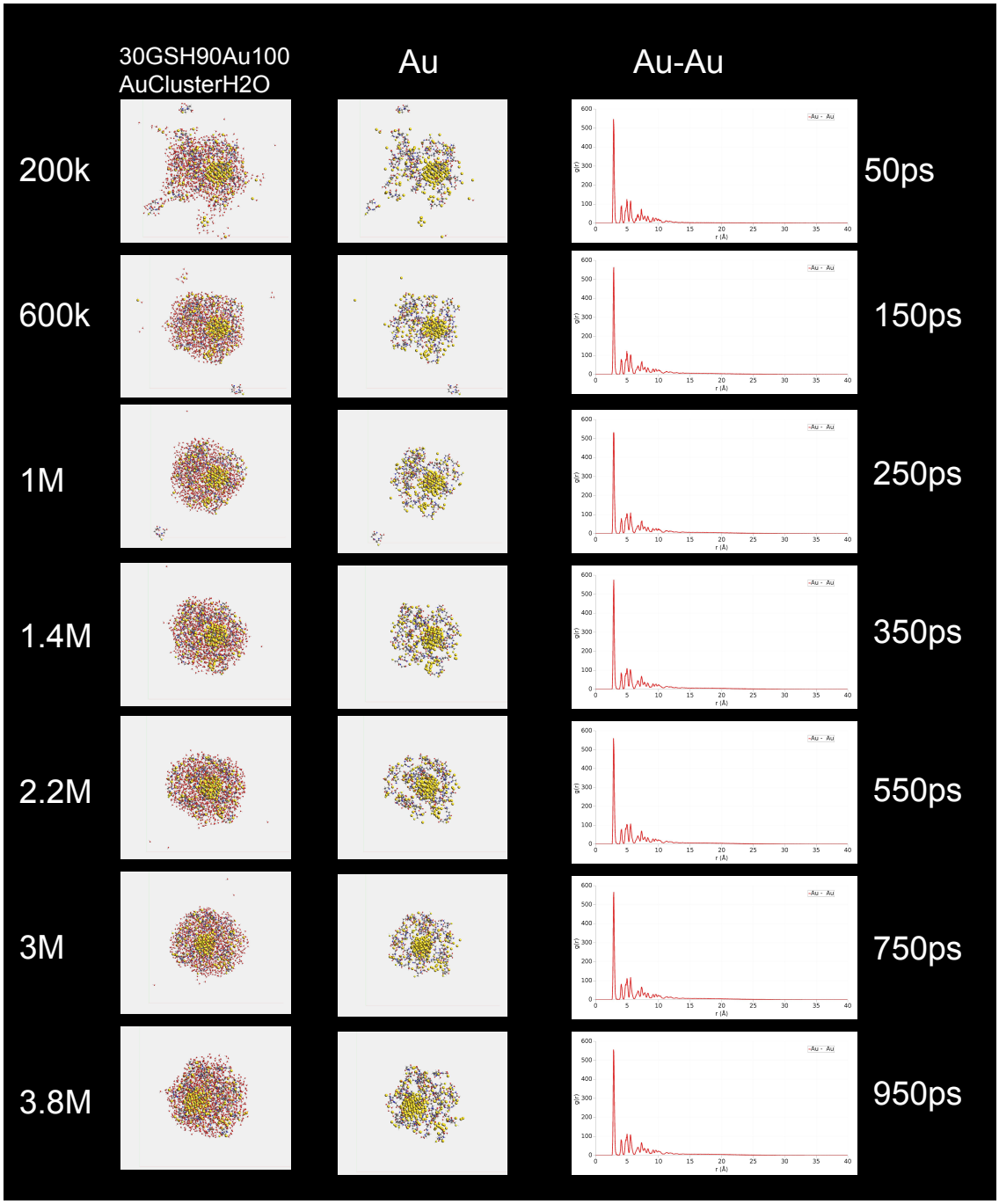


Figure A.3.20 Snapshot of the simulation box with RDF on all timestep for 30 glutathione, 90 free Au atoms, 100-Au cluster, 1000 water molecules

Others

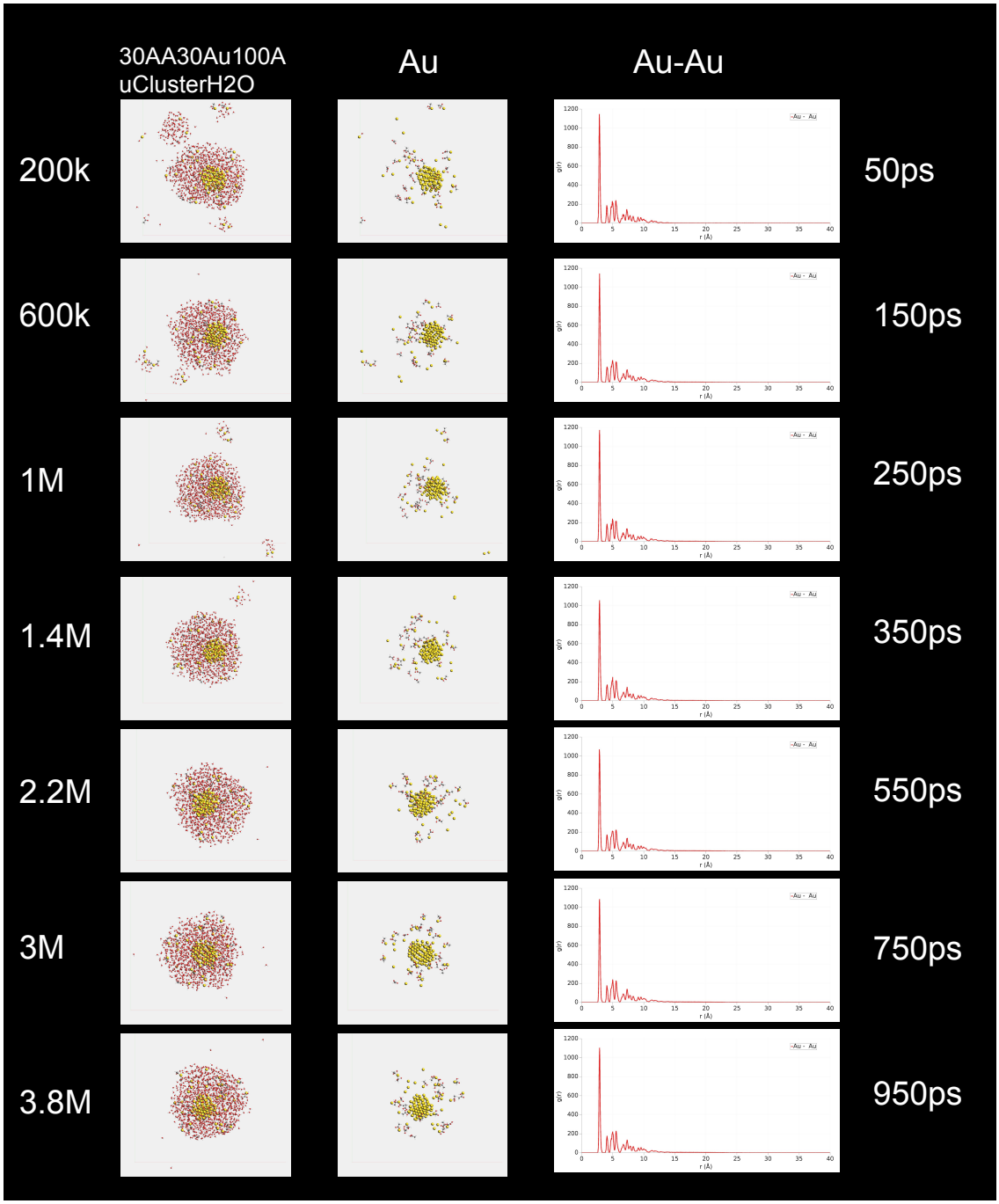


Figure A.3.21 Snapshot of the simulation box with RDF on all timestep for 30 acetic acid, 30 free Au atoms, 100-Au cluster, 1000 water molecules

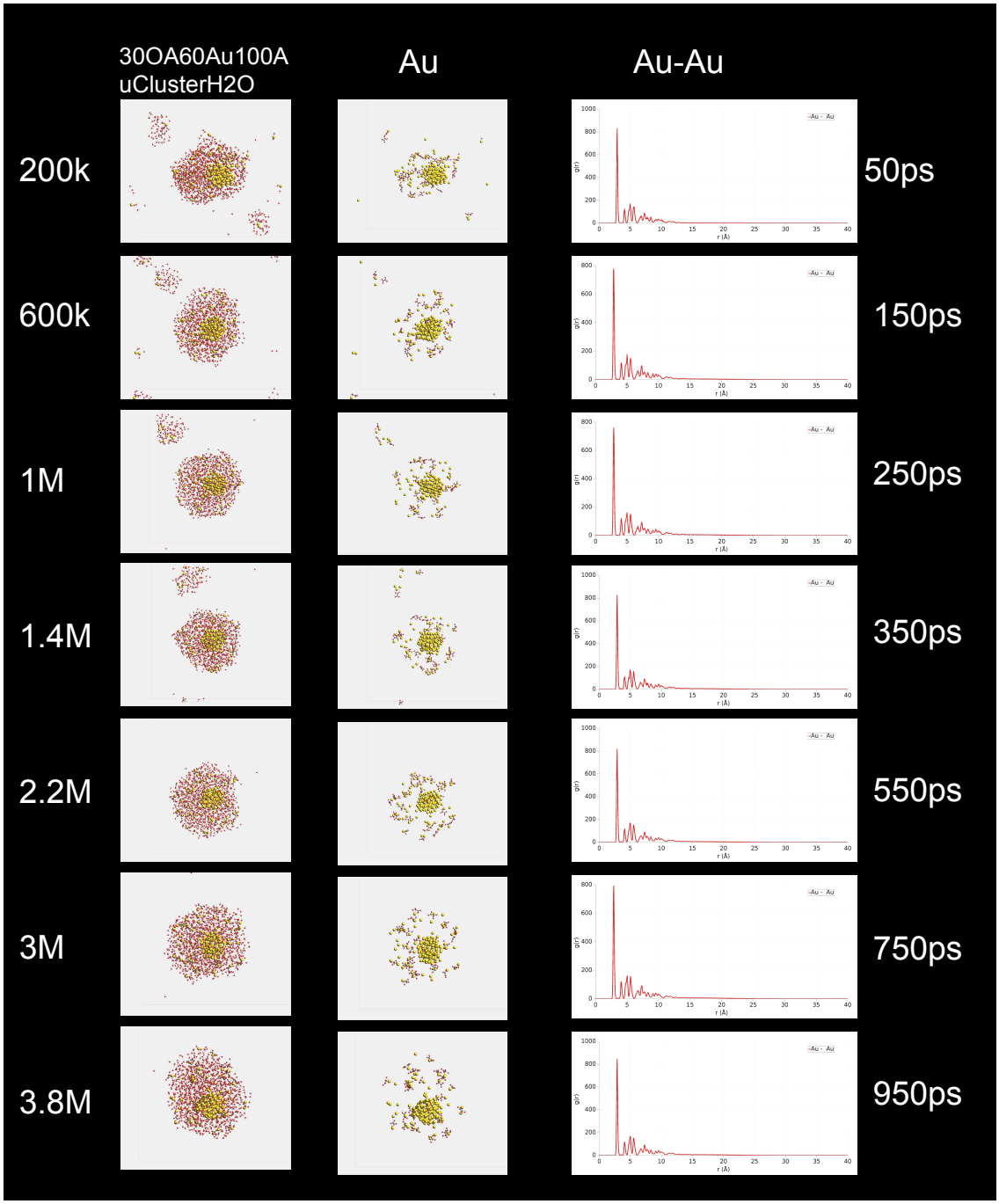


Figure A.3.22 Snapshot of the simulation box with RDF on all timestep for 30 oxalic acid, 60 free Au atoms, 100-Au cluster, 1000 water molecules

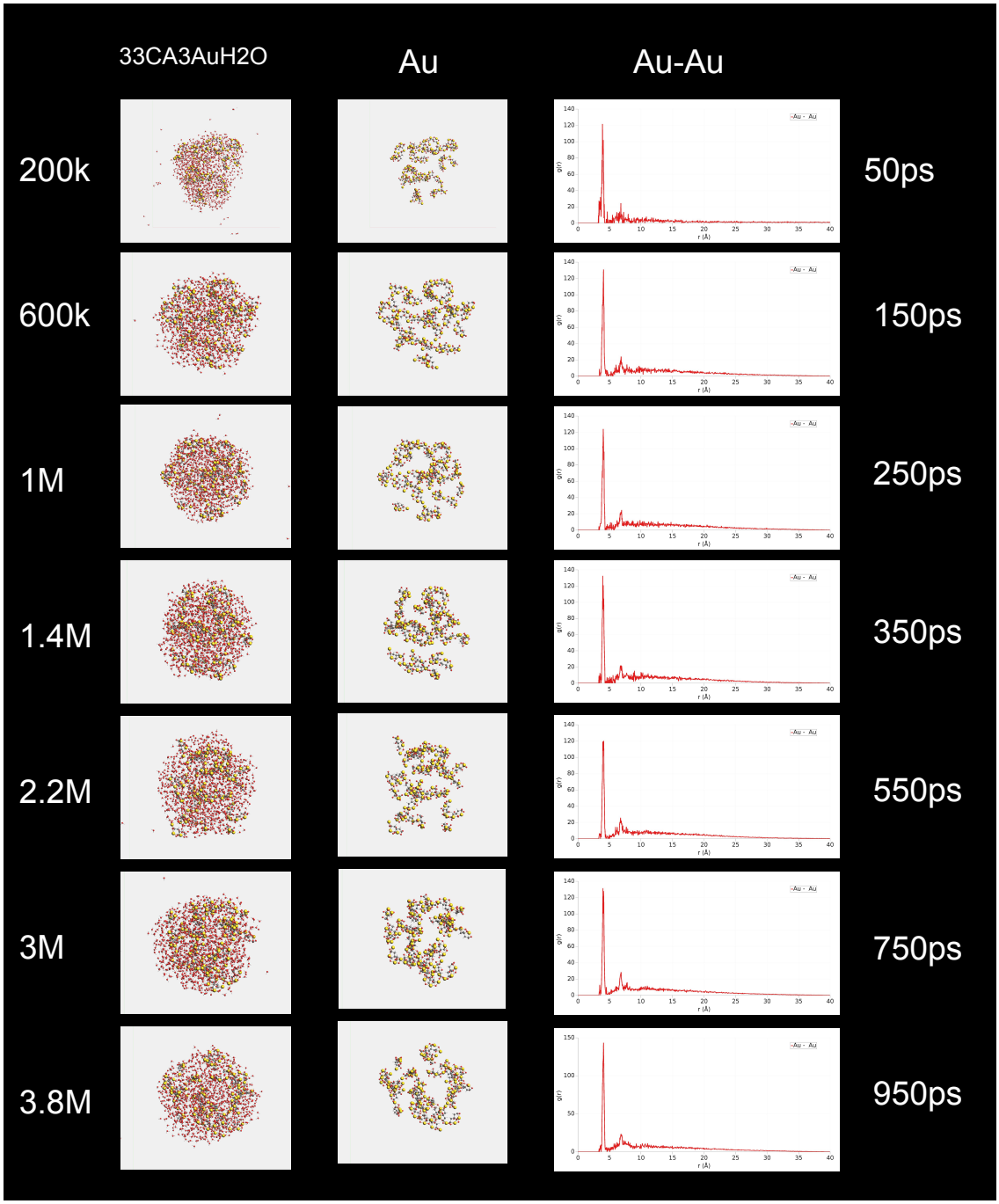


Figure A.3.23 Snapshot of the simulation box with RDF on all timestep for 30 citric acids bonded with 3 Au each, 1000 water molecules

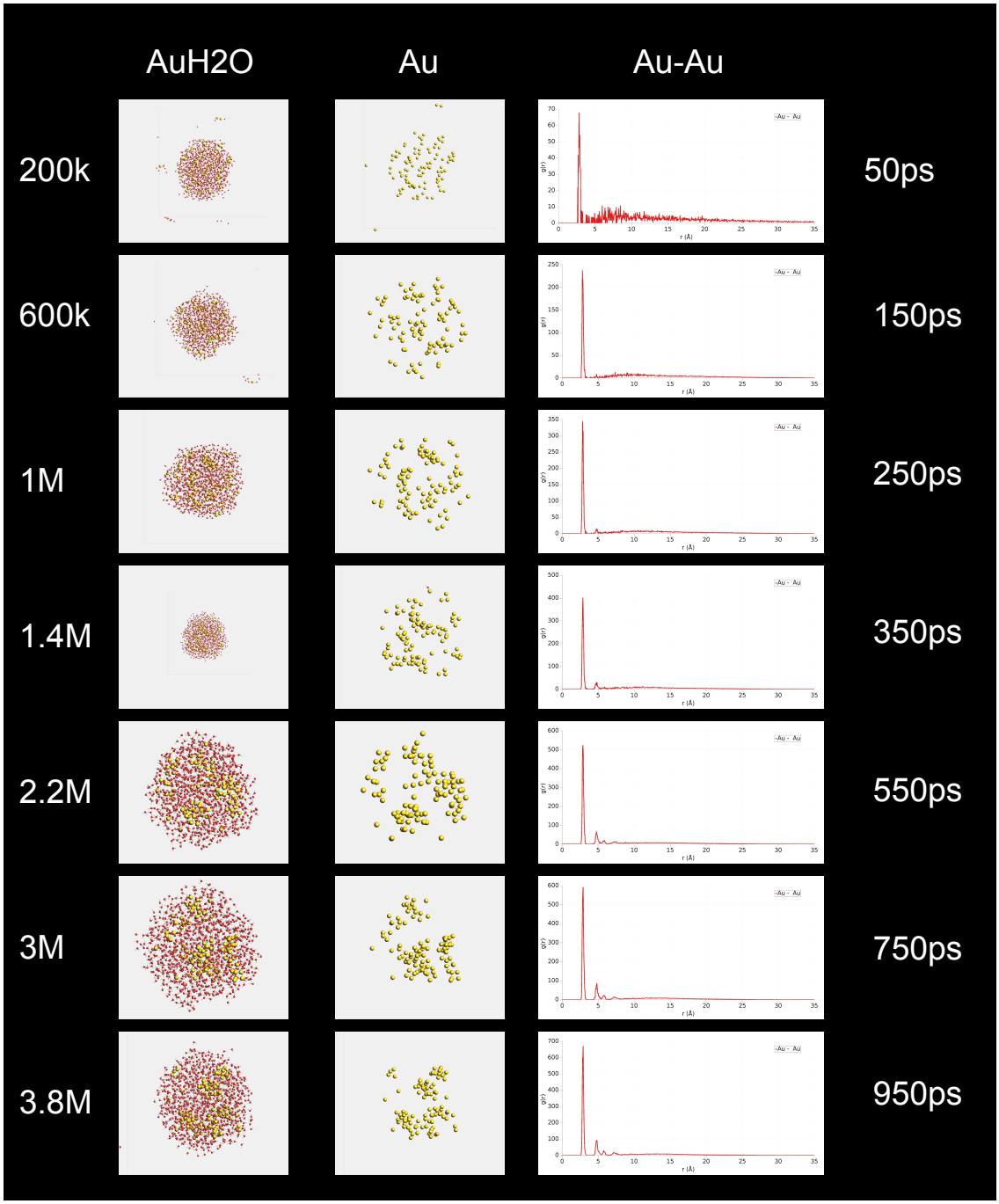


Figure A.3.24 Snapshot of the simulation box with RDF on all timestep for 100 free Au atoms, 1000 water molecules

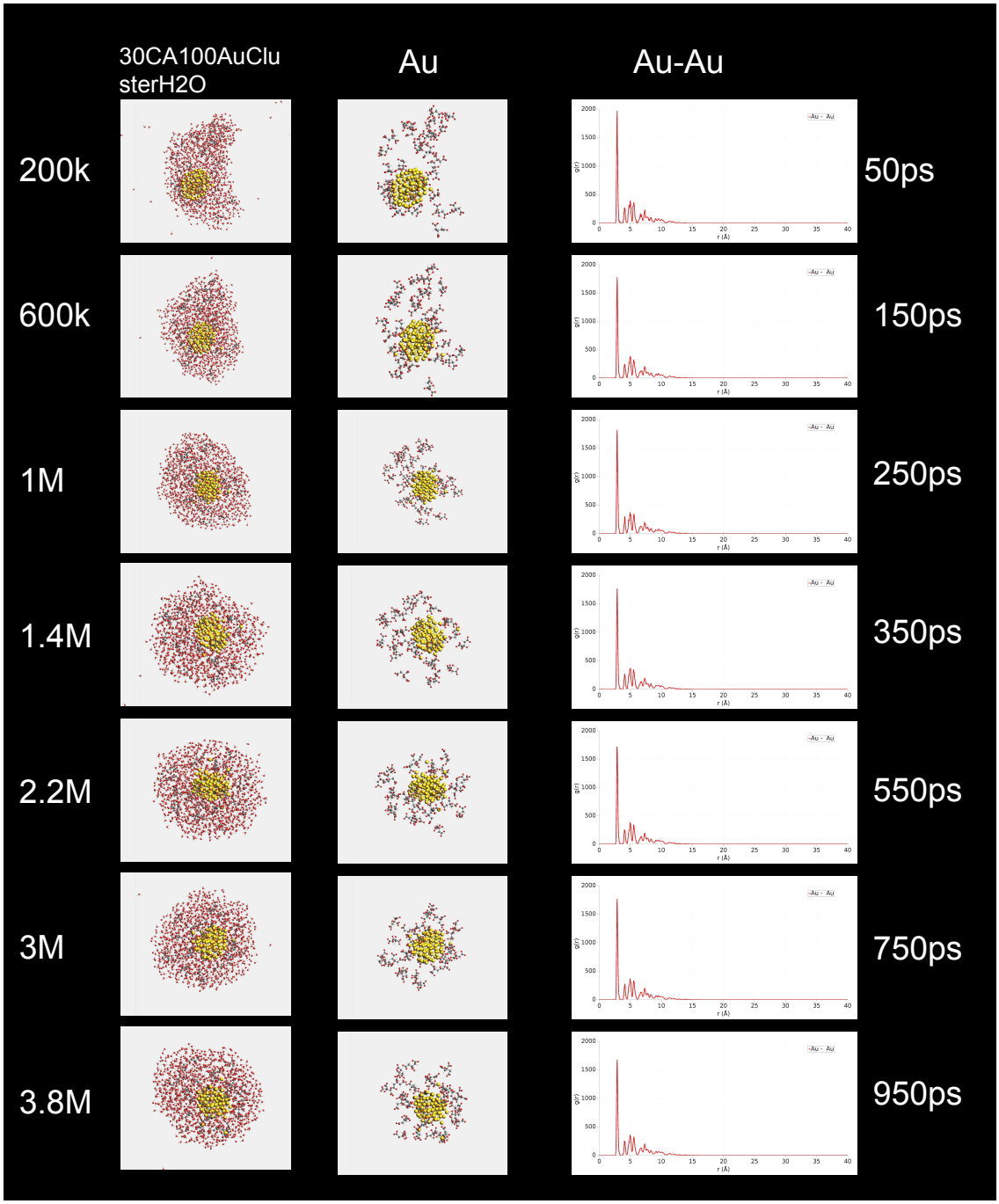


Figure A.3.25 Snapshot of the simulation box with RDF on all timestep for 30 citric acid, 100-Au cluster, 1000 water molecules.